



**HAL**  
open science

# Semiconductor Quantum Dots and Metallic Nanoparticles Based-Systems for Visible-light Redox Photocatalysis of Radical Reactions

Ali Dabbous

► **To cite this version:**

Ali Dabbous. Semiconductor Quantum Dots and Metallic Nanoparticles Based-Systems for Visible-light Redox Photocatalysis of Radical Reactions. Theoretical and/or physical chemistry. Université Grenoble Alpes [2020-..], 2022. English. NNT : 2022GRALV077 . tel-04812229

**HAL Id: tel-04812229**

**<https://theses.hal.science/tel-04812229v1>**

Submitted on 30 Nov 2024

**HAL** is a multi-disciplinary open access archive for the deposit and dissemination of scientific research documents, whether they are published or not. The documents may come from teaching and research institutions in France or abroad, or from public or private research centers.

L'archive ouverte pluridisciplinaire **HAL**, est destinée au dépôt et à la diffusion de documents scientifiques de niveau recherche, publiés ou non, émanant des établissements d'enseignement et de recherche français ou étrangers, des laboratoires publics ou privés.

## THÈSE

Pour obtenir le grade de

### DOCTEUR DE L'UNIVERSITÉ GRENOBLE ALPES

École doctorale : CSV- Chimie et Sciences du Vivant

Spécialité : Chimie Physique Moléculaire et Structurale

Unité de recherche : Systèmes Moléculaires et Nano Matériaux pour l'Énergie et la Santé- UMR SyMMES 5819 CEA-CNRS-UGA

### **Systèmes à Base de Quantum Dots et Nanoparticules Métalliques pour la Photocatalyse Redox de Réactions Radicalaires en Lumière Visible**

### **Quantum Dots and Metallic Nanoparticles Based-Systems for Visible-Light Redox Photocatalysis of Radical Reactions**

Présentée par :

**Ali DABBOUS**

Direction de thèse :

**Vincent MAUREL**

CEA

Directeur de thèse

**Jean-marie MOUESCA**

CEA

Co-Directeur de thèse

Rapporteurs :

**Fabrice ODOBEL**

DIRECTEUR DE RECHERCHE, CNRS délégation Bretagne et Pays de la Loire

**Adam PRON**

PROFESSEUR, Politechnika Warszawska

Thèse soutenue publiquement le **29 novembre 2022**, devant le jury composé de :

**Frédérique LOISEAU**

PROFESSEUR DES UNIVERSITES, Université Grenoble Alpes

Président du Jury

**Fabrice ODOBEL**

DIRECTEUR DE RECHERCHE, CNRS délégation Bretagne et Pays de la Loire

Rapporteur

**Adam PRON**

PROFESSEUR, Politechnika Warszawska

Rapporteur

**Raphaël SCHNEIDER**

PROFESSEUR, Université de Lorraine

Examineur

**Vincent MAUREL**

DIRECTEUR DE RECHERCHE, CEA centre de Grenoble

Directeur de thèse

**Jean-Marie MOUESCA**

DIRECTEUR DE RECHERCHE, CEA centre de Grenoble

Co-Directeur de thèse





***“Out of clutter, find Simplicity. From discord, find Harmony. In the middle of difficulty lies Opportunity.”***

**– Albert Einstein**



***Quantum Dots and Metallic  
Nanoparticles Based-Systems for  
Visible-Light Redox Photocatalysis of  
Radical Reactions***

**– Ali DABBOUS**



# Table of Content

Acknowledgements .....	1
List of abbreviations .....	4
General Introduction .....	7
CHAPTER I: .....	15
Semiconductor Quantum Dots' Systems for Photoredox Catalysis: State of the Art .....	15
I-1. Visible Light Photocatalysis: exploitation of the solar energy for synthetic chemistry.....	17
I-2. Background on Semiconductor Quantum Dots.....	20
I-2.1. Semiconductor Quantum Dots: Discovery of the Quantum confinement effect. ....	20
I-2.2. Quantum Dots' preparation.....	24
I-2.3. Core-shell Quantum Dots.....	27
I-2.3. Quantum Dots as redox photocatalyst: working principle. ....	29
I-2.4. Quantum Dots electronic properties: Estimation of the band edge energies.....	30
I-2.5. Challenges in Quantum Dots' Photocatalysis: Optimization of the Ligand layer. ....	34
I-3. Application of Quantum Dots as photocatalysts in organic transformations. ....	38
I-3.1. QDs-photocatalyzed net reductive reactions. ....	41
I-3.2. CdS QDs as powerful photoreductants for dehalogenation reaction initiated by Auger processes.....	46
I-3.3. QDs-photocatalyzed net oxidative reactions. ....	48
I-3.3. QDs-photocatalyzed bond formation reactions. ....	52
I-3.4. CdSe QDs as photocatalyst for triplet excited state reactions.....	66
I-3.6. Quantum Dot Gels as efficient photocatalysts for organic reactions.....	67
I-3.6. Other photocatalytic reactivities Using Quantum Dots .....	68
I-4. Enhancing the photogenerated charge separation: Quantum Dots connected to metal nanoparticles.....	71
I-4.1. Suppressing the photogenerated charge recombination in QDs. ....	71
I-4.2. Fast charge transfer from photoexcited semiconductors to metal nanoparticles. ....	73
I-4.3. Quantum Dots and metal nanoparticles hybrid structure for enhanced photocatalytic activities. ....	77
Conclusion.....	80
References .....	81

<b>CHAPTER II:</b> .....	<b>93</b>
<b>Quantum Dots mediated photoredox C-C bonds formation: oxidation of Aryl-amines leading to Tropane skeletons after two successive allylations</b> .....	<b>93</b>
<b>II-1. Introduction</b> .....	<b>95</b>
<b>II-2. Investigation of the suitable kinds of Quantum Dots for the desired oxidations: DFT calculations for the redox potential of 1-Phenylpyrrolidine (PhPyr)</b> .....	<b>97</b>
<b>II-3. Synthesis and characterization of the Quantum Dots.</b> .....	<b>99</b>
<b>II.4. Charge transfer between the Quantum Dots and the reaction's substrate.</b> .....	<b>104</b>
<b>II-4.1. Photoluminescence Quenching of the Quantum Dots by 1-Phenyl-pyrrolidine (PhPyr).</b> .....	<b>104</b>
<b>II-4.1. Charge transfer from the photoexcited QDs, and the effect of the energy levels positions in the core-shell QDs.</b> .....	<b>107</b>
<b>II-4. Photocatalytic activity of the Quantum Dots</b> .....	<b>109</b>
<b>II-4.1. Screening the as-synthesized QDs for the C-C Vinylation reaction.</b> .....	<b>109</b>
<b>II-4.2. Test of selected as-synthesized QDs for the 2-step reaction of the synthesis of tropane derivative.</b> .....	<b>113</b>
<b>II-4.3. Surface ligands optimization: Case of CdS and CdSe QDs</b> .....	<b>114</b>
<b>II-4.4. Effect of the ligands optimization of the different QDs for the C-C vinylation reaction.</b> .....	<b>117</b>
<b>II-4.5. Effect of the ligands optimization of different QDs for the 2-step reaction of the synthesis of tropane derivatives.</b> .....	<b>122</b>
<b>II-5. Scope of radical traps</b> .....	<b>126</b>
<b>II-6. Reaction scope with different N- aryl amines</b> .....	<b>127</b>
<b>II-7: Purification and re-use of the QDs after the reactions</b> .....	<b>132</b>
<b>II-8. Optimization of the ligand layer: Effect on the stability and the reusability of the QDs.</b> ....	<b>132</b>
<b>II-9: Electrochemical analysis: Investigations of the mechanistic steps (reaction's stopping step) and impact of the para-substituents of the N-Arylamines.</b> .....	<b>135</b>
<b>II-10. Proposed catalytic mechanisms</b> .....	<b>140</b>
<b>II-10.1. Photocatalytic mechanism for the 1-step C-C vinylation coupling reaction.</b> .....	<b>140</b>
<b>II-10.2. Photocatalytic mechanism for the 2-step Tropane derivatives synthesis reaction.</b> ....	<b>142</b>
<b>II-10.3. Selectivity of the radical formation and the stability of the final product: pKa calculations</b> .....	<b>144</b>
<b>II-10.4. Photocatalytic activity of the different types of QDs: Insights into the mechanistic redox steps</b> .....	<b>146</b>
<b>Conclusion</b> .....	<b>148</b>
<b>References</b> .....	<b>149</b>
<b>Appendix Chapter II</b> .....	<b>153</b>

<b>CHAPTER III:</b> .....	<b>177</b>
<b>Hybrid CdSe/ZnS Quantum Dots-Gold Nanoparticles Composites Assembled by Click Chemistry: Towards Affordable and Efficient Redox Photocatalysts Working with Visible Light</b> .....	<b>177</b>
<b>Abstract</b> .....	<b>179</b>
<b>III- 1. Introduction</b> .....	<b>180</b>
<b>III-2. Synthesis and characterization of QD-AuNP composites</b> .....	<b>183</b>
<b>III-2.1 Synthesis and characterization of Gold nanoparticles (AuNP).</b> ....	<b>183</b>
<b>III-2.1 CdSe/ZnS core-shell Quantum Dots</b> .....	<b>187</b>
<b>III-2.3. Assembly of water-soluble CdSe/ZnS QD with AuNP by click reaction.</b> ....	<b>190</b>
<b>III-3. Probing the efficiency of QD-AuNP composites as photocatalysts</b> .....	<b>195</b>
<b>III-3.1. Effect of the QD concentration when using CdSe/ZnS QD alone as photocatalysts</b> .....	<b>195</b>
<b>III-3.2. Enhanced photocatalytic activity using QD-AuNP composites as photocatalysts</b> .....	<b>197</b>
<b>III-3.3. Quantitation of the photocatalytic activity improvement – Internal QY vs. QD absorbed photons.</b> ....	<b>202</b>
<b>III-3.3. Comparison of the photocatalytic activity of QD-AuNP by using irradiation in the QD exciton range (590nm) or in the AuNP plasmon resonance band range (528nm).</b> ....	<b>203</b>
<b>III-4 – Mechanistic Studies</b> .....	<b>206</b>
<b>III-4.1. Quenching of QD fluorescence in QD-AuNP composites</b> .....	<b>206</b>
<b>III-4.2-Blue shift of the plasmon band due to the accumulation of electrons when irradiating QD-AuNP composites in the presence of the electron donor.</b> ....	<b>207</b>
<b>III-4.3. Proposed mechanism for the charge separation within the QD-AuNP composite and for the charge transfers to the electron donor and acceptor during the different kinetic regimes.</b> .....	<b>211</b>
<b>III-4.4. Proposed mechanism for the absorption of light leading to photocatalysis with the QD-AuNP composites.</b> .....	<b>214</b>
<b>III-4.5 Possible enhancement of light absorption by QD in the QD-AuNP composites due to local electromagnetic field enhancement in the vicinity of AuNP</b> .....	<b>215</b>
<b>Conclusion</b> .....	<b>217</b>
<b>Appendix Chapter III:</b> .....	<b>218</b>
<b>References</b> .....	<b>232</b>

<b>CHAPTER IV:</b> .....	<b>237</b>
<b>Materials and Methods</b> .....	<b>237</b>
<b>Abstract</b> .....	<b>239</b>
<b>Solvents and chemicals</b> .....	<b>239</b>
<b>IV-1. Quantum Dots' Synthesis</b> .....	<b>240</b>
<b>IV-1.1. Synthesis and purification of CdS Quantum Dots</b> .....	<b>241</b>
<b>IV-1.2. Purification of the synthesized CdS QDs</b> .....	<b>242</b>
<b>IV-1.3. Synthesis of CdSe Quantum Dots</b> .....	<b>243</b>
<b>IV-1.4. Synthesis of Inverted type-I CdS-CdSe Quantum Dots</b> .....	<b>244</b>
<b>IV-1.5. Synthesis of Quasi Type-II CdSe-CdS Quantum Dots</b> .....	<b>246</b>
<b>IV-1.6. Synthesis of InP and InP-ZnS Quantum Dots</b> .....	<b>248</b>
<b>IV-2. Ligand exchange procedures</b> .....	<b>249</b>
<b>IV-2.1. Ligand exchange using Histidine and (4-azidobenzyl)phosphonic acid</b> .....	<b>249</b>
<b>IV-2.2. Ligand exchange using 3-phosphonoproponic (PPAc)</b> .....	<b>250</b>
<b>IV-2.3. Partial ligand exchange using octylphosphonic acid (OPAc)</b> .....	<b>251</b>
<b>IV-3. Synthesis and Functionalization of Gold Nanoparticles (AuNP)</b> .....	<b>251</b>
<b>IV-3.1 Synthesis of Gold Nanoparticles</b> .....	<b>251</b>
<b>IV-3.1 Functionalization of Gold Nanoparticles</b> .....	<b>252</b>
<b>IV-4. Synthesis of CdSe/ZnS-AuNP Nanocomposites (QD-AuNP)</b> .....	<b>252</b>
<b>IV-5. Estimation of the Quantum Dots characteristics: QDs' diameter, extinction coefficient, and concentration</b> .....	<b>253</b>
<b>IV-6. Irradiation Setups: Light power and Quantum Yield</b> .....	<b>254</b>
<b>IV-6.1. Visible light irradiation setups</b> .....	<b>254</b>
<b>IV-6.2. Measurement of the light power of the irradiation setups</b> .....	<b>255</b>
<b>IV-6.3. Calculation of the reactions' Quantum Yield</b> .....	<b>256</b>
<b>IV-7. Experimental protocols</b> .....	<b>264</b>
<b>IV-7.1 Photocatalysis Experiments</b> .....	<b>264</b>
<b>IV-7.2- Photoluminescence quenching</b> .....	<b>265</b>
<b>IV-7.3- Photochemical charging/discharging experiments in the case of QD-AuNP nanocomposites</b> .....	<b>265</b>
<b>IV-7.4- Cyclic voltammetry</b> .....	<b>266</b>
<b>IV-8 –Detection of reactions' products using UV-HPLC or UHPLC-MS</b> .....	<b>267</b>
<b>IV-9. Analyses and characterization techniques</b> .....	<b>268</b>
<b>References</b> .....	<b>269</b>
<b>General Conclusion and Perspectives</b> .....	<b>273</b>





## Acknowledgements

*In this section, I would like to thank the people without whom this Ph.D. work and its journey would never not end as it did. I hope I can express enough in the next lines as this section seems to be the most difficult part to write in this Thesis.*

*First, I would like to thank the Thesis jury members for their kind acceptance to review and evaluate my Ph.D. work, for their very supporting feedback on the Thesis manuscript, and for the nice discussion, comments, and advice during the defense. Thanks to **Pr. Adam Pron**, **Dr. Fabrice Odobel**, **Pr. Frédérique Loiseau** and **Pr. Raphaël Schneider**, for making my defense an unforgettable moment with many perspectives. Here, I would also like to thank the CSI members, **Dr. Jérôme Chauvin**, **Pr. Guy Royal**, and also **Pr. Raphaël Schneider**, your advice and comments during the two CSI meetings were very helpful for the progress of my work.*

*During my Ph.D. I developed a good knowledge and experienced many situations on both the scientific and the personal sides. During these times, I was always supported by my supervisors, **Dr. Vincent Maurel** and **Dr. Jean-Marie Mouseca**, whom I am so lucky and grateful to have worked with them. So, I would like to thank **Vincent** for his trust, support, and non-stopped motivation to do the best for this project. A project that completely fulfilled my ability to learn new areas under his kind and valuable supervision. I highly appreciate the support and the freedom to try any new idea and always knowing that I can knock on his door for any question or a discussion. During this Ph.D., I have learned more than I could expect; this is all because of all the knowledge that you transmitted to me, I have been entirely convinced by all your comments; in all the matters that came during this Ph.D., either during the experiments or during the writing of this manuscript and the papers. I am really grateful to have you as a supervisor who, besides the great scientific side, the personal and the human sides in you do not exist in anyone, the will and the care for helping in any problem, taking things as if they are yours. I will never forget your care when I got sick in Aussois. Also, your advice and help me choose a good post-doc position after my Ph.D. I know as much as I write or tell it will never be enough, but I am sure that you know very well all the rest. A big thank you to **Jean-Marie** for all what I learned from you, the interesting (not easy: D) calculations, and the constructive scientific discussions we had together. In addition to all the enjoyable discussions about the ancient languages. All those will for sure remain as pleasant memories for the future, and again, a thank you will never be enough, so I add one more in Arabic this time (شكرا).*

*As this Ph.D. project is a French-Swiss collaboration, I would like to thank **Pr. Philippe Renaud**, for this nice and very enjoyable collaboration. Also, thank you for always having the knowledge and the expertise to answer all our organic chemistry questions, and for sure for the warm welcome in your Lab when I went to Bern. I would also like to thank **Dr. Fabrice Dénès**, each meeting, discussion, or chat (especially when in Bern) was so fun. Also, coming to my defense all the way from Bern was much appreciated. Here, and for sure, I should thank **Eloïse Colson** (sorry, Dr. Eloïse!) for being the best partner in this journey. I am so grateful to have you as a co-worker/co-thinker during this project. All what we did together was a very nice adventure. Despite all the obstacles, we managed to finish the story with a good ending, which would never happen without your smartness and the continuous will to do the best. Thank you again for that, and I hope to meet you and maybe work together again in the future.*

*I would like to thank **Dr Fabien Dubois** for the nice collaboration even before starting the Ph.D. as he was also my co-supervisor for my Master Thesis. Thank you for the interesting science we did together and for all the knowledge in nanoparticles that I have acquired thanks to you and the discussions we had together. Thank you also to **Dr Pierre Bauer**, despite your short stay in Grenoble -no thanks to covid for sure- we managed to stabilize our Quantum Dots and Gold nanoparticles to design our dear QD-AuNP composites. Here, also thanks to **Dr Aude Barbara**, first for the questions you asked during the meetings at **Néel**, were tough but helped a lot for both the writings and the defense and a big thank for your FCS-DLS experiments which helped to characterize better our particles!*

*I would like to thank everyone in the **CAMPE** family, all without any exception, you were the best teammates I could hope for. I will keep very nice memories of everyone of you. I could not imagine a better working company than the one I had beside you. All the permanent and the non-permanent campers "Grand Merci". I should mention all your names here to keep a forever memory each time I open this Thesis. Starting from the "**Aile A**" thank you **Serge** for every nice chat or advice the **A wing** is less funny without you and is not same as in your presence, **Christian** -my savor- with every new helpful setup you prepared for me beside the nice chats we had each morning and for sure thanks to Vincent and Jean-Marie again. Going to "**Aile C**" was always enjoyable when meeting **Lionel** and each time welcoming by "what I can do for you"; indeed, you did a lot thank you for all the advice and comments, **Florence** no words can describe your kindness and your care for everyone in the team, sure everyone owe you a lot, **Julie** it was a short period but I have a lot of nice memories with you, the electrochemistry we did together, the stay in Aussois and each gathering around a cake or sweets :p, and **Yves** thank you for helping everyone in the lab, CAMPE really needs you more than you think. Big Thanks to all of you. For sure, I don't forget the non-permanent (Vive les non-permanent-**Omar** says :p) again mentioning names, thanks to **Omar** and **Yassine** for all the nice moments we had together inside and outside the CEA and for the real friendship we developed during the two last years that I am very sure that it will last. Thanks to **Maxime** for the nice moments we shared especially during the covid period that time when we were the only students in the Lab. **Aurelien**, thank you for each nice chat we had and for sure for all the nice cakes you prepared for us, this will be missed. **Matteo**, **Subash** and **Maneesha** you will be missed for sure. Again, **CAMPERS** thank you so much and I will miss everyone and every moment I had with you.*

*I would like to thank the training students who we worked together during the past three years, **Antoine**, **Debargha** and **Maureen**. Thank you for your patient when working with me and I hope that I was a good partner for you and I could taught you something helpful.*

*A very big thank you to **Dr Jean-Luc Ravanat**, I should tell that thanks to you, your help and all what you taught me, I managed to succeed in avoiding the **High Probability of Losing Control** when using the **HPLC** in the last period of my Ph.D. A very big thanks also to **Sylvain Caillat**, I can't tell in few words how much you helped me during the three years. You are the guy that each team needs and Cibest are quite lucky to have you. Thank you so much again. Thanks to **Michel bardet** for every nice discussion during each coffee break and also thank you to **Pierre-Alain Bayle** for all the help with the NMR experiments as well as for the nice coffee prepared for the breaks with **Michel** for sure!*

*Thanks to my friends from outside the Lab who were always supporting me during the three years of the Ph.D. and especially during all the challenging moments. A special thanks to the two guys who we started the trip together in France from day one, directly from Lebanon to Grenoble, Ali Rida and Ali Tarhini, "les 3mers". Not easy to mention everyone, but big thanks to all the friends in Grenoble and those in Lebanon.*

*My **Family**, my support system, my **Dad**, and my **Mom**, this is dedicated to you, and I hope it can compensate even a little of what you have paid of pain to afford me the best education and living environment you could. I will always work hard to make you proud and see the smile on your face despite all the challenges. My sister and my brother, **Darine** and **Hussien**, I hope to see and live with the best in the future. My bigger Family, the Dabbous and Tanana, I am glad to be a member of these two families and wish you a long life full of pleasant moments to share with you. I am grateful and thankful to each one of you.*

*Ali Hassan Dabbous*

## List of abbreviations

<b>A (Abs.)</b>	Absorbance
<b>AuNP</b>	Gold nanoparticle
<b>Ar</b>	Argon
<b>Ag</b>	Silver
<b>C.B.</b>	Conduction Band
<b>C.V.</b>	Cyclic Voltammogram
<b>CsOAC</b>	Cesium acetate
<b>CuAAC</b>	Copper Catalyzed Azide Alkyne Cycloaddition
<b>DFT</b>	Density Functional Theory
<b>DCM</b>	Dichloromethane
<b>DLS</b>	Dynamic Light Scattering
<b>E°</b>	Redox Potential
<b>E<sub>ox</sub></b>	Oxidation Potential
<b>e-</b>	Electron
<b>eV</b>	Electron Volt
<b>FCS</b>	Fluorescence Correlation Spectroscopy
<b>h+</b>	Hole
<b>HOMO</b>	Highest Occupied Molecular Orbital
<b>HPLC</b>	High-Performance Liquid Chromatography
<b>LED</b>	Light Emitting Diode
<b>LUMO</b>	Lowest Unoccupied Molecular Orbital
<b>MS</b>	Mass Spectrometry
<b>NO<sub>2</sub>PhAla</b>	Nitrophenylalanine
<b>NHE</b>	Normal Hydrogen Electrode
<b>ODE</b>	Octadecene
<b>OLAc</b>	Oleic acid
<b>OPAc</b>	Octylphosphonic acid
<b>OLAm</b>	Oleylamine
<b>ODAm</b>	Octadecylamine

<b>OclAm</b>	octylamine
<b>PhPyr</b>	Phenylpyrrolidine
<b>PPAc</b>	phosphonopropanoic acid
<b>QD</b>	Quantum Dot
<b>QY</b>	Quantum Yield
<b>SCE</b>	Saturated Calomel Electrode
<b>SEM</b>	Scanning Electron Microscope
<b>TON</b>	Turnover Number
<b>TFT</b>	Trifluorotoluene
<b>TEM</b>	Transmission Electron Microscopy
<b>TOP</b>	Trioctylphosphine
<b>UV-vis</b>	Ultraviolet-visible
<b>UHPLC</b>	Ultra-High-Performance Liquid Chromatography
<b>V.B.</b>	Valence Band
<b>V</b>	Volt
<b>8-oxo-dG</b>	8-Oxo-2'-desoxyguanosine



## General Introduction

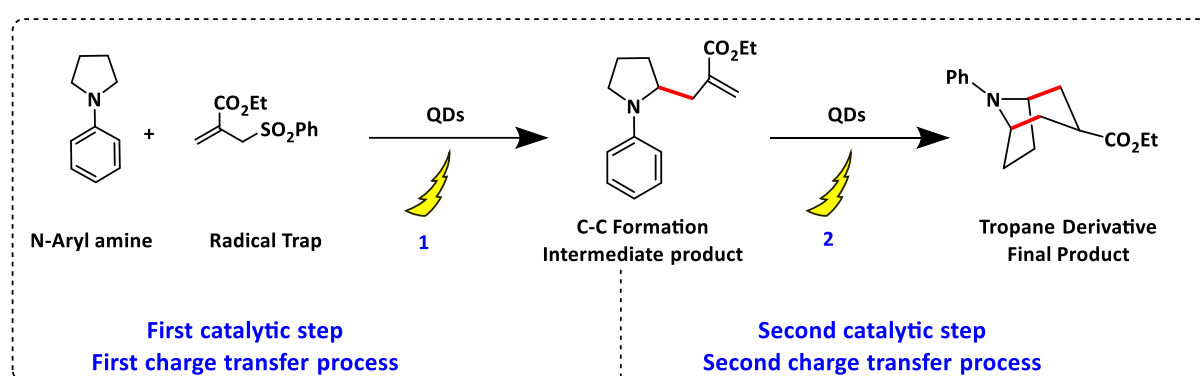
Photocatalysis has emerged at the forefront of the synthetic methodologies as a potent means for a wide range of transformations, such as bond-making or bond-breaking processes in organic chemistry. In particular, photoredox catalysis has experienced a significant evolution to be used as an efficient organic synthesis tool in the recent past years. Transition metal complex photocatalysts (mainly based on Ir and Ru elements), organic dyes and large band gap semiconductors such as Titanium Oxide (TiO<sub>2</sub>) have dominated the photoredox domain. Recently, a new class of semiconductor nanocrystals, known as Quantum Dots (QDs), has been reported as excellent candidates for visible-light harvesting photocatalysts performing various photoredox applications, particularly organic transformations such as oxidations and reductions.

Quantum Dots are semiconductor nanoparticles with relatively narrow band gaps (e.g., CdS, CdSe, InP, Etc.) of a few nanometers in diameter. Colloidal Quantum Dots are functionalized with surface ligands, stabilizing them in solution. Quantum Dots are promising candidates in photoredox catalysis due to their high photostability, large extinction coefficients, tunable optical properties and surface chemistry. Moreover, due to their nanometer scale size they exhibit the quantum confinement effect. Then, the optical and electronic properties of Quantum Dots are highly dependent on their size.

Thanks to their properties, Quantum Dots have been extensively explored as photocatalysts for applications such as hydrogen evolution, carbon dioxide reduction, and other related solar fuel applications. However, their use as photocatalysts for organic transformations, such as bond-formation reactions, remains relatively limited. Moreover, to the best of our knowledge, in all the reported QD-photocatalyzed organic reactions, only one type of Quantum Dots is studied without investigating different types of Quantum Dots for a given reaction.

In this context, the main objective of this thesis is to explore the use of different types and structures of semiconductor Quantum Dots for new carbon-carbon bond formation organic reactions. During the first part of this Thesis, we aim to develop new radical-based photoredox reactions leading to the synthesis of natural products of Tropane derivatives starting from N-Aryl Amines using Quantum Dots as photocatalysts. The success of the

photoredox reactions requires the accomplishment of two catalytic cycles to produce the final desired product. Then, the photocatalyst (Quantum Dots in our case) is supposed to perform two successive charge transfer processes to complete the two steps in one reaction pot (See Scheme 1). Therefore, we explore the photocatalytic activity of different types and structures of Quantum Dots (CdS, CdSe, InP core-QDs, and CdS-CdSe, CdSe-CdS, CdSe-ZnS, and InP-ZnS core-shell QDs) in order to select the most convenient type of Quantum Dots to photocatalyze the targeted reactions. In addition, we optimize the surface ligands of the Quantum Dots to ensure better interaction with the reactions' substrates and consequently improve their activity.

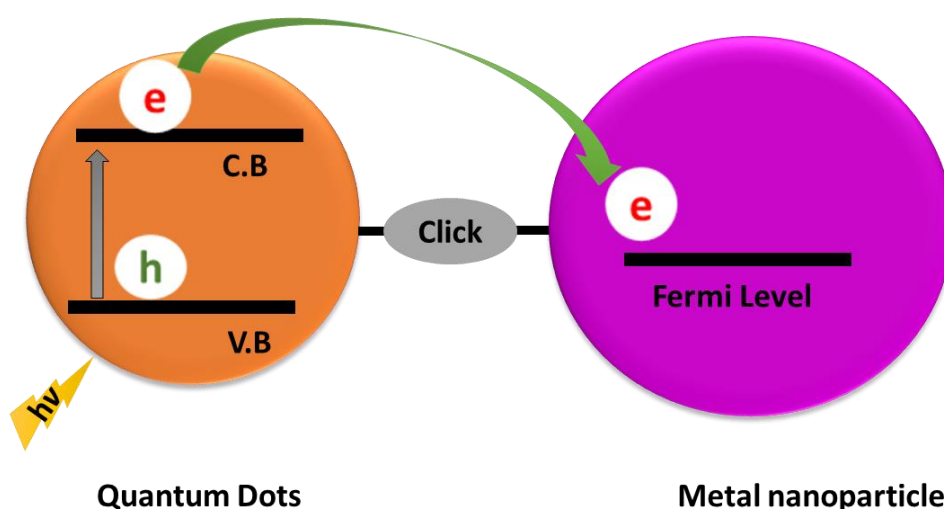


**Scheme 1:** Schematic illustration for the 2-step photoredox reaction of the Tropane derivatives synthesis using Quantum Dots.

However, it is well-reported that despite the encouraging properties of the semiconductor Quantum Dots, their use in photoredox reactions rarely exhibit high quantum yields, typically less than 1%, and usually the completion of the reactions requires long irradiation time (from 3 hours and up to 72 hours). This is attributed to the charge recombination processes. After the photoexcitation of Quantum Dots, the charge carriers could recombine, and no redox reactions could occur on their surface. Then, an essential challenge in Quantum Dots mediated photochemistry is to suppress the possible recombination processes after generating the charge pairs, and to create new pathways to improve the charge transfer from the photoexcited Quantum Dots to the organic substrates.

One of the explored strategies to limit the recombination of the charges generated from the excited semiconductor nanoparticles is to design hybrid nanostructures of semiconductor-metal nanoparticles. Up to now, the hybrid nanostructures used in photocatalysis are designed by the deposition or the growth of noble metal nanoparticles on

the surface of the semiconductor Quantum Dots. Such hybrid nanostructures are intended to promote the electron transfer from the excited QDs to the metal nanoparticles. The metallic nanoparticle can store the transferred electrons, thus limiting their recombination processes. Therefore, a second main objective of this Thesis is to design a new photocatalyst based on novel hybrid nanostructures of semiconductor Quantum Dots and metallic nanoparticles in order to enhance the efficiency of the QD-photocatalyzed reactions. Then, in the second part of the Thesis, we aim to connect Quantum Dots to Gold nanoparticles by covalent bond using a click chemistry approach (See Scheme 2). Such chemically assembled hybrid nanostructures are still very few examples in literature and, to the best of our knowledge, they were not reported in photocatalysis until now. Therefore, here we explore the photocatalytic activity of the newly designed hybrid nanostructures and compared it with that of bare Quantum Dots. Moreover, we studied the charge separation generated upon the photoexcitation of the Quantum Dot and the accumulation of the electrons on the gold nanoparticle.



**Scheme 2: Schematic illustration for the Quantum Dot-metal nanoparticle hybrid nanostructure:** Quantum Dot are connected to a metal nanoparticle by chemical bond between their surface ligands created using click reaction. The excitation of the Quantum Dot generates the electron-hole pair, then the electron is transferred to the metal nanoparticle.

## Scope of the Thesis

The manuscript of this thesis is organized into four main Chapters:

**Chapter I, entitled Semiconductor Quantum Dots' Systems for Photoredox Catalysis: State of the Art**, presents a general introduction to the use of semiconductor Quantum Dots systems in photoredox catalysis. This chapter commences with an introduction to the history of photocatalysis as a means of solar energy conversion. In addition, this introductory chapter introduces the discovery of the Quantum confinement in nanocrystals, a general background on the preparation of Quantum Dots, their different types, the optical and electronic properties of Quantum Dots, and the optimization of the surface chemistry.

Moreover, Chapter I summarizes the State-of-the-art concerning the recent application of Quantum Dots as visible-light photocatalysts for various photocatalytic organic reactions. We collect the literature reports on the QD-catalyzed organic reactions and classify them based on the type of the reaction. Furthermore, this chapter addresses some methodologies to enhance the efficiency of Quantum Dots by depositing noble metal nanoparticles on the surface of the Quantum Dots to improve the activity of the photogenerated charge carriers.

**Chapter II, entitled Quantum Dots mediated photoredox C-C bonds formation: oxidation of Aryl-amines leading to Tropane skeletons after two successive allylations**, shows our attempts to explore the ability of Semiconductor Quantum Dots to synthesize natural products of Tropane derivatives via photoredox methodology starting from N-Aryl-amines. This chapter discusses the difference in the efficiency of the different Types and structure of Quantum Dots to oxidize the reaction substrates based on their type and structure which helps to choose the most suitable type of Quantum Dots for performing the desired redox steps in the targeted reaction. We study different structure of Quantum Dots such as core or core-shell, in addition to different types of core-shell such as Type-I, quasi Type II and inverted Type-I Quantum Dots. We also shows the importance of optimizing the surface ligands of the Quantum Dots to improve the activity. In addition, this chapter presents the corresponding catalytic mechanism of the targeted reaction, showing the different generated radicals during the redox steps and the mechanistic investigation (DFT calculation, electrochemical analysis...) performed in order to support the proposed catalytic mechanism of the targeted reaction.

**Chapter III, entitled Hybrid CdSe/ZnS Quantum Dots-Gold Nanoparticles Composites Assembled by Click Chemistry: Towards Affordable and Efficient Redox Photocatalysts Working with Visible Light**, describes the methodology used for designing a new semiconductor-metal hybrid nanostructure by assembling CdSe-ZnS semiconductor Quantum Dots with Gold nanoparticles. Water-soluble Quantum Dots were prepared and functionalized with azide-clickable ligands, in parallel Gold nanoparticles were synthesized in water and functionalized with Alkyne- clickable ligands. Then, the Quantum Dots and the Gold nanoparticles were assembled via click chemistry using Copper-Catalyzed Azide-Alkyne Cycloaddition reaction. Moreover, this chapter shows the investigation of the photocatalytic activity of the designed hybrid nanostructures on a model redox system including 8-Oxo-2'-desoxyguanosine as an electron donor and nitrophenylalanine derivatives as electron acceptors. In addition, it discusses the proposed mechanistic process of the charge separation based on the spectroscopic tests proving the electron transfer to the Gold nanoparticles.

**Chapter IV** describes the **experimental methods** used for conducting all the experiments mentioned in the previous chapters. This chapter describes all the detailed procedures optimized for synthesizing the Quantum Dots and the Gold nanoparticles and their characterization, in addition to the protocols used for the surface ligand exchange for the Quantum Dots. It also discusses the ways followed for estimating the physical properties of the reactions, such as the Quantum yields and the turnover numbers. The protocols of the photocatalysis experiments and the analysis techniques are also described in this chapter.

This Ph.D. Thesis took place under the supervision of **Dr. Vincent MAUREL** and the co-supervision of **Dr. Jean-Marie MOUESCA**, researchers at **CEA-Grenoble**. This thesis work was initiated as a part of a French-Swiss collaboration between two French research groups and another Swiss research group. The French groups are from the **SyMMES** unit (Systèmes moléculaires et nanomatériaux pour l'énergie et la santé), **CAMPE** team (équipe conception d'architectures moléculaires et processus électroniques) at the **CEA** (Commissariat à l'énergie atomique et aux énergies alternatives) in Grenoble. The second French group is from **Institut Néel**, **OPTIMA** team (Optique et matériaux) at the **CNRS** (Centre national de la recherche scientifique) in Grenoble. The Swiss group is the **Renaud** research group from the **Department of Chemistry, Biochemistry and Pharmaceutical Sciences** at the **University of Bern**.

This thesis focuses on two main projects. The first project (represented in Chapter II) took place in close collaboration with Pr. Philippe RENAUD, Dr. Fabrice DÉNÈS and Eloïse COLSON from the **Renaud** research group. The main objective of this project is to develop Quantum Dots-photocatalyzed carbon-carbon bond formation reactions leading to useful natural products. The Two groups (**CAMPE** and **Renaud** teams) shared the responsibilities of this project depending on their expertise. The **CAMPE** group synthesized, characterized, and optimized all the semiconductor Quantum Dots. Then investigated the photocatalytic activities (at low reactions' scale) of all the semiconductor Quantum Dots to explore the most convenient type and structure for the desired reactions. In addition, the **CAMPE** group supported this project with the needed theoretical calculations (DFT calculations) and the Physico-chemical analysis (spectroscopic and electrochemical measurements...). In parallel, the responsibility of the **Renaud** group was to develop new photoredox radical reactions for carbon-carbon bonds formation using classical photocatalysts and then test the ability of the developed semiconductor Quantum Dots by the **CAMPE** team to catalyze the same reactions using preparative chemistry scales. Moreover, the **Renaud** group synthesized the reactions' substrates and the corresponding reactions' products references needed for the analyses at the **CAMPE** labs.

The second project (represented in Chapter III) took place in close collaboration with Dr. Fabien DUBOIS, Dr. Aude BARBARA and Dr. Pierre BAUER from the **OPTIMA** team. The main objective of this project is to design a novel type of photocatalyst based on a hybrid nanostructures of semiconductor Quantum Dots (QDs) and Gold nanoparticles (AuNPs) covalently assembled by a click reaction. In this project, the **CAMPE** group prepared, optimized and characterized the semiconductor Quantum Dots and tested their photocatalytic activity. Then the **CAMPE** group functionalized the Quantum Dots with the desired surface ligands needed for the click reaction. The **CAMPE** group provided the **OPTIMA** group with samples of the functionalized Quantum Dots. The **OPTIMA** group prepared and characterized the Gold nanoparticles. The **OPTIMA** group used the functionalized QDs and AuNPs and performed the click reaction to prepare the QD-AuNP hybrid nanostructures. Then, the **CAMPE** group performed all the photocatalysis using the newly designed QD-AuNP hybrid nanostructures. Moreover, the **CAMPE** group studied the photo-induced electron transfer in the QD-AuNP

hybrid nanostructures and estimated the number of electrons accumulated at the gold nanoparticles.

It is worth mentioning that the DFT calculations performed in the **CAMPE** group are done by Dr. Jean-Marie MOUESCA, and apart from the theoretical calculations, all the experimental work by the **CAMPE** group is done by the author of this Thesis.



# CHAPTER I:

## Semiconductor Quantum Dots' Systems for Photoredox Catalysis: State of the Art

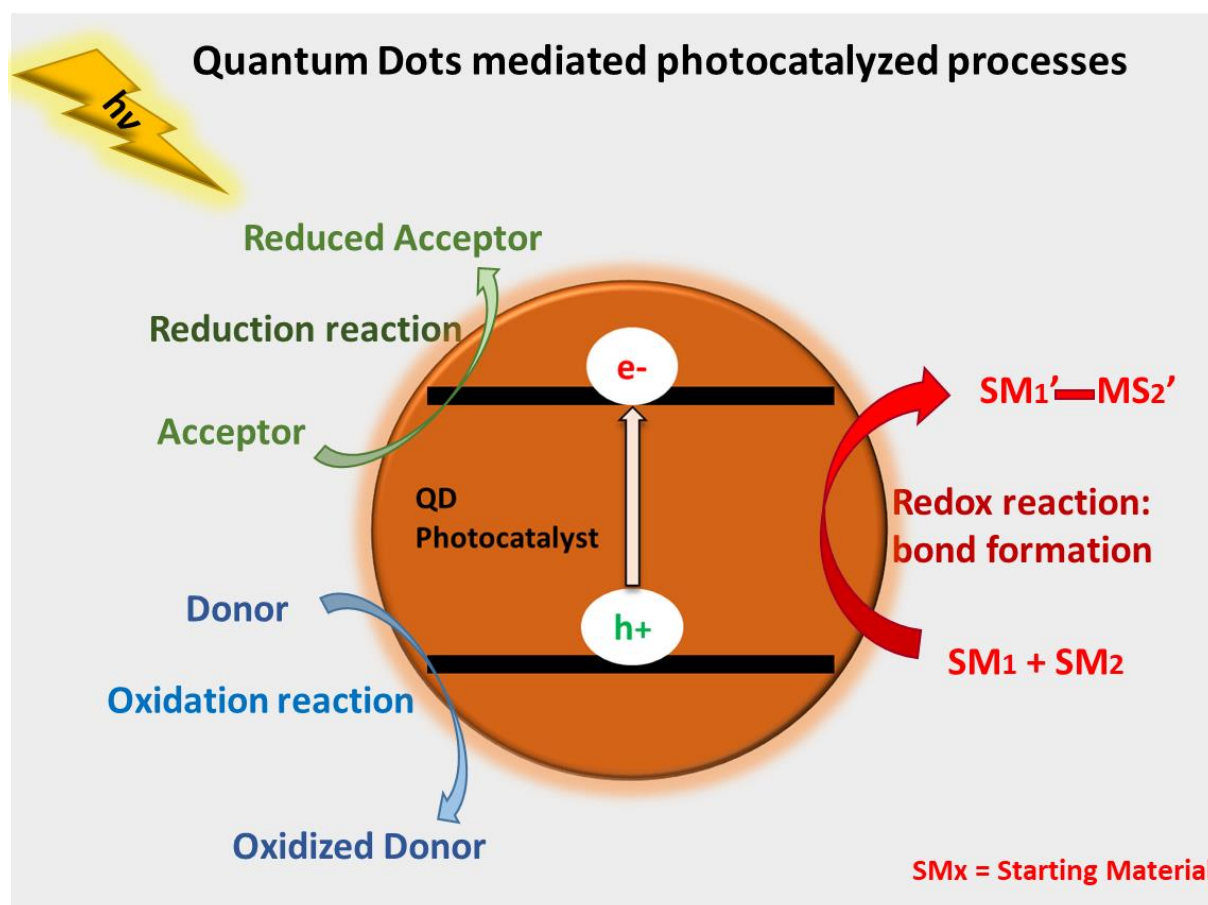


## Table of Content

CHAPTER I: .....	15
Semiconductor Quantum Dots' Systems for Photoredox Catalysis: State of the Art .....	15
I-1. Visible Light Photocatalysis: exploitation of the solar energy for synthetic chemistry.....	17
I-2. Background on Semiconductor Quantum Dots.....	20
I-2.1. Semiconductor Quantum Dots: Discovery of the Quantum confinement effect. ....	20
I-2.2. Quantum Dots' preparation.....	24
I-2.3. Core-shell Quantum Dots.....	27
I-2.3. Quantum Dots as redox photocatalyst: working principle.....	29
I-2.4. Quantum Dots electronic properties: Estimation of the band edge energies.....	30
I-2.5. Challenges in Quantum Dots' Photocatalysis: Optimization of the Ligand layer. ....	34
I-3. Application of Quantum Dots as photocatalysts in organic transformations. ....	38
I-3.1. QDs-photocatalyzed net reductive reactions. ....	41
I-3.2. CdS QDs as powerful photoreductants for dehalogenation reaction initiated by Auger processes.....	46
I-3.3. QDs-photocatalyzed net oxidative reactions. ....	48
I-3.3. QDs-photocatalyzed bond formation reactions. ....	52
I-3.4. CdSe QDs as photocatalyst for triplet excited state reactions.....	66
I-3.6. Quantum Dot Gels as efficient photocatalysts for organic reactions.....	67
I-3.6. Other photocatalytic reactivities Using Quantum Dots .....	68
I-4. Enhancing the photogenerated charge separation: Quantum Dots connected to metal nanoparticles.....	71
I-4.1. Suppressing the photogenerated charge recombination in QDs. ....	71
I-4.2. Fast charge transfer from photoexcited semiconductors to metal nanoparticles. ....	73
I-4.3. Quantum Dots and metal nanoparticles hybrid structure for enhanced photocatalytic activities. ....	77
Conclusion.....	80
References .....	81

## I-1. Visible Light Photocatalysis: exploitation of the solar energy for synthetic chemistry.

The growing energy demands nowadays make the search for sustainable energy resources one of the main concerns in many research fields. Among the various types of sustainable energy resources, solar energy is regarded as one of the most attractive renewable resources. Solar energy is considered as an abundant and inexhaustible environmental resource. Sunlight, as a clean and safe source of energy, provides the earth's surface with nearly 173 000 TWh of energy each day-hour or about  $3 \times 10^{24}$  Joules per year in the form of solar radiation. This is orders of magnitude more than the annual global humans demand for energy (10 000 times more than the global energy consumption)<sup>1,2</sup>. In this context, many research projects were released to address the efficient solar energy conversion.

Throughout history, human beings were inspired by Nature to develop new solutions for their daily problems. One of the natural phenomena that have caught people's attention is the natural photosynthesis, a process that leads to chemical transformations by harvesting sunlight. In the last decades, light harvesting used for chemical reactions appeared among the many emerging solar energy applications<sup>3</sup>. This kind of processes is known as photocatalysis. In this process, light irradiation is used as the main energy source<sup>4</sup>.

Photocatalytic processes were defined in the IUPAC Book as *'a change in the rate of a chemical reaction or its initiation under the action of ultraviolet, visible or infrared radiation in the presence of a substance—the photocatalyst—that absorbs light and is involved in the chemical transformation of the reaction partners'*.<sup>5</sup> According to N. Serpone and co-authors<sup>6</sup>, the terms photocatalysis and photocatalyst (**photokatalyse** and **photokatalytisch**) were reported in the literature for the first time in 1910 by J. Plotnikow in his Textbook about photochemistry. Then, in 1911, these terms were used by Alexander Eibner to describe the effect of irradiating Zinc oxide (ZnO) materials on the degradation of Prussian blue dyes<sup>7</sup>. Two years after, in 1913<sup>8</sup>, M.Landau introduced the word **photocatalyse** in France in his report "Le phénomène de la photocatalyse" (in French). Although these reports can be regarded as a breakthrough step in introducing the photocatalysis domain, photocatalytic processes were not gaining enough attention until the report by Honda and Fujishima published in Nature in

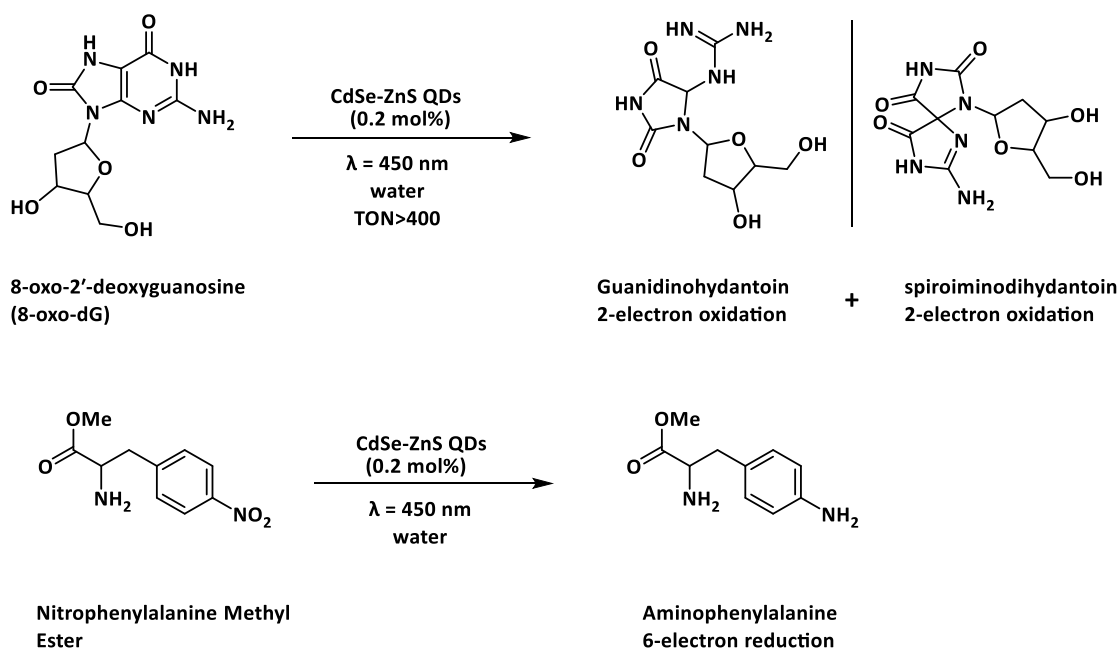
1972<sup>9</sup>, where they performed their seminal work on the electrochemical photolysis of water at a semiconductor electrode.

Following the work reported by Honda and Fujishima<sup>9</sup>, photocatalysis based on metal oxide semiconductors gained enormous attraction, which gave rise to their applications in water splitting<sup>10</sup>, CO<sub>2</sub> reductions<sup>11</sup>, pollutant degradation<sup>12</sup> and organic reactions<sup>14</sup>. Interestingly, Albini and co-workers<sup>13</sup> demonstrated, in 1998, the use of TiO<sub>2</sub> as a photocatalyst to induce C–C bond formation under solar irradiation. Then, the use of various types of metal oxides as photocatalyst for organic reactions starts to emerge and being widely used<sup>14</sup>. However, the traditional metal oxides photocatalysts, such as TiO<sub>2</sub>, need to be excited under an ultraviolet irradiation, which only accounts for less than 5% of the solar spectrum.

Then, to exploit the renewable visible solar energy, efforts have been made to design and synthesize visible light active photocatalysts. Therefore, early in the 80s, the first reports on the photoluminescence properties of visible light active transition metal complexes such as Ruthenium (II) complexes came out<sup>15</sup>. Soon after, in 1984, Deronzier and co-workers<sup>16</sup> reported the first use of such a ruthenium (II) complex as photoredox catalyst in an organic transformation.

In 2008, a significant increase in the research area of visible light photocatalysis was evident, as a rapid increase in scientific contributions demonstrating the use of transition metal-based photocatalysts for synthetic organic chemistry. In details, MacMillan<sup>17</sup> showed the utility of a Ruthenium-based transition complex to catalyze a C-C coupling reaction of a direct  $\alpha$ -alkylation of aldehydes. In the same year, Yoon<sup>18</sup> succeeded to develop a [2+2] Enone Cycloadditions reaction also using a Ruthenium-based transition complex photocatalyst. One year after, in 2009, Stephenson<sup>19</sup> reported the ability of the transition metal complexes to perform a reductive dehalogenation reaction by visible light photocatalysis. These findings were the building blocks for developing an important and significant amount of synthetic processes based on photocatalysis<sup>20–24</sup>(see references 20-24 for reviews). In parallel, organic dyes<sup>25,26</sup> (see references 25 and 26 for reviews) and some bulk semiconductor materials<sup>14,27</sup> (see references 14 and 27 for reviews )were also investigated as photocatalysts for organic transformations. These Topics will not be reviewed in this Thesis Chapter. However, the reader is kindly referred to read the cited reviews for more details.

Recently in the last decade, semiconductor nanocrystals, commonly known as Quantum Dots (QDs), start to appear as promising new efficient type of photocatalysts, especially for CO<sub>2</sub> reduction<sup>28–30</sup>, H<sub>2</sub> production<sup>31–33</sup>, and also in photoredox organic transformations<sup>34–37</sup>. They are considered suitable for visible light photocatalysis due to their high extinction coefficients ( $>10^5 \text{ M}^{-1} \text{ cm}^{-1}$ ) in the visible region, which makes them efficient visible light-harvesting materials<sup>38</sup>. In addition, they possess a tunable and size-dependent redox potentials and the presence of a large fraction of surface atoms ensures a highly reactive surface area<sup>39</sup>. In this context, our group (Currently, CEA/IRIG/SyMMES/CAMPE), in 2015 demonstrated the use of water-soluble core-shell structured CdSe-ZnS QDs to photocatalyze a complete redox system. In this work, it was reported that CdSe-ZnS core-shell QDs are efficient visible light photocatalyst for the 2-electron oxidation of 8-oxo-2'-deoxyguanosine as an electron donor in the reaction system, and simultaneously, for the reduction of Nitrophenylalanine derivatives by achieving up to 6-electron reduction (Scheme I-1). The system was proved to work efficiently without the need for any sacrificial agents, and resulted into a good turnover number for the QDs reaching more than 400 TON, although a modest Quantum Yield of 0.06% was obtained<sup>40</sup>.



*Scheme I-1: CdSe-ZnS QDs for photoredox catalysis: Simultaneous 2-electron oxidation of 8-oxo-dG and 6-electron reduction of nitrophenylalanine derivatives using water soluble CdSe-ZnS QDs.*

In this thesis, we aim to develop new radical-based photoredox reactions leading to carbon-carbon bond formation and using Quantum Dots as photocatalysts. Therefore, in this introductory chapter, we present an overview of the state of the art concerning the use of Quantum Dots for photoredox organic reactions. In section I-2, we introduce a general background about Quantum Dots, their preparation and optimization, their properties and the working principle making them act as photocatalysts. Section I-3 focuses on the selected literature examples of photoredox organic transformations catalyzed by using different types of Semiconductor Quantum Dots. In section I-4, we introduce some reported attempts to enhance the photocatalytic activity of Quantum Dots-based systems, particularly the coupling of Quantum Dots with metal nanoparticles.

## I-2. Background on Semiconductor Quantum Dots.

### I-2.1. Semiconductor Quantum Dots: Discovery of the Quantum confinement effect.

Semiconductor Quantum Dots (QDs) are tiny zero-dimensional semiconductor particles. Their size is generally between 2 and 10 nanometers<sup>41</sup>. These nanometer-scale particles are promising light-harvesting materials since they possess special optical and photophysical properties<sup>42</sup> such as larger extinction coefficients<sup>43</sup>, size-tunable light emission, and good photo and thermal stability protecting them against photobleaching<sup>44</sup>. In addition to the tunability and flexibility of their surface chemistry<sup>45-48</sup>, these particles are well known to be size-dependent materials, as their properties can vary due to their size variation.<sup>49-51</sup> Nowadays, Quantum Dots (QDs) are among the most types of nanoparticles gaining attention in the nanoscale field due to their wide range of applications.

In bulk semiconductors, the material's properties mainly depend on their chemical composition and crystalline structure. However, when the semiconductors are prepared in Quantum Dots form, the inorganic structure of these particles is composed of only hundreds to thousands of atoms for particles with size between 1.5 nm to 10 nm range. Then, the edges of the valence and the conduction bands of the semiconductor evolve towards quantized energy levels (for simplicity, in the following of this Thesis, the quantized energy levels of the Quantum Dots are noted as "conduction band level" and "valence band level" as in most of the literature reports about QDs photocatalysis). Moreover, the semiconductor Quantum Dots

are characterized by larger band gaps than their bulk counterparts<sup>29,52–55</sup>. In Quantum Dots, the photo-generated charge carriers are confined within a very small volume, and so the distance between them tends to be close or smaller than the Bohr's radius.<sup>56</sup> The Bohr's radius is the separation distance between electrons and holes in the excitons of bulk semiconductors. For CdS and CdSe bulk semiconductors the Bohr's radius is around 5 nm<sup>57</sup>. Then, when CdS and CdSe are smaller, this creates the quantum confinement effect that characterizes the Quantum Dots' electronic properties. Due these properties, Quantum Dots can emit different wavelengths over a broad range from visible to infrared of the light spectrum<sup>58</sup> depending on their sizes. (See figure I-1).

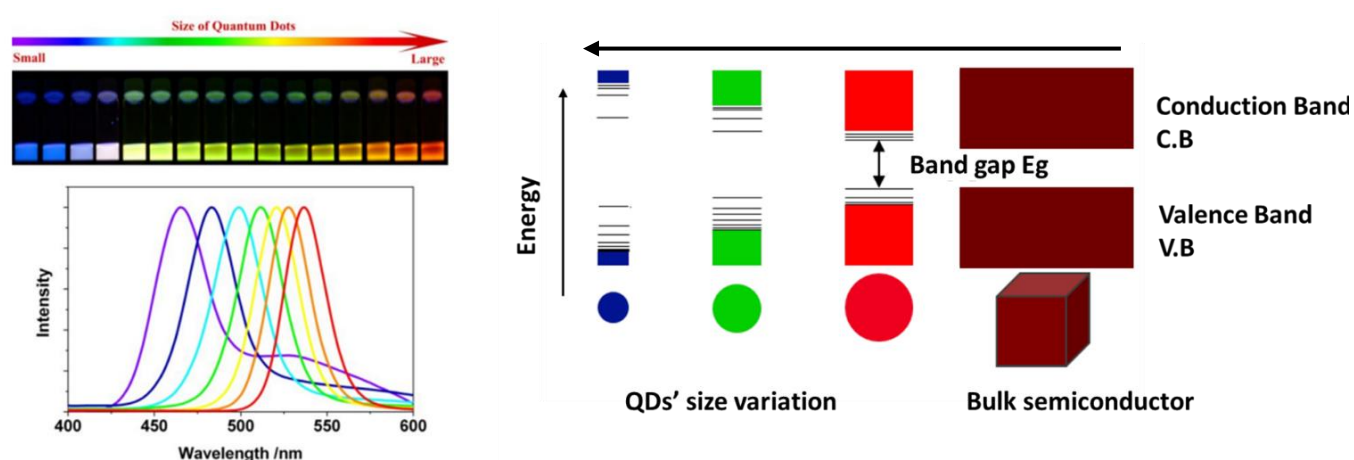


**Figure I-1: Quantum confinement and the optical properties of colloidal Quantum Dots.** (Left) Size-dependent optical properties of QDs, the variation of the emission based on the QDs' size (figure with the spectra collected from reference 58) and (Right) schematic representation of the evolution of the energy of the band gap with the size variation

During the 70th and 80th, two separated research groups, one from Russia (Alexei Ekimov and Alexander Efros) and the second from the USA (Louis Brus)<sup>59</sup>, started studying semiconductors' properties and developing theoretical explanations for the observed size-dependent properties. Ekimov and Efros conducted their studies on semiconductor-doped glasses, while Brus investigated semiconductor particles in liquid colloids. Despite the difference between semiconductor-doped glasses and colloidal semiconductors, they showed that in both cases, the nanocrystal form of the semiconductors exhibited similar properties depending on their size.

Focusing on liquid colloidal semiconductor particles, the observation of the quantum size effect by Brus was accidental as he mentioned<sup>59</sup>. This came up when he was performing photochemistry on the surface of CdS particles. While preparing some aqueous CdS colloids,

he realized that the absorbance spectra were changing with the aging of the particles. He expected that the observed spectral change was due to a size effect of the CdS particles. To confirm this hypothesis, he tried to control the growth of the CdS nanoparticles by decreasing the synthesis temperature and lowering the precursor's concentration in order to obtain smaller particles. Regarding the spectral evolution of the CdS particles as a function of the size, he observed a blue shift in the position of CdS absorption peak by decreasing the size from 12.5 nm to 4.5 nm (see Figure I-2). This absorption peak represents the exciton (electron-hole pair) position of photoexcited CdS particles. Motivated by this demonstration, Brus extended his studies on other semiconductor materials such as ZnS, PbS, ZnSe and CdSe observing very similar behaviors of the optical properties based on their size variation<sup>60-62</sup>

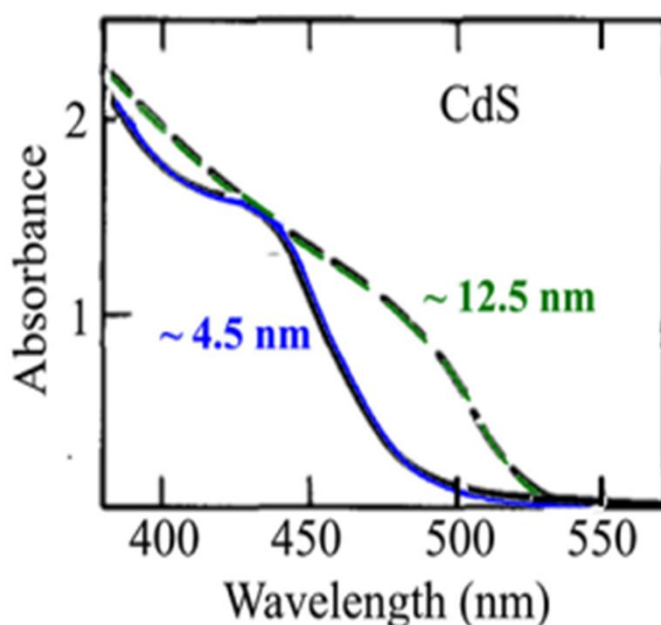


**Figure I-2: Absorbance spectra for CdS nanocrystals of different sizes:** A) The variation of the absorption properties of CdS nanocrystals after their aging and size variation from 12.5 nm having a wavelength peak above 450 nm. Then, after the size decreased to 4.5 nm the absorption peak decreased to around 420 nm. (Figures adapted from reference 59)

Early in the 21<sup>st</sup> century, researchers from different groups, such as Peng<sup>43</sup>, Jasieniak<sup>63</sup> and Reiss<sup>64</sup>, further explored the size-dependent properties of Quantum Dots. In this context, model relations were developed based on polynomial fitting of experimental data to describe the relationship between the size and the spectral properties (exciton position) of different kinds of QDs. These relations were developed based on some experimental characterization of a few types of Quantum Dots by coupling the observed properties to the variation of the Quantum Dots' size. Table 1 present the corresponding relations for the determination of the

size (diameter) and the extinction coefficient ( $\epsilon$ ) of selected types of QDs such as CdS,<sup>43</sup> CdSe<sup>63</sup> and InP<sup>46,64</sup> Quantum Dots.

QDs	Relation between QDs' exciton wavelength ( $\lambda_{nm}$ ) and their diameter ( $D_{nm}$ )	Ref
CdS	$D = (-6.6521 \times 10^{-8})\lambda^3 + (1.9557 \times 10^{-4})\lambda^2 - (9.2352 \times 10^{-2})\lambda + (13.29)$	43
CdSe	$D = (1.62974 \times 10^{-9})\lambda^4 - (2.85743 \times 10^{-6})\lambda^3 + (1.8873 \times 10^{-3})\lambda^2 - (0.54736)\lambda + 59.60816$	63
InP	$D = (-3.7707 \times 10^{-12})\lambda^5 + (1.0262 \times 10^{-8})\lambda^4 - (1.0781 \times 10^{-5})\lambda^3 + (5.4550 \times 10^{-3})\lambda^2 - (1.3122)\lambda + 119.9$	64
QDs	Relation between QDs' extinction coefficient ( $\epsilon_{L/mol.cm}$ ) and their diameter ( $D_{nm}$ )	Ref
CdS	$\epsilon = 21536 (D)^{2.3}$	43
CdSe	$\epsilon = 5857 (D)^{2.65}$	64
InP	$\epsilon = (3046.1) (D)^3 - (76532) (D)^2 + (5.5137 \times 10^5) (D) - (8.9839 \times 10^5)$	64

**Table I-1: Relationships between the size of CdS, CdSe, and InP QDs and the position of the excitonic peak in their absorption spectra and with the molar extinction coefficient.**

Using the equations shown in Table I-1, one can plot the variation of the QDs' diameter as a function of their corresponding exciton position over a range of wavelengths at which the Quantum confinement of the QDs is respected, for example, between 400 nm and 480 nm for CdS QDs and between 400nm and 600 nm for CdSe and InP (Figure I-3-A), and consequently the corresponding estimated extinction coefficient of the QDs (Figure I-3-B). This representation shows the obvious variation of the optical properties, the exciton absorption wavelength, as well as the variation of the band gap width and the extinction coefficient of the QDs with the change in their diameter size. These equations and calibration curves are used for characterizing the prepared Quantum Dots in our case in the following chapters of this Thesis.

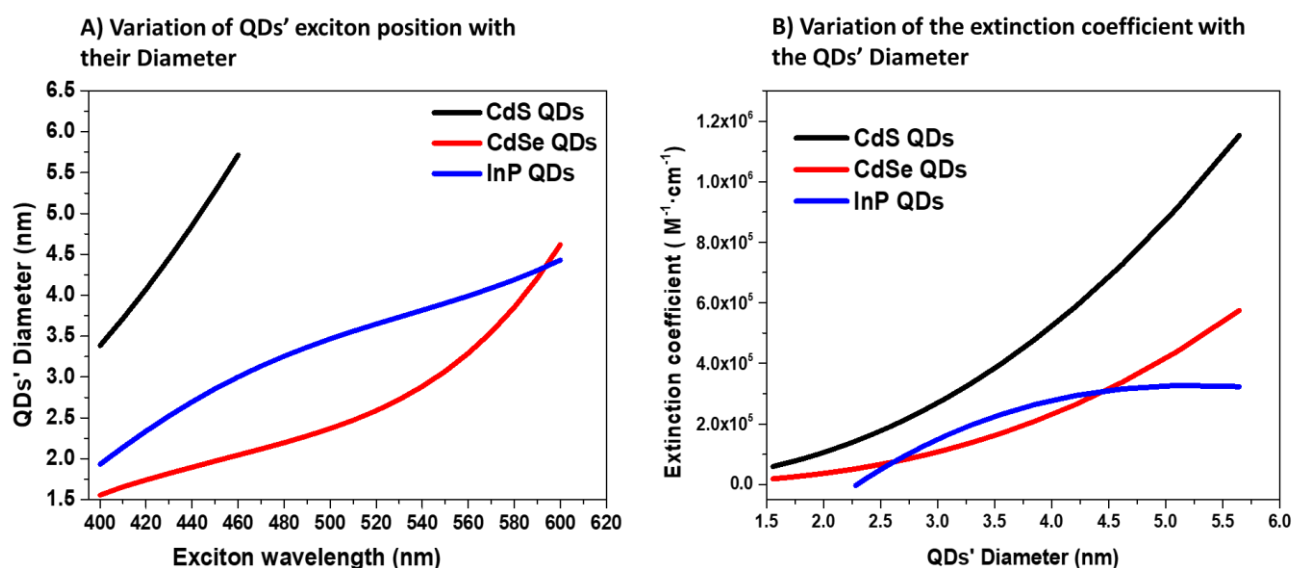


**Figure I-3: Relation between the QDs' size and their corresponding optical and electric properties:** (A) the variation of the size of the QDs with the variation of the wavelength position of the absorption peak of the exciton. (B) The extinction coefficient of the QDs' based on the change of their diameter.

## I-2.2. Quantum Dots' preparation.

In 1993, Bawendi and coworkers<sup>41,59</sup> reported the first synthesis protocol of monodisperse core structure and tunable particle size of Quantum Dots based on a hot injection strategy. This synthesis protocol was first optimized for CdSe QDs. The synthesis relies on mixing Dimethyl cadmium ( $Me_2Cd$ ) as a cadmium precursor with trioctylphosphine (TOP) and trioctylphosphine oxide (TOPO) acting as solvents and surface ligands, in the presence of a selenium precursor of TOP-Se. The QDs' growth was monitored at a high reaction temperature ( $300^\circ C$ ) and they could control the size of the QDs by following their spectral evolution (Figure I-4). This synthesis strategy represented a breakthrough in the colloidal Quantum Dots synthesis. However, a main drawback of the Bawendi method is the use of  $Me_2Cd$  as cadmium precursor, which is highly toxic, expensive, not very stable, and explosive.

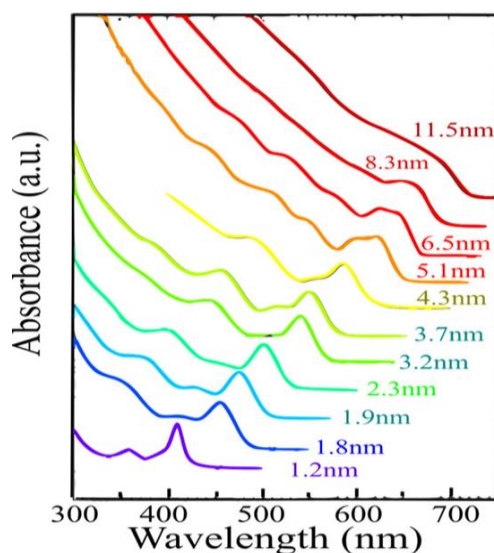


**Figure I-4 : Absorbance spectra for CdSe Quantum Dots of different sizes:** A) The variation of the absorption properties of CdSe based on the variation of their size between 1.2 nm and 11.5 nm. (Figure from reference 59)

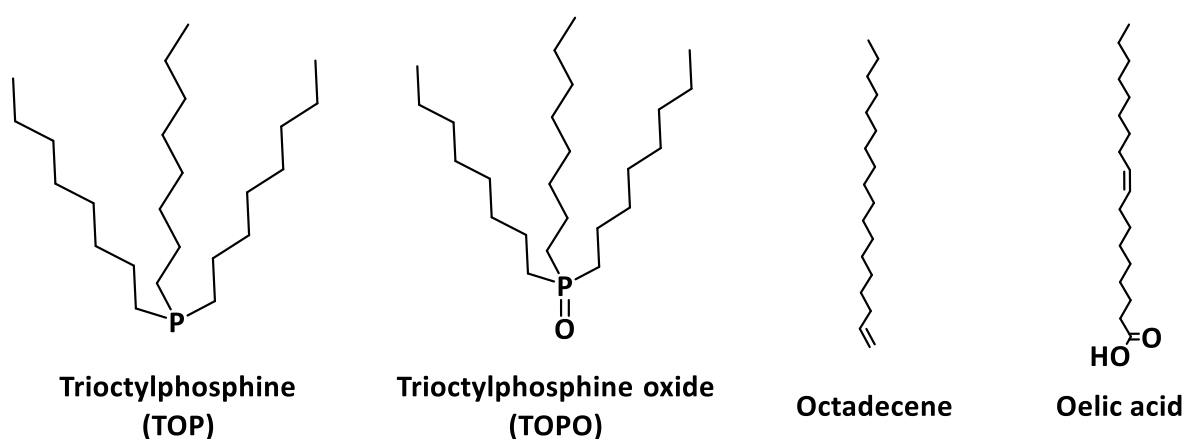
In order to avoid the use of  $\text{Me}_2\text{Cd}$ , Peng et al.<sup>65</sup> in 2001, developed a new methodology for preparing colloidal Cd-based Quantum Dots by replacing  $\text{Me}_2\text{Cd}$  with cadmium oxide (CdO) as a new cadmium precursor, while still using the TOP and TOPO during the synthesis as described by Bawendi. At that time, the Peng's synthesis protocol was considered the most used methods to prepare highly luminescent II–VI QDs. Moreover, beside the synthesis of CdSe, it became a standard methodology for the synthesis of other types of high-quality colloidal QDs with controlled growth such as CdS and CdTe. However, the use of TOP and TOPO was not very attractive due to the impurities they include. Some phosphonic acid based compounds were identified within TOP and TOPO and considered to have a role while controlling the growth of the QDs.<sup>66</sup>

One year after, in 2002, Peng and co-worker<sup>67</sup> developed a new QDs' synthesis method using a non-coordinating solvent, octadecene, and in the presence of oleic acid used as ligands functionalizing the surface of the QDs, but still in presence of TOP for preparing the selenium precursor. This new method provided tunable surface for the QDs with high colloidal stability. In 2005, Jasieniak et al.<sup>68</sup> optimized a phosphine free CdSe QDs' synthesis protocol. The method relies on using octadecene as the main solvent and oleic acid as the only surfactant capping the QDs' surface. The selenium precursor was prepared from elemental selenium suspended in octadecene, and the cadmium precursor is still from cadmium oxide. This

protocol resulted in high-quality CdSe Quantum Dots functionalized with Oleic acid as the only surface ligand. Table I-2 and Scheme I-2 summarize the ligands and the main precursors used in the different synthesis protocols mentioned above. It is worth mentioning that the protocol developed by Jasieniak and co-workers<sup>68</sup> for the synthesis of cadmium-based Quantum Dots was used as the main strategy for the synthesis of the Quantum Dots used in this Ph.D. work, even though few additional optimization were applied when needed. Knowing that this Thesis work doesn't aim at developing new synthesis protocols for Quantum Dots or reviewing in details the Quantum Dots' synthesis methodologies, but the reader is kindly referred to the cited reviews and publications about the synthesis of nanocrystals<sup>69</sup>. (See for instance references 41, 59, 65, 66, 67, 68 and 69)

Protocol (year)	Cadmium source	Selenium source	Solvent	Surface ligands
Bawendi (1993)	Dimethyl-cadmium (Me <sub>2</sub> Cd)	TOP-Se	TOP/TOPO	TOP/TOPO
Peng (2001)	Cadmium Oxide (CdO)	TOP-Se	TOP/TOPO	TOP/TOPO
Peng (2002)	Cadmium Oxide (CdO)	TOP-Se	Octadecene	TOP/Oleic acid
Jasieniak (2005)	Cadmium Oxide (CdO)	Se/ Octadecene	Octadecene	Oleic acid

**Table I-2: Summary of the main reagents used during the different synthesis protocols reported for the QDs growth optimization**



**Scheme I-2: Schematic representation of the ligands and solvents used during the QDs' synthesis.**

### I-2.3. Core-shell Quantum Dots.

Core-type Quantum Dots are made of single component materials with a unique internal composition composed of one type of inorganic semiconductor. Core QDs are composed of a few hundreds to a few thousands of atoms surrounded by an organic outer layer of ligand molecules<sup>64</sup>. Nevertheless, core structured QDs exhibit surface-related trap states leading to non-radiative recombination channels for the photogenerated charge carriers, therefore reducing their fluorescence efficiency, which is a critical factor in luminescence-related applications<sup>70</sup>.

An important method used to improve QDs' surface passivation and to limit the charge carriers recombination or their trapping by the surface trap states, is the growth of an inorganic shell of a second semiconductor material, resulting in core-shell structured QDs<sup>64</sup>. This methodology was proved to enhance the fluorescence efficiency by ensuring a high fluorescence lifetime<sup>71</sup> for certain types of core-shell QDs (Discussed below). In other cases, the formation of core-shell structured of various types of semiconductor QDs has enhanced their stability against their photo-oxidation<sup>72,73</sup>.

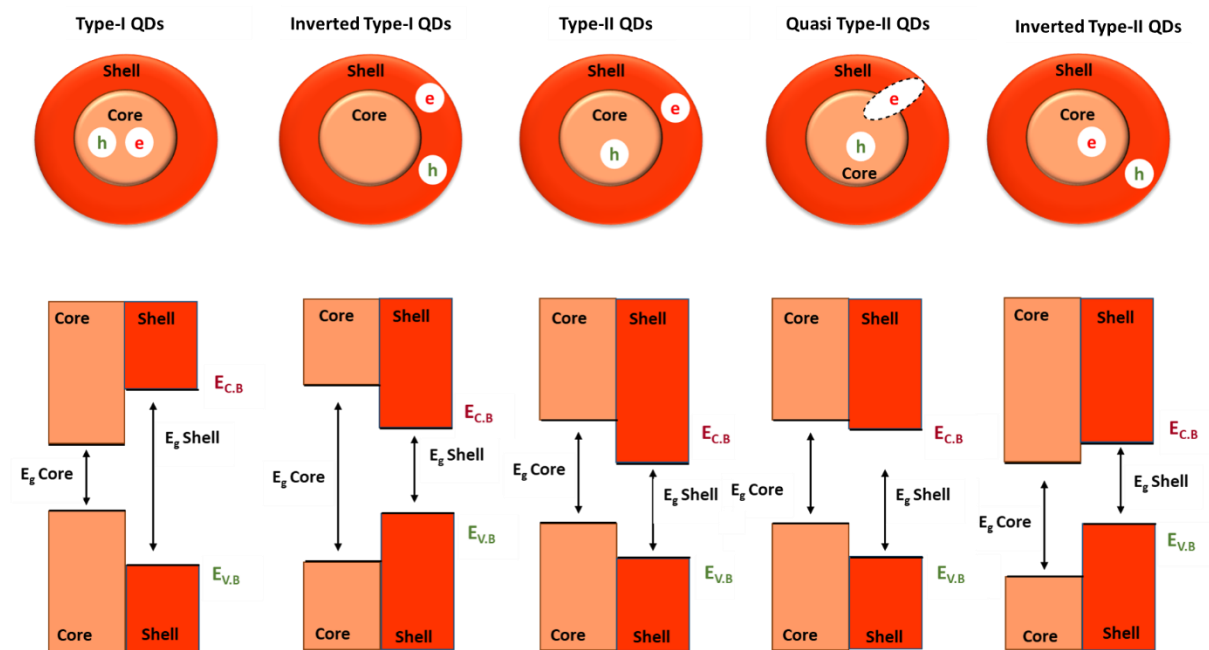


**Figure I-5: The types of core-shell QDs based on conduction and valence bands alignment; where  $h$  is for hole,  $e$  is for electron,  $E_{C,B}$  is the energy of the conduction Band,  $E_{V,B}$  is the energy of the Valence Band and  $E_g$  is the band gap energy.**

Interestingly, the distribution of the photogenerated charge carriers in the core-shell QDs depends on the position of the energy bands edges of both core and shell semiconductor materials. According to the positions of bands edges in the core-shell QDs, they are classified into four main types: Type I, Inverted Type I, Type II, and Inverted Type II<sup>74,75</sup>. In Type I QDs, the band gap of the core is smaller than that of the shell, and the position of the energy bands of the band gap of the core falls within the gap of the shell (see Figure I-5). CdSe-ZnS core-shell QDs are one the most documented examples of this Type-I QDs, and were primarily designed to enhance the photoluminescence of the QDs by avoiding the interaction of the photoexcited charges localized in the CdSe core with the surrounding medium<sup>76</sup>.

In the inverted Type-I QDs, the band gap of the core is larger than that of the shell, and the energy bands of the shell are aligned within that of the core (see Figure I-5). In such a case, the two types of generated charges will be localized in the outer shell of the QDs. As an example of this type of QDs, CdS-CdSe QDs were assigned as an inverted Type-I core-shell QDs<sup>77</sup>.

In the case of Type II core-shell QDs, the valence band edge of the core is within the band gap of the shell, and the conduction band edge of the shell falls within the band gap of the core. Consequently, the hole will be localized in the core of the QDs and the electron is delocalized in the shell.

In some particular cases the conduction band of the core and the shell are very close in energy, then the electron is delocalized between the core and shell. Thus, the Quantum Dots are of a quasi-Type-II core-shell. This type of QDs, CdSe-CdS QDs the most reported example, was proved to induce high photoluminescence life time and quantum yield compared with their CdSe core counterpart. The photoluminescence quantum yield increased by almost 3 times in the case of the core-shell CdSe-CdS compared to that of the core CdSe<sup>71,78</sup>. In addition, they were reported to be highly efficient for photocatalytic application where photogenerated electrons are essential for the desired reactivity<sup>79,80</sup>.

Furthermore, in the case of the inverted Type-II QDs the conduction band edge of the core is within the band gap of the shell and the valence band of the shell within the band gap of the core. This means that the electrons will be localized in the core of the QDs, and in this case, the holes will be localized in the shell of the QDs.<sup>64</sup>

Core-shell Quantum Dots are mostly synthesized in a two-step procedure, first the synthesis of core Quantum Dots, followed by a purification step, and then subsequent shell growth reaction. During the shell growth step, the number of monolayers can be decided to be grown on the cores. In order to prevent the uncontrolled nucleation of the shell materials, the temperature for the shell growth is generally lower than that used for the core synthesis. Furthermore, the shell precursors are slowly injected, for example, by means of a syringe injection.<sup>64,81</sup>

### **I-2.3. Quantum Dots as redox photocatalyst: working principle.**

Photocatalytic mechanisms based on semiconductor materials rely essentially on the charge transfer between the semiconductors acting as a photocatalyst and the reaction's reagents. Similar to other semiconductors, the first step for a Quantum Dot to act as a photocatalyst is the absorption of light. The irradiation with the convenient light wavelength excites the QD to generate the charge carriers. The electron initially localized at a level of the valence band acquires the sufficient energy needed to cross the band gap and reach the conduction band of the QD. At this stage, the electron occupies a level at the conduction band and leaves a hole (positive charge) at the corresponding valence band level of the QDs. Then, in the presence of an electron acceptor, the electron can be transferred and reduce the electron acceptor molecules to perform a reduction process. Moreover, in the presence of an electron donor, it is possible for the QD to accept an electron and therefore oxidize the electron donor molecule by performing an oxidation process<sup>23</sup> (see Figure I-6). Taking the oxidation and the reduction steps together, a complete photoredox process is described.

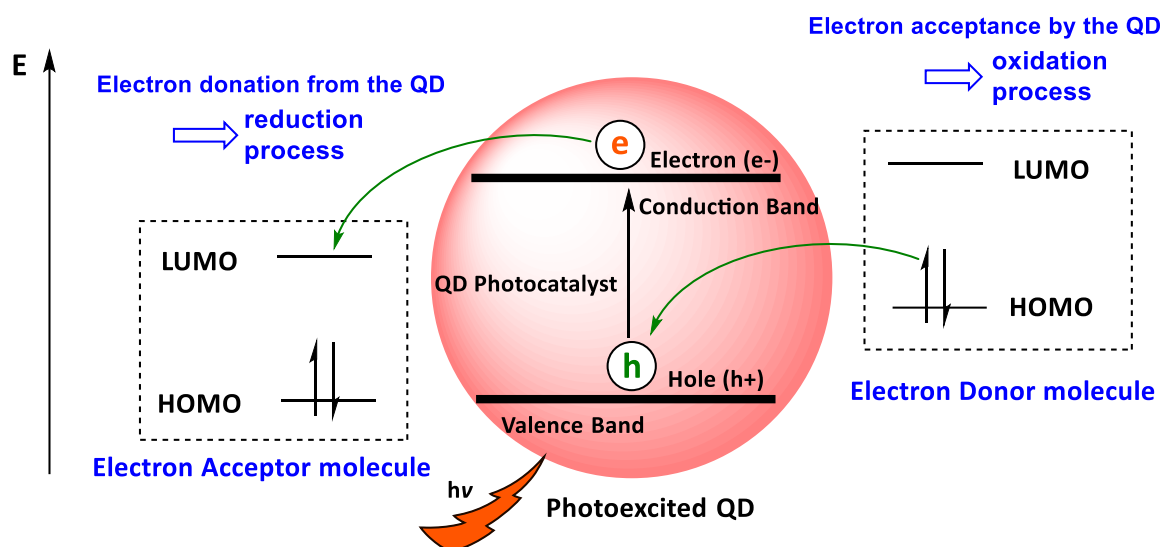


**Figure I-6: The photocatalytic mechanism at the basis of semiconductor Quantum Dots:** The photogeneration of the charge carriers pair, electron and holes (exciton), followed by their transfer to afford a redox reaction.

The efficiency of the redox processes initiated by Quantum Dots depends on the presence of a reasonable driving force for the charge transfer to occur<sup>82</sup>. The driving force is determined by the position of the valence and conduction bands of QDs with respect to the redox potentials of the molecules to be oxidized or reduced. For example, to have an oxidation process, the position of the valence band edge of the QDs should be lower in energy (i.e., more positive in potential) than the HOMO of the molecule to be oxidized. In similar manner, to have a reduction process, the position of the conduction band edge of the QDs should be higher in energy (i.e., more negative in potential) than the LUMO of the molecule to be reduced.

#### I-2.4. Quantum Dots electronic properties: Estimation of the band edge energies.

The experimental estimation of the exact position of the valence and conduction bands of QDs is always complicated during the experiments due to the aggregation in the QDs' sample or due to uncertainties in the used method for the estimation of these bands. Among the experimental approaches used, cyclic voltammetry<sup>49,83</sup>, differential pulse voltammograms<sup>51</sup>, and photoelectron spectroscopy analysis<sup>50</sup> were shown to be useful in

estimating the experimental values for the positions of the QDs' bands. Nevertheless, in some cases, these methods revealed different values for the energy of the QDs' band edges, particularly for the conduction band. For example, even for the same size of CdSe QDs, the variation between the values estimated from different methods could reach 1 eV difference<sup>50</sup> (See Figure I-7).

As mentioned before, the variation of the QDs' size directly affects their optical properties and the width of their band gap. Similarly, the variation of the QDs' size was also proved to have a direct effect on the variation of the position of the valence and conduction band gap of the QDs. In this context, Jasienak et.al<sup>50</sup> used photoelectron spectroscopy analysis to investigate the effect of the QDs' size on the valence band energy for some kinds of QDs such as CdSe, CdTe, PbS, and PbSe. Then they used the experimentally determined optical band gaps to obtain the energy of the conduction bands of the tested QDs. They compared their results to those of previous reports using other methods (see Figure I-7 for the data reported for CdSe QDs).

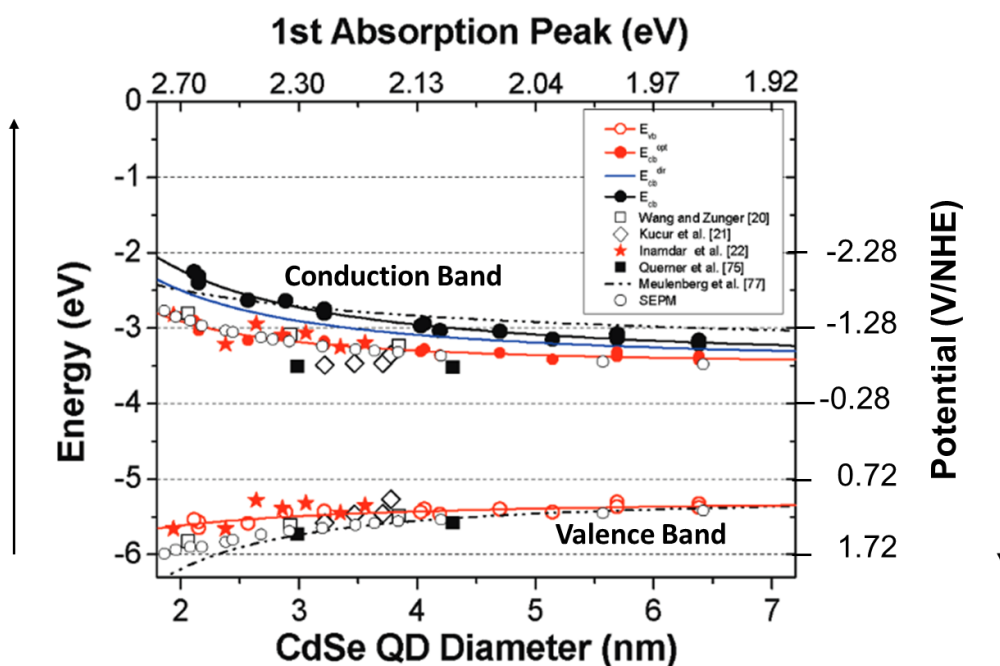


**Figure I-7: The experimental estimation of the energies of the band gap edges of CdSe QDs using different techniques. Figure adapted from reference 50.**

The variation of the band edges energy presented in Figure I-7 shows clearly the effect of the size of the QDs on the position of their valence and conduction bands. The decrease in the QDs size induces lower energy for the valence band and, consequently, a more positive potential making the QDs' holes more oxidizing in redox reactions. The variation of the QDs' size also affects the conduction band energy; the smaller size of the QDs induces higher energy for the conduction band, which means a more negative potential. The more negative potential of the conduction band makes it more reducing in the redox process. In the case of the conduction band energy, the change in the QDs' size could significantly vary the corresponding energy of the conduction band. However, the effect on the valence band energy seems to be less significant compared to that of the conduction band.

In the report by Jasienak et.al<sup>50</sup> they also examined the effect of the surface ligands of the QDs on the variation of their ionization energy and consequently the band edge energies (they considered CdSe QDs with 4.7 nm diameter). They observed that the ionization energy could shift by as much as 0.35 eV due to a change in the surface ligands (Table I-3). Their tests were done on CdSe QDs of same size but changing the QDs' ligands using alkyl amines, TOPO, oleic acid ligands, alkane thiols, or pyridine (Table I-3). Each type of ligand was observed to induce a different ionization energy of the QDs. Then, this study showed the important of the surface ligands of the Quantum Dots on the redox potential of their valence band which could vary by 0.35 eV.

<b>Surface Ligand</b>	<b>Ionization Energy for 4.7 nm CdS QDs (eV)</b>
alkyl amines	5.40 eV
trioctylphosphine oxide	5.45 eV
oleic acid	5.60 eV
alkane thiols	5.65 eV
pyridine	5.75 eV

*Table I-3: The variation of the ionization energy of 4.7 nm CdSe QDs based on their surface Ligand. Data collected from reference 49.*

Recently, new reports were published estimating the valence and conduction band potentials of InP-ZnS QDs using cyclic voltammetry. Pillai and co-workers<sup>84</sup> performed cyclic voltammetry for 2.9 nm sized InP-ZnS QDs functionalized with Myristic acid as surface ligands (Figure I-8-A). The position of the conduction band was estimated using the electrochemical

study, where one peak corresponding to the reduction process ( $E_{\text{red}} \sim -0.76$  V/NHE) was observed in the cyclic voltammogram which reveals the position of the conduction band to be  $-0.76$  V/NHE or  $-3.68$  eV vs vacuum. Then by combining the absorption spectroscopic analysis, the position of the valence band was calculated from the optical band gap energy ( $\sim 450$  nm or  $2.75$  eV) obtained from the absorption spectrum of InP-ZnS QDs. The energy value of valence band was estimated to be  $+1.99$  V/NHE or  $-6.43$  eV vs vacuum. Despite the high potential they reported for the InP-ZnS QDs valence band, they only investigated the oxidation activity of these QDs toward tertiary amines having oxidation potential close to  $0.8$  V/NHE.

A second attempt to estimate the band gap energies of InP-ZnS QDs was reported by Shan Yu et.al.<sup>85</sup>. They relied on the electrochemical analysis using cyclic voltammetry to estimate the valence and conduction band of  $3$  nm sized InP-ZnS QDs functionalized with Oleylamine ligands (Figure I-8-B). The reported values are relatively different from the ones reported by Pillai. Here, they obtained a potential value of  $+1.35$  V/NHE for the valence band of the InP-ZnS QDs, and a potential value of  $-0.92$  V/NHE corresponding to the conduction band of the InP-ZnS QDs. The reported values for the energy of the conduction and valence bands do not match exactly with the band gap of the tested QDs. The InP-ZnS QDs they test have a band gap of  $2.36$  eV ( $525$  nm). However, a band gap of  $2.27$  eV could be deduced from the reported values for the valence and conduction bands.

Furthermore, considering the similar size of the InP-ZnS QDs used in both cases, the difference in the estimated values for the band edges energies could probably be attributed to the different surface ligands, and to the difficulties and uncertainties faced during this kind of experiments. The mentioned studies on the estimation of the potential of the QDs' band gap energies show the difficulty of precisely determining the positions of the QDs' band edges and therefore suggest the importance of performing different experimental trials such as photoluminescence quenching before employing the QDs in the reactions.

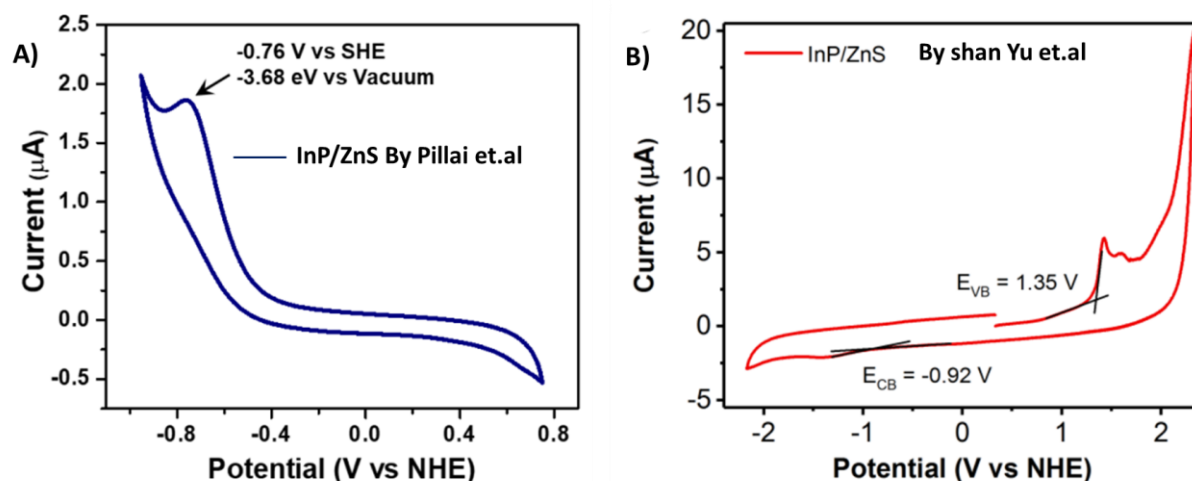


**Figure I-8: Electrochemical analysis to estimate the band gap energies of InP-ZnS QDs:** A) cyclic voltammogram of InP-ZnS QDs functionalized with Myristic acid ligands (adapted from reference 84). Cyclic voltammogram of InP-ZnS QDs functionalized with Oleylamine ligands (adapted from reference 85).

### I-2.5. Challenges in Quantum Dots' Photocatalysis: Optimization of the Ligand layer.

Colloidal QDs are typically synthesized in the presence of ligands with long aliphatic chains (C-18 chains), such as oleic acid<sup>67,86</sup> and oleylamine<sup>78</sup> or TOP and TOPO<sup>65,66</sup>. These ligands are known as native ligands that functionalize the surface of the Quantum Dots and stabilize them in the solvent medium. These long chain native ligands could be an obstacle for the reaction's substrates to approach the QD closely, thus, probably decreasing the QD's catalytic activity. Therefore, in most of the cases it is helpful to remove or exchange at least a portion of the native ligand shell with shorter ligands to disorder the ligand layer and enhance the permeability to the reaction's substrate<sup>87</sup>.

In this context, ligand exchange protocols were reported, especially for the complete phase transfer (i.e. changing solvent polarity). In such cases, complete ligand exchange by replacing the native long chain ligands with shorter ones were used. These cases are interesting when a polar solvent is needed as the ligand exchange could offer a good solubility for the QDs in polar solvents such as water. Several short-chained ligands were shown to be efficient in affording the complete phase transfer of the QDs. Among the most frequently used ligands are thiols-based ligands such as 3-Mercaptopropionic acid(MPA)<sup>88</sup>. However, thiols ligands are not attractive in some photocatalytic cases due to their ability to trap the

photogenerated holes. In these cases, it is possible to use ligands that are analogous to thiolates but which are less reactive with the holes generated by the QDs, such as 3-phosphonopropionic acid (PPAc)<sup>89</sup>.

Besides the effect of the ligand optimization on the catalytic activity, the effect on the behavior of the colloidal QDs was also investigated<sup>45</sup>. For example, Wang et al.<sup>90</sup> explored the effect of the organic ligand layer on CdSe colloidal nanorods' dispersity in solution. They tested the impact of the ligands by varying the length of alkylphosphonic acid ligands used during the preparation of the nanorods. Figure I-9 shows the optical transmission spectroscopy images obtained for CdSe colloidal samples prepared with different ligand lengths. They observed that the preparation of the CdSe rods with relatively short ligands, 8-carbon chain octylphosphonic acid (OPA), enabled to obtain the best dispersed samples. The samples with long chains (C-18) resulted in more aggregated particles. They reported that, when phosphonic acid ligand mixtures are used, the shorter ligands selectively remain on the inorganic surface of the CdSe nanorods. Their results demonstrated the possibility of systematically optimizing the dispersity and properties of CdSe nanorods by selecting the good length of the ligands to functionalize the surface.

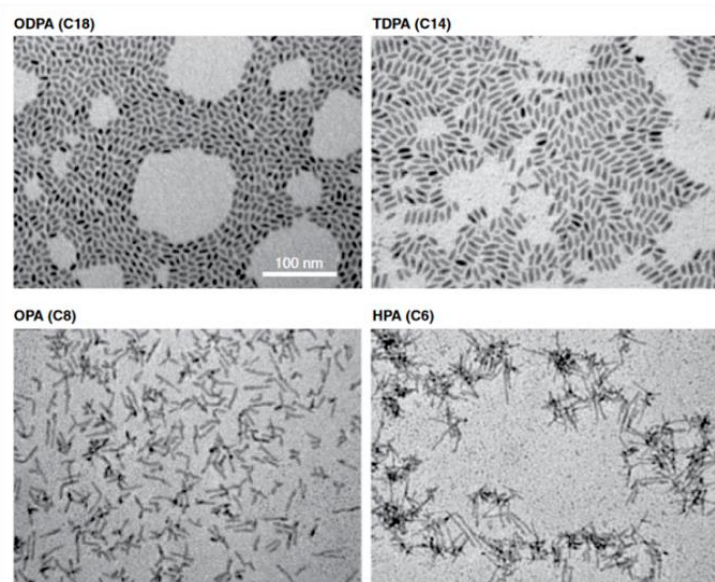


**Figure I-9: The effect of the QDs' surface ligands on their in solution:** TEM images of CdSe colloidal nanorods functionalized with different ligand lengths chains (adapted from reference 90).

Moreover, Weidman et al.<sup>91</sup> investigated the impact of ligands coverage and ligand length on the structure of PbS colloidal Quantum Dots. In this report, they experimentally explore how the surface ligands affect the physical behavior of the QDs in solution by investigating their ability to aggregate or to be better dispersible. They showed that the ligand coverage on QDs surfaces had a significant influence on their self-assembly (aggregation) and the formation of more or less ordered particles. They measured the interparticle spacing between the QDs using grazing-incidence small-angle X-ray scattering (GISAXS) and TEM microscopy as a function of the number of carbon atoms in the surface ligand of the QDs. They mixed ligands of long chains and shorter ones starting from oleic acid (C-18), dodecanoic acid (C-12), decanoic acid (C-10), and hexanoic acid (C-6). They compared the interparticle spacing for the cases of two ligand lengths and one ligand length between neighboring Quantum Dots (see Figure I-10). They showed that surface ligand length is of significant impact on the dispersity of the QDs, and the possibility of obtaining less aggregated particles was achieved by having a mix of shorter ligands.

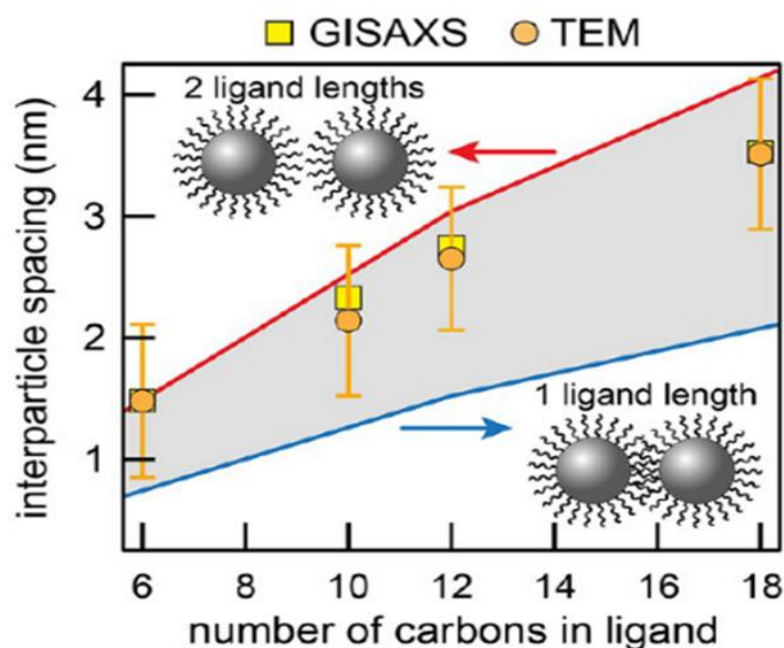


**Figure I-10: The effect of the QDs' surface ligands on their behavior in solution: Measured interparticle spacing as a function of ligand length (number of carbon atoms) compared with the distance of two ligand lengths (adapted from reference 91)**

An interesting study by Weiss and co-workers.<sup>92</sup> showed the effect of the optimization of the ligand shell permeability on the photocatalytic activity of the QDs. In this study, they enhanced the permeability of the ligand layer of CdS QDs by exchanging some of their native oleic acid ligands (C-18) with shorter octylphosphonic acid ligands (C-8). This partial ligand exchange induced an intermolecular disorder in the ligand layer while retaining the photophysical and electronic properties of the QDs, as well as the same solvent for the QDs' solution. Then, they tested the effect of the enhanced permeability of the ligand layer by employing the QDs in a C-C coupling reaction starting from a tertiary amine (see section I-3.3.2, page 56, for the reaction description). In this case, the initial rate of a tested C-C coupling reaction photocatalyzed by the QDs, increased by a factor of 2.3, and the amount of the reaction's product increased significantly leading to a better catalyst efficiency (higher turnovers number) which improved by a factor of 1.6 (Figure I-11).

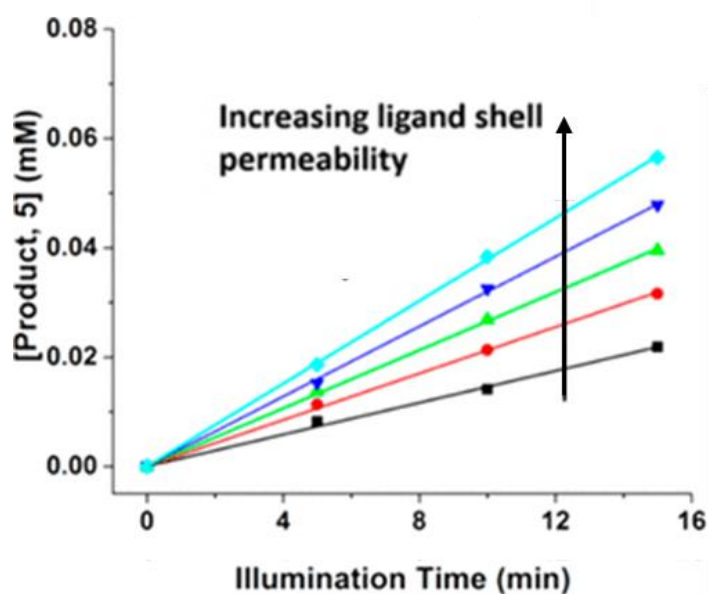
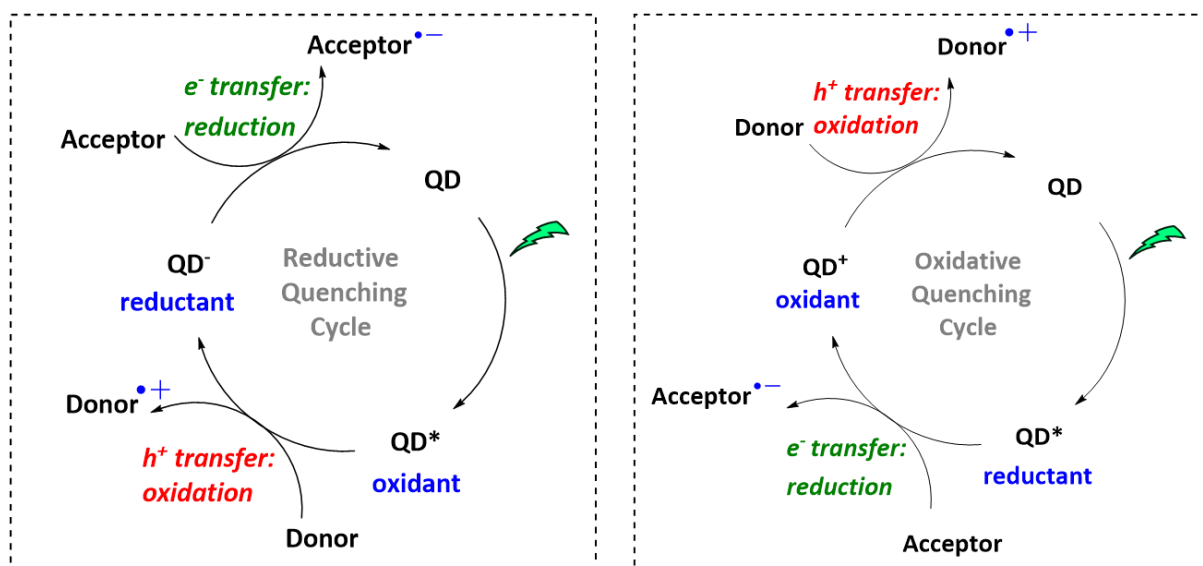


**Figure I-11: Effect of ligand shell permeability on the photocatalytic activity of QDs.** Increasing the reactions' product and the catalytic activity of CdS QDs by enhancing the permeability of the ligand layer (adapted from reference 92).

### I-3. Application of Quantum Dots as photocatalysts in organic transformations.

Since 2015, Quantum Dots provided a new and efficient type of photocatalyst for many synthetic routes and under mild reaction conditions. The use of QDs is mainly focused on core-type CdS or CdSe QDs, with few other reports employing core-shell structured QDs. To the best of our knowledge, this section summarizes all the recent reports of QD-photocatalyzed reactions and categorized according to the different types of reactivity (Summarized in Table I-4 and detailed in the following section).

The general catalytic mechanism using QD as a photocatalyst is represented in Scheme I-3. The catalytic cycles of the QDs can be classified based on the starting step of the reaction as an oxidative quenching cycle (Scheme I-3 Right frame) or a reductive quenching cycle (Scheme I-3 Left frame). Upon visible light irradiation, the QD reaches its first exciton excited state (QD\*), a stage at which a hole or an electron transfer can take place with a neighbor molecule leading to its oxidation or reduction based on the required mechanism. Then, when the QD is in an ionic state (QD<sup>-</sup> or QD<sup>+</sup>), and the required charge transfer occurs leading to closure of the catalytic cycle.



**Scheme I-3: General Photocatalytic mechanism using Quantum dot photocatalyst.** (Left): Reductive quenching catalytic cycle and (Right) Oxidative quenching catalytic cycle.

Reaction Type	QDs	Sacrificial agents	Solvent/co-catalysts/reagents	Light source	Ref.(year)/Page
<b>Net Reductive or Oxidative Reactions</b>					
Oxidation of DNA bases (8-oxo-dG) and reduction of Nitrophenylalanine derivatives	CdSe-ZnS	none	H <sub>2</sub> O	halogen lamp equipped with a 420 nm high-pass filter	40 (2015) P.19
Reduction of nitrobenzene	CdS	MPA	H <sub>2</sub> O:MeOH	405 nm LEDs	93 (2016) P.41
Dehalogenation of aryl Iodide	CdSe	Bu <sub>3</sub> N	MeCN	Blue LEDs	94 (2017) P.42
Dehalogenation of aryl Bromide	ZnSe-CdS	none	Hexane DIPEA	455 nm LEDs	95 (2017) P.42
Reduction of Imines	CdSe-CdS	Thiophenol	Toluene	Green or Solar light	79 (2018) P.43
Borylation of diazonium salts	CdSe	none	DCM: H <sub>2</sub> O	Blue LEDs	96 (2019) P.44
Removal of sulfonyl protecting groups	CuInS <sub>2</sub> -ZnS	TEA	DMSO	532 nm LED	97 (2020) P.45
Dehalogenation of aryl Chloride	CdS	TAEA	DMPU	Blue LEDs	98 (2022) P.46
Oxidation of benzyl alcohol	CdS	none	D <sub>2</sub> O:CD <sub>3</sub> OD	405 nm LEDs	103 (2018) P.48
Oxidation of aliphatic benzyl alcohol	CdSe	none	H <sub>2</sub> O Nickel salts	410 nm LEDs	104 (2017) P.49
Oxidation of boronic acid	CdSe	Oxygen molecule	Acetone Tertiary amine Lewis base	Blue LEDs	105 (2018) P.50
Dehalogenation of aryl Bromide	CdS Gel	Bu <sub>3</sub> N	MeCN	Blue LEDs	123(2022) P.67
<b>Bonds Formation Reactions</b>					
β-alkylation	CdSe	DABCO	H <sub>2</sub> O:DME Cy <sub>2</sub> NH DABCO TFA	Blue LEDs	94 (2017) P.52
β-aminoalkylation	CdSe	DABCO	DMPU Azepane TFA	Blue LEDs	94 (2017) P.53
Amine arylation	CdSe	DABCO	DMA NiBr <sub>2</sub>	Blue LEDs	94 (2017) P.54
Decarboxylative radical addition to styrene	CdSe	Hantzsch ester/ DIPEA	DCM	Blue LEDs	94 (2017) P.55

	Bonds	Formation	Reactions		
C-H arylation	ZnSe-CdS	none	Hexane DIPEA Pyrrole	455 nm LEDs	95 (2017) P.42
C-C vinylation coupling	CdS or InP-ZnS	none	Benzene	405 nm LEDs	92 (2017) 84 (2019) P.56
Cyclization of difluoromethyl chlorides	CdS	none	NMP	Blue LEDs	111 (2019) P.57
Reduction of aromatic ketone for C-C coupling	CdS	TEA	MeCN:H <sub>2</sub> O Nickel salts	Blue LEDs	112 (2021) P.58
Reduction of Aryl aldehydes for C-C bonds	CdSe-CdS	Thiophenol	Hexane	Green LED	113 (2021) P.59
Pinacol formation integrated with CO <sub>2</sub> reduction	CdSe-CdS	none	DMF	Blue LEDs	114 (2019) P.60
Radical-radical coupling : Formation of disulfide	CdSe	none	H <sub>2</sub> O or H <sub>2</sub> O:THF Nickel salts	>400 nm LEDs	115 (2014) P.61
Radical-radical coupling : Activation of $\alpha$ -C-H bonds	CdSe	none	THF	450 nm LEDs	116 (2021) P.62
Radical-radical coupling : Alkylation and arylation of allylic C(sp <sup>3</sup> )-H bonds	CdSe	none	DMF Nickel salts	Blue LEDs	117 (2021) P.64
Radical-radical coupling : for C-S bond formation	CdSe	none	MeCN Nickel salts	Blue LEDs	118 (2021) P.64
C-P bond formation	CdSe	none	DMF	450 nm LEDs	119 (2022) P.65
Triplet excited state reactions	CdSe	none	THF	450 nm LED	120 (2019) P.66
Radical-radical coupling: $\alpha$ -amino arylation reaction	CdS Gel	none	DMA	Blue LEDs	123 (2022) P.67

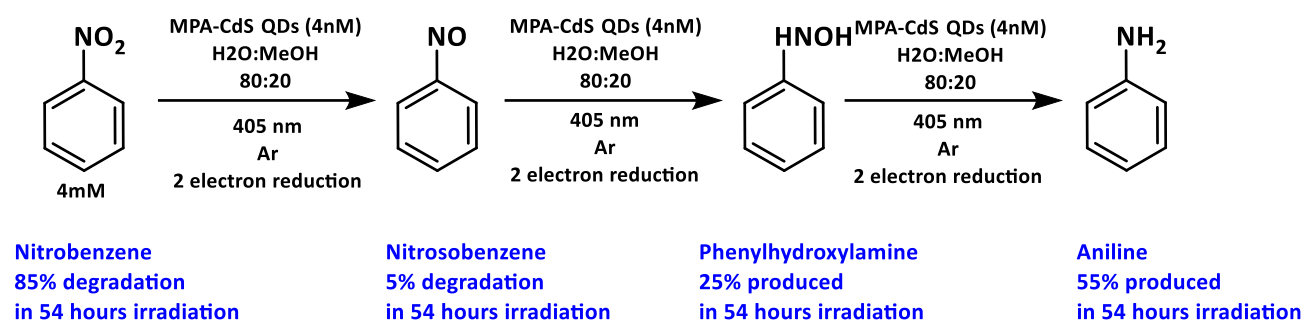
	Bond	Cleavage	Reaction		
Reductive deprotection	CdS	TAEA	DMPU	Blue LEDs	98 (2022) P.48
Reductive ring opening	CdS	TAEA	DMPU	Blue LEDs	98 (2022) P.48
Breaking $\beta$ -O-4 bonds in lignin	CdS	none	MeCN	Blue LEDs	124 (2018) P.68
Breaking $\alpha$ C-O bonds in lignin	CdSe	none	MeCN	White LEDs	125 (2019) P.69
		Photo-	polymerization	Reactions	
Polymerization of (meth)acrylates and styrene	CdSe	DIPEA	THF	Blue LEDs	126 (2018) P.69
PET-RAFT Polymerization reaction	CdSe	none	H <sub>2</sub> O	532 nm LED	127 (2019) P.70

**Table I-4: Summary for the selected QD-Photocatalyzed reactions.** Experimental details, mechanisms, yields and the full name of the abbreviations are specified in the following text.

### I-3.1. QDs-photocatalyzed net reductive reactions.

#### I-3.1.1- Photocatalytic reduction of nitrobenzene using water-soluble CdS QDs.

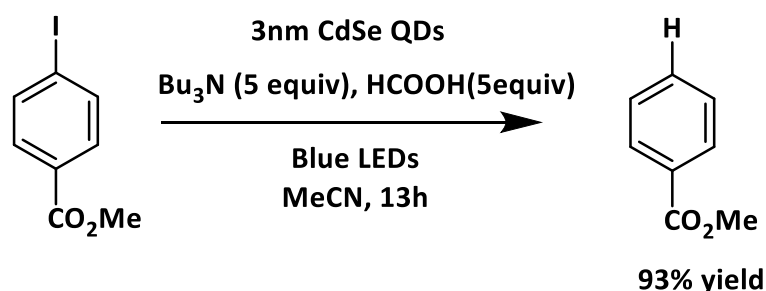
Early in 2016, Jensen et al.<sup>93</sup> reported the use of water-soluble CdS QDs for the 6-electron reduction reaction of nitrobenzene to aniline under visible-light (Scheme I-4). CdS QDs were functionalized by 3-mercaptopropionic acid ligands (MPA), which afford their transfer to water as a solvent. The reaction was optimized using MPA-capped CdS QDs (3.7 nm) as a redox photocatalyst in the presence of an additional excess of MPA in the reaction mixture. The addition of the MPA served as a sacrificial agent for trapping the holes from the photoexcited QDs. The reaction medium was further optimized in a mixture of 80:20 water:methanol. The addition of methanol was helpful for the trapping of holes during the reaction mechanism. Notably, the reduction of nitrobenzene requires a six-electron reduction process to reach aniline. In this case, CdS QDs were shown to be efficient in accomplishing the needed steps for reducing nitrobenzene through the identified intermediates nitrosobenzene and phenylhydroxylamine to the final aniline product (Scheme I-4). The reaction was monitored over 54 hours of continuous irradiation, and the evolution of the reduction of nitrobenzene was confirmed from the identified products at the end of the reaction.



Scheme I-4: Reduction of nitrobenzene to aniline using MPA-capped CdS QDs in water:methanol medium after 54 hours of visible light irradiation. Adapted from reference 93.

### I-3.1.2- Photocatalytic reductive dehalogenation aryl halides using CdSe QDs.

In their seminal work in 2017, Weix and Krauss<sup>94</sup> used oleate-capped CdSe QDs to reproduce previously demonstrated photoredox reactions using molecular photocatalysts. In one of the reported reactions in this work, they involved CdSe QDs in a reduction reaction of aryl iodide substrate. They showed that the CdSe QDs are efficient in providing electrons to initiate the first catalytic step due to the good reduction power of the photoexcited QDs. The reaction was developed in the presence of tributylamine ( $\text{Bu}_3\text{N}$ ) as a sacrificial electron donor to ensure the consumption of the photogenerated holes. Notably, the reaction was highly efficient, providing the desired product in a high yield of 93% (Scheme I-5).

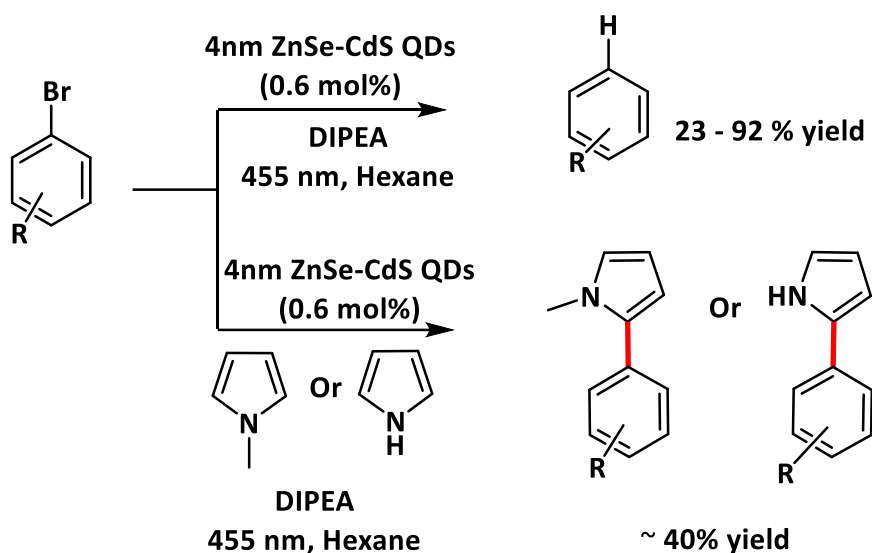


Scheme I-5: Reductive dehalogenation of aryl iodide using CdSe QDs. Adapted from reference 94.

### I-3.1.3- Photocatalytic reductive dehalogenation and C–H arylation reactions using ZnSe-CdS core-shell QDs.

In 2017, Pal et al.<sup>95</sup> designed ZnSe-CdS core-shell QDs and employed them as photocatalyst for reductive dehalogenations and C–H arylation reactions from aryl bromides under visible light. The growth of one-layer CdS shell on the surface of the ZnSe core enabled the visible light absorption of the ZnSe-based QDs without compromising the very reductive potential of the conduction band of ZnSe QDs. In this work, they showed that (Hetero)Aryl

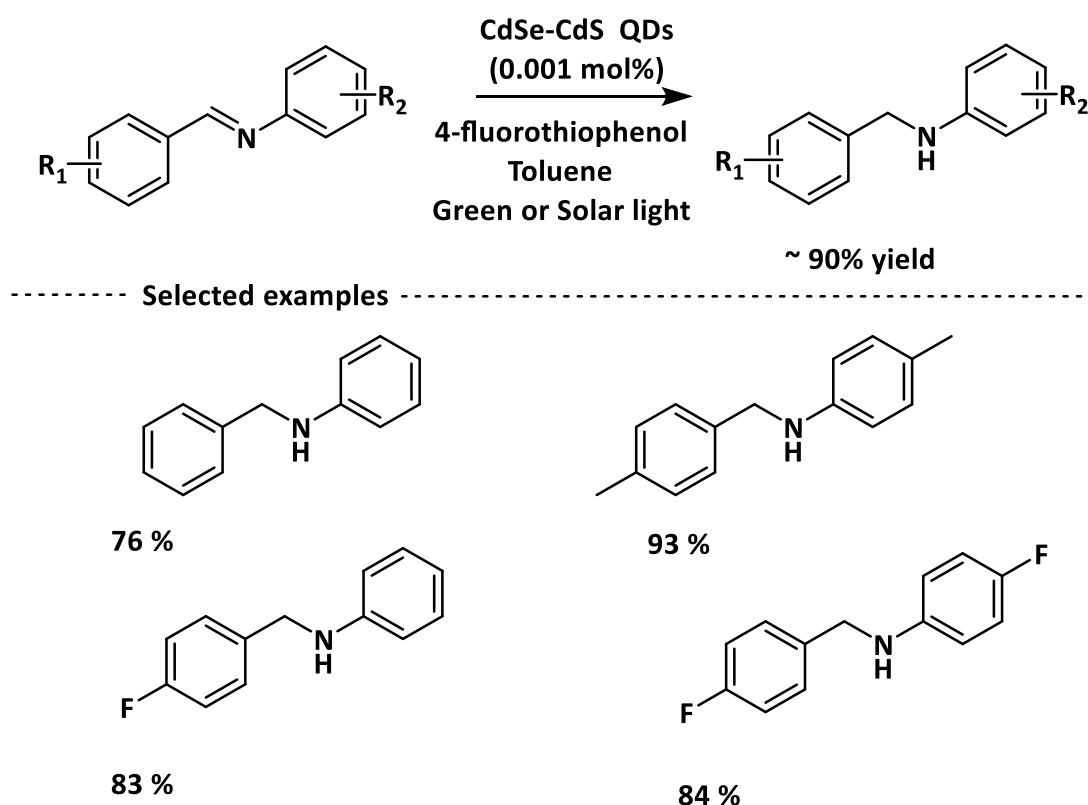
Bromide accepted electrons from the photoexcited QDs. Then dehalogenation took place to form the corresponding (hetero)-aryl compounds reaching up to 92% yield. Interestingly, in the presence of pyrrole derivatives as hole trapping reagents the C–H arylated product were favorably produced with a yield range close to 40% (Scheme I-6)



Scheme I-6: Reductive dehalogenations and C–H arylation reactions of aryl bromides using ZnSe-CdS QDs. Adapted from reference 95.

#### I-3.1.4- Photocatalytic reduction of imines to form amines using CdSe-CdS core-shell QDs.

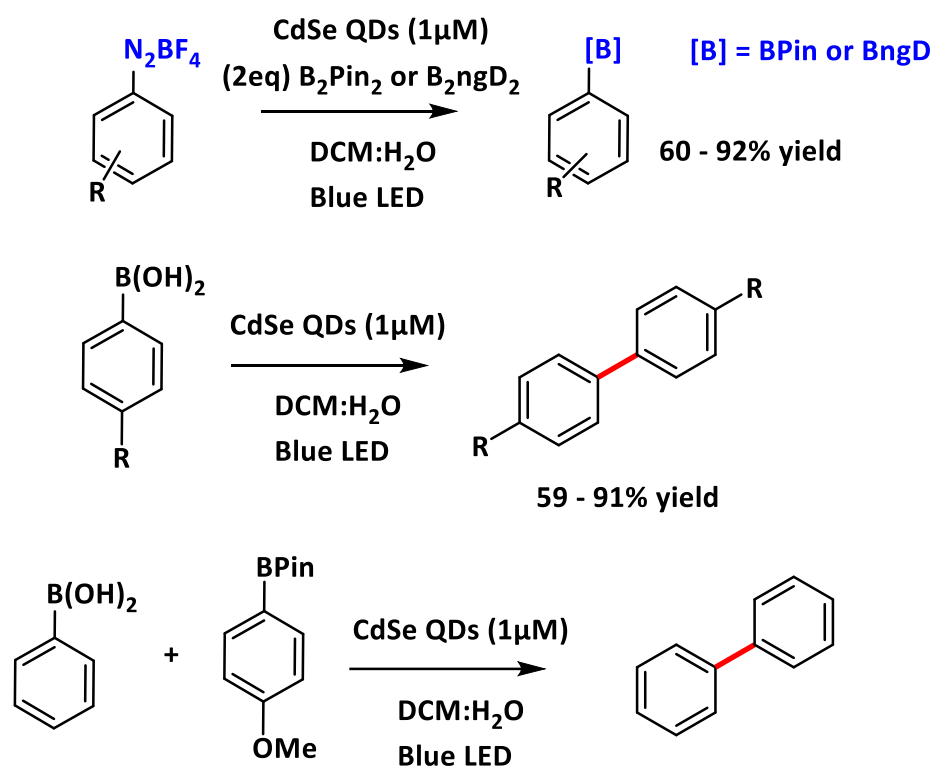
In 2018, Shan et al.<sup>79</sup> used quasi Type-II CdSe-CdS QDs (described in section I-2, page 27) as a redox photocatalyst in a one-pot reaction for photoreduction of imines to the corresponding amines in the presence of thiophenol as sacrificial donor (Scheme I-7). The reaction system was applied to a wide scope of substrates. The desired reactions were obtained in high yields (up to 90%) using very low catalytic loading of the QDs (0.001mol %), which was enabled by the very high turnover number achieved by the QDs. (TON  $\sim 10^5$ ).



Scheme I-7: The photoreduction of imines to amines using CdSe-CdS QDs. Adapted from reference 79.

### I-3.1.5- Photocatalytic borylation using water-soluble CdSe QDs.

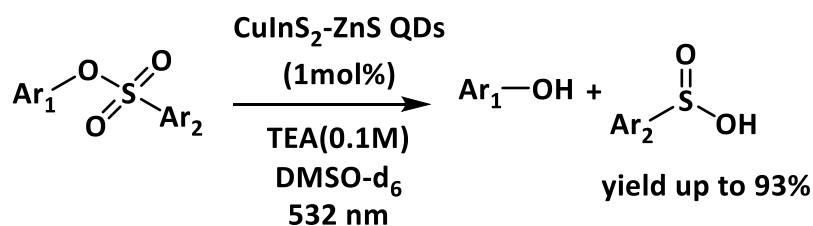
In 2019 Chandrasekhar et al.<sup>96</sup> reported a photoredox method for the borylation of diazonium salts photocatalyzed using water-soluble CdSe QDs without any sacrificial additive. They optimized the reaction conditions in a mixture of water and dichloromethane to ensure a relatively acidic condition (pH~6). The optimized conditions were critical to avoid the decomposition of diazonium salt and to prevent the formation of disulfide by-product from the mercaptopropionic acid (MPA) ligands. Moreover, the corresponding biphenyl products were obtained by photocatalytic coupling of final borane products or boric acid under the action of visible light excited CdSe QDs (Scheme I-8). Notably, the photocatalytic reaction system was highly efficient as a very high TON value close to TON  $\sim 10^5$  was achieved.



Scheme I-8: Photoredox borylation of diazonium salts photocatalyzed using water-soluble CdSe QDs. Adapted from reference 96.

### I-3.1.6- Photoreductive removal of sulfonyl-based protecting groups using CuInS<sub>2</sub>-ZnS core-shell QDs.

In 2020, Perez et al.<sup>97</sup> reported the use of the CuInS<sub>2</sub>-ZnS core-shell QDs as a strong reductive type of QDs as photocatalyst for a photocatalytic deprotection of the aryl sulfonyl-protected phenols in the presence of triethylamine (TEA) as a sacrificial hole scavenger (Scheme I-9). They found that the rate of deprotection for a substrate containing carboxylic acid moieties, which is known to bind to the QDs' surface efficiently, was accelerated by more than a factor of 10. In this case, the substrate was easily absorbed on the surface of the QDs to afford the two electrons' transfer needed for initiating the reaction. The obtained results showed that the deprotection was selective. The sulfonyl groups with electron-withdrawing groups were easier to be removed. Moreover, the electrochemical analysis showed that the CuInS<sub>2</sub>-ZnS QDs are efficient reductant for the aryl sulfonyl deprotection by reaching redox potential of -1.81V/SCE.



Scheme I-9: Photocatalytic deprotection of the aryl sulfonyl-protected phenols using CuInS<sub>2</sub>-ZnS QDs. Adapted from reference 97.

### I-3.2. CdS QDs as powerful photoreductants for dehalogenation reaction initiated by Auger processes.

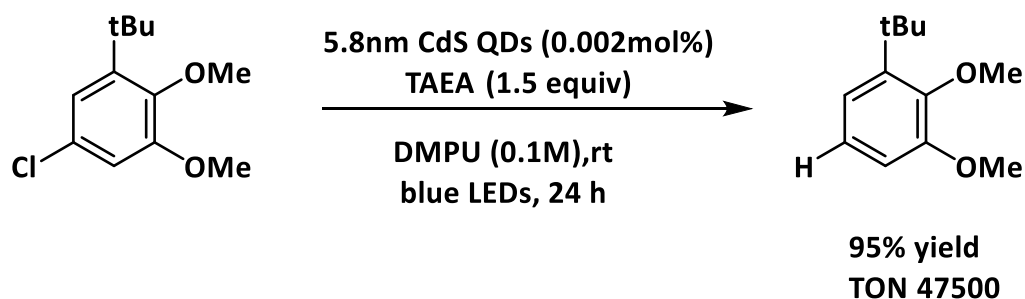
Recently in 2022, Weix, Krauss and co-workers<sup>98</sup> presented CdS QDs as strong photoreductants for organic reactions by demonstrating an efficient hydrodechlorination reaction using CdS QDs (Scheme I-10-A). They reported the ability of CdS QDs to act as powerful photoreductants by presenting evidence that a highly reducing electron is generated due to Auger processes resulted from two consecutive photoexcitation of CdS QDs (Scheme I-10-B). They tested the reductive hydrodechlorination of 4-chloro-2,6-di-tert-butylanisole which has a highly negative reduction potential ( $E_{\text{red}} = -3.4 \text{ V/SCE}$ ) which is in principle out of reach by the conduction band of CdS QDs ( $-2.24 \text{ V/SCE}$  based on the authors' citations in this work who selected the most negative reported value for the electrons in the conduction band of CdS QDs<sup>99,100</sup>).

They optimized the reaction conditions in polar aprotic solvents such as N,N'-dimethylpropylene urea (DMPU) which provided the highest yield of dehalogenated product (95%). In order to afford a good electron generation and transfer, sacrificial electron donors such as tris(2-aminoethyl)amine (TAEA) were effective and showed to be strong ligands for the CdS QDs' surface. Moreover, they compared the activity of the CdS QDs to other different 2-photon catalysts. The results show the advantage of using CdS QDs over other catalysts as a higher efficiency of the CdS QDs was obtained with a higher Turnover number, 47500 TONs obtained with CdS QDs compared to a maximum of 27 TON obtained with Ir-based transition metal complexes.

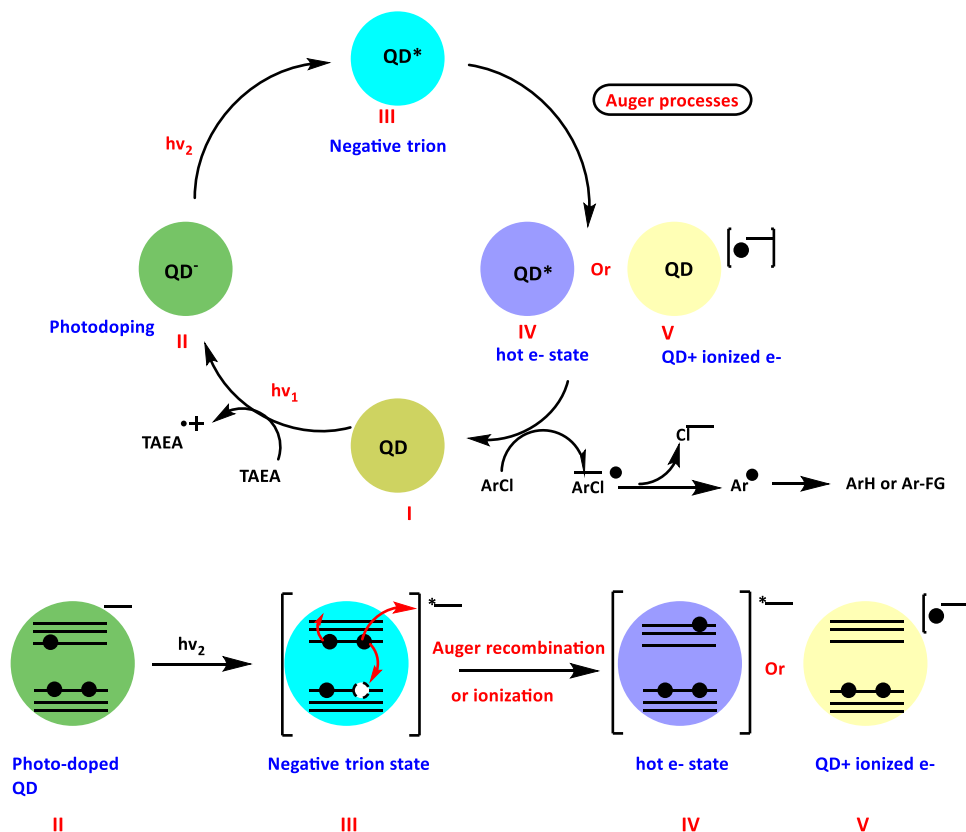
Based on their obtained results, they proposed the photoreduction mechanism as follows (Scheme I-10-B). After excitation, the neutral QD (I) generates its exciton and then becomes negatively charged after the hole transfer to TAEA to generate anionic QD (II). After

a second photon absorption, QD (II) can generate a negative trion state (III), which can undergo Auger processes to generate a hot-electron state (IV) or an ionized electron (V) with a highly negative potential, which at such a state, can reduce the aryl halide substrates. Then, the reduced substrates can undergo fragmentation and hydrogen atom transfer to produce the dehalogenated product.

A)



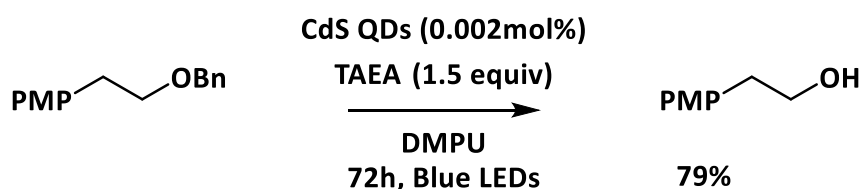
B)



Scheme I-10: Photocatalytic hydrodechlorination reaction using CdS QDs initiated by Auger processes. Adapted from reference 98.

Then, they explored the use of CdS QDs for other reductive transformations that could require high reduction power. Scheme I-11 shows two selected reductive reactions. For example, Scheme I-11-A shows the reductive deprotection of alkyl benzyl ether to the corresponding alcohol, which was obtained in 79% yield. The deprotection of Benzyl moieties requires a reduction potential of  $E_{\text{red}} = -3.1 \text{ V} / \text{SCE}^{101}$ . In addition, they also explored the use of the CdS QDs for the reductive ring opening of cyclopropyl carbonyl derivatives (Scheme I-11-B), which successfully obtained a reaction yield of 71%. This reductive C–C bond cleavage could be achieved via reduction of the ester, which requires  $E_{\text{red}} = -2.8 \text{ V vs SCE}^{102}$ .

#### A) Reductive deprotection



#### B) Reductive ring opening of cyclopropyl carbonyl derivatives



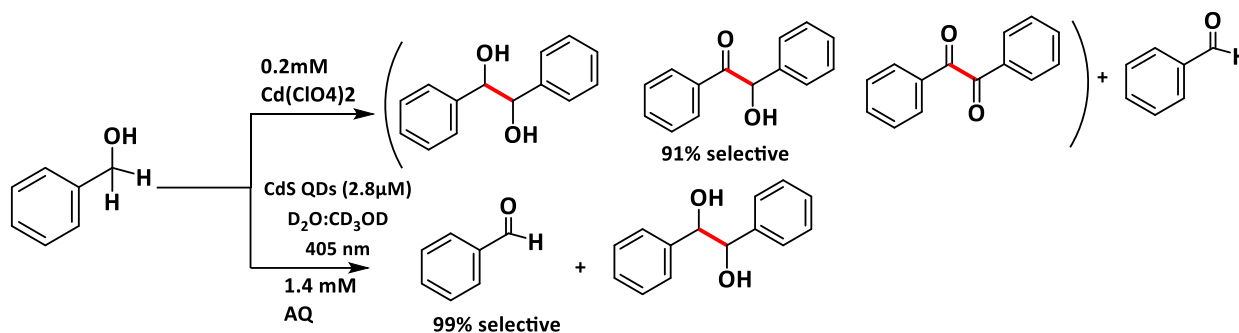
Scheme I-11: Reductive organic transformation using CdS QDs. Adapted from reference 98.

### I-3.3. QDs-photocatalyzed net oxidative reactions.

#### I-3.3.1- Photooxidation of benzyl alcohol using CdS QDs.

Late in 2018, McClelland and Weiss<sup>103</sup> reported the photo-oxidation of benzyl alcohol to benzaldehyde with 99% selectivity, or to hydrobenzoin by carbon–carbon coupling reaction with 91% selectivity using colloidal CdS QDs. They observed that the control of reaction's selectivity was influenced by the amount of Cd<sup>0</sup> deposited on the surfaces of the QDs and by the concentration of benzyl alcohol. The deposition of Cd<sup>0</sup> on QDs, by the addition of Cd(ClO<sub>4</sub>)<sub>2</sub>, afforded the benzaldehyde to undergo a new reduction to form the C–C coupling

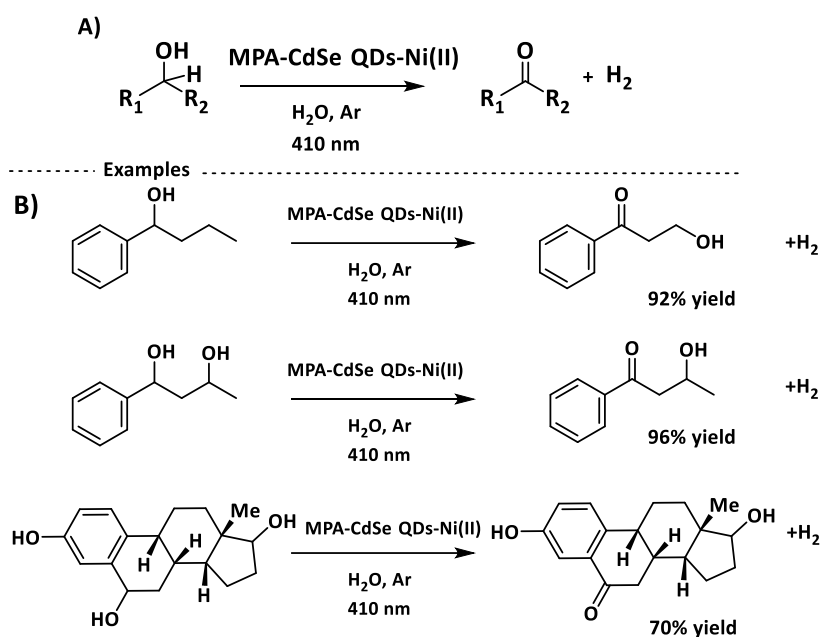
products (Scheme I-12). However, by adding anthroquinone-2-sulfonate (AQ), as an electron acceptor, the photocatalytic system favored the formation of benzaldehyde with high selectivity (Scheme I-12). Moreover, using the optimized conditions a maximum Quantum yield value of 0.9% was obtained for the QD-photocatalyzed reactions.



*Scheme I-12: The oxidation of benzyl alcohol using CdS QDs with a controlled selectivity toward the products. Adapted from reference 103.*

### I-3.3.2- Photooxidation of alcohols using water-soluble CdSe QDs.

In 2017, Zhao Wu et al.<sup>104</sup> showed that the selective oxidation of alcohols to aldehydes or ketones using water soluble MPA-capped CdSe QDs in the presence of Ni(II) salts is efficient (Scheme I-13-A). The photo-excitation of the QDs initiated the oxidation of the alcohols, in addition to a reactive thiyl radical generated from the thiolate anion adsorbed at the QDs surface coming from the MPA ligands. This radical was proved to help in eliminating a hydrogen atom from the C-H bond in the alcohols. Furthermore, the reactions tested using benzyl alcohols (Scheme I-13-B) were also efficient due the fact that benzyl alcohols are easier to oxidize. In this reaction, they added nickel salts to profit from the corresponding Ni(II) ions to act as co-catalyst facilitating the hydrogen formation.

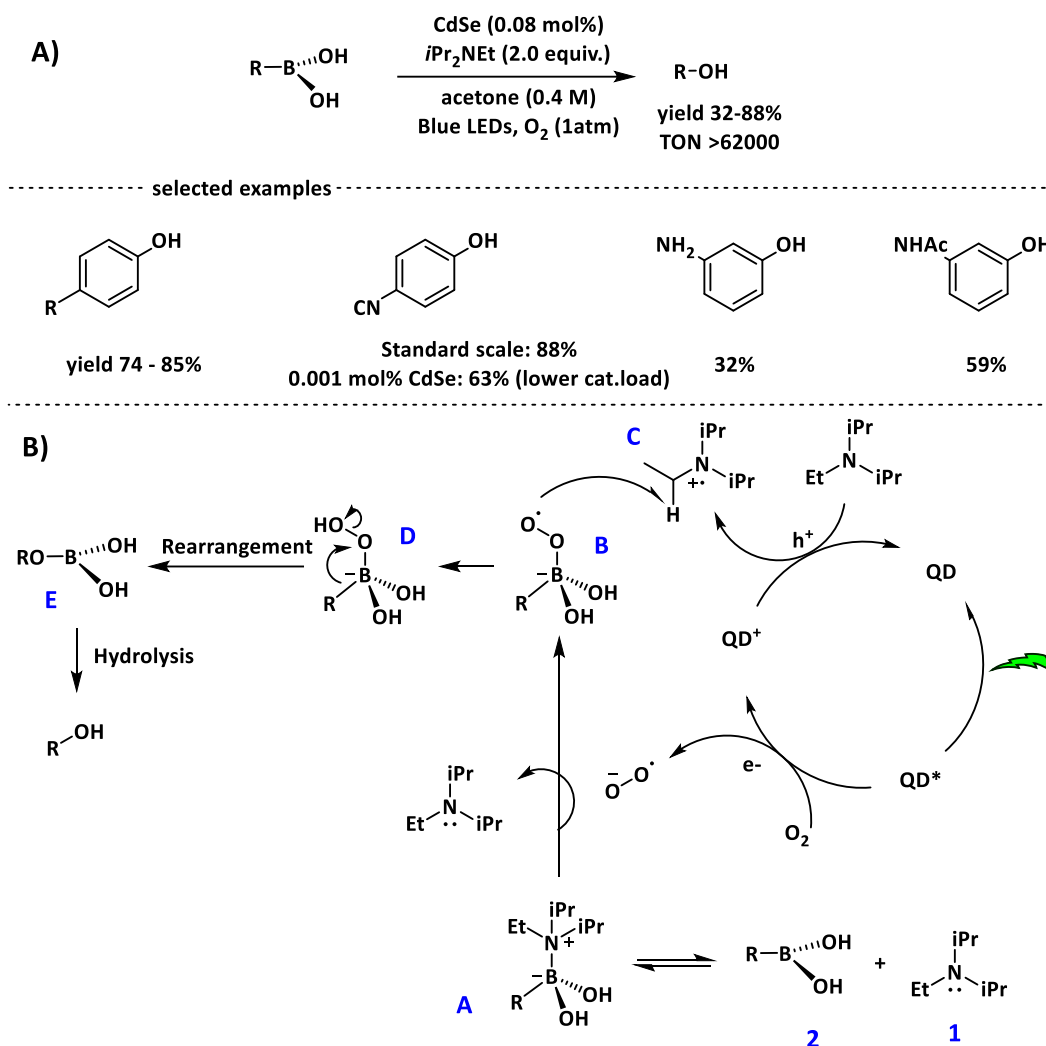


Scheme I-13: Photocatalytic oxidation of alcohols using CdSe QDs. Adapted from reference 104.

### I-3.3.3- Photocatalytic aerobic oxidation of boronic acids using CdSe QDs.

Simlandy et al.<sup>105</sup> used oleylamine-capped CdSe to photocatalyze aerobic oxidation of boronic acids reaction. Notably, the protocol developed for this reaction required mild conditions and very low catalyst loading of 0.08 mol% for standard reaction optimization and even lower 0.001 mol% for high-scale reactions. The resulting products were produced in good to high yields (up to 88%), with turnover numbers reaching 62000 TON (Scheme I-14-A). In this work, they observed that the boronic acid starting material could be responsible for increasing the QDs' emission lifetime, probably due to the passivation of the QDs' surface. The reaction optimization revealed the requirement of tertiary amine Lewis base (*i*Pr<sub>2</sub>NEt) to accomplish the first electron transfer, and to form with the boronic acid a Lewis acid–base adduct (A) which acts as the electron acceptor afterwards and prevents the boronic acid from interacting directly with QDs (See scheme I-14-B for the mechanism). Moreover, The reaction requires molecular oxygen, since it is proposed that the electron transfer produces the superoxide radical anion that eliminates *i*Pr<sub>2</sub>NEt to form a boronic acid-superoxide radical anion (B) (Scheme I-14-B). Then, the hole transfer from the QD to the tertiary amine produces an ammonium radical cation (C) which closes the catalytic cycle with the QDs. Next, a hydrogen atom transfer from the radical cation (C) with the superoxide radical in (B) leads to the

peroxyboronate intermediate (D). After the rearrangement of D to form E, hydrolysis of E takes place and produces the final desired alcohol.



Scheme I-14: Photocatalytic aerobic oxidation of boronic acids reaction using CdSe QDs. B/ proposed catalytic mechanism. Adapted from reference 105.

### I-3.3. QDs-photocatalyzed bond formation reactions.

The use of semiconductor Quantum Dots in redox neutral reactions useful in synthesis chemistry represents an attractive application of Quantum Dots. The advances of photocatalytic in bond-forming or cleavage reactions using Quantum Dots are collected in the following sections.

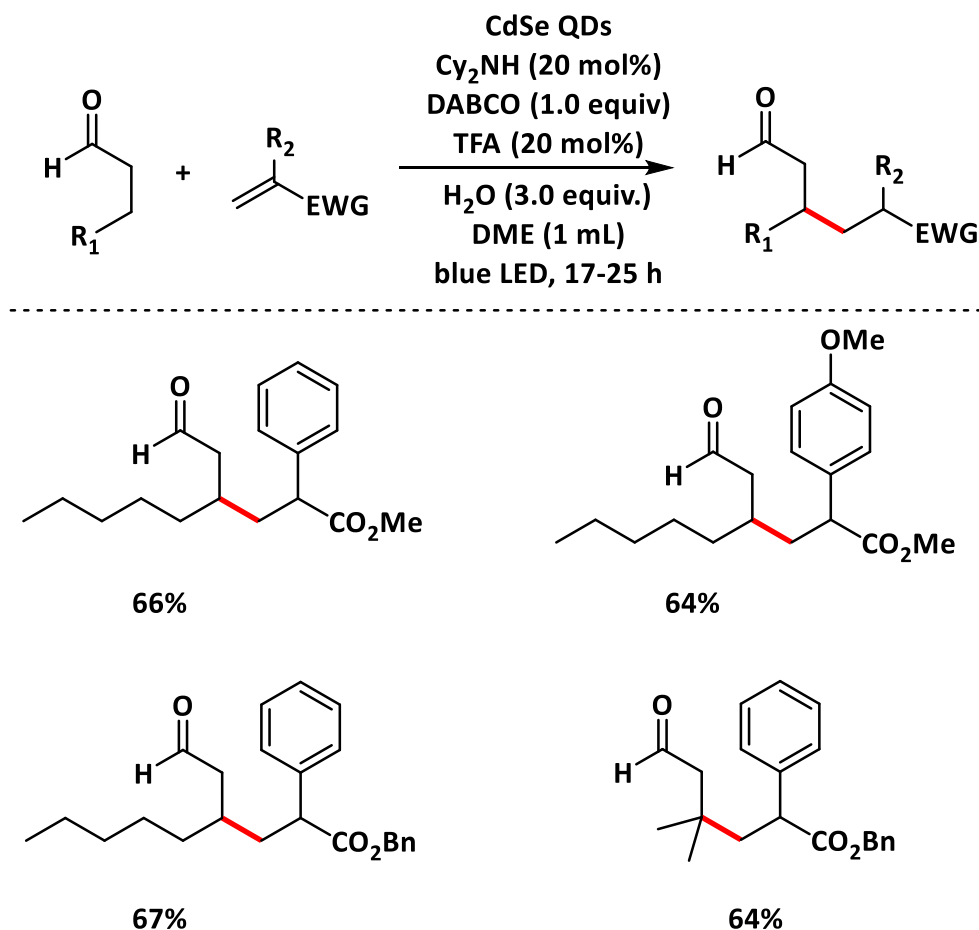
#### I-3.3.1. QDs-photocatalyzed bond formation reactions: the seminal work by Weix and Krauss.

To demonstrate the ability of Quantum Dots to photocatalyze organic reactions, researchers have explored the activity of Quantum Dots by employing them as photocatalysts for previously developed reactions using transition-metal complexes such as Iridium or Ruthenium catalysts. In 2017, Weix, Krauss and their co-workers<sup>94</sup> reported the use of oleate-capped CdSe QDs as visible light photocatalyst for five different organic transformation reactions previously demonstrated using transition metal photocatalysts. The use of low catalytic loading of CdSe QDs was efficient to photocatalyze four C–C coupling reactions ( $\beta$ -alkylation of aldehydes,  $\beta$ -aminoalkylation of ketones, amine arylation, and decarboxylative radical addition to styrene) beside one example of a reductive dehalogenation reaction (mentioned in section I-3.1, page 42). The CdSe QDs were able to achieve a high turnover number reaching up to 79100 TON, which surpassed in some cases the TON achieved for the best-reported traditional organic dyes photocatalysts. The QDs-photocatalyzed reaction exhibited a quantum yield close to 0.31%. Such a value is among the highest for the QDs-catalyzed photoredox reactions for organic transformations. The reactions developed in this work are summarized below.

##### A- $\beta$ -alkylation of aldehydes via an enamine intermediate

In this seminal work by Weix and Krauss, the first tested bond formation reaction was a  $\beta$ -alkylation reaction of aldehydes (Scheme I-15). This  $\beta$ -alkylation of aldehydes in the presence of olefin reaction is a combination between photoredox and organocatalysis ( $Cy_2NH$ ) which was reported before by MacMillan and co-workers<sup>106</sup>. The essential photoredox steps in this reaction's process is the ability of the CdSe QDs (acting as a photoredox catalyst) to oxidize the enamine intermediate (produced from the organocatalysis cycle), and to reduce a carbon radical intermediate trapped with an activated olefin presented in the reaction medium. This is considered as an important example of alpha-ester radical reduction.

Interestingly, it was possible to perform the reaction optimization on four different substrates leading to the corresponding product in a good range of yields between 60 and 70% (Scheme I-15).

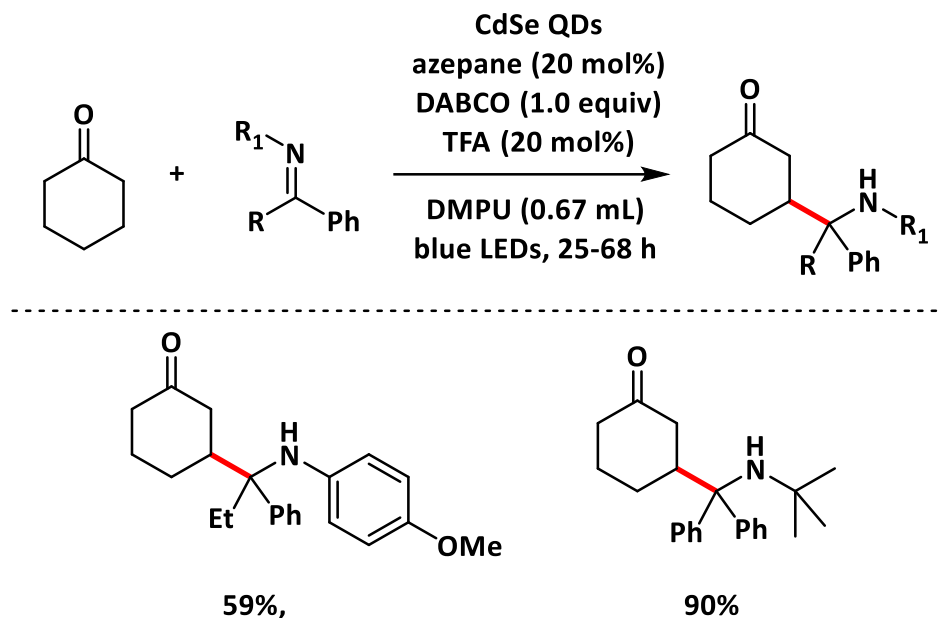


*Scheme I-15:  $\beta$ -alkylation of aldehydes in the presence of CdSe QDs. Adapted from reference 94.*

### B- Photocatalytic $\beta$ -aminoalkylation of ketones

The second example of the bond formation reactions in the work by Weix and Krauss is the  $\beta$ -aminoalkylation of ketones which is also a combination between organocatalysis (using azepane) and photoredox catalysis using the same kind of CdSe QD. This reaction was developed previously by MacMillan and co-workers using an iridium-based photoredox catalyst<sup>107</sup>. In this reaction, they proposed that the first catalytic step by the QD is the oxidation of DABCO presents in the medium that acts as an electron transfer agent to form the enamine radical cation during the organocatalytic cycle. Then, the QD reduces the imine substrate. It is also possible that a direct radical addition to the imine takes place to generate

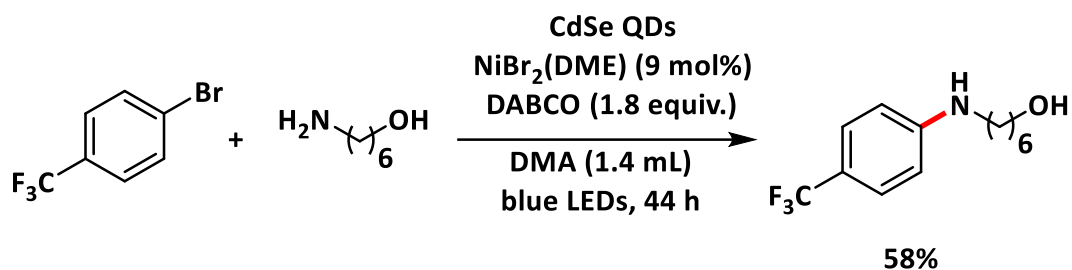
an intermediate that could be reduced by the QD. They were able to apply the protocol of this reaction to two examples of substrates and obtained 59% and 90% yields (Scheme I-16).



Scheme I-16:  $\beta$ -aminoalkylation of ketones in the presence of CdSe QDs. Adapted from reference 94

### C- Photocatalytic Amine arylation

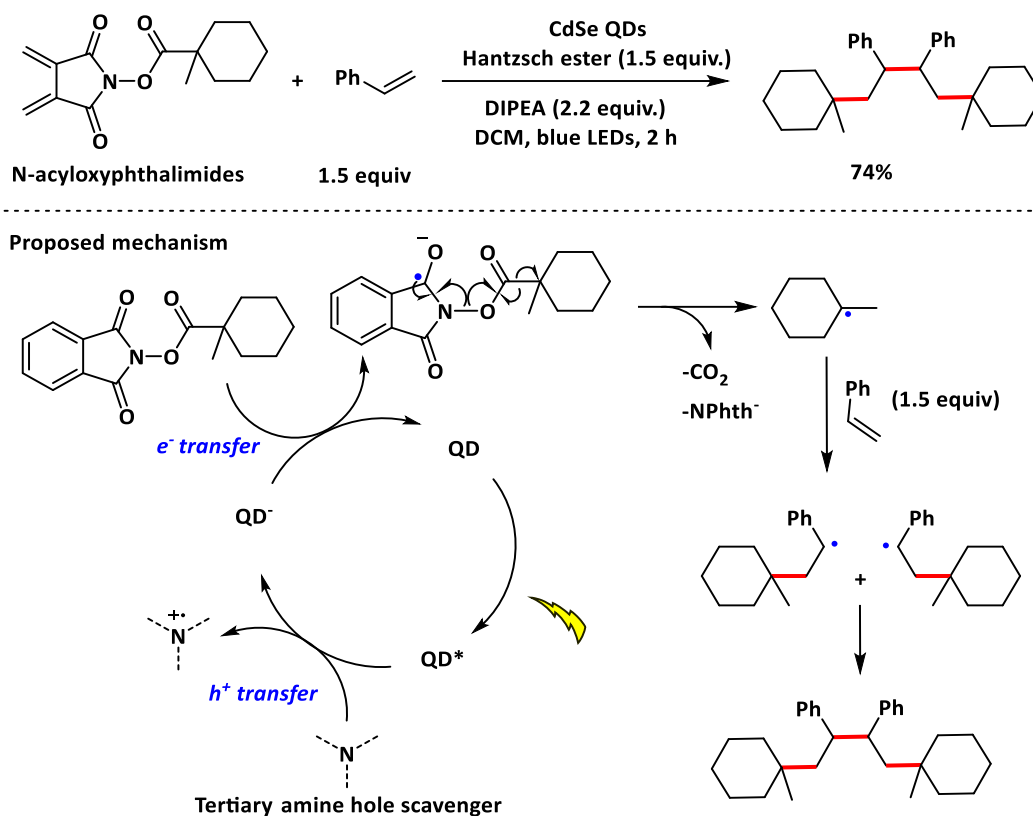
Next, in the same report, an amine arylation reaction between 1-bromo-4-(trifluoromethyl) benzene and aminoalcohol is reported. This reaction combines a photoredox catalysis and a nickel catalysis ( $\text{NiBr}_2$ ). The reaction was initially described by MacMillan using iridium-based catalyst for the photoredox cycle<sup>108</sup>. For the reaction mechanism, it is proposed that the photocatalyst (CdSe QDs by Weix and Krauss and iridium complex by MacMillan) is able to oxidize a nickel (II) complex into a nickel(III). The nickel (II) complex is formed during the nickel catalysis cycle between the nickel salt and the aryl bromide. Thus, an essential redox step occurs in the photoredox cycle is to promote a C-N reductive elimination. The resulting nickel (I) can be reduced by the photocatalyst (CdSe QD or Ir-complex) to nickel (0). Using CdSe QDs the reaction afforded the final C-N aniline product with a 58% yield (Scheme I-17).



Scheme I-17: Amine arylation using CdSe QDs and nickel catalyst. Adapted from reference 94.

#### D- Decarboxylative radical addition to styrene using CdSe QDs

The last example of the report by Weix and Krauss is the decarboxylative radical addition to styrene. Initially, this reaction was developed by Lackner et al.<sup>109</sup> using Ruthenium transition metal photocatalyst. In this reaction, a tertiary amine was used as a sacrificial hole scavenger to trap the holes of the photoexcited QDs. Then, the QD could transfer electrons for the reduction step in order to be used for the decarboxylative radical formation from N-acyloxyphthalimides (Scheme I-18-mechanism). Then, in the presence of a styrene derivative, benzylic radicals are generated and promoted the formation of the desired product in a 74% yield (Scheme I-18).



Scheme I-18: Decarboxylative radical addition to styrene using CdSe QDs. Adapted from reference 94 and 109.

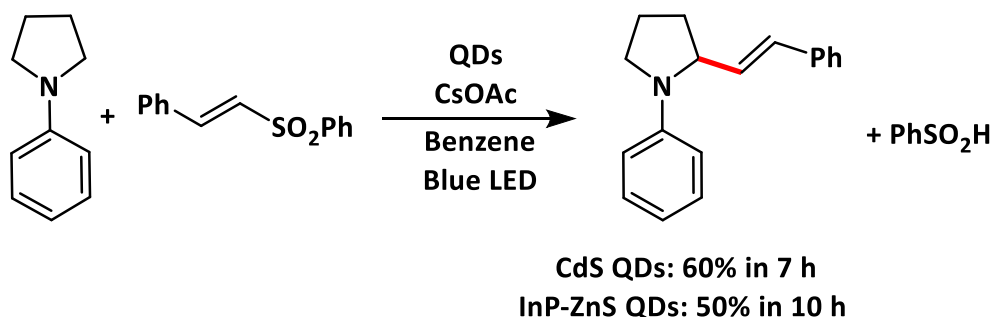
### I-3.3.2- QDs-photocatalyzed C-C vinylation coupling reaction.

For the first time in 2017, Weiss and co-workers<sup>92</sup> developed the use of CdS QDs for a C-C coupling reaction without the need of co-catalyst or sacrificial reagents. They explored the use of CdS QDs as visible light photocatalyst for the C-C vinylation coupling reaction between 1-phenyl pyrrolidine and phenyl trans-styryl sulfone (Scheme I-19). They proved that no sacrificial agent or co-catalyst were needed beside the CdS QDs. Interestingly, this photoredox C-C coupling reaction was demonstrated before by MacMillan et al. in 2014<sup>110</sup>, but using an iridium based transition metal complex ( $\text{Ir}\{\text{dF}(\text{CF}_3)\text{ppy}\}_2(\text{dtbpy})\text{PF}_6$  in this case) as photocatalyst. The QD-photocatalyzed reaction was compared to the Ir-catalyzed reaction and showed to proceed in a very similar manner with very comparable results. Furthermore, they enhanced the reaction rate by optimizing the QDs surface ligand layer. They added octylphosphonate ligands (OPA) to replace some of the native oleate ligands (As described in section I-2, page 37). The ligand exchange disordered the ligand shell and increased the reaction's rate by a factor of 2.3, and the turnover number of the QDs by a factor of 1.6, in

addition to a quantum yield of 0.2%. This example of using CdS QDs for a C-C coupling reaction was a breakthrough in the field of using QDs for bond-making photoredox reactions.

Interestingly, in 2019, Pillai and co-workers<sup>84</sup> reported the use of InP-ZnS QDs to photocatalyze the same Carbon-Carbon vinylation (Scheme I-19) which was reported before by Weiss<sup>92</sup> using CdS core QDs. In the work by Pillai et al., they used the same reaction conditions as the one used by Weiss for CdS QDs. The InP-ZnS QDs photocatalyzed reaction resulted in a slightly lower reaction yield of 50% compared to 60% using CdS QDs. Moreover, the InP-ZnS catalyzed reaction was slower than with CdS QDs as the reaction needed 10 hours to reach maximum yield compared with 7 hours in the CdS QDs case.

It is worth mentioning that, due to the interest of this reaction as an example of carbon-carbon bond formation reaction taking place without the need of any sacrificial agent or co-catalysts, and as it was proved to be reproducible using two different types of Quantum Dots, this reaction will represent a model reaction for the optimization of our own QDs' systems in the next Chapter of this Thesis.

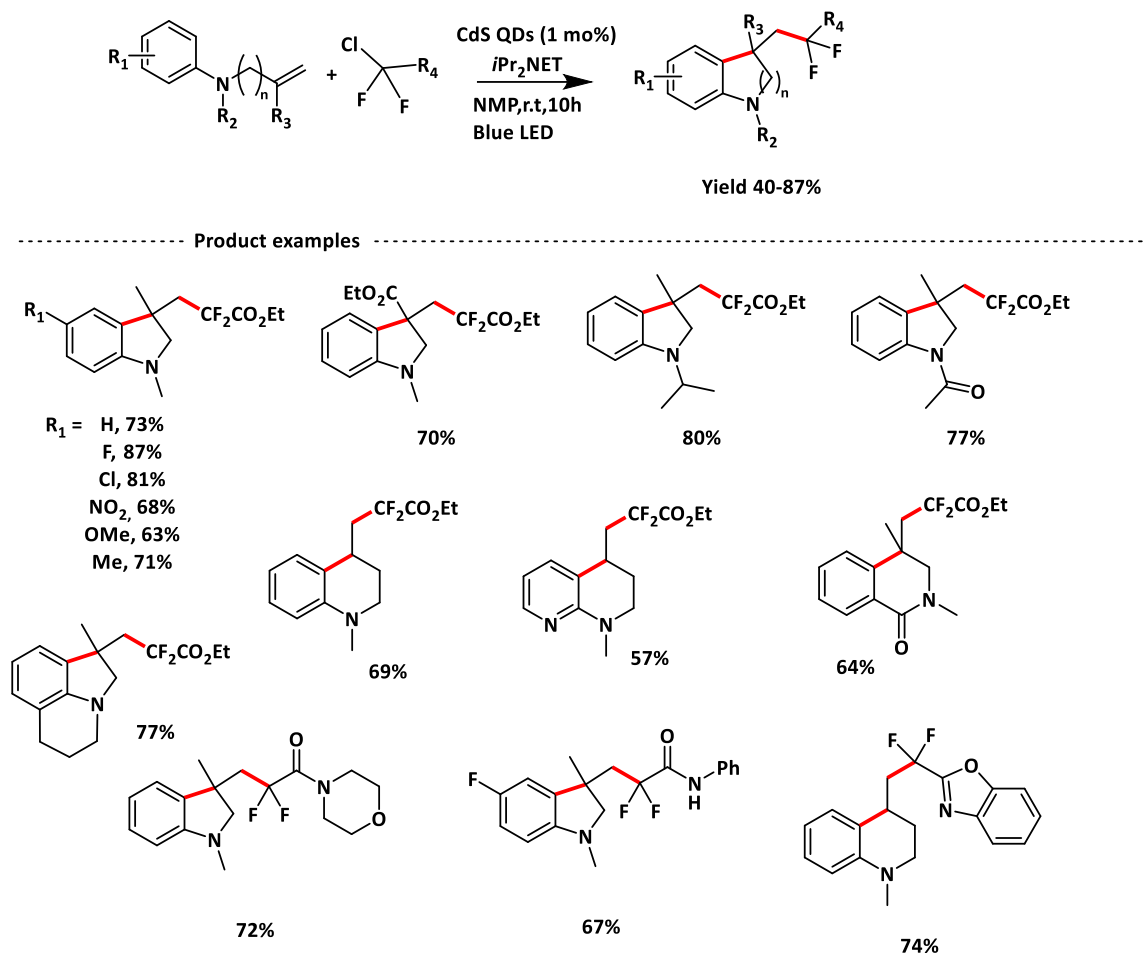


*Scheme I-19: The C-C vinylation coupling reaction between 1-phenyl pyrrolidine and phenyl trans-styryl sulfone using CdS or InP-ZnS QDs. Adapted from reference 92.*

### I-3.3.3- CdS QDs-photocatalyzed cyclization of functionalized difluoromethyl chlorides and inactivated olefins.

In 2019, Feng and co-workers<sup>111</sup> presented a report of CdS QDs-photocatalyzed cyclization of functionalized difluoromethyl chlorides and inactivated olefins to afford the desired difluoromethylated products (Scheme I-20). The reaction proceeds by breaking the carbon (sp<sup>3</sup>)-chlorine bond of difluoromethyl chlorides. The reaction was possible and successful for different difluoromethyl chlorides as fluorine sources and for a scope of a series

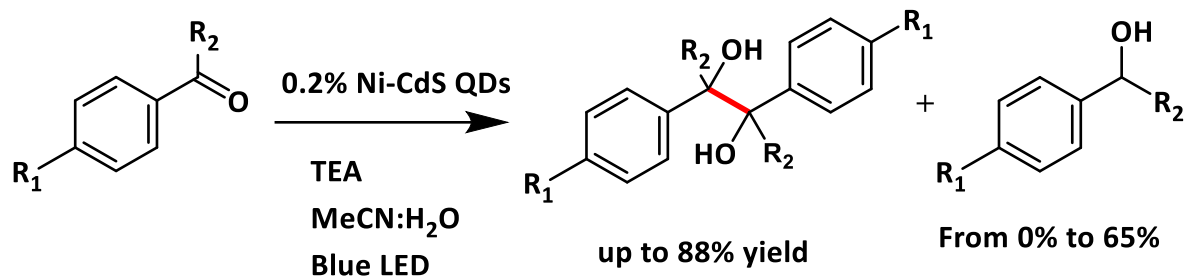
of reaction's substrates for the preparation of CF<sub>2</sub>-containing azaheterocycles compounds (Scheme I-20).



Scheme I-20: The photocatalytic cyclization of CClCF<sub>2</sub>COOEt and olefins using CdS QDs. Adapted from reference 111.

### I-3.3.4- Photocatalytic reduction of aromatic ketone for carbon-carbon coupling using CdS QDs.

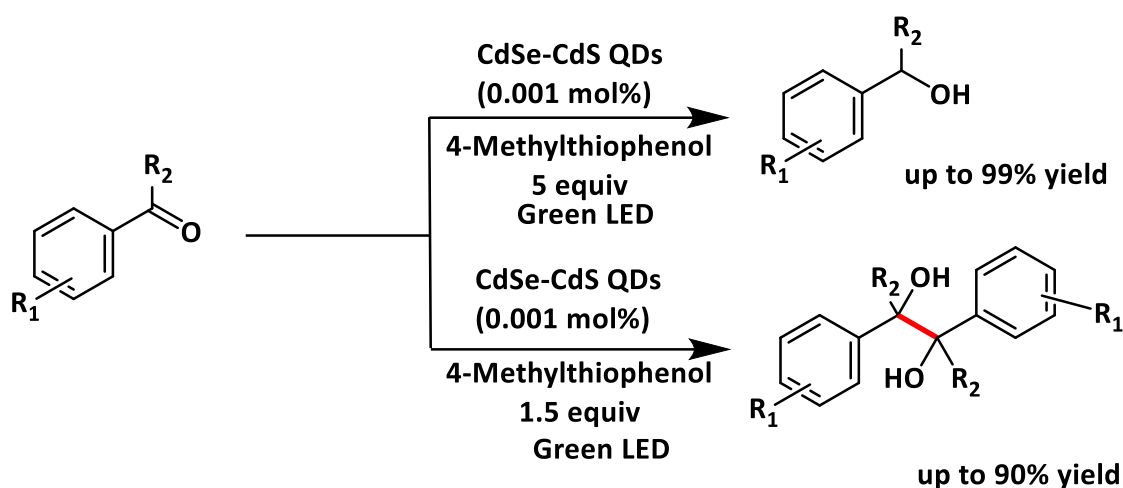
In 2021, Hu et al.<sup>112</sup> reported a photocatalytic reductive coupling for carbon-carbon formation reaction. They demonstrated the selective reduction of aromatic ketones into pinacol using Ni-doped CdS QDs as photocatalyst (Scheme I-21). They showed that selectivity was possible for a variety of substrates reaching a yield of 88%. The reduction to the corresponding alcohols was less favorable with the exception of a few examples and reaching 65% yield.



Scheme I-21: The photocatalytic reduction of aromatic ketones to the formation of pinacol via C-C bond formation using CdS QDs. Adapted from reference 112.

### I-3.3.5- Photocatalytic reduction of Aryl aldehydes for carbon-carbon coupling using CdS QDs.

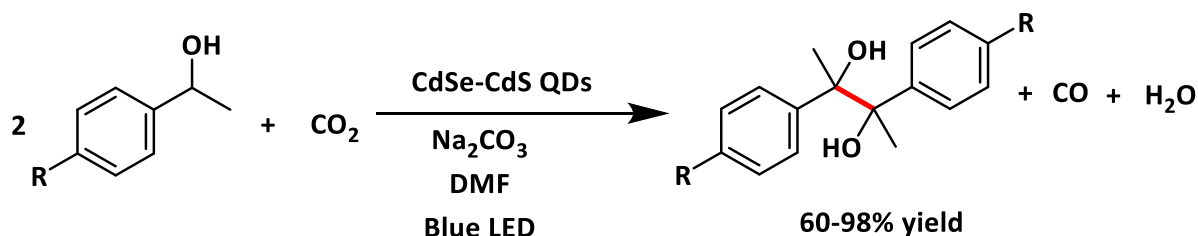
In the same year 2021, Peng and co-workers<sup>113</sup> used a Quasi type-II CdSe-CdS QDs to photocatalyze the reduction of aryl aldehydes for the selective formation either of alcohols or of pinacol products (Scheme I-22). The CdSe-CdS core shell QDs were highly active at very low catalytic loading and provided high reaction yields (> 90%) and high TONs ( $10^5$ ). Interestingly, the selectivity of the reaction was controlled by optimizing the amount of thiophenol sacrificial reagent. They also reported that the CdSe-CdS QDs could be reused ten times while maintaining the same catalytic activity and selectivity in the pinacol coupling reactions. The interest of this reports is represented by the very high turnover number achieved by the CdSe-CdS core-shell QDs for a carbon-carbon coupling reaction. The high efficiency of this reaction could be attributed to the used Quasi-Type-II core-shell QDs, which were proved to exhibit an enhanced photo-induced charge separation and high photoluminescence Quantum yield<sup>71</sup>. The use of this Type of QDs will be investigated in our photoredox systems with different kind of reactivity described in the next chapter.



Scheme I-22: The photoreduction of aryl aldehydes toward formation either of alcohols or of pinacol products using CdSe-CdS QDs. Adapted from reference 113.

### I-3.3.6- Photocatalytic pinacol formation integrated with CO<sub>2</sub> reduction.

Guo et al.<sup>114</sup> reported the efficient use of CdSe-CdS core-shell QDs for the combination of the photoreduction of CO<sub>2</sub> to CO in the presence of the organic transformation reaction of the oxidation of alcohols (Scheme I-23). The used both the electron and hole photogenerated charges in the CdSe-CdS QDs by making the electrons interact with the CO<sub>2</sub> to reduce it to CO, while simultaneously, the generated holes were used for the coupling reaction of the oxidized alcohols.

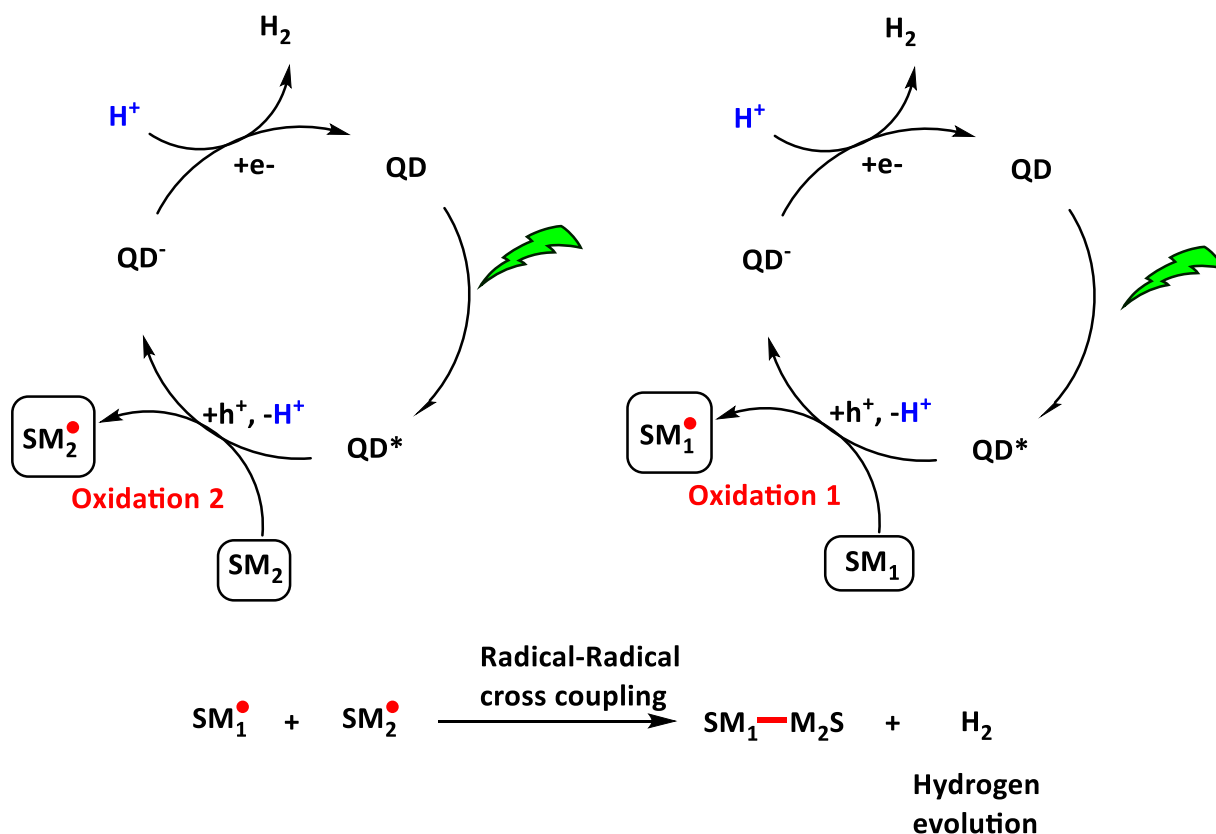


Scheme I-23: CdSe-CdS QDs as photocatalysts for CO<sub>2</sub> reduction and alcohols oxidation. Adapted from reference 114.

### I-3.3.6- Photocatalytic radical-radical cross coupling reactions.

Among the bond formation reactions' mechanisms initiated by CdSe QDs, radical-radical cross-coupling after two oxidations of the starting materials is one of the most reported mechanisms (Scheme I-24). In this context, Li-Zhu Wu and co-workers recently reported a few photoredox reactions initiated by CdSe QDs to prepare value-added products. The reactions proceed after oxidizing the starting materials by the QDs, and generating the corresponding radical of each substrate. In parallel, electron transfer from the excited QDs takes place to

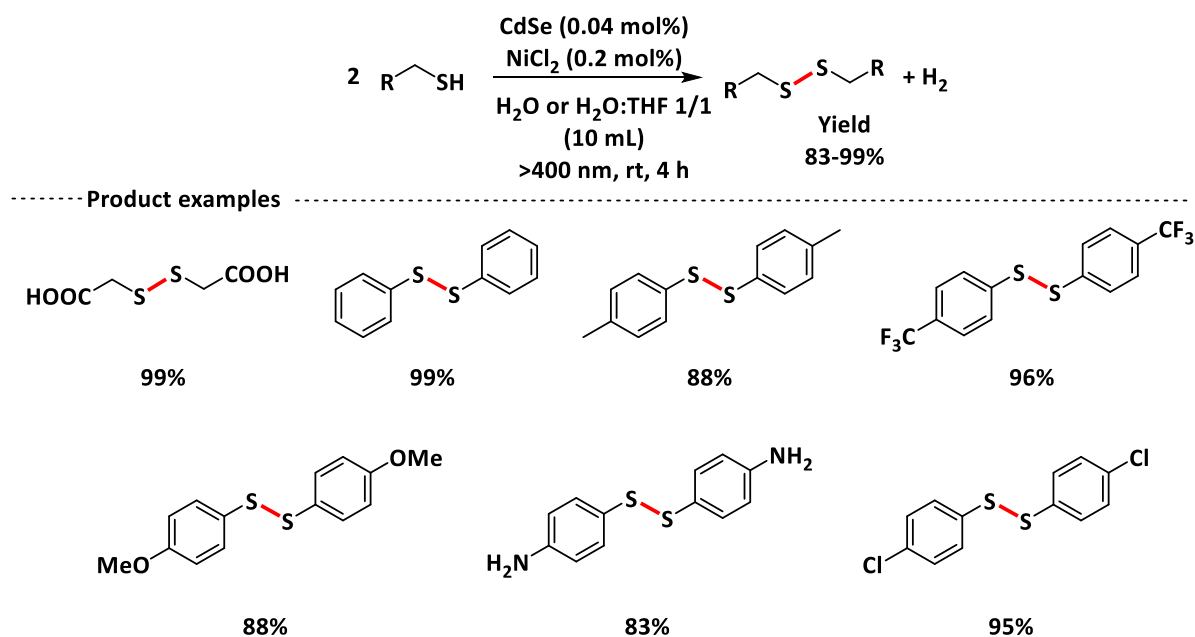
reduce a proton and ends with hydrogen evolution (Scheme I-24). It is worth mentioning that most of the CdSe QDs used by Li-Zhu Wu in the below-mentioned examples were treated with nitric acid to wash the QDs from residual ligands not bound to the surface of the QDs. The nitric acid treatment could play a role in modifying the surface of the QDs and could participate in some oxidation processes due to its high oxidizing power.



*Scheme I-24: General catalytic mechanism for the radical-radical coupling reactions after oxidation of the starting material (SM) by the QDs in the presence of hydrogen production*

In 2014 the first report by Li et al<sup>115</sup> showed an efficient approach for the coupling of thiols using CdSe QDs as photocatalysts (Scheme I-25). The reaction resulted in high-yielded (>80%) coupling of a variety of thiols to give disulfides in addition to in situ H<sub>2</sub> production. The reaction proceeded without the need for sacrificial reagents or external oxidants. However, the addition of small amounts of nickel(II) salts improved the efficiency of the reaction, especially by facilitating the formation of hydrogen due to a faster regeneration of the ground-state of the QDs. Their mechanistic analysis showed that the coupling reaction occurs on the

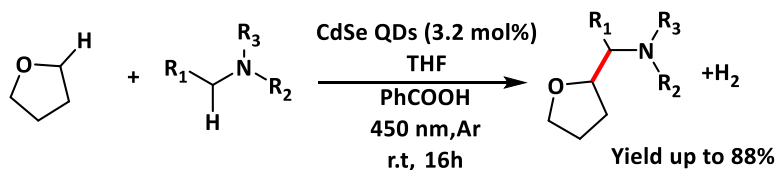
QD surfaces showing a new route as to how these QDs may be used for similar photocatalytic applications.



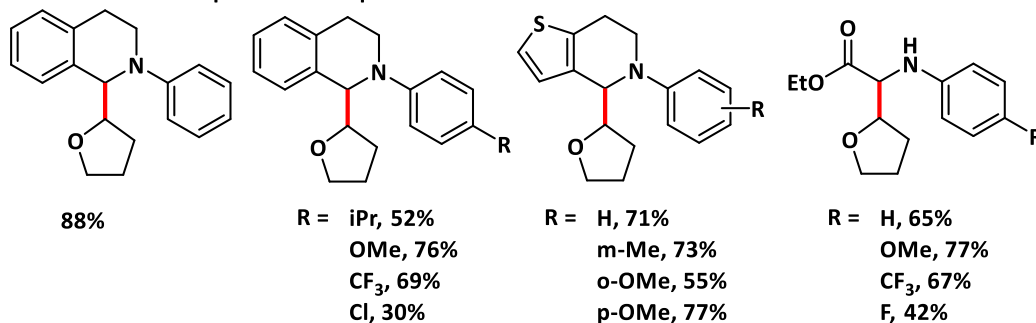
Scheme I-25: The photocatalytic formation of disulfides via radical-radical cross coupling using CdSe QDs. Adapted from reference 115.

In 2021, three different reports from the group of Li-Zhu Wu were published for three model photoredox reactions using CdSe QDs. First, they used CdSe QDs to activate the  $\alpha$ -C-H bond of tetrahydrofuran (THF) followed by radical cross-coupling or radical addition reactions<sup>116</sup> (Scheme I-26). In this work, the first step of the reactions is the formation of QDs/THF conjugates. The QDs/THF conjugates formed after the oxygen atom of THF binds to the QD's surface. Then, under visible light irradiation, the formed alkoxyalkyl radical directly undergoes a radical cross coupling with  $\alpha$ -amino radical from amino C-H bonds or radical addition with alkene or phenylacetylene.

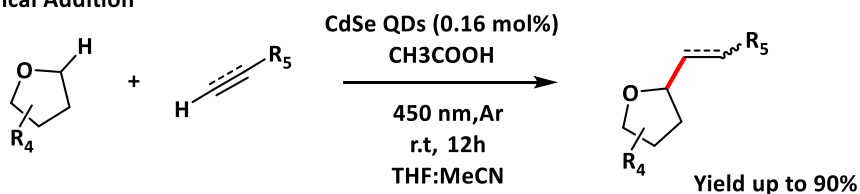
## A) Radical cross-coupling



## ----- Selected product examples -----

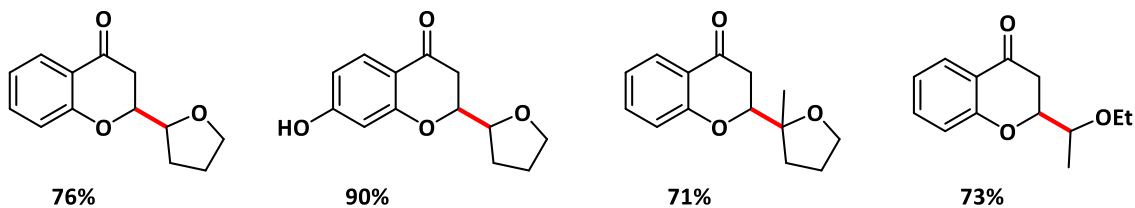


## B) Radical Addition

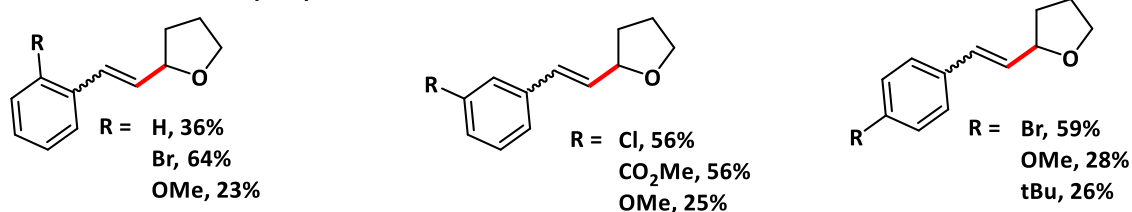


## ----- Selected product examples -----

## Addition to chromones

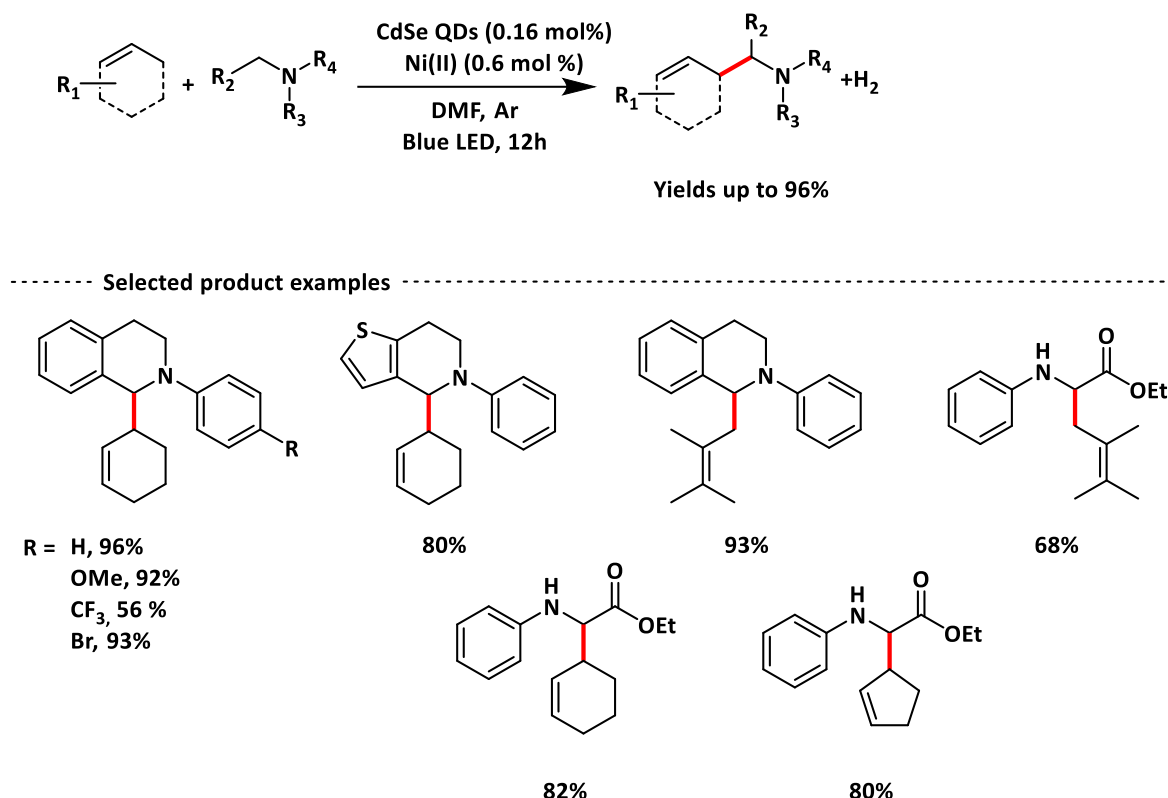


## Addition to terminal arylalkynes



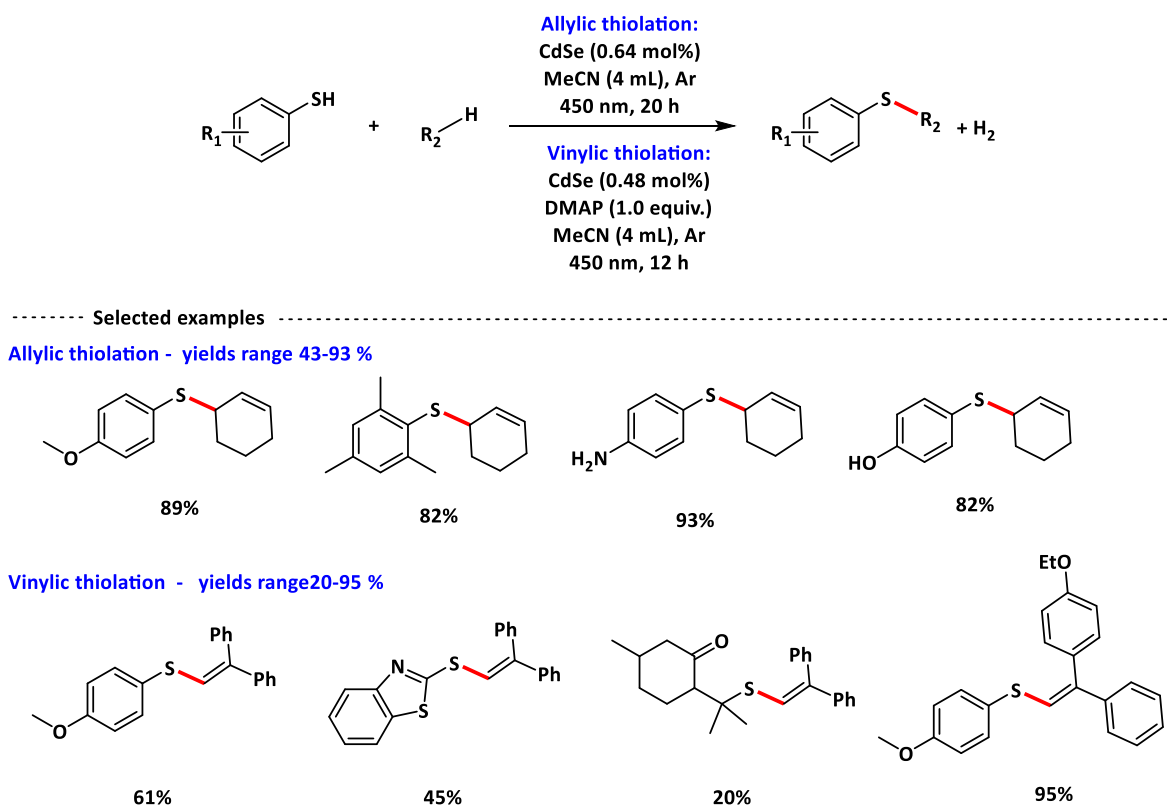
Scheme I-26: Activation of the  $\alpha$ -C-H bond in THF using CdSe QDs followed by radical cross coupling or radical addition. Adapted from reference 116.

Again in 2021, Huang et al.<sup>117</sup> reported the direct alkylation and arylation of allylic C(sp<sup>3</sup>)-H bonds using CdSe QDs coupled with hydrogen production. More precisely, they demonstrated the coupling of a broad range of allylic C(sp<sup>3</sup>)-H bonds with  $\alpha$ -amino C-H bonds or heteroarenes using CdSe QDs under visible-Light irradiation (Scheme I-27). They developed a general and mild strategy for the targeted couplings good number of examples of the final products with reactions' yield reached 96% in some cases (Scheme I-27).



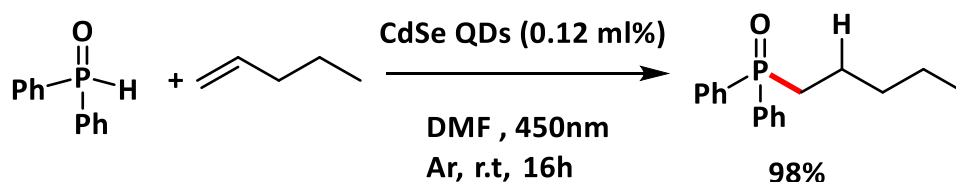
Scheme I-27: Alkylation and arylation of allylic C(sp<sup>3</sup>)-H bonds using CdSe. Adapted from reference 117.

Right after, Li-Zhu Wu and co-workers<sup>118</sup> reported the direct Allylic C(sp<sup>3</sup>)-H and Vinylic C(sp<sup>2</sup>)-H thiolation using CdSe QDs coupled with hydrogen production. In this work, they presented an efficient and economic thiolation of allylic C(sp<sup>3</sup>)-H and thiol S-H bonds under visible light irradiation using CdSe QDs (Scheme I-28). The C-S bond formation did not require external oxidants, and hydrogen (H<sub>2</sub>) production during the reaction was facilitated by adding some Ni (II) salts. When vinylic C(sp<sup>2</sup>)-H was used instead of allylic C(sp<sup>3</sup>)-H bond, it was similarly possible to obtain the radical-radical cross-coupling of C(sp<sup>2</sup>)-H and S-H also coupled with hydrogen formation.



Scheme I-28: Direct allylic C-H bond activation for C-S bond formation using CdSe QDs. Adapted from reference 118.

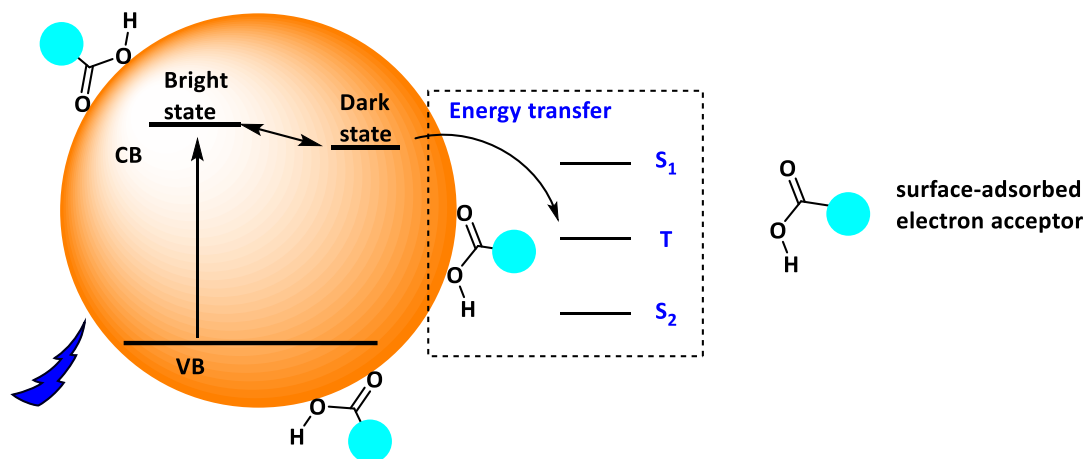
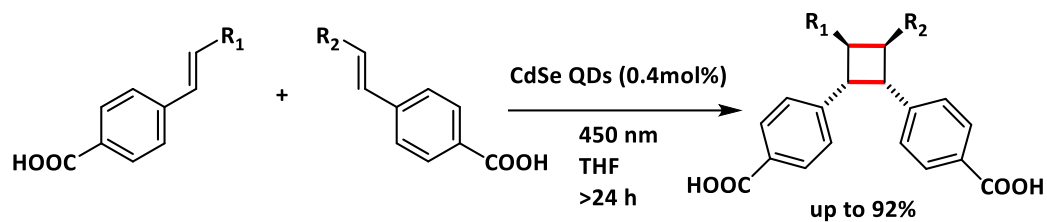
More recently in 2022, Li-Zhu Wu and co-workers<sup>119</sup> reported an efficient method for the formation of C-P bonds using CdSe QDs under visible light. They presented their findings concerning the ability of CdSe QDs to act as a photoredox catalyst to convert diphenylphosphine oxide into the phosphoryl radical under visible light irradiation. Then, they showed that the generated radical species could undergo radical addition with alkene or radical coupling with  $\alpha$ -amino C-H bonds to form a C-P bond (Scheme I-29). The importance of this methodology is that it provides a new photocatalytic C-P bond formation reaction involving phosphoryl radicals using QDs without the need of any sacrificial reagent.



Scheme I-29: Photocatalytic C-P bond formation using CdSe QDs. Adapted from reference 119.

### I-3.4. CdSe QDs as photocatalyst for triplet excited state reactions

Weiss and co-workers<sup>120-122</sup> reported the activity of the triplet-excited state in CdSe QDs and achieved regioselective and diastereoselective intermolecular [2+2] cycloadditions of 4-vinylbenzoic acid (Scheme I-30). They showed in this work that CdSe QDs were acting as triplet exciton donors to surface adsorbed substrates. The triplet energy of the QDs was tunable by controlling the size of the QDs to selectively produce one component among the reaction system of the cycloadditions. The change in the QDs size showed the QDs could selectively transfer energy to one of the substrates, while with different QDs size the selectivity was favored toward other substrates. Moreover, CdSe QDs photocatalyzed reactions provided non-normal syn-products with a diastereomeric ratio of >40:1. However the metal complexes catalyzed reactions generated anti-products with diastereomeric ratio of <12:1. They showed that the selectivity resulted from the carboxylate of the substrate being adsorbed to the QD surface, creating an intermolecular  $\pi$ - $\pi$  interaction among the 4-vinylbenzoic acid derivatives. In addition, head-to-head (HH) products or head-to-tail (HT) products were selectively formed by optimizing the position of carboxylate in the substrates. However, despite the originality of these findings using CdSe QDs, they are limited to reaction substrates with carboxylic moieties that could adsorb to the surface of the QDs.

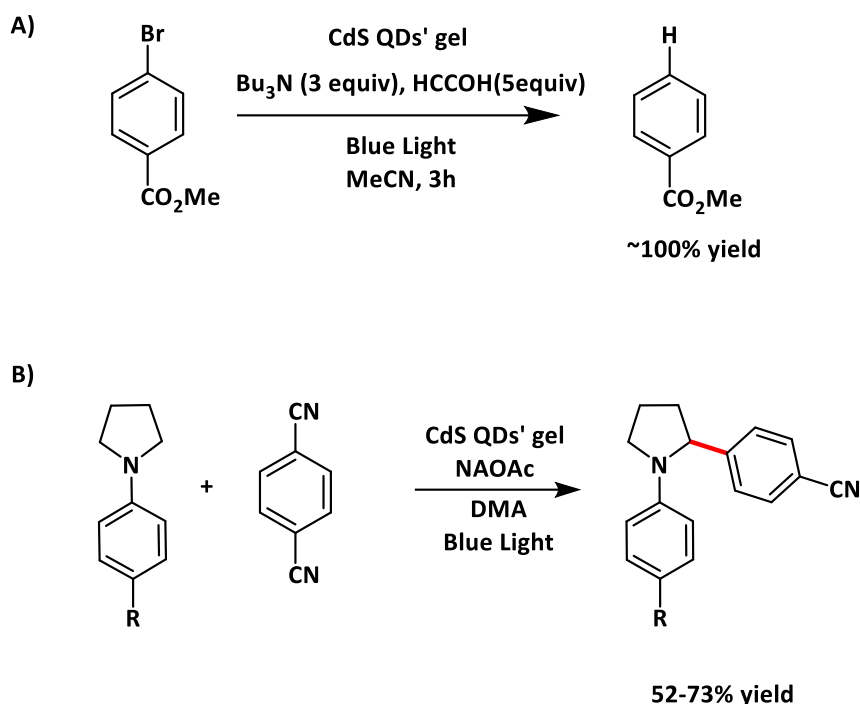


Scheme I-30: Intermolecular [2+2] cycloadditions of 4-vinylbenzoic acid bonded to QDs surface using CdSe QDs. Adapted from reference 120.

### I-3.6. Quantum Dot Gels as efficient photocatalysts for organic reactions

Very recently in September 2022, Liu et al.<sup>123</sup> reported a new methodology for enhancing the activity of CdS QDs in the photocatalytic reaction. In this work, they synthesized TOPO-capped CdS QDs and then transformed them into CdS QDs gels in two steps passing by typical ligand exchange using thiolate-capped QDs. After preparing the thiolate-capped QDs, the thiolate ligands were oxidatively removed as disulfides, and then the CdS QDs were further oxidized to form interparticle dichalcogenide bonds between the QDs during electrogelation, forming a QD network. The goal of preparing such a gel structure of QDs is to improve the interaction between the QDs' surface and the reactions' substrates by enhancing the ligand layer permeability by removing most of the native surface ligands. They tested the photocatalytic performance of CdS QDs gel using the reductive dehalogenation of methyl 4-bromobenzoate as a model reaction (Scheme I-31-A) and compared the results to TOPO and thiolate-capped CdS QDs. The activity of the QDs gel was much efficient than the TOPO and thiolate-capped CdS QDs by obtaining almost 100 % yield in 3 hours compared to a maximum of 64% in 5 hours using the thiolate-capped CdS QDs. Moreover, they also tested the activity

of the QD gels on other reactions. For example, they employed the QDs gels in a cross-coupling reaction of an  $\alpha$ -amino arylation reaction in the presence of dicyanobenzene (Scheme I-31-B). In these reactions, the QDs gel were able to oxidize the N-aryl amines and reduce the dicyanobenzene generating the corresponding radicals, then a cross-coupling of the two radicals occurs to form the desired products in a yield range between 52 and 73%.



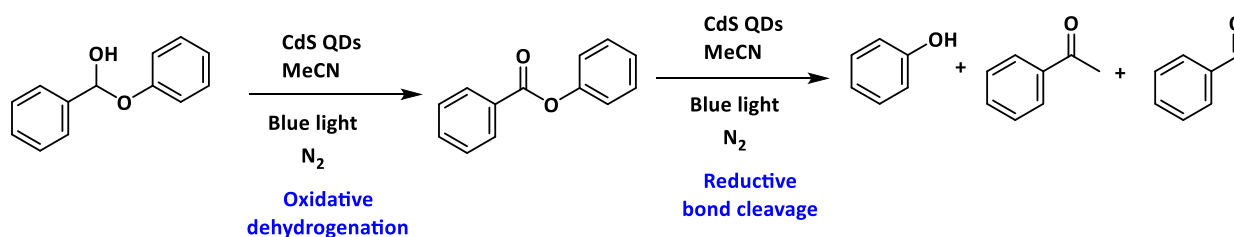
Scheme I-31: Quantum Dot Gels as efficient photocatalysts for organic reactions: A) QDs gel as photocatalyst for a dehalogenation reaction and B) QDs gel as photocatalyst for a cross-coupling reaction of an  $\alpha$ -amino arylation reaction in the presence of dicyanobenzene. Adapted from reference 123.

### I-3.6. Other photocatalytic reactivities Using Quantum Dots

#### I-3.6.1- Bond cleavage in Lignin based molecules using QDs: Photooxidation followed by photoreduction.

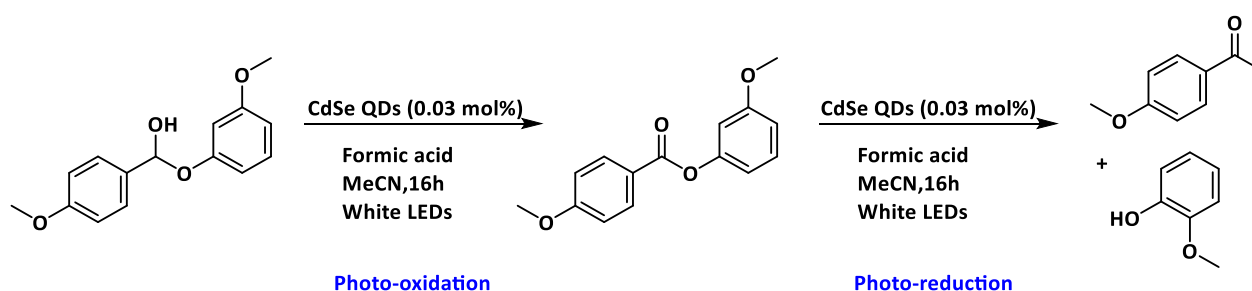
In 2018, Ye Wang et al.<sup>124</sup> proved that CdS QDs are efficient photocatalysts for breaking the  $\beta$ -O-4 bonds in various lignin models (e.g., 2-phenoxy-1-phenyl ethanol (PP-ol)). They also showed the possibility to transform native lignin into functionalized aromatics within biomass and without affecting other components in lignocellulose. The reaction was performed under mild condition using visible light activation for the CdS QDs (Scheme I-32).

The mechanistic processes started by an Oxidative dehydrogenation of alcohol based lignin substrates. Then, a reductive cleavage occurs to break the  $\beta$ -O-4 bonds.



Scheme I-32: The photolytic cleavage of the  $\beta$ -O-4 bond in lignin compounds using CdS QDs. Adapted from reference 124.

Then in 2019, Cossairt and co-workers.<sup>125</sup> reported the use of CdSe QDs for the cleavage of the  $\alpha$  C-O bonds in lignin model substrates after their oxidation to the corresponding ketone then followed by reductive bond cleavage (Scheme I-33) under mild and ambient temperature reaction conditions. The obtained yields were comparable to the best transition-metal-based molecular photocatalysts (up to 100%), but CdSe QDs were used in lower catalytic loading (0.03 mol %) and consequently achieved higher turnover number (>3000) and frequencies. Another demonstration of this work is that the use of short-chain trans-4-cyanocinnamic acid ligand on the QDs' surface could significantly improve the conversion rate due to optimized QDs surface.

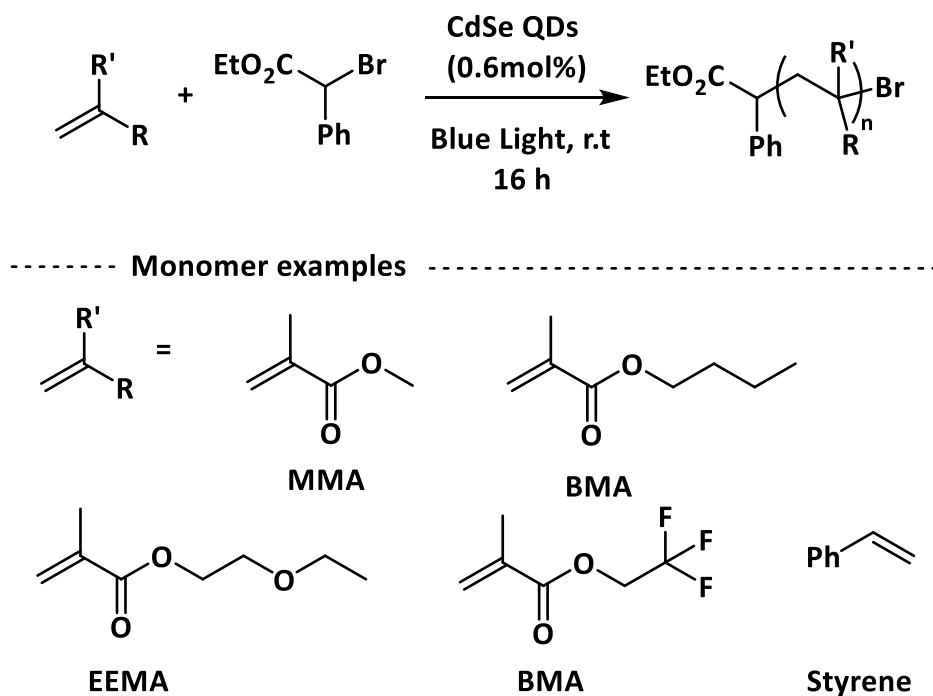


Scheme I-33: the photolytic cleavage of the  $\alpha$  C-O bonds in lignin substrates using CdSe QDs. Adapted from reference 125.

### I-3.6.2- Photopolymerization initiated by photoexcited QDs.

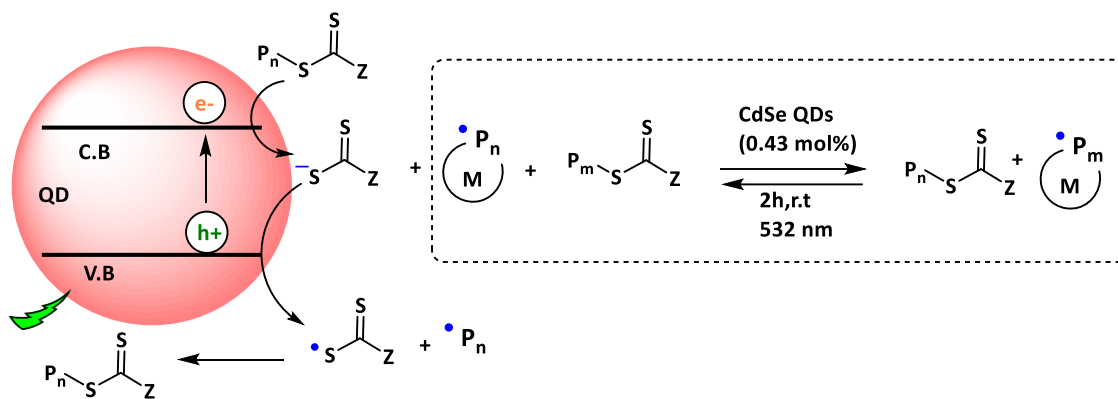
Egap and co-workers<sup>126</sup> investigated the use of CdSe QDs for a visible light mediated radical polymerization of (meth)acrylates and styrene to produce block copolymers (Scheme I-34). CdSe QDs were employed as photocatalyst for the atom transfer radical polymerization

(ATRP) to achieve various types of polymerization reactions. CdSe QDs photocatalyzed polymerization resulted in high conversion and narrow polydispersity. This report illustrated that QDs are a promising catalyst in the field of photopolymerization.



Scheme I-34: Photopolymerization of (meth)acrylates and styrene using CdSe QDs. Adapted from reference 126.

After the report by Egap concerning the CdSe QDs-mediated photopolymerization reactions, late in 2019 Weiss and co-workers<sup>127</sup> described the use of CdSe QDs for a photoinduced electron transfer reversible addition–fragmentation chain transfer (PET-RAFT) polymerization reaction of a series of acrylamides and acrylates (Scheme I-35). The photocatalytic activity of the CdSe QDs allowed the polymerization to occur with high efficiency and low dispersity using a very low catalyst loading.



Scheme I-35: PET-RAFT polymerization reaction of acrylamides and acrylates using CdSe QDs. Adapted from reference 127.

As revealed from the examples mentioned above for the QDs-photocatalyzed reaction, the use of QDs as redox photocatalysts emerged as an efficient visible light harvesting photocatalysts with comparable activities to the other traditional photocatalysts. The use of Quantum Dots for organic chemistry reaction was demonstrated for already developed reactions replacing Iridium or Ruthenium transition metal complexes. In addition, new reactivity based on Quantum Dots-catalyzed reactions were also developed. However, up to date, the use of QDs in photocatalysis is limited to a few types of QDs without a wide investigation of the activity of the different possible types of existing QDs structures, and only one type of QDs is tested per study as mentioned in the previous examples. Furthermore, in most of the reported cases of the QD-catalyzed reaction, the obtained Quantum Yield is mainly less than 1%.

## I-4. Enhancing the photogenerated charge separation: Quantum Dots connected to metal nanoparticles.

### I-4.1. Suppressing the photogenerated charge recombination in QDs.

A fundamental challenge in Quantum Dots' photochemistry is to limit the possible recombination processes of the photo-generated electron-hole pairs. After photoexcitation of Quantum Dots the charge carriers can fastly recombine<sup>128</sup>, and then no redox reactions could occur using the QDs' photo-induced charges. Moreover, long reaction times and low quantum yield of the photocatalytic reactions, typically less than 1%,<sup>92,94</sup> is usually obtained for QDs-photocatalyzed organic transformations due to the charges recombination processes.<sup>129</sup>

An effective way to improve the photocatalytic activity of Quantum dots and maximize the charge separation is by depositing or growing noble metal nanoparticles (NPs) to the semiconductor ones<sup>130</sup>. In this case, it is hypothesized that formation of hybrid heterostructures of the semiconductor and metal nanoparticles, such as Gold (Au), silver (Ag) or platinum (Pt), would create a flow of electrons from the excited semiconductor part to the metal nanoparticles<sup>131</sup>. The electrons would then be transferred and stored at the surface of the nanoparticles, minimizing electron-hole recombination<sup>132</sup>. (Figure I-12)

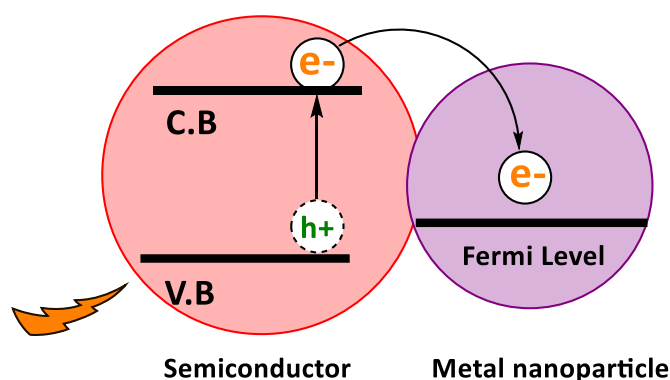


*Figure I-12: Electron transfer from the excited semiconductor QDs to metal nanoparticle affording a better charge separation.*

Several research groups investigated the use of semiconductor-metal nanostructures to employ them in several applications due to the expected efficient charge separation in such well-engineered heterostructures<sup>132</sup>. Recently, a few methods were investigated to prepare semiconductor-metal hybrid materials<sup>130</sup>. The most explored method is the deposition of metal particles<sup>133</sup> or growing metallic shells<sup>134</sup> on the surface of the semiconductor particles. In addition, self-assembled nanostructures driven by particles functionalized with complementary proteins<sup>135</sup> or DNA bases<sup>136</sup> appeared recently also an efficient method to prepare semiconductor-metal structures, however, these latter are not yet investigated for charge separation and photocatalysis.

Understanding the charge carriers' transfer and their separation in the semiconductor-metal nanostructures is essential before using them for the targeted applications. In these semiconductor-metal nanostructures, two main mechanisms for the charge transfer are expected depending on which domain absorbs the light. If the semiconductor absorbs the photon, electron-hole pairs are generated, and the electrons are transferred to the metallic part (Mechanism A- Figure I-13). However, if the metal particles

absorb the light, an opposite pathway is expected. In this case, an electron is generated in the metallic particles and could be transferred to the conduction band of the semiconductor<sup>137,138</sup> (Mechanism B- Figure I-13).

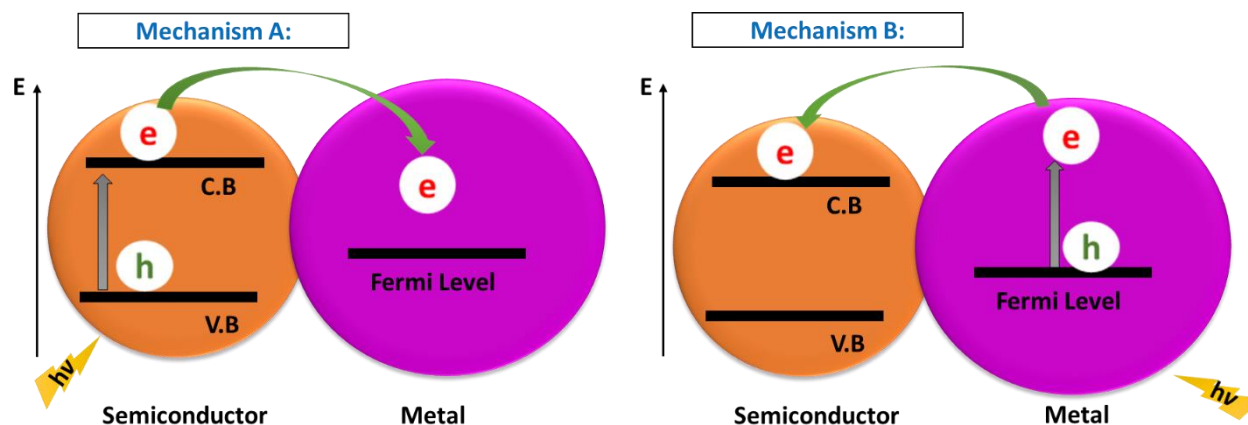


**Figure I-13: Schematic illustration of two possible mechanisms of charge carriers transfer in nanoparticles containing a semiconductor-metal nanostructures : mechanism-A) Absorption of light by the semiconductor part and transfer of an electron from its conduction band to the metal part, mechanism -B) Absorption of light by the metal part in its plasmon band and transfer of an electron to the semiconductor.**

#### I-4.2. Fast charge transfer from photoexcited semiconductors to metal nanoparticles.

Researchers have paid a lot of effort to prove that charge transfer process indeed occurs in semiconductor-metal nanostructures. The primary method to follow the charge transfer in these structures is to follow their optical properties upon being excited. In the examples below, we focus on the examples corresponding to light absorption by the semiconductor and the possible charge transfer to the metallic part.

In this context, O'Connor et al.<sup>139</sup> prepared a ZnSe-CdS dot-in-rod semiconductor coupled with Pt metal as heterostructure. They used ultrafast transient absorption spectroscopy to investigate the nature of the photoinduced charge transfer processes taking place in the semiconductor-metal nanostructures. The measurements demonstrated that the electron-hole separation is fast and resulted in the localization of the holes in the semiconductor domain while the electrons transferred to the metallic part. In particular, they

showed that the photoinduced holes became localized within the ZnSe domain in less than 2 ps, while electron transfer took approximately 15 ps to transition into the Pt part (Figure I-14).

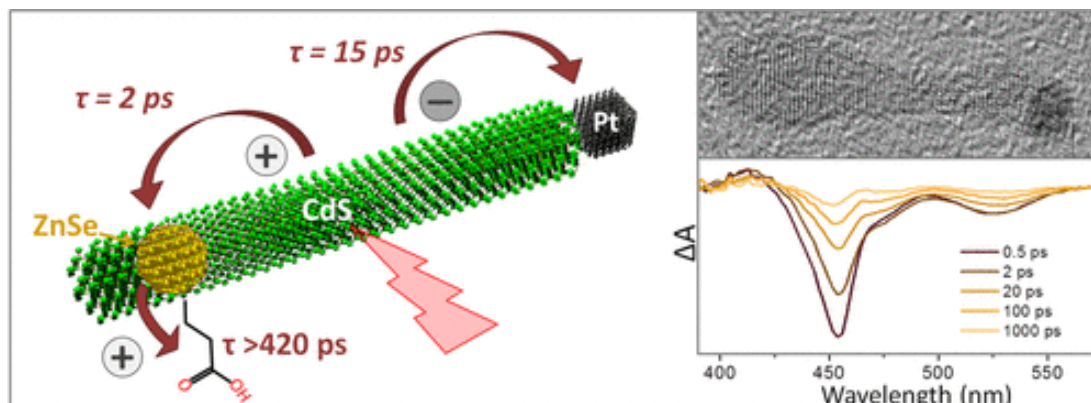


Figure I-14: Photoinduced electron-hole separation within a ZnSe-CdS semiconductor coupled with Pt metal nanostructure. Figure adapted from reference 139.

Chakraborty et al.<sup>140</sup> designed a semiconductor-metal nanostructure of colloidal CdSe nanowires (NW) decorated with gold. They investigated the influence of the gold deposited on CdSe on the photoconductive properties of this heterostructure. They showed that the new CdSe-Au nanostructure has at least a ten-fold higher photocurrent than the bare CdSe (Figure I-15)

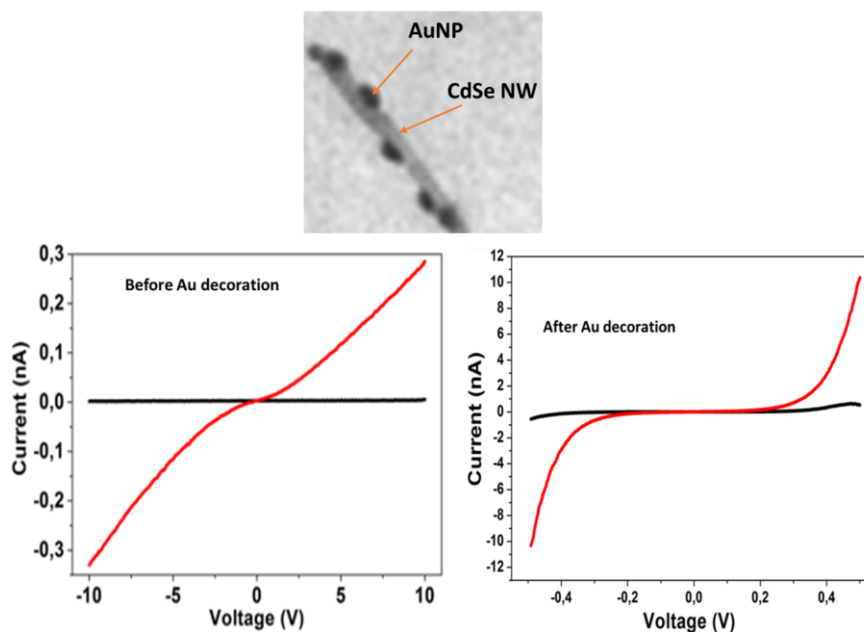
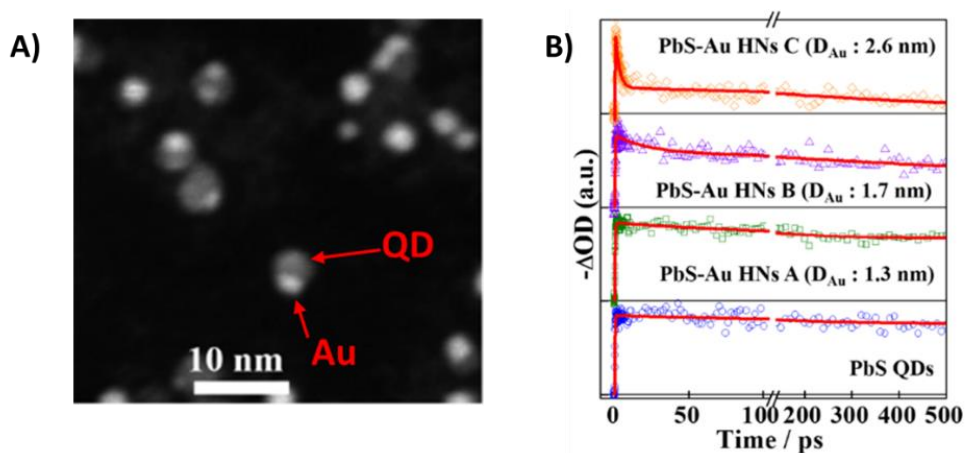


Figure I-15: CdSe nanowires (CdSe NW) decorated with Gold NPs (AuNP): Top: TEM images for the obtained CdSe-Au heterostructure. Bottom: Measurement of the photocurrent of CdSe-Au nanostructure compared to bare CdSe (before Au decoration (left) and after decoration (right)). Figure adapted from reference 140.

Moreover, in 2015 Okuhata et al.<sup>141</sup> prepared a hybrid nanostructure (HN) of PbS QDs and gold nanoparticles deposited at the QDs' surface (Figure I-16-A). They examined the charge carriers' dynamics by femtosecond near-IR pump-probe spectroscopy. A decrease in band-edge bleach yields was clearly observed in PbS-Au hybrid nanostructure (HN) as compared to bare PbS QDs under excitation. The edge bleach was more important in the case of bigger AuNP. They compared bare PbS QDs with PbS-Au HNs with different diameters of AuNP on the surface of the PbS QDs (Figure I-16-B). This observation suggests the existence of ultrafast electron transfer from PbS QDs to gold nanoparticles and more efficiently in the case of bigger AuNP.



**Figure I-16: PbS QDs and AuNP hybrid nanostructures.** A) TEM images showing the growth of the AuNP at the surface of the PbS QD. B) Monitoring the 1S bleach dynamics in bare QDs compared with PbS-Au nanostructures. Adapted from reference 141.

Few years after, Okuhata et al.<sup>142</sup> prepared hybrid nanostructures of CdSe QDs with Au nanoparticles grown on the QDs' surface (See Figure I-17-A) and tested the electron transfer from the CdSe QDs to the AuNPs using femtosecond pump-probe spectroscopy. They found the existence of ultrafast electron transfer with a very short lifetime ( $\ll 60$  fs) from CdSe QDs to Au NPs. They also tested the steady state photoluminescence quenching of bare CdSe QDs and nanostructures of CdSe QDs attached to different sizes of gold particles. The nanostructures exhibited a very efficient photoluminescence quenching compared with bare CdSe QDs (Figure I-17-B). The observed photoluminescence quenching indicated that charge recombination was suppressed.

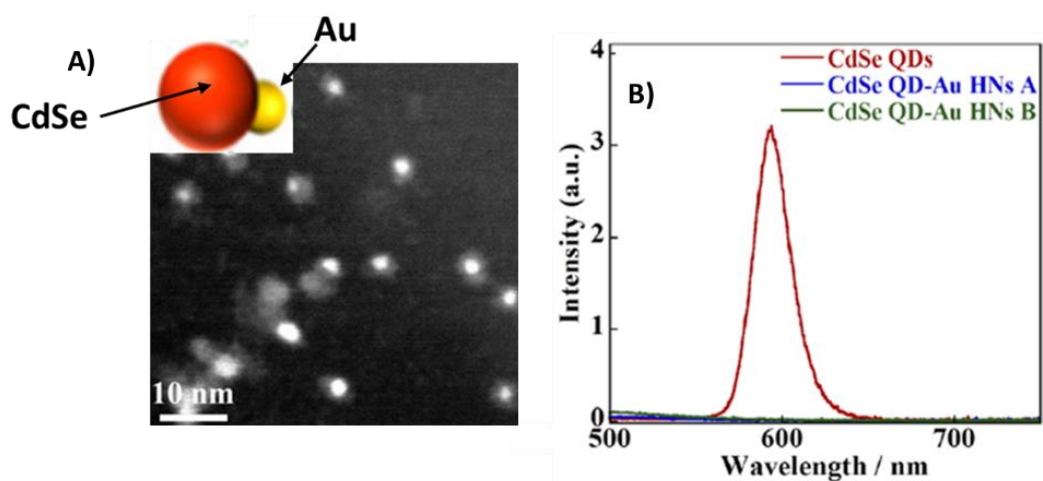


**Figure I-17: CdSe QDs and AuNP hybrid nanostructures.** A) TEM images showing the growth of the AuNP at the surface of the CdSe QD. B) Monitoring the photoluminescence quenching in the CdSe-Au nanostructures. Adapted from reference 142.

Similarly, Dana et al.<sup>143</sup> prepared CdSe-Au nanostructures and studied the charge transfer from photoexcited CdSe QDs to Au NPs (Figure I-18-A). They used time-resolved emission and femtosecond transient absorption spectroscopy to measure ultrafast charge-transfer dynamics from CdSe QDs to gold. The electron-transfer time from photoexcited CdSe was found to be  $\sim 270$  fs. The charge separation was confirmed by both steady-state and time-resolved photoluminescence. The steady-state photoluminescence analysis showed a complete quenching of the photoluminescence in the QDs-Au structure compared to the bare CdSe QDs (Figure I-18-B). The results were also confirmed using time-resolved photoluminescence (Figure I-18-B inset). All the spectroscopic analysis suggested an efficient charge transfer from the photoexcited CdSe QDs to the attached gold nanoparticles.

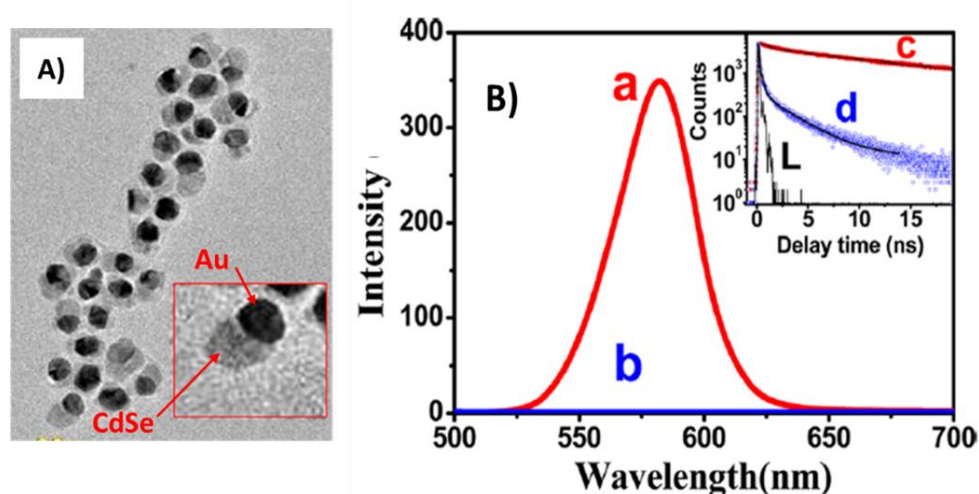
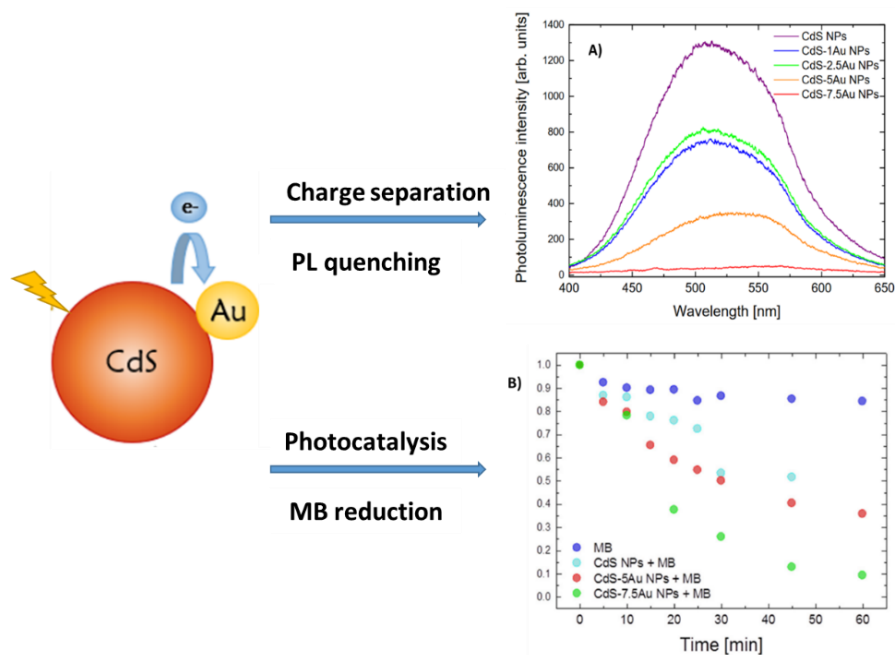


**Figure I-18: CdSe QDs and AuNP hybrid nanostructures:** A) TEM images showing the growth of the AuNP at the surface of the CdSe QD. B) Monitoring the photoluminescence quenching in the CdSe-Au nanostructures. Adapted from reference 143.

### I-4.3. Quantum Dots and metal nanoparticles hybrid structure for enhanced photocatalytic activities.

The published findings concerning the very efficient charge separation in the semiconductor-metal nanostructure and the possible suppressing of charge carriers' recombination after excitation of the semiconductors encouraged researchers in the field to test such materials as photocatalysts to photocatalyze some photocatalytic processes<sup>144</sup>.

Recently, Nawrot et al.<sup>145</sup> prepared a CdS-Au nanostructure to test the charge separation within this heterostructure as well as their photocatalytic activity. They showed that the prepared CdS-Au nanostructure exhibits a photoluminescence quenching indicating an efficient charge separation (See Figure I-19). They prepared CdS-Au structures with different gold amounts and showed that the increase of concentration of Au attached at the surface of CdS resulted in better photoluminescence quenching, suggesting more efficient charge separation (Figure I-19- A). For the photocatalytic activity of the CdS-Au nanostructures, they tested the reduction of methylene blue (MB). They performed absorption measurements under irradiation in the presence of CdS-Au nanostructures. After one hour of irradiation, it was observed that the absorbance of MB decreased drastically in the presence of CdS-Au nanostructures as photocatalysts (Figure I-19- B). These observations indicate that the reduction of MB was caused by electrons effectively transferred to the



metallic part.

**Figure I-19: Charge separation and photocatalytic activity of CdS-Au nanostructures.** A): photoluminescence quenching of CdS QDs when Au particles were attached on their surfaces. B) Decomposition of Methylene Blue (MB) under the action of bare CdS or CdS-Au nanostructures under light irradiation. Figure adapted from reference 145.

Moreover, Dana et al.<sup>146</sup> synthesized heterostructures of semiconductor CdSe-CdS core Shell QDs with Au nanoparticles of different sizes grown on the QDs' surface. The charge separation in these heterostructures was tested using spectroscopic analysis, such as steady state photoluminescence spectroscopy. The recorded photoluminescence intensities of the bare QDs or of the heterostructures of QDs decorated with gold nanoparticles showed quenched photoluminescence in the case of QDs-Au heterostructures (Figure I-20-A), indicating an efficient charge separation. For photocatalytic studies, they tested the reduction of Rhodamine B (RhB) dye in the presence of bare Au nanoparticles, bare CdSe-CdS QDs, and in the presence of the two types QDs-Au heterostructures (different sizes of AuNP). The results showed higher efficiency of the heterostructures of QDs-Au particles compared with bare QDs or gold (Figure I-20-B).

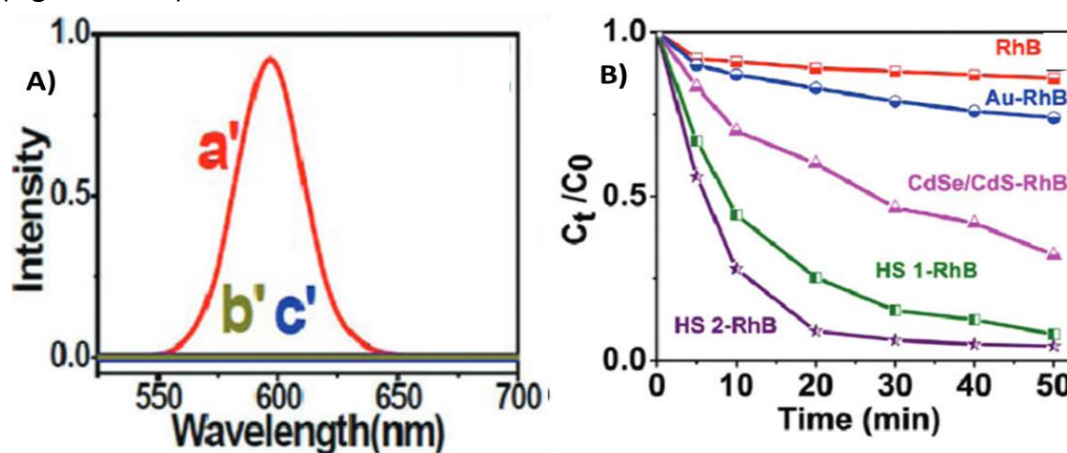


**Figure I-20: Charge separation and photocatalytic activity of CdSe-CdS-Au nanostructures.** A): photoluminescence quenching of CdSe-CdS QDs when Au particles were attached on their surfaces. B) Decomposition of Rhodamine B (RhB) under the action of bare Au, bare QDs or QD-Au heterostructures (HS) under light irradiation. HS 1 for the heterostructure with smaller AuNP (1.25 nm) and HS 2 with the bigger (2.5nm) AuNP. Figure adapted from reference 146.

In addition to the examples mentioned above for photocatalytic dyes degradation using semiconductor-metal hybrid nanostructures, other examples were also reported. For example, Soni et al.<sup>147</sup> prepared different samples of CdSe-Au hybrid nanostructures, tested the charge separation, and showed their higher efficiency toward reducing Methylene Blue

compared to bare CdSe counterparts. Moreover, Chauhan et al.<sup>148</sup> prepared nanostructures of CdSe-CdS core-shell QDs attached to Au nanoparticles exhibiting enhanced charge separation. Then, they showed their efficiency as photocatalysts for the degradation of Methylene Blue and Methyl orange. Han et al.<sup>149</sup> tested the photocatalytic activity of CdS-Au nanostructures toward the degradation of Rhodamine B. The results showed a significant increase in the photocatalytic degradation of Rhodamine B when using CdS-Au nanostructures as photocatalysts compared to others tested.

Beside the use of the semiconductor-metal nanostructures in dyes and pollutants degradation, some groups tested the photocatalytic activity of such nanostructures for other applications such as hydrogen production. Simon et al.<sup>150</sup> decorated CdS nanorods with platinum nanoparticles of different morphologies. They showed that, with tip-platinum decorated CdS nanorods (Figure I-21-A), the quantum yield of H<sub>2</sub> production can reach nearly 90%, providing an efficient mechanism of mediated charge separation with optimized hole extraction using hole scavengers (such as Sodium sulfite and ethanol). The comparison of the photocatalytic H<sub>2</sub> production using bare CdS nanorods showed the highly enhanced activity in the case of CdS-Pt cases and, in particular, when the Pt particles are attached to the tip on the CdS rods (Figure I-21-B).

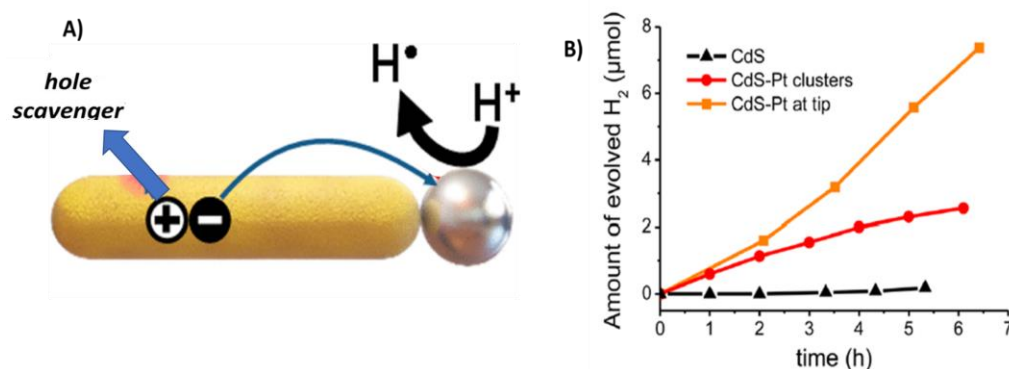


**Figure I-21: CdS-Pt nanostructure for photocatalytic hydrogen production.** A) Schematic representation of the structure of CdS-Pt having the Pt attached on the tip of the CdS nanorods. B) Comparison of the photocatalytic H<sub>2</sub> production using bare CdS and two different structures of CdS-Pt. Figure adapted from reference 150.

Therefore, as revealed from the examples mentioned above, the use of well-designed semiconductor-metal hybrid nanostructures presents a promising route for visible-light photocatalysis. These nanostructures exhibit a very good charge separation, thus minimizing the recombination of the photo-induced charge carriers. The photocatalytic activity of these hybrid nanostructures appeared to possess an enhanced activity compared to their bare

counterparts, even though their employment in complete redox reaction for organic transformations is still limited, which will be explored in this Thesis.

### Conclusion

In conclusion, to benefit from the high energy provided by sustainable solar energy for synthetic applications, researchers made great efforts to develop different types of visible light harvesting photocatalysts. In this context, the use of semiconductor Quantum Dots as photocatalysts for various photocatalytic processes showed encouraging results. Semiconductor Quantum Dots are efficiently used for interesting oxidation and reduction transformation. The possible use of Quantum Dots for already developed organic reaction was proved by replacing transition metal complexes such as Iridium and Ruthenium based photocatalysts. Quantum Dots are also used for new organic transformations such as new radical-based reactions. Due to their electronic properties, the use of Quantum Dots for original organic application initiated by Auger recombination and triplet excited state activity is proved to be efficient. However, the use of Quantum Dots for organic reactions is still limited to one type of Quantum Dots per reaction without investigating the difference between the existing types of Quantum Dots. Therefore, the exploration of different types of Quantum Dots for new organic reactions will be investigated in this Thesis.

Despite the promising application of semiconductor Quantum Dots, their photocatalytic reactions exhibit low Quantum yields, and the reactions require a long irradiation time to complete. This is mainly attributed to the recombination of the photo-induced charges. Therefore, the improvement of the photocatalytic activity of Quantum Dots by minimizing their charge recombination was targeted. The preparation of heterostructures of semiconductor Quantum Dots and metal nanoparticles represents one of the most used methods to enhance the activity of semiconductor Quantum Dots. These nanostructures are mainly prepared by the deposition of metal nanoparticles on the surface of the Quantum Dots. The semiconductor-metal heterostructures induce a better charge separation by affording the electron transfer from the photoexcited semiconductor Quantum Dots to the metal nanoparticles. The photocatalytic activity of these heterostructures was explored especially for pollutants degradation, and their activity is compared to the bare Quantum Dots showing much better results. Moreover, the preparation of semiconductor-metal nanostructures using bonds through their surface ligands is not yet well explored, and their use in photocatalysis is

not reported. The use of such chemically assembled semiconductor-metal nanostructures will be explored in Chapter III of this Thesis.

## References

- (1) Ritchie, H.; Roser, M.; Rosado, P. Energy. *Our World in Data* **2020**.
- (2) Grätzel, M. Photoelectrochemical Cells. *Nature* **2001**, *414* (6861), 338–344. <https://doi.org/10.1038/35104607>.
- (3) Oelgemöller, M. Solar Photochemical Synthesis: From the Beginnings of Organic Photochemistry to the Solar Manufacturing of Commodity Chemicals. *Chem. Rev.* **2016**, *116* (17), 9664–9682. <https://doi.org/10.1021/acs.chemrev.5b00720>.
- (4) Cambié, D.; Noël, T. Solar Photochemistry in Flow. In *Accounts on Sustainable Flow Chemistry*; Noël, T., Luque, R., Eds.; Topics in Current Chemistry Collections; Springer International Publishing: Cham, 2020; pp 1–27. [https://doi.org/10.1007/978-3-030-36572-1\\_1](https://doi.org/10.1007/978-3-030-36572-1_1).
- (5) Braslavsky, S. E. Glossary of Terms Used in Photochemistry, 3rd Edition (IUPAC Recommendations 2006). *Pure and Applied Chemistry* **2007**, *79* (3), 293–465. <https://doi.org/10.1351/pac200779030293>.
- (6) Serpone, N.; Emeline, A. V.; Horikoshi, S.; Kuznetsov, V. N.; Ryabchuk, V. K. On the Genesis of Heterogeneous Photocatalysis: A Brief Historical Perspective in the Period 1910 to the Mid-1980s. *Photochem. Photobiol. Sci.* **2012**, *11* (7), 1121–1150. <https://doi.org/10.1039/C2PP25026H>.
- (7) *Historical Development of Inorganic Photochemistry* | SpringerLink. [https://link.springer.com/chapter/10.1007/978-3-030-63713-2\\_1](https://link.springer.com/chapter/10.1007/978-3-030-63713-2_1) (accessed 2022-07-19).
- (8) Coronado, J. M. A Historical Introduction to Photocatalysis. In *Design of Advanced Photocatalytic Materials for Energy and Environmental Applications*; Coronado, J. M., Fresno, F., Hernández-Alonso, M. D., Portela, R., Eds.; Green Energy and Technology; Springer: London, 2013; pp 1–4. [https://doi.org/10.1007/978-1-4471-5061-9\\_1](https://doi.org/10.1007/978-1-4471-5061-9_1).
- (9) Fujishima, A.; Honda, K. Electrochemical Photolysis of Water at a Semiconductor Electrode. *Nature* **1972**, *238* (5358), 37–38. <https://doi.org/10.1038/238037a0>.
- (10) Kudo, A.; Miseki, Y. Heterogeneous Photocatalyst Materials for Water Splitting. *Chemical Society Reviews* **2009**, *38* (1), 253–278. <https://doi.org/10.1039/B800489G>.
- (11) Habisreutinger, S. N.; Schmidt-Mende, L.; Stolarczyk, J. K. Photocatalytic Reduction of CO<sub>2</sub> on TiO<sub>2</sub> and Other Semiconductors. *Angewandte Chemie International Edition* **2013**, *52* (29), 7372–7408. <https://doi.org/10.1002/anie.201207199>.
- (12) Chen, C.; Ma, W.; Zhao, J. Semiconductor-Mediated Photodegradation of Pollutants under Visible-Light Irradiation. *Chemical Society Reviews* **2010**, *39* (11), 4206–4219. <https://doi.org/10.1039/B921692H>.
- (13) Cermenati, L.; Albini, A.; Cermenati, L.; Richter, C.; Albini, A. Solar Light Induced Carbon–Carbon Bond Formation via TiO<sub>2</sub> Photocatalysis. *Chem. Commun.* **1998**, No. 7, 805–806. <https://doi.org/10.1039/A709172I>.
- (14) Riente, P.; Noël, T. Application of Metal Oxide Semiconductors in Light-Driven Organic Transformations. *Catal. Sci. Technol.* **2019**, *9* (19), 5186–5232. <https://doi.org/10.1039/C9CY01170F>.

- (15) Kalyanasundaram, K. Photophysics, Photochemistry and Solar Energy Conversion with Tris(Bipyridyl)Ruthenium(II) and Its Analogues. *Coordination Chemistry Reviews* **1982**, *46*, 159–244. [https://doi.org/10.1016/0010-8545\(82\)85003-0](https://doi.org/10.1016/0010-8545(82)85003-0).
- (16) Cano-Yelo, H.; Deronzier, A. Photocatalysis of the Pschorr Reaction by Tris-(2,2'-Bipyridyl)Ruthenium(II) in the Phenanthrene Series. *J. Chem. Soc., Perkin Trans. 2* **1984**, No. 6, 1093–1098. <https://doi.org/10.1039/P29840001093>.
- (17) Nicewicz, D. A.; MacMillan, D. W. C. Merging Photoredox Catalysis with Organocatalysis: The Direct Asymmetric Alkylation of Aldehydes. *Science* **2008**, *322* (5898), 77–80. <https://doi.org/10.1126/science.1161976>.
- (18) Ischay, M. A.; Anzovino, M. E.; Du, J.; Yoon, T. P. Efficient Visible Light Photocatalysis of [2+2] Enone Cycloadditions. *J. Am. Chem. Soc.* **2008**, *130* (39), 12886–12887. <https://doi.org/10.1021/ja805387f>.
- (19) Narayanam, J. M. R.; Tucker, J. W.; Stephenson, C. R. J. Electron-Transfer Photoredox Catalysis: Development of a Tin-Free Reductive Dehalogenation Reaction. *J. Am. Chem. Soc.* **2009**, *131* (25), 8756–8757. <https://doi.org/10.1021/ja9033582>.
- (20) Prier, C. K.; Rankic, D. A.; MacMillan, D. W. C. Visible Light Photoredox Catalysis with Transition Metal Complexes: Applications in Organic Synthesis. *Chem. Rev.* **2013**, *113* (7), 5322–5363. <https://doi.org/10.1021/cr300503r>.
- (21) Yoon, T. P.; Ischay, M. A.; Du, J. Visible Light Photocatalysis as a Greener Approach to Photochemical Synthesis. *Nature Chem* **2010**, *2* (7), 527–532. <https://doi.org/10.1038/nchem.687>.
- (22) Shaw, M. H.; Twilton, J.; MacMillan, D. W. C. Photoredox Catalysis in Organic Chemistry. *J. Org. Chem.* **2016**, *81* (16), 6898–6926. <https://doi.org/10.1021/acs.joc.6b01449>.
- (23) Bell, J. D.; Murphy, J. A. Recent Advances in Visible Light-Activated Radical Coupling Reactions Triggered by (i) Ruthenium, (ii) Iridium and (iii) Organic Photoredox Agents. *Chem. Soc. Rev.* **2021**, *50* (17), 9540–9685. <https://doi.org/10.1039/D1CS00311A>.
- (24) Tucker, J. W.; Stephenson, C. R. J. Shining Light on Photoredox Catalysis: Theory and Synthetic Applications. *J. Org. Chem.* **2012**, *77* (4), 1617–1622. <https://doi.org/10.1021/jo202538x>.
- (25) Nicewicz, D. A.; Nguyen, T. M. Recent Applications of Organic Dyes as Photoredox Catalysts in Organic Synthesis. *ACS Catal.* **2014**, *4* (1), 355–360. <https://doi.org/10.1021/cs400956a>.
- (26) Fukuzumi, S.; Ohkubo, K. Organic Synthetic Transformations Using Organic Dyes as Photoredox Catalysts. *Organic & Biomolecular Chemistry* **2014**, *12* (32), 6059–6071. <https://doi.org/10.1039/C4OB00843J>.
- (27) Kisch, H. Semiconductor Photocatalysis—Mechanistic and Synthetic Aspects. *Angewandte Chemie International Edition* **2013**, *52* (3), 812–847. <https://doi.org/10.1002/anie.201201200>.
- (28) Arcudi, F.; Đorđević, L.; Nagasing, B.; Stupp, S. I.; Weiss, E. A. Quantum Dot-Sensitized Photoreduction of CO<sub>2</sub> in Water with Turnover Number > 80,000. *J. Am. Chem. Soc.* **2021**. <https://doi.org/10.1021/jacs.1c06961>.
- (29) Wu, H.-L.; Li, X.-B.; Tung, C.-H.; Wu, L.-Z. Semiconductor Quantum Dots: An Emerging Candidate for CO<sub>2</sub> Photoreduction. *Advanced Materials* **2019**, *31* (36), 1900709. <https://doi.org/10.1002/adma.201900709>.
- (30) Kuehnel, M. F.; Orchard, K. L.; Dalle, K. E.; Reisner, E. Selective Photocatalytic CO<sub>2</sub> Reduction in Water through Anchoring of a Molecular Ni Catalyst on CdS Nanocrystals. *J. Am. Chem. Soc.* **2017**, *139* (21), 7217–7223. <https://doi.org/10.1021/jacs.7b00369>.

- (31) Li, X.-B.; Tung, C.-H.; Wu, L.-Z. Semiconducting Quantum Dots for Artificial Photosynthesis. *Nat Rev Chem* **2018**, *2* (8), 160–173. <https://doi.org/10.1038/s41570-018-0024-8>.
- (32) Burke, R.; Chakraborty, S.; P. McClelland, K.; Jelušić, J.; M. Matson, E.; L. Bren, K.; D. Krauss, T. Light-Driven Hydrogen Production with CdSe Quantum Dots and a Cobalt Glutathione Catalyst. *Chemical Communications* **2021**, *57* (16), 2053–2056. <https://doi.org/10.1039/D0CC07364D>.
- (33) Han, Z.; Qiu, F.; Eisenberg, R.; Holland, P. L.; Krauss, T. D. Robust Photogeneration of H<sub>2</sub> in Water Using Semiconductor Nanocrystals and a Nickel Catalyst. *Science* **2012**, *338* (6112), 1321–1324. <https://doi.org/10.1126/science.1227775>.
- (34) Yuan, Y.; Jin, N.; Saghy, P.; Dube, L.; Zhu, H.; Chen, O. Quantum Dot Photocatalysts for Organic Transformations. *J. Phys. Chem. Lett.* **2021**, *12* (30), 7180–7193. <https://doi.org/10.1021/acs.jpcclett.1c01717>.
- (35) Wang, D.-Y.; Yin, Y.-Y.; Feng, C.-W.; Rukhsana; Shen, Y.-M. Advances in Homogeneous Photocatalytic Organic Synthesis with Colloidal Quantum Dots. *Catalysts* **2021**, *11* (2), 275. <https://doi.org/10.3390/catal11020275>.
- (36) Huang, C.; Li, X.-B.; Tung, C.-H.; Wu, L.-Z. Photocatalysis with Quantum Dots and Visible Light for Effective Organic Synthesis. *Chemistry – A European Journal* **2018**, *24* (45), 11530–11534. <https://doi.org/10.1002/chem.201800391>.
- (37) Hu, Q.; Yu, X.; Gong, S.; Chen, X. Nanomaterial Catalysts for Organic Photoredox Catalysis-Mechanistic Perspective. *Nanoscale* **2021**, *13* (43), 18044–18053. <https://doi.org/10.1039/D1NR05474K>.
- (38) Smith, A. M.; Nie, S. Semiconductor Nanocrystals: Structure, Properties, and Band Gap Engineering. *Acc. Chem. Res.* **2010**, *43* (2), 190–200. <https://doi.org/10.1021/ar9001069>.
- (39) Pal, A.; Srivastava, S.; Saini, P.; Raina, S.; Ingole, P. P.; Gupta, R.; Sapra, S. Probing the Mechanism of Fluorescence Quenching of QDs by Co(III)-Complexes: Size of QD and Nature of the Complex Both Dictate Energy and Electron Transfer Processes. *J. Phys. Chem. C* **2015**, *119* (39), 22690–22699. <https://doi.org/10.1021/acs.jpcc.5b06795>.
- (40) Chauviré, T.; Mouesca, J.-M.; Gasparutto, D.; Ravanat, J.-L.; Lebrun, C.; Gromova, M.; Jouneau, P.-H.; Chauvin, J.; Gambarelli, S.; Maurel, V. Redox Photocatalysis with Water-Soluble Core-Shell CdSe-ZnS Quantum Dots. *J. Phys. Chem. C* **2015**, *119* (31), 17857–17866. <https://doi.org/10.1021/acs.jpcc.5b04396>.
- (41) Murray, C. B.; Norris, D. J.; Bawendi, M. G. Synthesis and Characterization of Nearly Monodisperse CdE (E = Sulfur, Selenium, Tellurium) Semiconductor Nanocrystallites. *J. Am. Chem. Soc.* **1993**, *115* (19), 8706–8715. <https://doi.org/10.1021/ja00072a025>.
- (42) Dabbousi, B. O.; Rodriguez-Viejo, J.; Mikulec, F. V.; Heine, J. R.; Mattoussi, H.; Ober, R.; Jensen, K. F.; Bawendi, M. G. (CdSe)ZnS Core-Shell Quantum Dots: Synthesis and Characterization of a Size Series of Highly Luminescent Nanocrystallites. *J. Phys. Chem. B* **1997**, *101* (46), 9463–9475. <https://doi.org/10.1021/jp971091y>.
- (43) Yu, W. W.; Qu, L.; Guo, W.; Peng, X. Experimental Determination of the Extinction Coefficient of CdTe, CdSe, and CdS Nanocrystals. *Chem. Mater.* **2003**, *15* (14), 2854–2860. <https://doi.org/10.1021/cm034081k>.
- (44) Dennis, A. M.; Mangum, B. D.; Piryatinski, A.; Park, Y.-S.; Hannah, D. C.; Casson, J. L.; Williams, D. J.; Schaller, R. D.; Htoon, H.; Hollingsworth, J. A. Suppressed Blinking and Auger Recombination in Near-Infrared Type-II InP/CdS Nanocrystal Quantum Dots. *Nano Lett.* **2012**, *12* (11), 5545–5551. <https://doi.org/10.1021/nl302453x>.

- (45) Calvin, J. J.; Brewer, A. S.; Alivisatos, A. P. The Role of Organic Ligand Shell Structures in Colloidal Nanocrystal Synthesis. *Nat Synth* **2022**, *1* (2), 127–137. <https://doi.org/10.1038/s44160-022-00025-4>.
- (46) Adam, S.; Talapin, D. V.; Borchert, H.; Lobo, A.; McGinley, C.; de Castro, A. R. B.; Haase, M.; Weller, H.; Möller, T. The Effect of Nanocrystal Surface Structure on the Luminescence Properties: Photoemission Study of HF-Etched InP Nanocrystals. *J. Chem. Phys.* **2005**, *123* (8), 084706. <https://doi.org/10.1063/1.2004901>.
- (47) Grandhi, G. K.; M., A.; Viswanatha, R. Understanding the Role of Surface Capping Ligands in Passivating the Quantum Dots Using Copper Dopants as Internal Sensor. *J. Phys. Chem. C* **2016**, *120* (35), 19785–19795. <https://doi.org/10.1021/acs.jpcc.6b04060>.
- (48) Owen, J. S.; Park, J.; Trudeau, P.-E.; Alivisatos, A. P. Reaction Chemistry and Ligand Exchange at Cadmium–Selenide Nanocrystal Surfaces. *J. Am. Chem. Soc.* **2008**, *130* (37), 12279–12281. <https://doi.org/10.1021/ja804414f>.
- (49) Liu, J.; Yang, W.; Li, Y.; Fan, L.; Li, Y. Electrochemical Studies of the Effects of the Size, Ligand and Composition on the Band Structures of CdSe, CdTe and Their Alloy Nanocrystals. *Phys. Chem. Chem. Phys.* **2014**, *16* (10), 4778–4788. <https://doi.org/10.1039/C3CP55226H>.
- (50) Jasieniak, J.; Califano, M.; Watkins, S. E. Size-Dependent Valence and Conduction Band-Edge Energies of Semiconductor Nanocrystals. *ACS Nano* **2011**, *5* (7), 5888–5902. <https://doi.org/10.1021/nn201681s>.
- (51) Amelia, M.; Impellizzeri, S.; Monaco, S.; Yildiz, I.; Silvi, S.; Raymo, F. M.; Credi, A. Structural and Size Effects on the Spectroscopic and Redox Properties of CdSe Nanocrystals in Solution: The Role of Defect States. *ChemPhysChem* **2011**, *12* (12), 2280–2288. <https://doi.org/10.1002/cphc.201100300>.
- (52) Green, M. *Semiconductor Quantum Dots*; 2014. <https://doi.org/10.1039/9781782628354>.
- (53) Rosa, M. L. Development of Luminescent Semiconductor Nanocrystals (Quantum Dots) for Photoinduced Applications. 146.
- (54) *Semiconductor–Polymer Hybrid Materials* | SpringerLink. [https://link.springer.com/chapter/10.1007/12\\_2014\\_295](https://link.springer.com/chapter/10.1007/12_2014_295) (accessed 2022-07-24).
- (55) Green, M. *Semiconductor Quantum Dots: Organometallic and Inorganic Synthesis*; Royal Society of Chemistry, 2014.
- (56) Rabouw, F. T.; de Mello Donega, C. Excited-State Dynamics in Colloidal Semiconductor Nanocrystals. *Top Curr Chem (Z)* **2016**, *374* (5), 58. <https://doi.org/10.1007/s41061-016-0060-0>.
- (57) Mushonga, P.; Onani, M. O.; Madiehe, A. M.; Meyer, M. Indium Phosphide-Based Semiconductor Nanocrystals and Their Applications. *Journal of Nanomaterials* **2012**, *2012*, e869284. <https://doi.org/10.1155/2012/869284>.
- (58) Bera, D.; Qian, L.; Tseng, T.-K.; Holloway, P. H. Quantum Dots and Their Multimodal Applications: A Review. *Materials* **2010**, *3* (4), 2260–2345. <https://doi.org/10.3390/ma3042260>.
- (59) Efros, A. L.; Brus, L. E. Nanocrystal Quantum Dots: From Discovery to Modern Development. *ACS Nano* **2021**, *15* (4), 6192–6210. <https://doi.org/10.1021/acsnano.1c01399>.
- (60) Rossetti, R.; Hull, R.; Gibson, J. M.; Brus, L. E. Excited Electronic States and Optical Spectra of ZnS and CdS Crystallites in the  $\approx 15$  to 50 Å Size Range: Evolution from Molecular to

- Bulk Semiconducting Properties. *J. Chem. Phys.* **1985**, *82* (1), 552–559. <https://doi.org/10.1063/1.448727>.
- (61) Rossetti, R.; Hull, R.; Gibson, J. M.; Brus, L. E. Hybrid Electronic Properties between the Molecular and Solid State Limits: Lead Sulfide and Silver Halide Crystallites. *J. Chem. Phys.* **1985**, *83* (3), 1406–1410. <https://doi.org/10.1063/1.449407>.
- (62) Chestnoy, N.; Hull, R.; Brus, L. E. Higher Excited Electronic States in Clusters of ZnSe, CdSe, and ZnS: Spin-orbit, Vibronic, and Relaxation Phenomena. *J. Chem. Phys.* **1986**, *85* (4), 2237–2242. <https://doi.org/10.1063/1.451119>.
- (63) Jasieniak, J.; Smith, L.; van Embden, J.; Mulvaney, P.; Califano, M. Re-Examination of the Size-Dependent Absorption Properties of CdSe Quantum Dots. *J. Phys. Chem. C* **2009**, *113* (45), 19468–19474. <https://doi.org/10.1021/jp906827m>.
- (64) Reiss, P.; Protière, M.; Li, L. Core/Shell Semiconductor Nanocrystals. *Small* **2009**, *5* (2), 154–168. <https://doi.org/10.1002/sml.200800841>.
- (65) Peng, Z. A.; Peng, X. Formation of High-Quality CdTe, CdSe, and CdS Nanocrystals Using CdO as Precursor. *J. Am. Chem. Soc.* **2001**, *123* (1), 183–184. <https://doi.org/10.1021/ja003633m>.
- (66) Wang, F.; Tang, R.; Buhro, W. E. The Trouble with TOPO; Identification of Adventitious Impurities Beneficial to the Growth of Cadmium Selenide Quantum Dots, Rods, and Wires. *Nano Lett.* **2008**, *8* (10), 3521–3524. <https://doi.org/10.1021/nl801692g>.
- (67) Yu, W. W.; Peng, X. Formation of High-Quality CdS and Other II–VI Semiconductor Nanocrystals in Noncoordinating Solvents: Tunable Reactivity of Monomers. *Angewandte Chemie International Edition* **2002**, *41* (13), 2368–2371. [https://doi.org/10.1002/1521-3773\(20020703\)41:13<2368::AID-ANIE2368>3.0.CO;2-G](https://doi.org/10.1002/1521-3773(20020703)41:13<2368::AID-ANIE2368>3.0.CO;2-G).
- (68) Jasieniak, J.; Bullen, C.; van Embden, J.; Mulvaney, P. Phosphine-Free Synthesis of CdSe Nanocrystals. *J. Phys. Chem. B* **2005**, *109* (44), 20665–20668. <https://doi.org/10.1021/jp054289o>.
- (69) Park, J.; Joo, J.; Kwon, S. G.; Jang, Y.; Hyeon, T. Synthesis of Monodisperse Spherical Nanocrystals. *Angewandte Chemie International Edition* **2007**, *46* (25), 4630–4660. <https://doi.org/10.1002/anie.200603148>.
- (70) Shao, L.; Gao, Y.; Yan, F. Semiconductor Quantum Dots for Biomedical Applications. *Sensors* **2011**, *11* (12), 11736–11751. <https://doi.org/10.3390/s111211736>.
- (71) Pu, C.; Peng, X. To Battle Surface Traps on CdSe/CdS Core/Shell Nanocrystals: Shell Isolation versus Surface Treatment. *J. Am. Chem. Soc.* **2016**, *138* (26), 8134–8142. <https://doi.org/10.1021/jacs.6b02909>.
- (72) Aldana, J.; Wang, Y. A.; Peng, X. Photochemical Instability of CdSe Nanocrystals Coated by Hydrophilic Thiols. *J. Am. Chem. Soc.* **2001**, *123* (36), 8844–8850. <https://doi.org/10.1021/ja016424q>.
- (73) Pu, C.; Qin, H.; Gao, Y.; Zhou, J.; Wang, P.; Peng, X. Synthetic Control of Exciton Behavior in Colloidal Quantum Dots. *J. Am. Chem. Soc.* **2017**, *139* (9), 3302–3311. <https://doi.org/10.1021/jacs.6b11431>.
- (74) AbouElhamd, A. R.; Al-Sallal, K. A.; Hassan, A. Review of Core/Shell Quantum Dots Technology Integrated into Building's Glazing. *Energies* **2019**, *12* (6), 1058. <https://doi.org/10.3390/en12061058>.
- (75) Vasudevan, D.; Gaddam, R. R.; Trinchì, A.; Cole, I. Core–Shell Quantum Dots: Properties and Applications. *Journal of Alloys and Compounds* **2015**, *636*, 395–404. <https://doi.org/10.1016/j.jallcom.2015.02.102>.

- (76) Wang, Y.-F.; Wang, H.-Y.; Li, Z.-S.; Zhao, J.; Wang, L.; Chen, Q.-D.; Wang, W.-Q.; Sun, H.-B. Electron Extraction Dynamics in CdSe and CdSe/CdS/ZnS Quantum Dots Adsorbed with Methyl Viologen. *J. Phys. Chem. C* **2014**, *118* (31), 17240–17246. <https://doi.org/10.1021/jp5024789>.
- (77) Maity, P.; Debnath, T.; Ghosh, H. N. Ultrafast Charge Carrier Delocalization in CdSe/CdS Quasi-Type II and CdS/CdSe Inverted Type I Core–Shell: A Structural Analysis through Carrier-Quenching Study. *J. Phys. Chem. C* **2015**, *119* (46), 26202–26211. <https://doi.org/10.1021/acs.jpcc.5b08913>.
- (78) Zhou, J.; Zhu, M.; Meng, R.; Qin, H.; Peng, X. Ideal CdSe/CdS Core/Shell Nanocrystals Enabled by Entropic Ligands and Their Core Size-, Shell Thickness-, and Ligand-Dependent Photoluminescence Properties. *J. Am. Chem. Soc.* **2017**, *139* (46), 16556–16567. <https://doi.org/10.1021/jacs.7b07434>.
- (79) Xi, Z.-W.; Yang, L.; Wang, D.-Y.; Pu, C.-D.; Shen, Y.-M.; Wu, C.-D.; Peng, X.-G. Visible-Light Photocatalytic Synthesis of Amines from Imines via Transfer Hydrogenation Using Quantum Dots as Catalysts. *J. Org. Chem.* **2018**, *83* (19), 11886–11895. <https://doi.org/10.1021/acs.joc.8b01651>.
- (80) Qiu, F.; Han, Z.; Peterson, J. J.; Odoi, M. Y.; Sowers, K. L.; Krauss, T. D. Photocatalytic Hydrogen Generation by CdSe/CdS Nanoparticles. *Nano Lett.* **2016**, *16* (9), 5347–5352. <https://doi.org/10.1021/acs.nanolett.6b01087>.
- (81) Toufanian, R.; Piryatinski, A.; Mahler, A. H.; Iyer, R.; Hollingsworth, J. A.; Dennis, A. M. Bandgap Engineering of Indium Phosphide-Based Core/Shell Heterostructures Through Shell Composition and Thickness. *Frontiers in Chemistry* **2018**, *6*, 567. <https://doi.org/10.3389/fchem.2018.00567>.
- (82) Zhang, F.; Wang, X.; Liu, H.; Liu, C.; Wan, Y.; Long, Y.; Cai, Z. Recent Advances and Applications of Semiconductor Photocatalytic Technology. *Applied Sciences* **2019**, *9* (12), 2489. <https://doi.org/10.3390/app9122489>.
- (83) Inamdar, S. N.; Ingole, P. P.; Haram, S. K. Determination of Band Structure Parameters and the Quasi-Particle Gap of CdSe Quantum Dots by Cyclic Voltammetry. *ChemPhysChem* **2008**, *9* (17), 2574–2579. <https://doi.org/10.1002/cphc.200800482>.
- (84) Chakraborty, I. N.; Roy, S.; Devatha, G.; Rao, A.; Pillai, P. P. InP/ZnS Quantum Dots as Efficient Visible-Light Photocatalysts for Redox and Carbon–Carbon Coupling Reactions. *Chem. Mater.* **2019**, *31* (7), 2258–2262. <https://doi.org/10.1021/acs.chemmater.9b00086>.
- (85) Yu, S.; Fan, X.-B.; Wang, X.; Li, J.; Zhang, Q.; Xia, A.; Wei, S.; Wu, L.-Z.; Zhou, Y.; Patzke, G. R. Efficient Photocatalytic Hydrogen Evolution with Ligand Engineered All-Inorganic InP and InP/ZnS Colloidal Quantum Dots. *Nat Commun* **2018**, *9* (1), 4009. <https://doi.org/10.1038/s41467-018-06294-y>.
- (86) Cademartiri, L.; Bertolotti, J.; Sapienza, R.; Wiersma, D. S.; von Freymann, G.; Ozin, G. A. Multigram Scale, Solventless, and Diffusion-Controlled Route to Highly Monodisperse PbS Nanocrystals. *J. Phys. Chem. B* **2006**, *110* (2), 671–673. <https://doi.org/10.1021/jp0563585>.
- (87) Kodaimati, M. S.; McClelland, K. P.; He, C.; Lian, S.; Jiang, Y.; Zhang, Z.; Weiss, E. A. Viewpoint: Challenges in Colloidal Photocatalysis and Some Strategies for Addressing Them. *Inorg. Chem.* **2018**, *57* (7), 3659–3670. <https://doi.org/10.1021/acs.inorgchem.7b03182>.

- (88) Luan, W.; Yang, H.; Wan, Z.; Yuan, B.; Yu, X.; Tu, S. Mercaptopropionic Acid Capped CdSe/ZnS Quantum Dots as Fluorescence Probe for Lead(II). *J Nanopart Res* **2012**, *14* (3), 762. <https://doi.org/10.1007/s11051-012-0762-3>.
- (89) Calzada, R.; Thompson, C. M.; Westmoreland, D. E.; Edme, K.; Weiss, E. A. Organic-to-Aqueous Phase Transfer of Cadmium Chalcogenide Quantum Dots Using a Sulfur-Free Ligand for Enhanced Photoluminescence and Oxidative Stability. *Chem. Mater.* **2016**, *28* (18), 6716–6723. <https://doi.org/10.1021/acs.chemmater.6b03106>.
- (90) Wang, W.; Banerjee, S.; Jia, S.; Steigerwald, M. L.; Herman, I. P. Ligand Control of Growth, Morphology, and Capping Structure of Colloidal CdSe Nanorods. *Chem. Mater.* **2007**, *19* (10), 2573–2580. <https://doi.org/10.1021/cm0705791>.
- (91) Weidman, M. C.; Nguyen, Q.; Smilgies, D.-M.; Tisdale, W. A. Impact of Size Dispersity, Ligand Coverage, and Ligand Length on the Structure of PbS Nanocrystal Superlattices. *Chem. Mater.* **2018**, *30* (3), 807–816. <https://doi.org/10.1021/acs.chemmater.7b04322>.
- (92) Zhang, Z.; Edme, K.; Lian, S.; Weiss, E. A. Enhancing the Rate of Quantum-Dot-Photocatalyzed Carbon–Carbon Coupling by Tuning the Composition of the Dot’s Ligand Shell. *J. Am. Chem. Soc.* **2017**, *139* (12), 4246–4249. <https://doi.org/10.1021/jacs.6b13220>.
- (93) Jensen, S. C.; Bettis Homan, S.; Weiss, E. A. Photocatalytic Conversion of Nitrobenzene to Aniline through Sequential Proton-Coupled One-Electron Transfers from a Cadmium Sulfide Quantum Dot. *J. Am. Chem. Soc.* **2016**, *138* (5), 1591–1600. <https://doi.org/10.1021/jacs.5b11353>.
- (94) Caputo, J. A.; Frenette, L. C.; Zhao, N.; Sowers, K. L.; Krauss, T. D.; Weix, D. J. General and Efficient C–C Bond Forming Photoredox Catalysis with Semiconductor Quantum Dots. *J. Am. Chem. Soc.* **2017**, *139* (12), 4250–4253. <https://doi.org/10.1021/jacs.6b13379>.
- (95) Pal, A.; Ghosh, I.; Sapra, S.; König, B. Quantum Dots in Visible-Light Photoredox Catalysis: Reductive Dehalogenations and C–H Arylation Reactions Using Aryl Bromides. *Chem. Mater.* **2017**, *29* (12), 5225–5231. <https://doi.org/10.1021/acs.chemmater.7b01109>.
- (96) Chandrashekar, H. B.; Maji, A.; Halder, G.; Banerjee, S.; Bhattacharyya, S.; Maiti, D. Photocatalyzed Borylation Using Water-Soluble Quantum Dots. *Chem. Commun.* **2019**, *55* (44), 6201–6204. <https://doi.org/10.1039/C9CC01737B>.
- (97) Perez, K. A.; Rogers, C. R.; Weiss, E. A. Quantum Dot-Catalyzed Photoreductive Removal of Sulfonyl-Based Protecting Groups. *Angewandte Chemie International Edition* **2020**, *59* (33), 14091–14095. <https://doi.org/10.1002/anie.202005074>.
- (98) Widness, J. K.; Enny, D. G.; McFarlane-Connelly, K. S.; Miedenbauer, M. T.; Krauss, T. D.; Weix, D. J. CdS Quantum Dots as Potent Photoreductants for Organic Chemistry Enabled by Auger Processes. *J. Am. Chem. Soc.* **2022**. <https://doi.org/10.1021/jacs.2c03235>.
- (99) Haram, S. K.; Quinn, B. M.; Bard, A. J. Electrochemistry of CdS Nanoparticles: A Correlation between Optical and Electrochemical Band Gaps. *J. Am. Chem. Soc.* **2001**, *123* (36), 8860–8861. <https://doi.org/10.1021/ja0158206>.
- (100) Ingole, P. P.; Markad, G. B.; Saraf, D.; Tatikondewar, L.; Nene, O.; Kshirsagar, A.; Haram, S. K. Band Gap Bowing at Nanoscale: Investigation of CdS<sub>x</sub>Se<sub>1-x</sub> Alloy Quantum Dots through Cyclic Voltammetry and Density Functional Theory. *J. Phys. Chem. C* **2013**, *117* (14), 7376–7383. <https://doi.org/10.1021/jp400021u>.
- (101) Montenegro, M. I. The Electrochemical Cleavage of Protecting Groups. *Electrochimica Acta* **1986**, *31* (6), 607–620. [https://doi.org/10.1016/0013-4686\(86\)87027-X](https://doi.org/10.1016/0013-4686(86)87027-X).

- (102) Miyazaki, T.; Maekawa, H.; Yonemura, K.; Yamamoto, Y.; Yamanaka, Y.; Nishiguchi, I. Mg-Promoted Facile and Selective Intramolecular Cyclization of Aromatic  $\delta$ -Ketoesters. *Tetrahedron* **2011**, *67* (8), 1598–1602. <https://doi.org/10.1016/j.tet.2010.12.030>.
- (103) McClelland, K. P.; Weiss, E. A. Selective Photocatalytic Oxidation of Benzyl Alcohol to Benzaldehyde or C–C Coupled Products by Visible-Light-Absorbing Quantum Dots. *ACS Appl. Energy Mater.* **2019**, *2* (1), 92–96. <https://doi.org/10.1021/acsaem.8b01652>.
- (104) Zhao, L.-M.; Meng, Q.-Y.; Fan, X.-B.; Ye, C.; Li, X.-B.; Chen, B.; Ramamurthy, V.; Tung, C.-H.; Wu, L.-Z. Photocatalysis with Quantum Dots and Visible Light: Selective and Efficient Oxidation of Alcohols to Carbonyl Compounds through a Radical Relay Process in Water. *Angewandte Chemie International Edition* **2017**, *56* (11), 3020–3024. <https://doi.org/10.1002/anie.201700243>.
- (105) Simlandy, A. K.; Bhattacharyya, B.; Pandey, A.; Mukherjee, S. Picosecond Electron Transfer from Quantum Dots Enables a General and Efficient Aerobic Oxidation of Boronic Acids. *ACS Catal.* **2018**, *8* (6), 5206–5211. <https://doi.org/10.1021/acscatal.8b01078>.
- (106) Terrett, J. A.; Clift, M. D.; MacMillan, D. W. C. Direct  $\beta$ -Alkylation of Aldehydes via Photoredox Organocatalysis. *J. Am. Chem. Soc.* **2014**, *136* (19), 6858–6861. <https://doi.org/10.1021/ja502639e>.
- (107) Jeffrey, J. L.; Petronijević, F. R.; MacMillan, D. W. C. Selective Radical–Radical Cross-Couplings: Design of a Formal  $\beta$ -Mannich Reaction. *J. Am. Chem. Soc.* **2015**, *137* (26), 8404–8407. <https://doi.org/10.1021/jacs.5b05376>.
- (108) *Aryl amination using ligand-free Ni(II) salts and photoredox catalysis | Science.* <https://www.science.org/doi/full/10.1126/science.aag0209> (accessed 2022-09-17).
- (109) Lackner, G. L.; Quasdorf, K. W.; Pratsch, G.; Overman, L. E. Fragment Coupling and the Construction of Quaternary Carbons Using Tertiary Radicals Generated From Tert-Alkyl N-Phthalimidoyl Oxalates By Visible-Light Photocatalysis. *J. Org. Chem.* **2015**, *80* (12), 6012–6024. <https://doi.org/10.1021/acs.joc.5b00794>.
- (110) Noble, A.; MacMillan, D. W. C. Photoredox  $\alpha$ -Vinylolation of  $\alpha$ -Amino Acids and *N*-Aryl Amines. *J. Am. Chem. Soc.* **2014**, *136* (33), 11602–11605. <https://doi.org/10.1021/ja506094d>.
- (111) Hu, J.; Pu, T.-J.; Xu, Z.-W.; Xu, W.-Y.; Feng, Y.-S. Cadmium Sulfide Quantum-Dot-Photocatalyzed Cascade Cyclization of Functionalized Difluoromethyl Chlorides with Unactivated Olefins. *Advanced Synthesis & Catalysis* **2019**, *361* (4), 708–713. <https://doi.org/10.1002/adsc.201801246>.
- (112) Hu, R.; Xie, W.-H.; Wang, H.-Y.; Guo, X.-A.; Sun, H.-M.; Li, C.-B.; Zhang, X.-P.; Cao, R. Visible Light-Driven Carbon-Carbon Reductive Coupling of Aromatic Ketones Activated by Ni-Doped CdS Quantum Dots: An Insight into the Mechanism. *Applied Catalysis B: Environmental* **2022**, *304*, 120946. <https://doi.org/10.1016/j.apcatb.2021.120946>.
- (113) Xi, Z.-W.; Yang, L.; Wang, D.-Y.; Feng, C.-W.; Qin, Y.; Shen, Y.-M.; Pu, C.; Peng, X. Visible Light Induced Reduction and Pinacol Coupling of Aldehydes and Ketones Catalyzed by Core/Shell Quantum Dots. *J. Org. Chem.* **2021**, *86* (3), 2474–2488. <https://doi.org/10.1021/acs.joc.0c02627>.
- (114) Guo, Q.; Liang, F.; Li, X.-B.; Gao, Y.-J.; Huang, M.-Y.; Wang, Y.; Xia, S.-G.; Gao, X.-Y.; Gan, Q.-C.; Lin, Z.-S.; Tung, C.-H.; Wu, L.-Z. Efficient and Selective CO<sub>2</sub> Reduction Integrated with Organic Synthesis by Solar Energy. *Chem* **2019**, *5* (10), 2605–2616. <https://doi.org/10.1016/j.chempr.2019.06.019>.

- (115) Li, X.-B.; Li, Z.-J.; Gao, Y.-J.; Meng, Q.-Y.; Yu, S.; Weiss, R. G.; Tung, C.-H.; Wu, L.-Z. Mechanistic Insights into the Interface-Directed Transformation of Thiols into Disulfides and Molecular Hydrogen by Visible-Light Irradiation of Quantum Dots. *Angewandte Chemie International Edition* **2014**, *53* (8), 2085–2089. <https://doi.org/10.1002/anie.201310249>.
- (116) Qiao, J.; Song, Z.-Q.; Huang, C.; Ci, R.-N.; Liu, Z.; Chen, B.; Tung, C.-H.; Wu, L.-Z. Direct, Site-Selective and Redox-Neutral  $\alpha$ -C–H Bond Functionalization of Tetrahydrofurans via Quantum Dots Photocatalysis. *Angewandte Chemie International Edition* **2021**, *60* (52), 27201–27205. <https://doi.org/10.1002/anie.202109849>.
- (117) Huang, C.; Qiao, J.; Ci, R.-N.; Wang, X.-Z.; Wang, Y.; Wang, J.-H.; Chen, B.; Tung, C.-H.; Wu, L.-Z. Quantum Dots Enable Direct Alkylation and Arylation of Allylic C(Sp<sup>3</sup>)–H Bonds with Hydrogen Evolution by Solar Energy. *Chem* **2021**, *7* (5), 1244–1257. <https://doi.org/10.1016/j.chempr.2021.01.019>.
- (118) Huang, C.; Ci, R.-N.; Qiao, J.; Wang, X.-Z.; Feng, K.; Chen, B.; Tung, C.-H.; Wu, L.-Z. Direct Allylic C(Sp<sup>3</sup>)–H and Vinylic C(Sp<sup>2</sup>)–H Thiolation with Hydrogen Evolution by Quantum Dots and Visible Light. *Angewandte Chemie International Edition* **2021**, *60* (21), 11779–11783. <https://doi.org/10.1002/anie.202101947>.
- (119) Ci, R.-N.; Huang, C.; Zhao, L.-M.; Qiao, J.; Chen, B.; Feng, K.; Tung, C.-H.; Wu, L.-Z. General and Efficient C–P Bond Formation by Quantum Dots and Visible Light. *CCS Chemistry* **2022**. <https://doi.org/10.31635/ccschem.021.202101615>.
- (120) Jiang, Y.; Weiss, E. A. Colloidal Quantum Dots as Photocatalysts for Triplet Excited State Reactions of Organic Molecules. *J. Am. Chem. Soc.* **2020**, *142* (36), 15219–15229. <https://doi.org/10.1021/jacs.0c07421>.
- (121) Jiang, Y.; Wang, C.; Rogers, C. R.; Kodaimati, M. S.; Weiss, E. A. Regio- and Diastereoselective Intermolecular [2+2] Cycloadditions Photocatalysed by Quantum Dots. *Nat. Chem.* **2019**, *11* (11), 1034–1040. <https://doi.org/10.1038/s41557-019-0344-4>.
- (122) Jiang, Y.; López-Arteaga, R.; Weiss, E. A. Quantum Dots Photocatalyze Intermolecular [2 + 2] Cycloadditions of Aromatic Alkenes Adsorbed to Their Surfaces via van Der Waals Interactions. *J. Am. Chem. Soc.* **2022**. <https://doi.org/10.1021/jacs.2c00833>.
- (123) Liu, D.; Nyakuchena, J.; Maity, R.; Geng, X.; Mahajan, J.; Hewa-Rahinduwage, C. C.; Peng, Y.; Huang, J.; Luo, L. Quantum Dot Gels as Efficient and Unique Photocatalysts for Organic Synthesis. *Chem. Commun.* **2022**. <https://doi.org/10.1039/D2CC03872B>.
- (124) Wu, X.; Fan, X.; Xie, S.; Lin, J.; Cheng, J.; Zhang, Q.; Chen, L.; Wang, Y. Solar Energy-Driven Lignin-First Approach to Full Utilization of Lignocellulosic Biomass under Mild Conditions. *Nat Catal* **2018**, *1* (10), 772–780. <https://doi.org/10.1038/s41929-018-0148-8>.
- (125) Enright, M. J.; Gilbert-Bass, K.; Sarsito, H.; Cossairt, B. M. Photolytic C–O Bond Cleavage with Quantum Dots. *Chem. Mater.* **2019**, *31* (7), 2677–2682. <https://doi.org/10.1021/acs.chemmater.9b00943>.
- (126) Huang, Y.; Zhu, Y.; Egap, E. Semiconductor Quantum Dots as Photocatalysts for Controlled Light-Mediated Radical Polymerization. *ACS Macro Lett.* **2018**, *7* (2), 184–189. <https://doi.org/10.1021/acsmacrolett.7b00968>.
- (127) McClelland, K. P.; Clemons, T. D.; Stupp, S. I.; Weiss, E. A. Semiconductor Quantum Dots Are Efficient and Recyclable Photocatalysts for Aqueous PET-RAFT Polymerization. *ACS Macro Lett.* **2020**, *9* (1), 7–13. <https://doi.org/10.1021/acsmacrolett.9b00891>.

- (128) Maity, P.; N. Ghosh, H. Strategies for Extending Charge Separation in Colloidal Nanostructured Quantum Dot Materials. *Physical Chemistry Chemical Physics* **2019**, *21* (42), 23283–23300. <https://doi.org/10.1039/C9CP03551F>.
- (129) Weng, B.; Qi, M.-Y.; Han, C.; Tang, Z.-R.; Xu, Y.-J. Photocorrosion Inhibition of Semiconductor-Based Photocatalysts: Basic Principle, Current Development, and Future Perspective. *ACS Catal.* **2019**, *9* (5), 4642–4687. <https://doi.org/10.1021/acscatal.9b00313>.
- (130) Banin, U.; Ben-Shahar, Y.; Vinokurov, K. Hybrid Semiconductor–Metal Nanoparticles: From Architecture to Function. *Chem. Mater.* **2014**, *26* (1), 97–110. <https://doi.org/10.1021/cm402131n>.
- (131) Yang, T.-T.; Chen, W.-T.; Hsu, Y.-J.; Wei, K.-H.; Lin, T.-Y.; Lin, T.-W. Interfacial Charge Carrier Dynamics in Core–Shell Au–CdS Nanocrystals. *J. Phys. Chem. C* **2010**, *114* (26), 11414–11420. <https://doi.org/10.1021/jp103294c>.
- (132) Yuan, L.; Geng, Z.; Xu, J.; Guo, F.; Han, C. Metal–Semiconductor Heterostructures for Photoredox Catalysis: Where Are We Now and Where Do We Go? *Advanced Functional Materials* **2021**, *31* (27), 2101103. <https://doi.org/10.1002/adfm.202101103>.
- (133) Habas, S. E.; Yang, P.; Mokari, T. Selective Growth of Metal and Binary Metal Tips on CdS Nanorods. *J. Am. Chem. Soc.* **2008**, *130* (11), 3294–3295. <https://doi.org/10.1021/ja800104w>.
- (134) Ji, B.; Giovanelli, E.; Habert, B.; Spinicelli, P.; Nasilowski, M.; Xu, X.; Lequeux, N.; Hugonin, J.-P.; Marquier, F.; Greffet, J.-J.; Dubertret, B. Non-Blinking Quantum Dot with a Plasmonic Nanoshell Resonator. *Nature Nanotech* **2015**, *10* (2), 170–175. <https://doi.org/10.1038/nnano.2014.298>.
- (135) Fernandez, M.; Urvoas, A.; Even-Hernandez, P.; Burel, A.; Mériadec, C.; Artzner, F.; Bouceba, T.; Minard, P.; Dujardin, E.; Marchi, V. Hybrid Gold Nanoparticle–Quantum Dot Self-Assembled Nanostructures Driven by Complementary Artificial Proteins. *Nanoscale* **2020**, *12* (7), 4612–4621. <https://doi.org/10.1039/C9NR09987E>.
- (136) Sun, D.; Tian, Y.; Zhang, Y.; Xu, Z.; Sfeir, M. Y.; Cotlet, M.; Gang, O. Light-Harvesting Nanoparticle Core–Shell Clusters with Controllable Optical Output. *ACS Nano* **2015**, *9* (6), 5657–5665. <https://doi.org/10.1021/nn507331z>.
- (137) Wu, K.; Chen, J.; McBride, J. R.; Lian, T. CHARGE TRANSFER. Efficient Hot-Electron Transfer by a Plasmon-Induced Interfacial Charge-Transfer Transition. *Science* **2015**, *349* (6248), 632–635. <https://doi.org/10.1126/science.aac5443>.
- (138) Wu, K.; Rodríguez-Córdoba, W. E.; Yang, Y.; Lian, T. Plasmon-Induced Hot Electron Transfer from the Au Tip to CdS Rod in CdS–Au Nanoheterostructures. *Nano Lett.* **2013**, *13* (11), 5255–5263. <https://doi.org/10.1021/nl402730m>.
- (139) O’Connor, T.; Panov, M. S.; Mereshchenko, A.; Tarnovsky, A. N.; Lorek, R.; Perera, D.; Diederich, G.; Lambright, S.; Moroz, P.; Zamkov, M. The Effect of the Charge-Separating Interface on Exciton Dynamics in Photocatalytic Colloidal Heteronanocrystals. *ACS Nano* **2012**, *6* (9), 8156–8165. <https://doi.org/10.1021/nn302810y>.
- (140) Chakraborty, R.; Greullet, F.; George, C.; Baranov, D.; Fabrizio, E. D.; Krahne, R. Broad Spectral Photocurrent Enhancement in Au-Decorated CdSe Nanowires. *Nanoscale* **2013**, *5* (12), 5334–5340. <https://doi.org/10.1039/C3NR00752A>.
- (141) Okuhata, T.; Kobayashi, Y.; Nonoguchi, Y.; Kawai, T.; Tamai, N. Ultrafast Carrier Transfer and Hot Carrier Dynamics in PbS–Au Hybrid Nanostructures. *J. Phys. Chem. C* **2015**, *119* (4), 2113–2120. <https://doi.org/10.1021/jp508406z>.

- (142) Okuhata, T.; Katayama, T.; Tamai, N. Ultrafast and Hot Electron Transfer in CdSe QD–Au Hybrid Nanostructures. *J. Phys. Chem. C* **2020**, *124* (1), 1099–1107. <https://doi.org/10.1021/acs.jpcc.9b09042>.
- (143) Dana, J.; Debnath, T.; Maity, P.; Ghosh, H. N. Enhanced Charge Separation in an Epitaxial Metal–Semiconductor Nanohybrid Material Anchored with an Organic Molecule. *J. Phys. Chem. C* **2015**, *119* (38), 22181–22189. <https://doi.org/10.1021/acs.jpcc.5b06055>.
- (144) Hou, W.; Cronin, S. B. A Review of Surface Plasmon Resonance-Enhanced Photocatalysis. *Advanced Functional Materials* **2013**, *23* (13), 1612–1619. <https://doi.org/10.1002/adfm.201202148>.
- (145) Nawrot, K. C.; Wawrzyńczyk, D.; Bezkrovnyi, O.; Kępiński, L.; Cichy, B.; Samoć, M.; Nyk, M. Functional CdS–Au Nanocomposite for Efficient Photocatalytic, Photosensitizing, and Two-Photon Applications. *Nanomaterials* **2020**, *10* (4), 715. <https://doi.org/10.3390/nano10040715>.
- (146) Dana, J.; Maity, P.; Ghosh, H. N. Hot-Electron Transfer from the Semiconductor Domain to the Metal Domain in CdSe@CdS{Au} Nano-Heterostructures. *Nanoscale* **2017**, *9* (27), 9723–9731. <https://doi.org/10.1039/C7NR02232H>.
- (147) Soni, U.; Tripathy, P.; Sapra, S. Photocatalysis from Fluorescence-Quenched CdSe/Au Nanoheterostructures: A Size-Dependent Study. *J. Phys. Chem. Lett.* **2014**, *5* (11), 1909–1916. <https://doi.org/10.1021/jz5006863>.
- (148) Chauhan, H.; Kumar, Y.; Dana, J.; Satpati, B.; Ghosh, H. N.; Deka, S. Photoinduced Ultrafast Charge Separation in Colloidal 2-Dimensional CdSe/CdS–Au Hybrid Nanoplatelets and Corresponding Application in Photocatalysis. *Nanoscale* **2016**, *8* (34), 15802–15812. <https://doi.org/10.1039/C6NR03610D>.
- (149) Han, S.; Hu, L.; Gao, N.; Al-Ghamdi, A. A.; Fang, X. Efficient Self-Assembly Synthesis of Uniform CdS Spherical Nanoparticles–Au Nanoparticles Hybrids with Enhanced Photoactivity. *Advanced Functional Materials* **2014**, *24* (24), 3725–3733. <https://doi.org/10.1002/adfm.201400012>.
- (150) Simon, T.; Carlson, M. T.; Stolarczyk, J. K.; Feldmann, J. Electron Transfer Rate vs Recombination Losses in Photocatalytic H<sub>2</sub> Generation on Pt-Decorated CdS Nanorods. *ACS Energy Lett.* **2016**, *1* (6), 1137–1142. <https://doi.org/10.1021/acsenergylett.6b00468>.



# CHAPTER II:

Quantum Dots mediated photoredox C-C bonds formation: oxidation of Aryl-amines leading to Tropane skeletons after two successive allylations

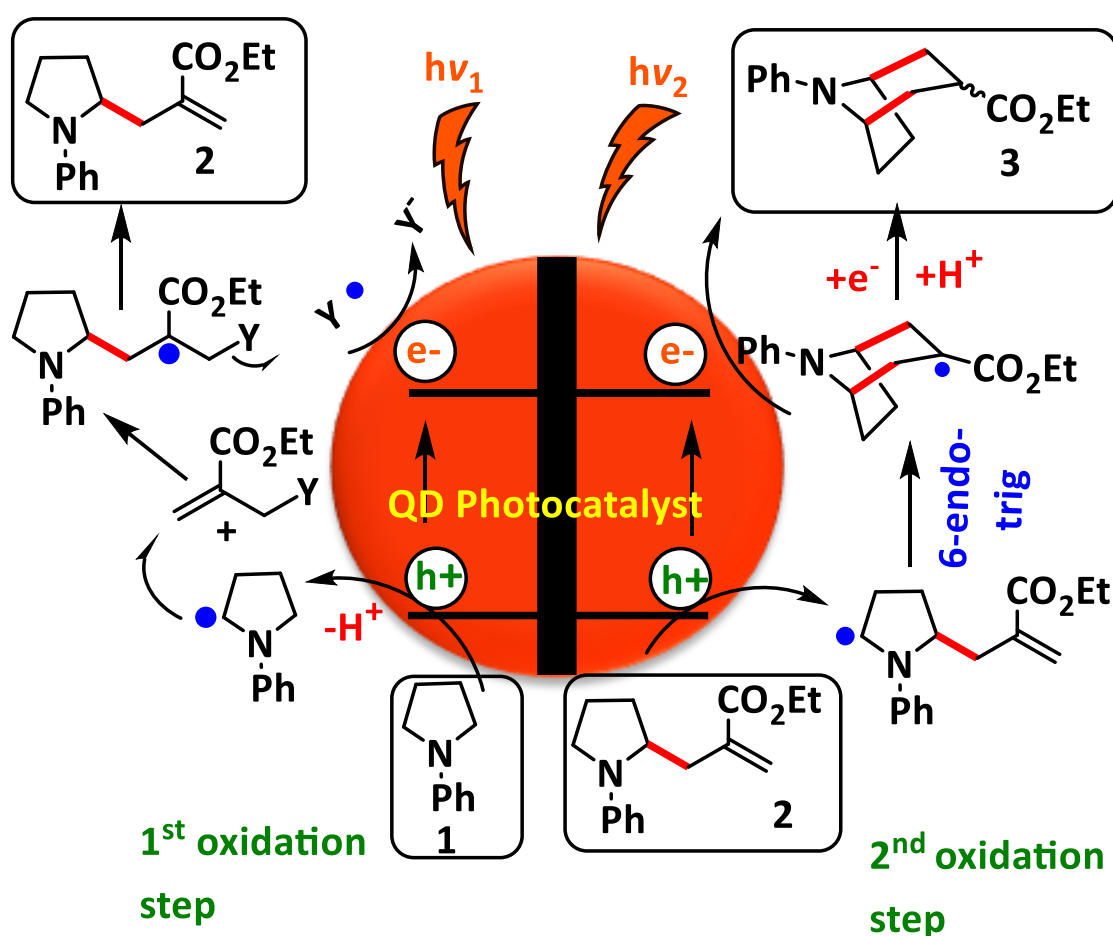
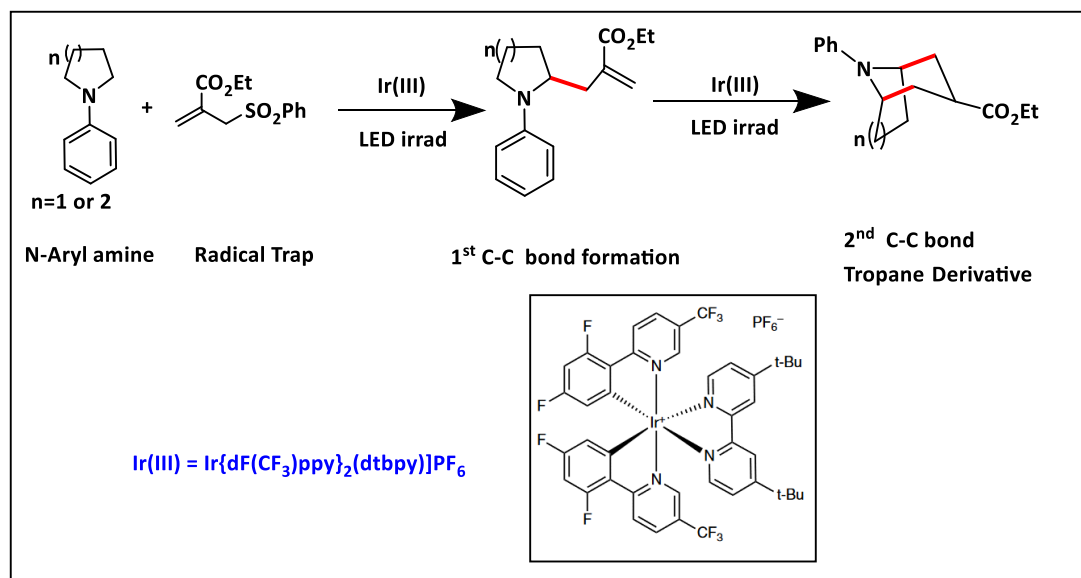


## Table of Content

CHAPTER II:.....	93
Quantum Dots mediated photoredox C-C bonds formation: oxidation of Aryl-amines leading to Tropane skeletons after two successive allylations.....	93
II-1. Introduction .....	95
II-2. Investigation of the suitable kinds of Quantum Dots for the desired oxidations: DFT calculations for the redox potential of 1-Phenylpyrrolidine (PhPyr).....	97
II-3. Synthesis and characterization of the Quantum Dots. ....	99
II.4. Charge transfer between the Quantum Dots and the reaction's substrate. ....	104
II-4.1. Photoluminescence Quenching of the Quantum Dots by 1-Phenyl-pyrrolidine (PhPyr). ....	104
II-4.1. Charge transfer from the photoexcited QDs, and the effect of the energy levels positions in the core-shell QDs. ....	107
II-4. Photocatalytic activity of the Quantum Dots.....	109
II-4.1. Screening the as-synthesized QDs for the C-C Vinylation reaction. ....	109
II-4.2. Test of selected as-synthesized QDs for the 2-step reaction of the synthesis of tropane derivative. ....	113
II-4.3. Surface ligands optimization: Case of CdS and CdSe QDs.....	114
II-4.4. Effect of the ligands optimization of the different QDs for the C-C vinylation reaction. ....	117
II-4.5. Effect of the ligands optimization of different QDs for the 2-step reaction of the synthesis of tropane derivatives. ....	122
II-5. Scope of radical traps.....	126
II-6. Reaction scope with different N- aryl amines.....	127
II-7: Purification and re-use of the QDs after the reactions.....	132
II-8. Optimization of the ligand layer: Effect on the stability and the reusability of the QDs. ....	132
II-9: Electrochemical analysis: Investigations of the mechanistic steps (reaction's stopping step) and impact of the para-substituents of the N-Arylamines. ....	135
II-10. Proposed catalytic mechanisms.....	140
II-10.1. Photocatalytic mechanism for the 1-step C-C vinylation coupling reaction. ....	140
II-10.2. Photocatalytic mechanism for the 2-step Tropane derivatives synthesis reaction. ....	142
II-10.3. Selectivity of the radical formation and the stability of the final product: pKa calculations.....	144
II-10.4. Photocatalytic activity of the different types of QDs: Insights into the mechanistic redox steps .....	146
Conclusion.....	148
References .....	149
Appendix Chapter II.....	153

## II-1. Introduction

This chapter presents the results corresponding to a publication that the writing of which is in progress. The synthesis of biologically active natural products is of great interest in the synthetic chemistry field.<sup>1</sup> In this context, Carbon-Carbon bond formation via photoinduced process turned out recently to be one of the efficient synthetic methodologies used for preparing this kind of natural products.<sup>2</sup> Tropane derivatives, which are nitrogenous bicyclic alkaloids found in plants, are attractive natural compounds for their broad biological activity and for their application as pharmaceutical products<sup>3</sup>. Recently, our collaborators from the group of Pr. Philippe Renaud (University of Bern-Switzerland), have demonstrated a new methodology for the preparation of tropane derivatives based on a one-pot two-step photoredox mediated [3+3] annulation process starting from N-Aryl amines using Ir{dF(CF<sub>3</sub>)ppy}<sub>2</sub>(dtbpy)]PF<sub>6</sub> [Ir(III)] transition metal photocatalysts<sup>4</sup> (see scheme II-1). Our group (CAMPE-CEA) collaborated in understanding the physical aspects of the different mechanistic steps of this work by the electrochemical studies and the DFT calculations.



*Scheme II-1: Photoredox catalyzed tropane derivatives synthesis starting from tertiary arylated amines<sup>4</sup>.*

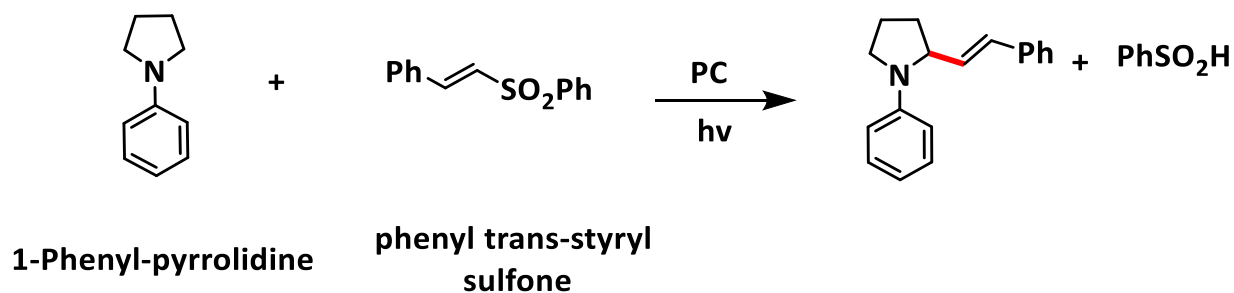
This developed annulation process relies on two oxidation steps starting from the activation of tertiary N-aryl amines, which act as radical precursors to react afterwards with allylic radical traps to produce a first C-C coupled intermediate product. Then, a second oxidation process takes place to produce a new  $\alpha$ -aminoalkyl radical, which undergoes an intramolecular 6-endo-cyclization to form a second C-C bond and finally produces a bicyclic skeleton of tropane derivatives (Scheme II-1).

In this chapter II, we describe our attempts to explore the ability of semiconductor Quantum Dots to photocatalyze the same reaction (scheme II-1) in similar conditions but using Quantum Dots instead of the Ir{dF(CF<sub>3</sub>)ppy}<sub>2</sub>(dtbpy)]PF<sub>6</sub> complex as a redox photocatalyst. We investigate the most convenient types of QDs for this kind of reaction. Therefore, we study the effect of both the structure and the type of the different Quantum Dots on their activity towards the photoredox reaction by comparing simple core-structured QDs to more elaborated core-shell QDs. Moreover, considering the catalytic mechanism, four different radicals are expected to be generated during the different redox steps of the reaction (see scheme at the front page of Chapter II). Then, the ability of the QDs to perform the desired oxidation or reduction process to close the reactions' cycles is also targeted and compared based on the activity of each type of QDs.

We prepared different types of cores (CdS, CdSe and InP) and core-shell Quantum Dots (inverted Type-I CdS-CdSe, quasi Type-II CdSe-CdS, Type-I CdSe-ZnS and InP-ZnS) to test their photocatalytic activity under visible light excitation. The selection of the CdSe-CdS quasi Type-II core-shell QDs is inspired from the reports by Peng and co-workers<sup>5,6</sup> showing the possibility of achieving very high turnovers when using this kind of QDs. We also study the activity of the inverted Type-I CdS-CdSe QDs which was proved to efficiently enhance the photocatalytic hydrogen production.<sup>7,8</sup> Moreover, to the best of our knowledge, CdS-CdSe inverted Type-I QDs were not reported previously for organic transformation reactions.

The photocatalytic activity of the selected QDs is tested, firstly towards the photo-oxidation of the model N-Aryl amine substrate (1-Phenyl-pyrrolidine) by checking the possible charge transfer from the QDs using DFT calculations to evaluate the substrates' redox potentials and by testing the photoluminescence quenching of the QDs. Then, we employ the Quantum Dots in the carbon-carbon vinylation coupling reaction between 1-Phenyl-pyrrolidine (PhPyr) and phenyl trans-styryl sulfone (Scheme II-2) reported by MacMillan using

the Ir[dF(CF<sub>3</sub>)ppy]<sub>2</sub>(dtbbpy)PF<sub>6</sub> complex (Ir(III) catalyst)<sup>9</sup>. The idea behind testing the activity of the prepared QDs for this reaction is that it is expected to proceed in a similar catalytic process as for the first cycle of our new two-step reaction. In addition, this vinylation reaction was proved to be efficiently catalyzed using Quantum Dots as Emily A. Weiss and co-workers showed using 3.7 nm-sized CdS QDs<sup>10</sup>, and more recently P. Pillai and co-workers using InP-ZnS QDs<sup>11</sup> (See Chapter I, section I-3, page 56).



*Scheme II-2: Carbon-Carbon vinylation coupling reaction between 1-Phenyl-pyrrolidine (PhPyr) and phenyl trans-styryl sulfone. PC being the photocatalyst.*

The best behaving QDs are selected for the two-step reaction developed to provide bicyclic Tropane derivatives. Finally, after engineering the surface ligand layer of the QDs to ensure an enhanced accessibility to the redox active QDs' surface, we demonstrate the ability of the QDs to accomplish the two catalytic cycles in the same reaction pot.

## II-2. Investigation of the suitable kinds of Quantum Dots for the desired oxidations: DFT calculations for the redox potential of 1-Phenylpyrrolidine (PhPyr).

In order to select the convenient Quantum Dots for the photocatalytic reactions, theoretical studies were performed in the first stage before the photocatalysis tests. As the first step in the desired reaction is the oxidation of the N-aryl amine, the possible charge transfer between the Quantum Dots and 1-Phenyl-pyrrolidine (model substrate in the targeted reaction) was checked by calculating the redox potential of this latter compound towards the one-electron oxidation and then comparing it with the expected position of the valence band edge of each kind of Quantum Dots. The Quantum Dots selected are based on CdS, and CdSe cores as these kinds of QDs are the most used in photocatalysis for organic transformations, in addition to InP based QDs, which were reported recently to exhibit good photocatalytic activities.

Then, to estimate the redox potential of the N-aryl amines in our experimental conditions, DFT calculations were performed by **Dr. Jean-Marie MOUESCA** (Co-director of this Thesis), using the ADF (Amsterdam Density Functional) code developed by E. J. Baerends and co-workers<sup>12</sup>. The redox potential for the one-electron oxidation of PhPyr was calculated to be  $E^\circ = 0.57$  V/SCE (0.81 V/NHE) in acetonitrile (MeCN) as a solvent or  $E^\circ = 0.64$  V/SCE (0.88 V/NHE) in trifluorotoluene (TFT)<sup>1</sup>. The calculated redox potential was compared to the position of the valence band edges of the bulk semiconductor counterparts of the Quantum Dots, and also to the valence band edges of the QDs structures relying on the values reported in the literature. The values are collected in Table II-1.

The position of the valence band corresponding to the bulk semiconductor was reported to vary with the pH of their medium. For example, for the CdS bulk semiconductor, the valence band at pH=1 is close to 1.86 V/SCE,<sup>13</sup> ; however, at pH= 7, it could reach 1.36 V/SCE<sup>14,15</sup>. In addition, when preparing the semiconductors in the Quantum Dots structure, the valence and conduction band positions vary according to the QDs' size<sup>16-18</sup>. The experimental estimation reported for the valence band edge of CdS QDs can be in the range between 1.24 V/SCE<sup>19</sup> to 1.66 V/SCE<sup>10</sup> (See Table II-1). Similar variation of the reported potentials of the band edges also applied for CdSe semiconductors, where the valence band of the corresponding bulk varies between 1.36 V/SCE at pH=1<sup>13</sup> to 1.06 V/SCE at pH =7<sup>14,18</sup>. Moreover, for CdSe Quantum Dots the reported valence band edge potential can be found between 0.66 and 1.2 V/SCE depending on the measurement techniques, the variation of their size and their surface ligands (See chapter I, section I-2, page 30).<sup>16</sup>

Considering InP bulk semiconductor the position of the valence band was reported only at pH=1 to be equal to 1.06 V/ SCE<sup>13,20</sup> .The two reported values for the valence band edge position of InP based QDs are 1.09 and 1.75 V / SCE<sup>11,21</sup>.

---

<sup>1</sup>Trifluorotoluene (TFT) is a well-used solvent in industries and was selected as a less volatile alternative to dichloromethane

SC	VB (V/ SCE) For bulk pH=1	VB (V/ SCE) For bulk pH=7	VB (V/ SCE) For QDs	E° of PhPyr V/ SCE (MeCN)	Driving Force $\Delta E = VB - E^\circ$ (V)
CdS	1.86	1.36	1.2 ↔ 1.66	0.57	>0.6
CdSe	1.36	1.06	0.66 ↔ 1.2	0.57	>0.1
InP	1.06	-	1.09 ↔ 1.75	0.57	>0.4

**Table II-1: Comparison between Valence band positions and the redox potential of PhPyr calculated by DFT.** SC for semiconductor, VB for valence band, E° for oxidation potential, and SCE for potential versus standard calomel electrode.

As presented in Table II-1, the valence band edges of CdS, CdSe, and InP semiconductor bulk<sup>20,22</sup> or Quantum Dots are high enough compared with the potential of PhPyr, this indicates that it is possible to have a good driving force for the exchange of one electron between these Quantum Dots and the PhPyr, and therefore the possibility of an oxidation process to take place. Thus, different types and structures of Quantum Dots based on CdS, CdSe and InP QDs are synthesized and tested in the photocatalytic reactions.

### II-3. Synthesis and characterization of the Quantum Dots.

For the photocatalysis tests, a series of Quantum Dots are synthesized, such as CdS and CdSe core QDs, CdS-CdSe, CdSe-CdS, and CdSe-ZnS core-shell, in addition to InP core and InP-ZnS core-shell Quantum Dots.

The semiconductor QDs were synthesized using hot-injection methods following literature procedures with certain modifications for each type of QDs, and then characterized by UV-Visible spectroscopy, Fluorescence spectroscopy and TEM microscopy. The exciton position of the QDs was targeted to fit with the wavelength of our LED irradiation setups ( $\lambda=455$  nm for blue light irradiation,  $\lambda=528$  nm for green light irradiation and  $\lambda=590$  nm for yellow irradiation). The detailed procedures for the synthesis are described in the materials and methods part in Chapter IV, section IV-1, page 240.

CdS core QDs were synthesized by preparing a cadmium precursor of cadmium oleate and a sulfur precursor of elemental sulfur in octadecene<sup>23</sup>. The growth of the CdS QDs was monitored based on their optical properties using UV-Vis spectroscopy, and then stopped after reaching the targeted exciton position at  $\lambda=460$  nm and an emission wavelength at 470

nm (Figure II-1-A and D). Based on the exciton position of the QDs, the diameter ( $D$ ) and extinction coefficient ( $\epsilon$ ) can be determined according to formulas reported by X. Peng and co-workers<sup>24</sup> (Detailed in the materials and methods part in chapter IV) to be  $D = 5.7$  nm. The average diameter was confirmed from the TEM images to be  $5.5 \pm 0.9$  nm (Figure II-2-A). At the exciton position the extinction coefficient was calculated to be  $\epsilon = 1.2 \times 10^6 \text{ M}^{-1} \cdot \text{cm}^{-1}$ .

CdSe core QDs were synthesized starting with cadmium oleate and then injecting a selenium suspension prepared in octadecene<sup>25</sup>. The growth of the QDs was kept until reaching the desired exciton position at wavelength  $\lambda = 540$  nm. The corresponding emission wavelength was obtained at  $\lambda = 560$  nm (Figure II-1 B and E). Considering the position of the exciton of the CdSe QDs, the extinction coefficient was calculated to be  $\epsilon = 1.8 \times 10^5 \text{ M}^{-1} \cdot \text{cm}^{-1}$  by using the formula reported by Jasieniak et al.<sup>26</sup>, and the diameter of the CdSe QDs was calculated to be equal 3.0 nm. The average physical size observed by the TEM images was  $3.1 \pm 0.25$  nm (figure II-2-C).

The core-shell CdS-CdSe QDs were synthesized starting from a previously prepared sample of core CdS QDs (core diameter = 5.7 nm) and then cadmium and selenium precursors were injected in oleylamine<sup>8</sup>. The growth of the CdSe shell was targeted for two monolayers and red-shifted the position of the exciton to  $\lambda = 530$  nm and the emission wavelength to  $\lambda = 550$  nm (Figure II-1-A and D). In this case, the extinction coefficient for CdS-CdSe QDs at  $\lambda_{\text{exciton}} = 530$  nm was calculated to be  $\epsilon = 1.7 \times 10^5 \text{ M}^{-1} \cdot \text{cm}^{-1}$  using the formula reported by Jasieniak et al.<sup>26</sup> by considering that the CdSe shell is the most absorbing at this wavelength (530 nm). The total size of core-shell CdS-CdSe QDs in this case was calculated to be 6.4 nm starting from 5.7 nm CdS core in addition to two CdSe layer each of 0.35 nm. The TEM images (Figure II-2-B) indicate an average diameter for the CdS-CdSe QDs of  $6.35 \pm 0.6$  nm.

CdSe-CdS core-shell QDs functionalized with oleylamine ligands were synthesized using a method reported by Niu. et al<sup>27</sup>. The growth of the 3 monolayers for the CdS shell red-shifted the position of the exciton to  $\lambda = 573$  nm and the emission wavelength to  $\lambda = 590$  nm (Figure II-1-B and E). The extinction coefficient at  $\lambda = 573$  nm was calculated to be  $\epsilon = 2.4 \times 10^5 \text{ M}^{-1} \cdot \text{cm}^{-1}$  according to Jasieniak et al.<sup>26</sup>. The diameter of the core-shell CdSe-CdS QDs was determined to be  $5.14 \pm 0.4$  nm using the TEM images (Figure II-2-D).

CdSe-ZnS core-shell QDs were commercially purchased from the NN-Labs (NN-Labs CdSe/ZnS CZ600-25). The optical characterization of the CdS-ZnS QDs showed the position of the first exciton to be at  $\lambda=600$  nm and the emission wavelength to  $\lambda=620$  nm (Figure II-1-B and E). Using again the formulas reported by Jasieniak et al.<sup>26</sup>, the extinction coefficient of CdSe-ZnS QDs was calculated to be  $3.6 \times 10^5 \text{ M}^{-1} \cdot \text{cm}^{-1}$ , and a total core-shell size of  $10 \pm 1$  nm was estimated from the TEM images (Figure II-2-E).

InP core QDs and InP-ZnS core-shell QDs were prepared starting from indium halide and aminophosphine precursors in oleylamine as described by Tessier et al.<sup>28</sup>. Similar to the previous cases of QDs synthesis, the optical properties were followed using UV-Vis absorbance spectroscopy. The synthesis of the InP core QDs was stopped after reaching an exciton position at  $\lambda=450$  nm (Figure II-1-C). The core QDs of InP are not fluorescing (this is in agreement to what was mention in the initial publication) so no photoluminescence spectrum was recorded for this type of QDs. Based on the position of the exciton and following the formulas reported by Reiss et.al<sup>20</sup> the size of the InP QDs calculated to be  $D=2.8$  nm and the extinction coefficient  $\epsilon= 1.2 \times 10^5 \text{ M}^{-1} \cdot \text{cm}^{-1}$ .

The growth of the ZnS shell on the InP core has induced a slight red-shift in the position of the exciton toward  $\lambda=470$  nm (Figure II-1-C). The core-shell InP-ZnS QDs appeared to be highly fluorescing, proving the shell successful growth of the ZnS Shell. The photoluminescence spectrum with emission wavelength at  $\lambda=520$  nm was recorded in this case (Figure II-1-F). The extinction coefficient was calculated to be  $\epsilon= 1.3 \times 10^5 \text{ M}^{-1} \cdot \text{cm}^{-1}$ . Considering the exciton position at 470 nm, the average diameter of the InP-ZnS QDs was estimated from the TEM image (Figure II-2-F) to be  $2.9 \pm 0.5$  nm. Moreover, commercially available oleate capped InP-ZnS core shell were purchased from NN-Labs (NN-Labs HEINP530-10). The idea behind testing oleate capped InP-ZnS QDs is to be able to compare them with the oleate capped Cd-based QDs. The optical properties of the commercial QDs are presented in figure II-1-C and F. The exciton position of the oleate InP-ZnS QDs is at  $\lambda=530$  nm (Figure II-1-C blue line) nm and their emission peak is  $\lambda=550$  nm (Figure II-1-F red line).

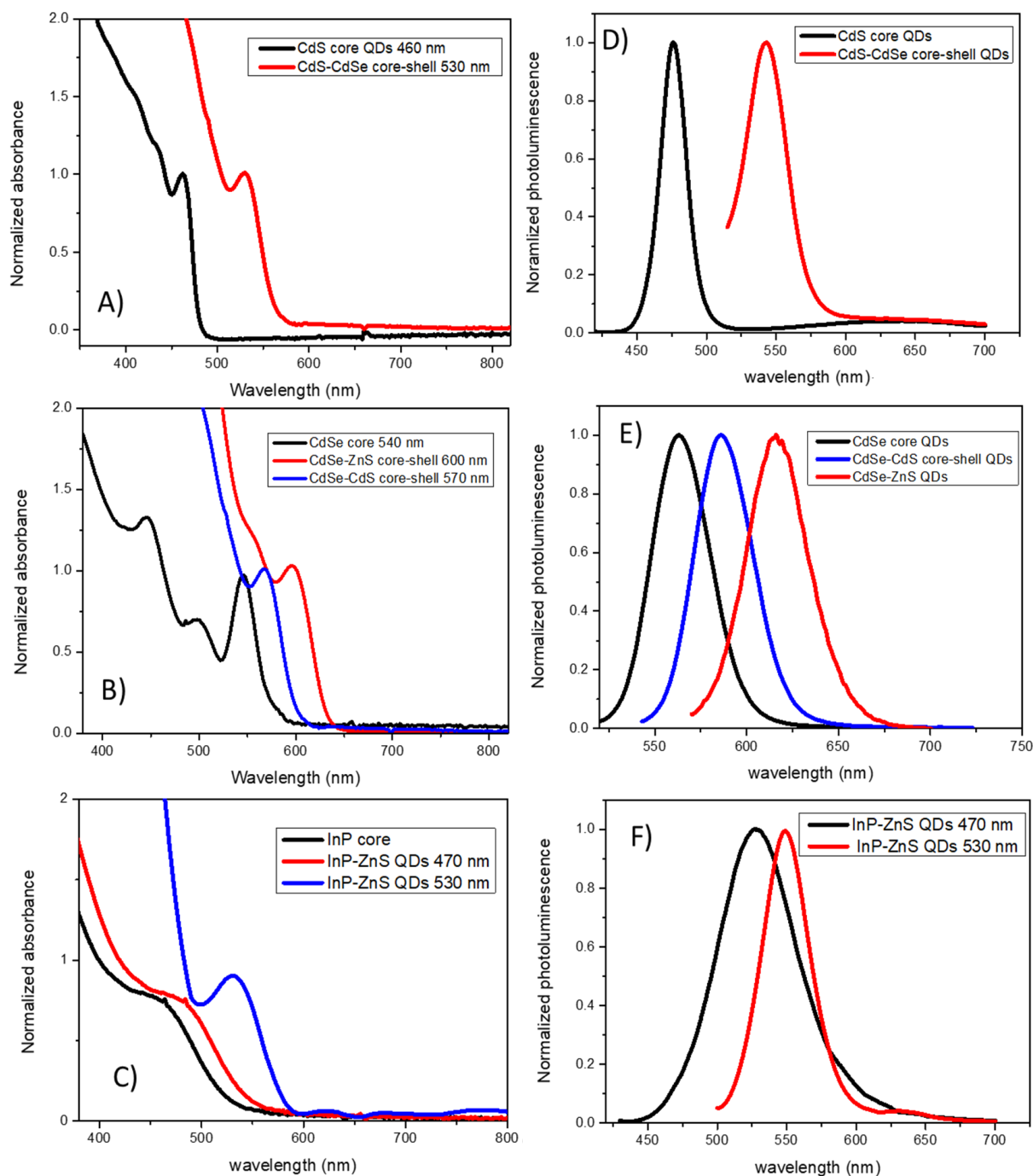


**Figure II-1: Optical properties of the Quantum Dots:** A -UV-Vis absorbance spectra of CdS core and CdS-CdSe core-shell QDs in toluene; B -UV-Vis absorbance spectra of CdSe core, CdSe-CdS and CdSe-ZnS core shell QDs in toluene; C -UV-Vis absorbance spectra of InP core and InP-ZnS core shell QDs in toluene. D - Photoluminescence spectra of CdS core (excited at 400 nm) and CdS-CdSe core shell QDs (excited at 470 nm) in toluene; E-Photoluminescence spectra of CdSe core (excited at 470 nm), CdSe-CdS (excited at 500 nm) and CdSe-ZnS core shell QDs (excited at 550 nm) in toluene; F-Photoluminescence spectra of InP-ZnS core shell QDs in toluene (excited at 400 nm).

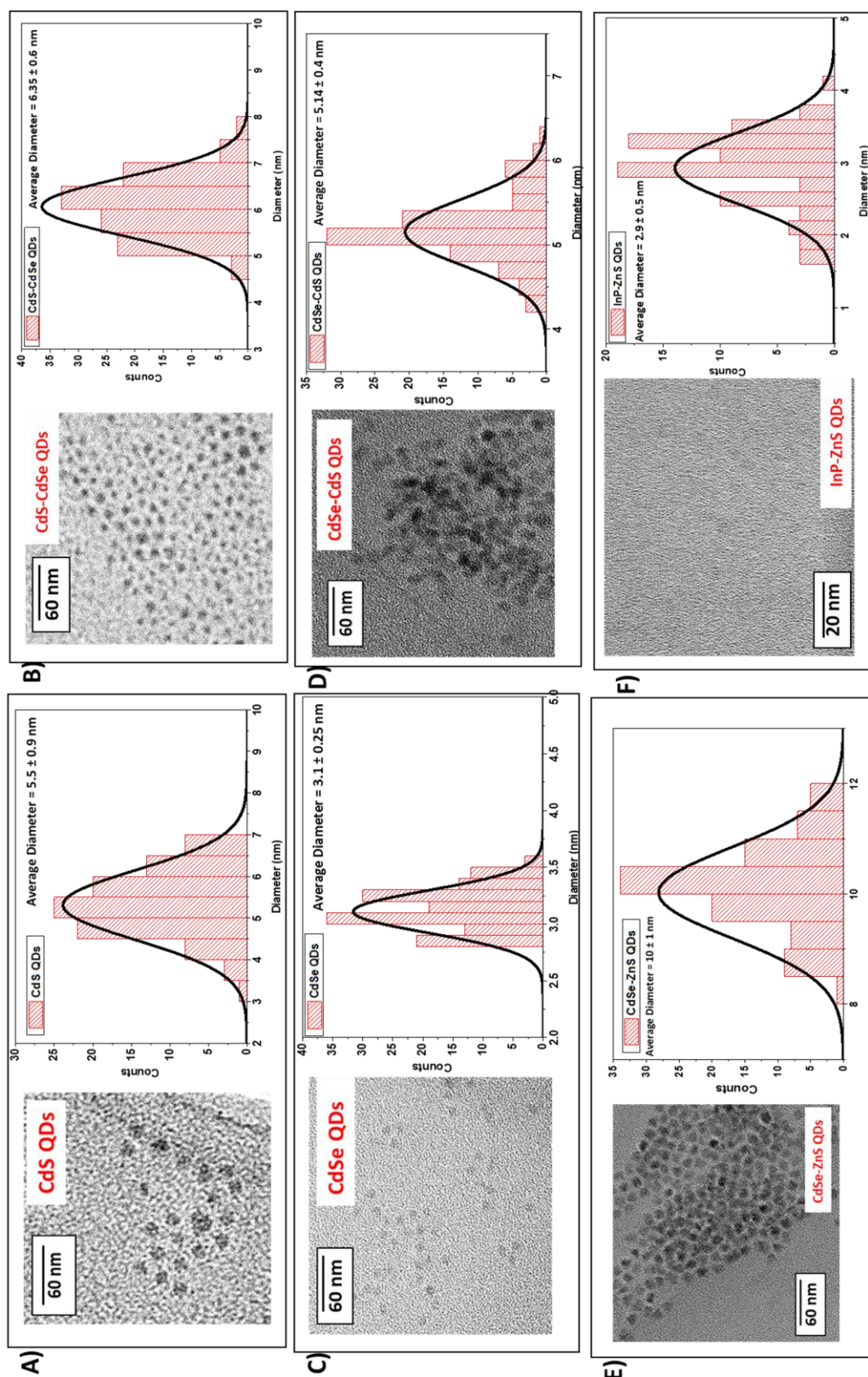


**Figure II-2: Microscopic characterization of the QDs:** A) TEM image of oleate capped CdS core QDs (average diameter =  $5.5 \pm 0.9$  nm); B) TEM image of CdS-CdSe core-shell QDs (average diameter =  $6.35 \pm 0.6$  nm); C) TEM image of oleate-capped CdSe core QDs (average diameter =  $3.1 \pm 0.25$  nm); D) TEM image of CdSe-CdS core-shell QDs (average diameter =  $5.14 \pm 0.4$  nm); E) TEM image of CdS-ZnS core-shell QDs (average diameter =  $10 \pm 1$  nm); F) TEM image of InP-ZnS core-shell QDs (average diameter =  $2.9 \pm 0.5$  nm).

## II.4. Charge transfer between the Quantum Dots and the reaction's substrate.

### II-4.1. Photoluminescence Quenching of the Quantum Dots by 1-Phenylpyrrolidine (PhPyr).

The possible charge transfer between the Quantum Dots and 1-Phenylpyrrolidine was experimentally tested by monitoring the photoluminescence quenching of each type of Quantum Dots. All the tested Quantum Dots have shown a quenched photoluminescence after adding 5mM of PhPyr in trifluorotoluene as a solvent. However, the different types of Quantum Dots exhibited different quenching efficiencies as quantified by the Stern–Volmer plot and quenching constant.

Figure II-3 shows a typical example of the monitored photoluminescence quenching of CdS QDs with the corresponding Stern-Volmer plot. In the case of CdS core QDs, the Stern–Volmer plot (Figure II-3-B) is approximately linear with a Stern-Volmer constant  $k_{S,V} = 320 \text{ L}\cdot\text{mol}^{-1}$ . The bimolecular quenching constant ( $k_q$ ) is estimated from the relation  $k_{S,V} = k_q \times \tau_{\text{QDs}}$  ( $\tau_{\text{QDs}}$  is the excited state lifetime of the QDs) to be  $k_q = 1.6 \times 10^{10} \text{ L}\cdot\text{mol}^{-1}\cdot\text{s}^{-1}$  by considering an approximated photoluminescence lifetime for the QDs of  $20 \text{ ns}^{29-31}$ . The diffusion rate constant ( $k_d$ ) is obtained using the equation of Schmoluchowski<sup>32</sup> to be  $3.16 \times 10^{10} \text{ L}\cdot\text{mol}^{-1}\cdot\text{s}^{-1}$  (see Table II-2 entry 1). The linear shape of the Stern–Volmer plot and the fact that  $k_q$  is close to the diffusion limit ( $k_d$ ) indicates that the model of dynamic quenching applies in this case. Thus a strong dynamic quenching is deduced in the case of CdS QDs and it is probable that an efficient electron transfer from PhPyr to the CdS QDs takes place.

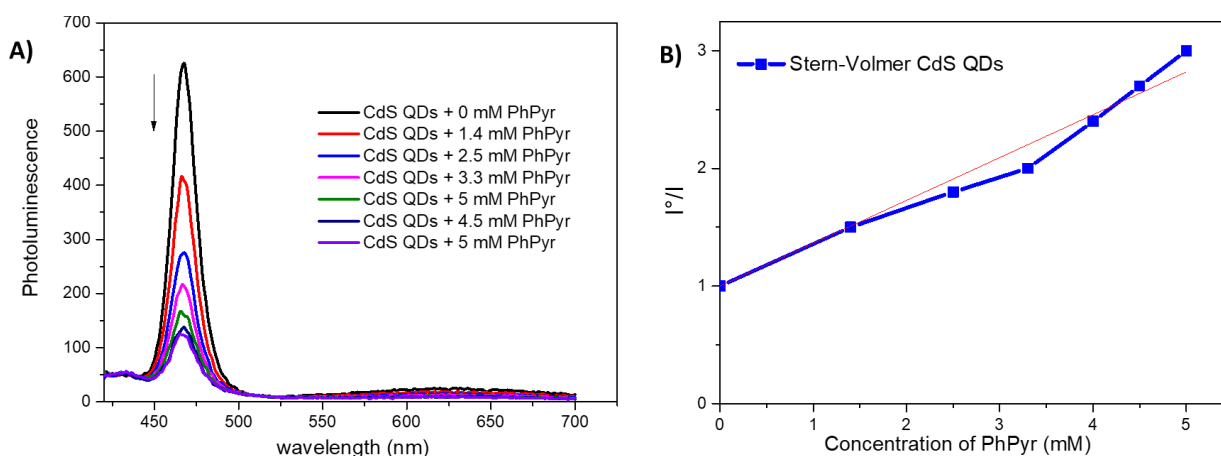


**Figure II-3: Photoluminescence quenching of CdS QDs in presence of PhPyr:** A) photoluminescence spectra of  $0.5 \mu\text{M}$  of CdS QDs excited at  $400 \text{ nm}$  upon successive addition of  $5 \text{ mM}$  of PhPyr in trifluorotoluene. B) Stern-Volmer plot of  $I_0/I$  as function of the concentration of PhPyr.

Similarly, in the case of CdSe core QDs, the Stern–Volmer plot is linear with a constant  $K_{S,V} = 205 \text{ L}\cdot\text{mol}^{-1}$  and bimolecular quenching constant  $k_q = 1.02 \times 10^{10} \text{ L}\cdot\text{mol}^{-1}\cdot\text{s}^{-1}$  (see Table II-2 entry 3 and Figure II-4 red curve). The linear Stern–Volmer plot and the value of  $k_q$  refer to a strong dynamic quenching of the CdSe QDs photoluminescence.

The behavior of core-shell QDs was also tested using the inverted Type-I CdS-CdSe, quasi Type II CdSe-CdS and Type-I CdSe-ZnS core shell. A dynamic quenching is obtained in the case of CdS-CdSe QDs with a Stern-Volmer constant  $K_{S,V} = 210 \text{ L}\cdot\text{mol}^{-1}$  and a quenching constant  $k_q = 1.05 \times 10^{10} \text{ L}\cdot\text{mol}^{-1}\cdot\text{s}^{-1}$ , however using CdSe-CdS QDs, lower values of the Stern-Volmer constant ( $K_{S,V} = 97 \text{ L}\cdot\text{mol}^{-1}$ ) and of the quenching constant ( $k_q = 4.8 \times 10^9 \text{ L}\cdot\text{mol}^{-1}\cdot\text{s}^{-1}$ ) are obtained compared to those in the case of CdS-CdSe QDs, but still indicating the presence of a dynamic quenching (Table II-2 entries 2 and 4, Figure II-4 blue and pink curves).

The quenching with the CdSe-ZnS QDs is the less efficient among the tested QDs with a Stern-Volmer constant  $K_{S,V} = 50 \text{ L}\cdot\text{mol}^{-1}$  and a quenching constant  $k_q = 2.5 \times 10^9 \text{ L}\cdot\text{mol}^{-1}\cdot\text{s}^{-1}$  (see Table II-2 entry 5, Figure II-4-green curve). These results indicate the possibility of charge transfer to PhPyr using these QDs but with an expected low efficiency in the photocatalytic process compared to CdS, CdSe and CdS- CdSe QDs.

Moreover, the photoluminescence quenching of the two types InP-ZnS QDs with either oleylamine or oleic acid ligands show similar quenching properties with PhPyr as quencher. In the case of the amine capped InP-ZnS QDs, the Stern-Volmer constant is calculated to be  $K_{S,V} = 109 \text{ L}\cdot\text{mol}^{-1}$ , which leads to a bimolecular quenching constant  $k_q = 5.4 \times 10^{10} \text{ L}\cdot\text{mol}^{-1}\cdot\text{s}^{-1}$  (see Table II-2 entry 6 and Figure II-4 light blue curve). In the case of the oleate capped InP-ZnS QDs, the Stern-Volmer constant in this case is calculated to be  $K_{S,V} = 130 \text{ L}\cdot\text{mol}^{-1}$  which leads to a bimolecular quenching constant  $k_q = 6.5 \times 10^{10} \text{ L}\cdot\text{mol}^{-1}\cdot\text{s}^{-1}$  (see Table II-2 entry 6 and Figure II-4 orange curve). This means that both kinds of InP-ZnS QDs are possibly able to do a charge transfer with Phenylpyrrolidine (The corresponding photoluminescence spectra are collected in Figure II-A1 of the Appendix II, page 153).

The variation in the photoluminescence quenching in the cases of the mentioned types of QDs could be attributed to the difference in the accessibility to the charges localized within the QDs. Then it is important to know the difference in the delocalization of the charge carriers

within the structure of the QDs based on the way of the alignment of the energy levels. This is discussed below.

Entry	QDs	Type	Stern-Volmer constant $k_{s,v}$ (L.mol <sup>-1</sup> )	Bimolecular quenching constant $k_q$ (L.mol <sup>-1</sup> .s <sup>-1</sup> )	Diffusion rate constant $k_d$ (L.mol <sup>-1</sup> .s <sup>-1</sup> )	Photoluminescence Quenching
1	CdS	Core	320	1.6 x10 <sup>10</sup>	3.167 x10 <sup>10</sup>	Strong dynamic
2	CdS-CdSe	Inverted Type I core-shell	210	1.05 x10 <sup>10</sup>	3.238 x10 <sup>10</sup>	Strong dynamic
3	CdSe	Core	205	1.025 x10 <sup>10</sup>	2.056 x10 <sup>10</sup>	Strong dynamic
4	CdSe-CdS	Quasi Type II core-shell	97	4.8 x10 <sup>9</sup>	2.837x10 <sup>10</sup>	Efficient dynamic
5	CdSe-ZnS	Type I core-shell	50	2.5 x10 <sup>9</sup>	4.863x10 <sup>10</sup>	Weak dynamic
6	InP-ZnS (amine ligands)	Type I core-shell	109	5.4 x10 <sup>9</sup>	2.012x10 <sup>10</sup>	Efficient dynamic
7	InP-ZnS (oleate ligands)	Type I core-shell	130	6.5 x10 <sup>9</sup>	2.103x10 <sup>10</sup>	Efficient dynamic

**Table II-2: Stern–Volmer analysis of the QDs photoluminescence in the presence of 5mM of PhPyr:** the Stern–Volmer constant obtained by linear fitting of the plot with  $I^0/I = 1 + k[\text{quencher}]$ . The bimolecular quenching constant was calculated by taking into account the reported life time of the photoluminescence of the QDs (~20 ns) and the diffusion rate constant was calculated using the equation of Schmoluchowski. The dynamic quenching model was confirmed by comparing  $k_q$  to  $k_d$ , if  $k_q < k_d$  this indicates the validity of the dynamic quenching model.

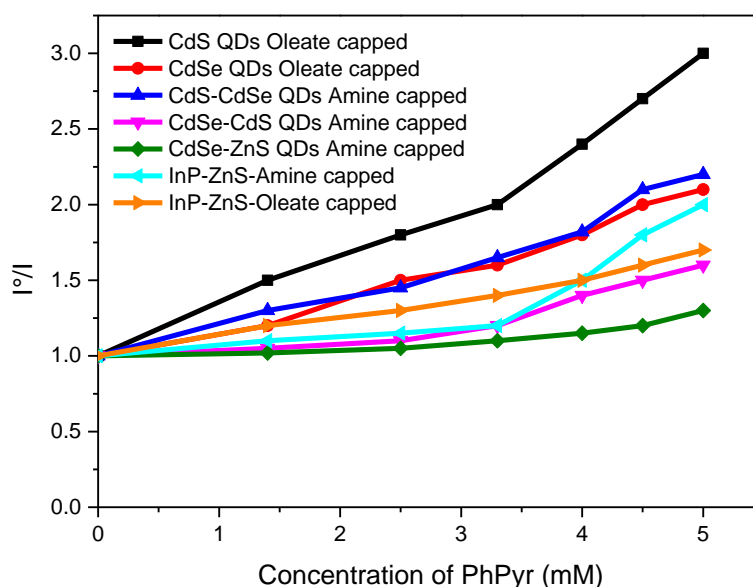


**Figure II-4: Stern-Volmer plots for the photoluminescence quenching of the QDs after adding 5mM of Phenylpyrrolidine in trifluorotoluene.** Black line for 0.5 $\mu$ M of CdS QDs, red line for 1 $\mu$ M CdSe QDs, blue line 0.5 $\mu$ M CdS-CdSe; pink line 0.5 $\mu$ M CdSe-CdS QDs, green line 0.5 $\mu$ M CdSe-ZnS QDs and light blue and orange for 0.1 $\mu$ M of the InP-ZnS QDs. The corresponding spectra are collected in Figure A1 in the appendix of chapter II page 153.

#### II-4.1. Charge transfer from the photoexcited QDs, and the effect of the energy levels positions in the core-shell QDs.

The efficiency of the charge transfer between the QDs and the reaction substrate (electron donor or acceptor) primarily depends on the accessibility to the charge carriers delocalized in the QDs. In the case of core QDs, the main limitation for the charge transfer is the suitable position of the valence band edge for the hole (h<sup>+</sup>) transfer and the position of the conduction band edge for the electron (e<sup>-</sup>) transfer.

However, in the case of core-shell structured QDs, the distribution of the charges depends on the alignment of the energy bands edge of the core and the shell. According to this alignment in the core-shell QDs, they are classified into four main types: Type-I, inverted Type-I, Type-II (or quasi Type-II), and inverted Type-II<sup>33,34</sup>.

In Type-I QDs, the band gap of the core is smaller than that of the shell, and the position of the energy bands of the band gap of the core falls within that of the shell (See Figure II-5). This makes the generated charge carriers completely localized in the core of the Type-I QDs and consequently induces difficult accessibility during the charge transfer process.

This clear from the photoluminescence quenching of Type-I CdS-ZnS QDs with the weakest quenching among the cases we reported here.

Interestingly, in the inverted Type-I QDs<sup>8,35,36</sup>, the band gap of the core is larger than that of the shell, and the energy bands edges of the shell are aligned within that of the core (See Figure II-5). In such a case, the generated charges will be delocalized in the outer shell of the QDs, which is expected to enhance the interaction with the substrate. This is the case of the CdS-CdSe QDs, which showed a better photoluminescence quenching than the case of the QDs with Type-I structure and also with very comparable results with that of the only-core CdSe QDs.

In the case of Type-II core-shell QDs (or quasi Type-II<sup>35</sup>), the Valence band edge of the core is aligned within the band gap of the shell, and the conduction band edge of the shell falls within the band gap of the core. Consequently, the hole will be maintained in the core of the QDs and then it will be less accessible, while the electron will be delocalized between the core and the shell. CdSe-CdS core shell QDs were tested as an example of this Type-II QDs and their photoluminescence quenching properties were less important than the other cases where the hole accessibility was easier (core QDs and inverted Type-I QDs).

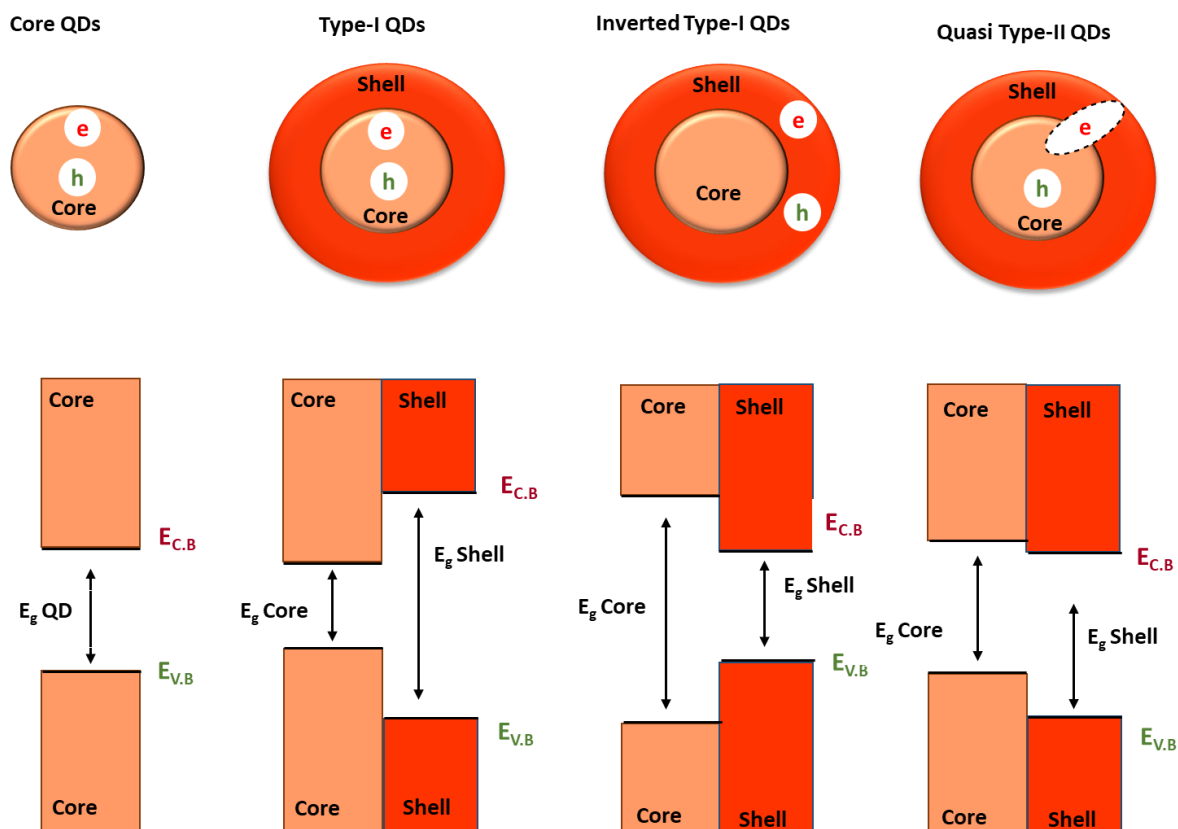


**Figure II-5:** The types of core-shell QDs based on conduction and valence bands alignment; where  $h$  is for hole,  $e$  is for electron,  $E_{C,B}$  is the energy of the conduction Band,  $E_{V,B}$  is the energy of the Valence Band and  $E_g$  is the band gap energy. Adapted from Chapter I.

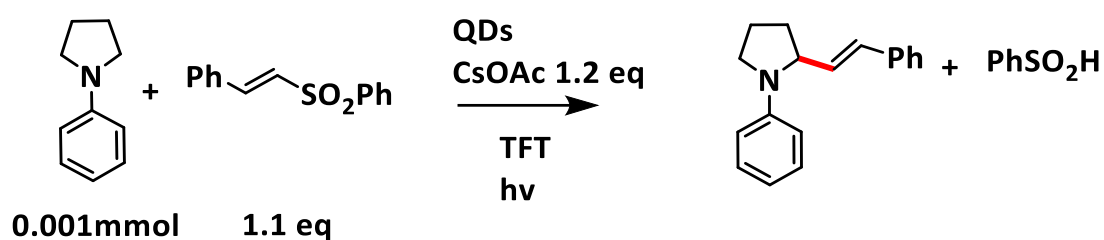
## II-4. Photocatalytic activity of the Quantum Dots.

### II-4.1. Screening the as-synthesized QDs for the C-C Vinylation reaction.

In order to study the photocatalytic activity of the selected Quantum Dots, we started our investigation by employing the prepared Quantum Dots in the one-step reaction of the C-C coupling  $\alpha$ -vinylation reaction reported by MacMillan using an Ir(III)-based complex<sup>9</sup>, then by Weiss using CdS QDs<sup>10</sup> and Pillai using InP-ZnS QDs<sup>11</sup>.

All the reactions were performed in a Nitrogen filled glovebox. In typical reaction conditions, the total volume was fixed to 1 ml of trifluorotoluene as a reaction solvent (Solvent optimization is summarized in the Table II-A1 in the Appendix page 156 of this Chapter), and PhPyr as a reaction substrate of 1mM (0.001 mmol) was reacted with 1.1 equiv. of the phenyl trans-styryl sulfone, in the presence of 1.2 equiv. of cesium acetate as a base. The concentration of the Quantum Dots in each reaction was decided based on their extinction coefficient and targeting an absorbance close to 1 (See Table II-3). The reaction evolution and the product formation were analyzed using UHPLC-MS analysis, and the reaction yield was

determined by integrating the area of UHPLC-MS peaks and comparing them to the peak of the corresponding standard of the reaction product (Representative chromatograms and MS spectra are presented in Figure II-A3 (page 158) and A4 (page 159) in the Appendix II of this Chapter).



Entry	QDs	Surface Ligands	cat.load % (Abs.)	Irradiation wavelength and Power	Irradiation Time for the max. Yield	Yield %	TON
1	CdS	OIAc	0.1% (A=1.1)	455 nm 10 mW	4 hours	49%	490
2	CdS-CdSe	OIAm	0.5% (A=0.9)	528 nm 50 mW	4 hours	48%	96
3	CdSe	OIAc	0.5% (A=0.9)	528 nm 50 mW	4 hours	51%	102
4	CdSe-CdS	OIAm	0.5% (A=1.2)	528 nm 50 mW	6 hours	30%	100
5	CdSe-ZnS	ODAm	0.3% (A=1.1)	590 nm 20 mW	22 hours	10%	33
6	InP	OIAm	0.7% (A=0.9)	455 nm 10 mW	6 hours	40%	57
7	InP-ZnS	OIAm	0.7% (A=0.9)	455 nm 10 mW	6 hours	42%	60
8	InP-ZnS	OIAc	0.7% (A=1)	528 nm 50 mW	6 hours	43%	61

**Table II-3: C-C Vinylation coupling photocatalytic results: Screening the activity of the as-synthesized QDs toward the oxidation of PhPyr and affording the C-C vinylation bond.** The formed C-C bond is indicated in red. All the reactions run on the 0.001 mmol scale in trifluorotoluene. The catalytic loading is computed versus the amount of the starting arylamines. The reaction yield is determined by integrating the UHPLC-MS peaks compared to the peak of the corresponding standard of the reaction product. Oleic acid (OIAc), oleylamine (OIAm) and octadecylamine (ODAm). The measurement of the LEDs power is described in Chapter IV section IV-6.

The use of CdS QDs with a 5.7 nm diameter makes this kind of QDs possess a high value for their corresponding extinction coefficient ( $10^6 \text{ M}^{-1} \cdot \text{cm}^{-1}$ ). This offers the possibility of using a low catalytic loading (0.1 mol % versus the PhPyr). Entry 1 of Table II-3 shows the photocatalytic result using CdS QDs functionalized with their native Oleic acid (OIAc) surface

ligands. The reaction mixture is irradiated using a blue LED (455 nm, 10 mW). After 4 hours of irradiation, the maximum yield is obtained at 49% and achieving 490 turnover number for the QDs. Weiss and co-workers<sup>10</sup> obtained 50% using 0.5% CdS QDs after 7.5 hours of Irradiation. In our experiments, the prolonged irradiation time (22 hours) led to a degradation of the C-C coupled product (Figure II-6-A black line), which we attribute to the low stability of this kind of products due to the presence of aryl amine and vinyl moieties.

In the case of 0.5mol % of CdSe core QDs (Entry 3 of Table II-3), irradiating the as-synthesized QDs using a green LED, and after 4 hours the maximum yield obtained is a 51% with 102 turnover number for the QDs. The kinetic of the reaction over 22 hours of irradiation is represented by the red line of figure II-6-A, which shows the degradation of the product in a manner similar to the previous case.

Using inverted Type-I CdS-CdSe (0.5 mol%) core-shell QDs, the reaction medium is irradiated using a green LED (528 nm) and a maximum yield of 48% is obtained in 4 hours, in this case 96 turnover number was achieved for the QDs. The over-irradiation also induced degradation of the product (Figure II-6-B green line).

Entries 4 and 5 show the results for the core-shell CdSe-CdS QDs (0.5 mol %) and CdSe-ZnS QDs (0.3 mol %) respectively. In the case of CdSe-CdS QDs a 30 % yield is obtained after 6 hours of irradiation (TON = 100), with comparable reaction kinetics as the previous cases (figure II-6B- dark blue line). However, only 10% yield is obtained using octadecylamine (ODAm) capped CdSe-ZnS QDs irradiated by an orange LED (590 nm, 20 mW) for 22 hours. The kinetics of the reaction with CdSe-ZnS QDs is represented in figure II-6-B gray line.

Finally, InP core QDs and InP-ZnS core-shell QDs were also tested as cadmium free QDs examples. Entry 6 of Table II-3 represent the results for the core InP case, using 0.7 mol % of InP core QDs irradiated by using the 455 nm LED, a maximum yield of 40% is obtained after 6 hours of irradiation where 57 TON were achieved. With exactly the same conditions but using oleylamine capped InP-ZnS core-shell QDs, a maximum yield of 42% and 60 TON were achieved after 6 hours of irradiation (Entry 7). The use of oleate capped InP-ZnS QDs (Entry 8) results in very similar results by obtaining 43% yield and 61 TON. The kinetics using InP and InP-ZnS QDs catalyzed reactions are represented in figure II-6-A blue line for the core InP and Figure II-6-B for the core-shell QDs. The use of InP-ZnS (450 nm) QDs by P. Pillai<sup>11</sup> resulted in a yield of 52 % after 10 hours of irradiation. This result is slightly better than ours probably because we didn't monitor our reaction at the 10 hours of irradiation to be exactly comparable.

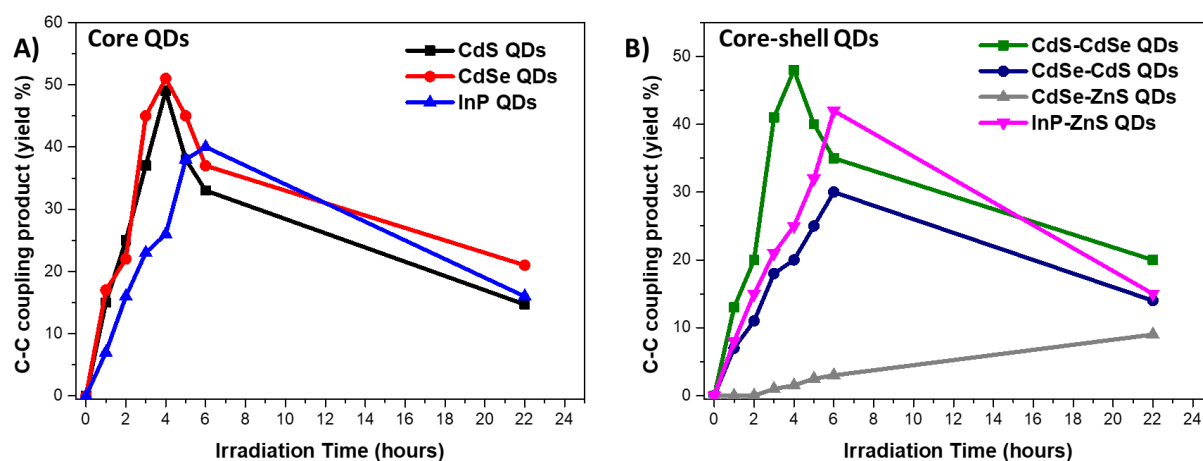


**Figure II-6: Evolution of the C-C coupling product during the photoredox vinylation reaction:** A) reaction kinetic using the as-synthesized core-structured CdS, CdSe and InP QDs. B) reaction kinetic using the as-synthesized core-shell CdS-CdSe, CdSe-CdS, CdSe-ZnS and InP-ZnS QDs. The data plotted are collected from the integration of the UHPLC-MS peaks of the analyzed reaction aliquots after the comparison with the corresponding standard sample of the product.

## II-4.2. Test of selected as-synthesized QDs for the 2-step reaction of the synthesis of tropane derivative.

Considering the obtained photocatalytic activity of the tested QDs for the photoredox vinylation reaction, we have selected CdS, CdSe, and InP-ZnS QDs for the first stage of tests to check the ability of the QDs to photocatalyze the two-step reaction leading to the bicyclic tropane derivatives skeletons. The reaction was performed starting from 1-phenylpyrrolidine and ethyl 2-((phenylsulfonyl)methyl)acrylate as a radical trap but reacting in trifluorotoluene (TFT). The reactions were run on a scale of 0.001 mmol of 1-phenylpyrrolidine, in the presence of 1.1 equivalents of the radical trap and 1.2 equivalents of cesium acetate base using the as-synthesized QDs (See the scheme of Table II-4). The results are summarized in Table II-4. The reactions' mixtures were set for irradiation under inert atmosphere in a nitrogen-filled glovebox. The reaction yields are determined similarly to the previous cases by integrating the UHPLC-MS peaks and comparing them to the peak of the corresponding standard of the reaction product. (Representative chromatograms spectra are presented in the Appendix II, Fig. A5,6 and 7).

Entry	QDs	Surface Ligands	Solvent	cat.load % (Abs.)	Irradiation wavelength and Power	Irradiation Time for the max. Yield	Intermediate product (2) Yield %	Final bicyclic product (3) Yield %
1	CdS	OIAc	TFT	0.1% (A=1.1)	455 nm 10 mW	24 hours	52%	12%
2	CdSe	OIAc	TFT	0.5% (A=0.9)	528 nm 50 mW	24 hours	49%	6%
3	InP-ZnS	OIAm	TFT	0.7% (A=0.9)	455 nm 10 mW	48 hours	42%	0%

**Table II-4: The photocatalytic results of QDs for the 2-step model reaction of the Tropane derivatives synthesis:** The formed C-C bonds are indicated in red. All the reactions run on the 0.001 mmol scale in trifluorotoluene or acetonitrile. The reaction yield is determined by integrating the UHPLC-MS peaks compared to the peak of the corresponding standard of the reaction products.

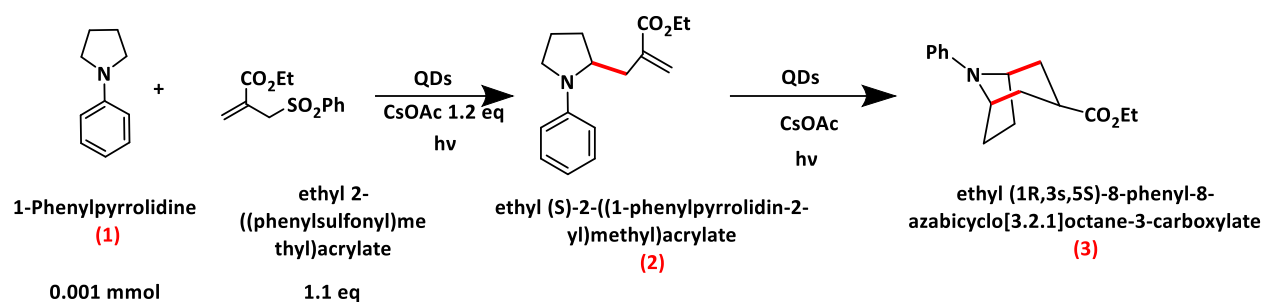
Entries 1 and 2 of Table II-4 show the results using CdS and CdSe QDs capped with their native oleic acid ligands in TFT. In these cases, the reaction did not show completion to the final bicyclic product during 24 hours of irradiation. In the case of CdS QDs, we obtained 52% of the intermediate carbon-carbon mono-allylated product (2) and only 12% of the final bicyclic product (3). Similarly, in the case of CdSe QDs, 49% of the intermediate product (2) but 6 % of the final bicyclic product (3) were obtained. Using InP-ZnS QDs (Entry 3, Table II-4) the reaction stops at the stage of the intermediate mono-allylated product without any formation of the final bicyclic product even after 48 hours of irradiation. Despite that, the reaction was not completed towards the desired final product, but the obtained results are promising and indicate the need for further optimization in order to afford better yields of the desired tropane derivatives final product.

### II-4.3. Surface ligands optimization: Case of CdS and CdSe QDs.

The as-synthesized Quantum Dots are prepared with long-chain ligands on their surface. For example, CdS and CdSe Quantum Dots are functionalized with oleic acid as surface ligands. InP-ZnS Quantum Dots are synthesized in oleylamine, which acts as a coordinating solvent during the synthesis and as surface ligands. These kinds of ligands contains 18-carbon atoms chains. The long chain of the ligands functionalizing the QDs is expected to create challenging accessibility of the reaction substrate to the surface of the QDs<sup>37</sup>. However, enhancing the interaction of the reaction substrate with the surface of the QDs, where the redox processes are supposed to take place, is expected to be an important factor for the photocatalysis with Quantum Dots. As discussed in chapter I section I-2 , it was reported by E.A.Weiss that applying a partial ligand exchange with a shorter ligand than the native one could induce a disordering of the ligand shell of the QDs by creating mixed ligand layers<sup>10</sup>.

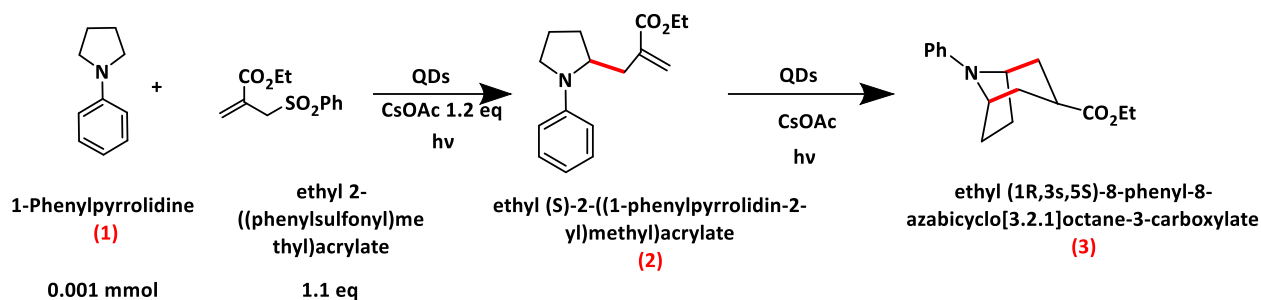
Based on the mentioned literature reports, we tested the effect of the ligand exchange on the photocatalytic activity of the QDs. We partially exchanged the oleic acid ligands (C-18 chain) functionalizing the CdS and CdSe core QDs with octylphosphonic acid ligands (C-8 chain). The molecular structures of the used ligands are presented in Scheme II-A1 in the Appendix II, page 155. The photocatalytic activity of the QDs after the ligand exchange is tested using the same conditions as for the previous series of reactions.

The effect of the partial ligand exchange using OPAC ligands was investigated systematically for CdS and CdSe QDs by mixing them with increasing quantities equivalents of OPAC ligands with respected to the QDs' concertation. The results are collected in Tables II-5 and II-6, respectively. As mentioned previously, the use of the QDs with their native ligands leads to reactions with low efficiency for the final bicyclic product by obtaining 12% and 6% for CdS and CdSe QDs, respectively, after 24 hours of irradiation (Entries 1, Table II-5 and II-6). Interestingly, the addition of 100 equiv. of OPAC ligands versus the QDs' concertation shows an enhancement in the yield of the final product by reaching 28% and 40% for CdS and CdSe, respectively (Entries 2 in Tables II-5 and II-6). Increasing the equivalents of OPAC reaching 300 equiv for CdSe QDs raised the reaction to the maximum yield of the final product by reaching 72% after 24 hours of irradiation (Table II-6 entry 4). However, adding higher excess of 400 equiv OPAC in the case of the CdSe QDs did not help to obtain a higher yield for the final product (Table II-6 entry 5). Then, we deduced that exchanging the as-synthesized oleate capped CdSe QDs with 300 equiv of OPAC is the optimal condition for the CdSe QDs. Similarly, in the case of CdS QDs the highest yield was obtained after treating the QDs with 380 equiv of OPAC (Table II-5 entry 5) by obtaining 74%. It was not possible to afford a higher yield after adding higher excess of 500 equiv of OPA (Table II-5 entry 6).



Entry	QDs	Surface ligands	cat.load % (Abs.)	Irradiation wavelength and Power	Intermediate product (2) Yield %	Final bicyclic product (3) Yield %
1	CdS	OAc	0.1% (A=1.1)	455 nm 10 mW	52%	12%
2	CdS	OAc+ 100 eq OPAc	0.1% (A=1.1)	455 nm 10 mW	30%	28%
3	CdS	OAc+ 200 eq OPAc	0.1% (A=1.1)	455 nm 10 mW	10%	50%
4	CdS	OAc+ 300 eq OPAc	0.1% (A=1.1)	455 nm 10 mW	8%	60%
5	CdS	OAc+ 380 eq OPAc	0.1% (A=1.1)	455 nm 10mW	0%	74%
6	CdS	OAc+ 500 eq OPAc	0.1% (A=1.1)	455 nm 10 mW	0%	65%

**Table II-5: Optimization of the surface ligand layer of the CdS QDs in TFT by different equivalents of OPAc ligands. Irradiation of 24 hours. The equivalent of the OPAc ligands is expressed versus the QDs' concentration.**



Entry	QDs	Surface ligands	cat.load % (Abs.)	Irradiation wavelength and Power	Intermediate product (2) Yield %	Final bicyclic product (3) Yield %
1	CdSe	OAc	0.5% (A=0.9)	528 nm 50 mW	49%	6%
2	CdSe	OAc+ 100 eq OPAc	0.5% (A=0.9)	528 nm 50 mW	27%	40%
3	CdSe	OAc+ 200 eq OPAc	0.5% (A=0.9)	528 nm 50 mW	15%	55%
4	CdSe	OAc+ 300 eq OPAc	0.5% (A=0.9)	528 nm 50 mW	0%	72%
5	CdSe	OAc+ 400 eq OPAc	0.5% (A=0.9)	528 nm 50 mW	0%	68%

**Table II-6: Optimization of the surface ligand layer of the CdSe in TFT QDs by different equivalents of OPAC ligands. Irradiation for 24 hours. The equivalent of the OPAC ligands is expressed versus the QDs' concentration.**

#### II-4.4. Effect of the ligands optimization of the different QDs for the C-C vinylation reaction.

Encouraged by the significant photocatalytic enhancement obtained using the surface ligand optimized QDs, we tested the effect of the partial ligand exchange on the different types and structure of the synthesized QDs. The first series of tests were done using the optimized condition investigated in section II-4.3 and applied on the simple 1-step vinylation reaction.

The results with surface ligands modified QDs are summarized in Table II-7. Entry 1 of Table II-7 represents the results with CdS QDs treated with 380 equivalents of octylphosphonic acid ligands (OPAc) with respect to the QDs' concentration. The ligand optimization shows an enhancement in the reaction yield by obtaining a maximum of 68% after 3 hours of irradiation

and increasing the turnover number to accomplish 680 TON, compared with 49% in 4 hours using the as-synthesized CdS QDs (See Table II-3). The reaction kinetics are presented in figure II-7-A (black line), showing that in this case the maximum product formation is reached after 3 hours of irradiation. The obtained yield in this case is very close to the one obtained by Weiss (60%) after optimizing the QDs with the same mix of ligands, but using 0.5 mol % as catalytic loading while we used 0.1 mol % in the case of our QDs. Moreover, at this stage, the Quantum Yield (QY) of the CdS QD-catalyzed reaction was measured to be 0.18%. The Quantum yield is estimated using both Ferrioxalate actinometry and the physical measurement of the light power sent by the irradiation setup used for the reaction (See Chapter IV section IV-6 for the detailed estimation of the QY). The value of the measured Quantum yield using CdS QDs (0.18%) is slightly lower than the value reported by Weiss (0.22%)<sup>10</sup> for the similar reaction.

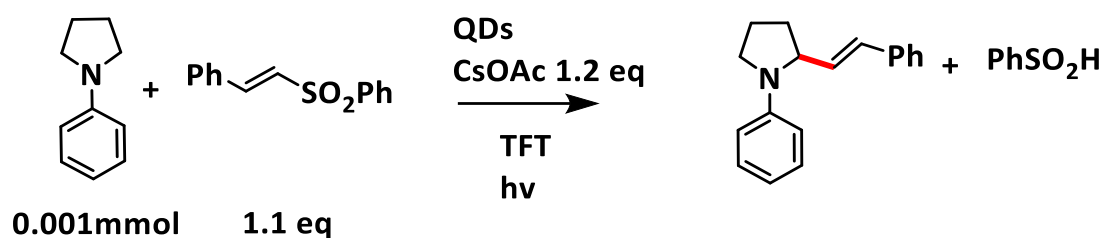
Using CdSe QDs after treating their surface with 300 equiv of OPAC ligand, the yield increased to 70 % (Entry 3 and Figure II-7-A red line). CdS-CdSe core-shell QDs treated with 400 equiv. of OPAC (Entry 2 and Figure II-7-B green line) also showed an enhancement in the reaction yield, which increased to 69% in a very similar manner to core CdSe QDs. In the two cases, a similar Quantum yields were measured to be 0.024% and 0.025%, respectively.

The effect of the partial ligand exchange was not significant in the case of CdSe-CdS and CdSe-ZnS core shell QDs as shown in entries 4 and 5 where the yields increased by only few percent to obtain a yield of 33% using CdSe-CdS QDs and 15% using CdSe-ZnS. Moreover, the reaction kinetics were very similar to the case of the non-modified QDs' ligands (See Figure II-7-B).

The amine coated InP core and InP-ZnS core shell QDs were treated with 500 equiv. of C-8 chained octylamine ligands (OclAm) to exchange with fraction of the native oleylamine ligands, but almost no effect was observed on the photocatalytic activity of the QDs since the yields by obtaining 42% and 45% respectively were obtained (entries 6 and 7) are very similar to ones obtained using the as-synthesized QDs (see Table II-3). Similar results were also obtained in the case of the oleate capped InP-ZnS QDs treated with OPAC ligands. The yield didn't improve after the partial ligand exchange as 45% yield was obtained in this case (Entry 8).

As mentioned before, the main aim for optimizing the surface ligand layer of the QDs is to increase the permeability of the ligand shell to the reaction substrate to enhance the accessibility to the charge carriers and consequently the redox processes. This permeability enhancement depends primarily on the density and the ordering of the ligands on the surface of the QDs which could be exchanged by other ligands. Moreover, the efficient ligand exchange relies on using a new ligand with a good binding affinity to the surface of the QDs.

The exchange with OPAC ligands seems efficient, probably due to the high affinity of the new phosphonate ligand compared to native carboxylate or amine ligand, which makes them easily displaced<sup>38</sup>. This applies as well to the oleate capped CdS and CdSe core QDs, and the amine capped inverted type-I CdS-CdSe QDs with enhancement of the photocatalytic results. However, in the case of the type-I oleate capped InP-ZnS QDs or amine capped Quasi type-II CdSe-CdS or type-I CdSe-ZnS QDs the exchange with OPAC was of no significant effect on the photocatalytic activity of these QDs. Considering the InP-ZnS QDs, the oleylamine capped QDs were partially exchanged with short octylamine ligands, but no significant improvement was observed after the ligand exchange. Taking all together, one can conclude that the ligand optimization can improve the photocatalytic activity of the QDs only if their charge (holes in our reactions case) accessibility is favorable as discussed above.



Entry	QDs	Surface Ligands	Solvent	cat.load % (Abs.)	Irradiation wavelength and power	Irradiation Time for the max. Yield	Yield %	TON
1	CdS	OIAc + OPAc	TFT	0.1% (A=1.1)	455 nm 10 mW	3 hours	68%	680
2	CdS-CdSe	OIAm + OPAc	TFT	0.5% (A=0.9)	528 nm 50 mW	4 hours	69%	138
3	CdSe	OIAc + OPAc	TFT	0.5% (A=0.9)	528 nm 50 mW	4 hours	70%	140
4	CdSe-CdS	OIAm + OPAc	TFT	0.5% (A=1.2)	528 nm 50 mW	6 hours	33%	110
5	CdSe-ZnS	ODAm + OPAc	TFT	0.3% (A=1.1)	590 nm 20 mW	22 hours	15%	30
6	InP	OIAm + OclAm	TFT	0.7% (A=0.9)	455 nm 10 mW	6 hours	42%	60
7	InP-ZnS	OIAm + OclAm	TFT	0.7% (A=0.9)	455 nm 10 mW	6 hours	45%	64
8	InP-ZnS	OIAc + OPAc	TFT	0.7% (A=1)	528 nm 50 mW	6 hours	45%	64
9	CdS	PPAc	MeCN	0.1% (A=1.1)	455 nm 10 mW	3 hours	67%	670
10	CdSe	PPAc	MeCN	0.5% (A=0.9)	528 nm 50 mW	3 hours	71%	142

**Table II-7: C-C vinylation coupling photocatalytic results after ligand exchange for the QDs: Screening the activity of the surface ligands modified QDs. All the reactions run on the 0.001 mmol scale in trifluorotoluene or acetonitrile. The reaction yield is determined by integrating the UHPLC-MS peaks compared to the peak of the corresponding standard of the reaction product.**

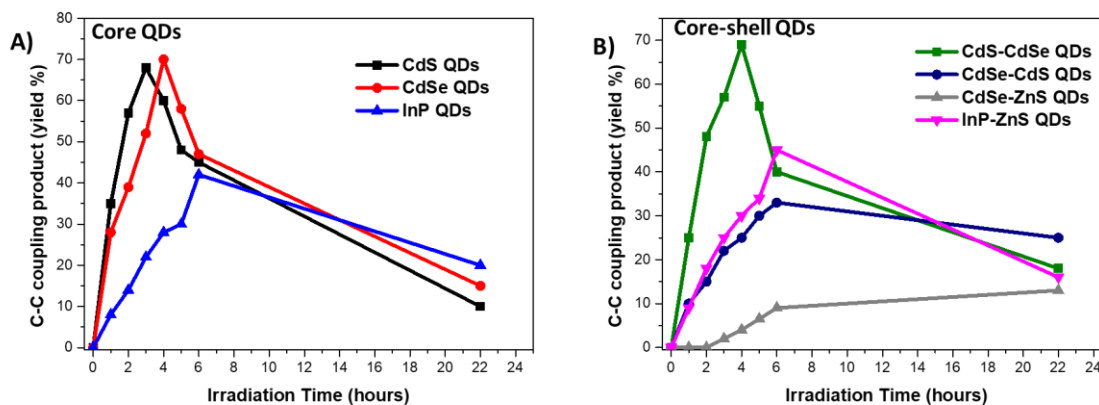


**Figure II-7: Evolution of the C-C coupling product during the photoredox vinylation reaction for the QDs after the partial ligand exchange with OPAC:** A) Reaction kinetic after the partial ligand exchange for core-structured CdS, CdSe and InP QDs. B) Reaction kinetic after the partial ligand exchange for core-shell CdS-CdSe, CdSe-CdS, CdSe-ZnS and InP-ZnS QDs. The data plotted are collected from the integration of the UHPLC-MS peaks of the analyzed reaction aliquots after the comparison with the corresponding standard sample of the product.

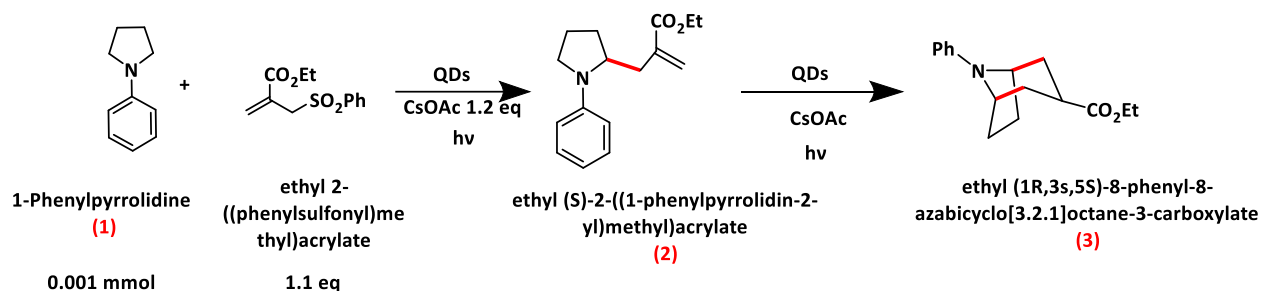
Furthermore, a complete ligand exchange procedure was applied for CdS and CdSe core QDs using 500 equiv. of phosphonopropanoic acid ligands (PPAc). The usage of the PPAc ligands can afford a complete phase transfer into polar solvents. This procedure was already reported to transfer the QDs into water using dimethylformamide as an intermediate polar solvent<sup>39</sup>. Using the PPAc ligands, we could disperse the CdS and CdSe core QDs in acetonitrile and then test their photocatalytic activity. Entries 9 and 10 of Table II-7 represent the results using the PPAc-capped CdS and CdSe QDs in acetonitrile. A good reaction yields of 67% and 71% using CdS and CdSe, respectively, are obtained after 3 hours of Irradiation. These results show clearly that the good permeability of the ligand layer on the surface of the QDs is an important factor to ensure a good interaction between the surface of the Quantum Dots and the reaction substrates and consequently to enhance to photocatalytic activity of the QD.

#### **II-4.5. Effect of the ligands optimization of different QDs for the 2-step reaction of the synthesis of tropane derivatives.**

Considering the obtained photocatalytic activity of the tested QDs for the photoredox vinylation reaction after the ligand optimization, we have selected CdS, CdSe, CdS-CdSe and InP-ZnS QDs to compare their activity towards the two-step reaction leading to the bicyclic tropane derivatives skeletons after the ligands exchange.

All the reactions were run on a scale of 0.001 mmol of 1-phenylpyrrolidine, in the presence of 1.1 equivalents of the radical trap and 1.2 equivalents of cesium acetate base. Two diastereoisomers were identified for the final bicyclic products (See chromatograms in the Figure II-A6 in the Appendix II). All the results are summarized in Table II-8 (some are re-collected from the previous Tables for simplifying the comparison). Entries 1 and 2 of Table II-8 show the results using CdS and CdSe QDs capped with their native oleic acid ligands in TFT where the reaction was not successful in producing the final tropane product.

After optimizing the ligand layer of the QDs, a much better photocatalytic performance was observed for CdS and CdSe QDs as an average of 75% and 73% yield of the final bicyclic product were obtained, respectively (Entries 3 and 4 of Table II-8). The reaction kinetics, in the CdS QDs case, is presented in figure II-8-A, which shows the complete consumption of the starting material (PhPyr) before the first 10 hours of irradiation. At almost the same time, the maximum formation of the mono-allylated intermediate product was reached. The conversion of the intermediate product to the final bicyclic product was accomplished by the end of 24 hours of irradiation.



Entry	QDs	Surface Ligands	Solvent	cat.load % (Abs.)	Irradiation wavelength and Power	Irradiation Time for the max. Yield	Intermediate product (2) Yield %	Final bicyclic product (3) Yield %
1	CdS	OIAc	TFT	0.1% (A=1.1)	455 nm 10 mW	24 hours	52%	12%
2	CdSe	OIAc	TFT	0.5% (A=0.9)	528 nm 50 mW	24 hours	49%	6%
3	CdS	OIAc + OPAC	TFT	0.1% (A=1.1)	455 nm 10 mW	24 hours	0%	75% <sup>a</sup>
4	CdSe	OIAc + OPAC	TFT	0.5% (A=0.9)	528 nm 50 mW	24 hours	0%	73% <sup>a</sup>
5	CdS-CdSe	OIAm+ OPAC	TFT	0.5% (A=0.9)	528 nm 50 mW	24 hours	0%	74%
6	CdS	PPAc	MeCN	0.1% (A=1.1)	455 nm 10 mW	24 hours	0%	74% <sup>b</sup>
7	CdSe	PPAc	MeCN	0.5% (A=0.9)	528 nm 50 mW	24 hours	0%	72% <sup>b</sup>
8	InP-ZnS	OIAm	TFT	0.7% (A=0.9)	455 nm 10 mW	48 hours	42%	0%
9	InP-ZnS	OIAm+ OclAm	TFT	0.7% (A=0.9)	455 nm 10 mW	48 hours	48%	0%

**Table II-8: The photocatalytic results of QDs for the 2-step model reaction of the Tropane derivatives synthesis:** The formed C-C bonds are indicated in red. All the reactions run on the 0.001 mmol scale in trifluorotoluene or acetonitrile. The reaction yield is determined by integrating the UHPLC-MS peaks compared to the peak of the corresponding standard of the reaction products. <sup>a</sup>average of four runs. <sup>b</sup> average of three runs. The representative UPLC-MS chromatograms are collected in the appendix II in figures II-A5, II-A6, II-A7 and II-A8, pages 160 to 164.

Moreover, performing the reaction in acetonitrile after exchanging the oleic acid ligands capping the CdS and the CdSe QDs with the PPAc ligands was also efficient. After 24 hours of irradiation, the final product was obtained in a 74% and 72% yield using CdS and CdSe QDs, respectively (Entries 6 and 7).

The use of the inverted type-I core shell CdS-CdSe QDs, resulted in very similar results to those of core CdS and CdSe QDs as 74% yield was obtained after 24 hours of irradiation (Entry 5). These results of these 3 types of QDs compare very well with those using Ir-(III) for

the same allylic radical trap, for which 60% yield was obtained after 16 hours of irradiation when running the reaction (but at a higher of scale 0.2 mmol, instead of 0.001 mmol in our case).

Interestingly, by using InP-ZnS QDs, it was possible to stop the reaction at the stage of the intermediate mono-allylated product without forming the final bicyclic product. Entry 8 shows the result using the as-synthesized oleylamine capped InP-ZnS QDs. After 48 hours of irradiation using blue light, the mono-allylated product was formed in a 42% yield. In addition, treating the surface of the InP-ZnS QDs with octylamine ligands has slightly increased the yield of the mono-allylated product to obtain a 48% yield (Entry 9). In both cases of InP-ZnS QDs, the elongated irradiation time (48 hours) did not afford the reaction toward the formation of final bicyclic product. The selectivity of the InP-ZnS QDs toward the first intermediated product is attributed to the limited reducing power of their conduction band compared to the radical to be reduced (see section II-10). The reaction kinetics in the case of entry 9 of Table II-8 was followed during the 48 hours of irradiation and is represented in figure II-8-B.

Therefore, these results show that it is possible to select the convenient type of QDs for obtaining the product of interest. The CdS, CdSe and CdS-CdSe QDs reached the final bicyclic product after passing the different redox steps of the reaction. However, by using the InP-ZnS, it is attainable for the preparation of the C-C monoallylated product by making the reaction stop at the first catalytic cycle. This selectivity toward the first catalytic cycle was not easy to achieve using other molecular catalysts such as Ir{dF(CF<sub>3</sub>)ppy}<sub>2</sub>(dtbpy)]PF<sub>6</sub> as shown in the previous work by our colleagues from the university of Bern.<sup>4</sup>

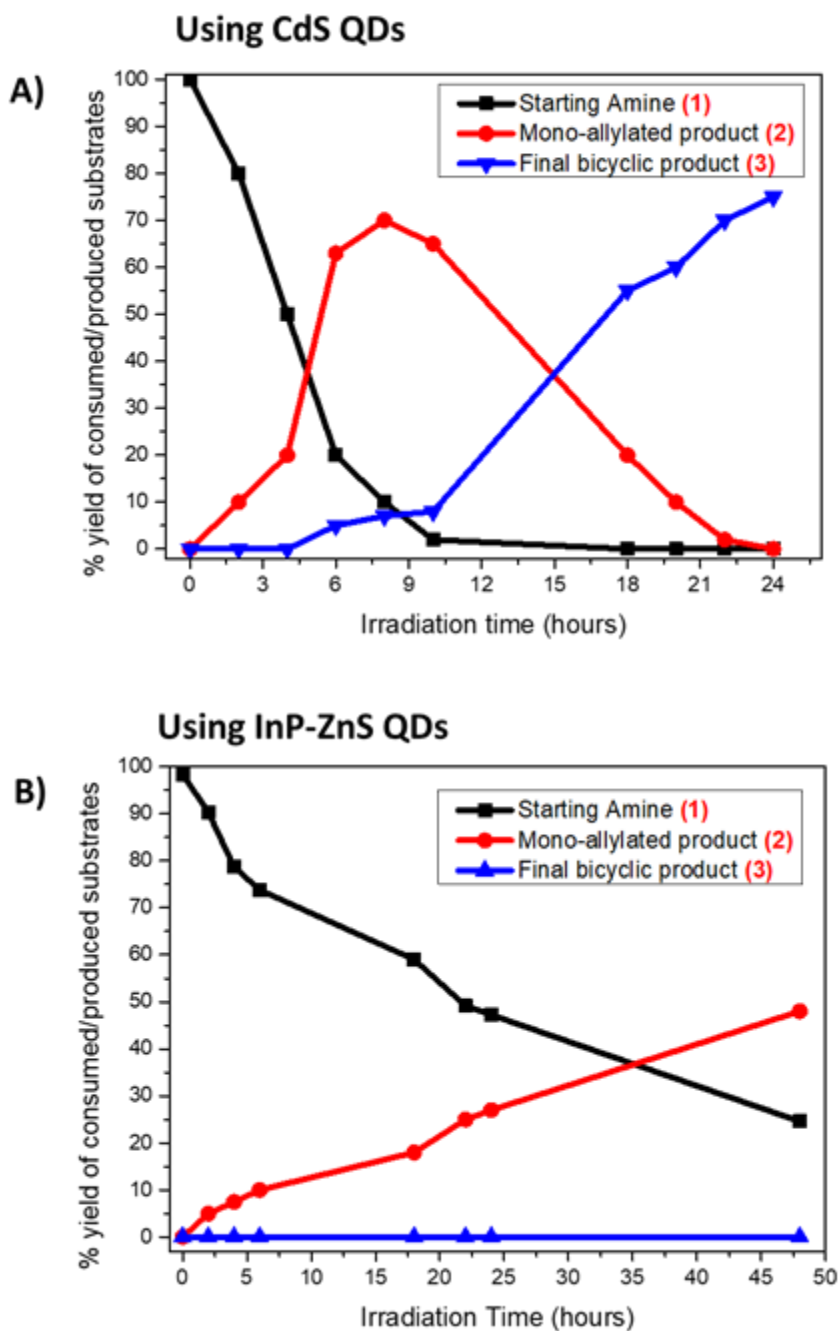


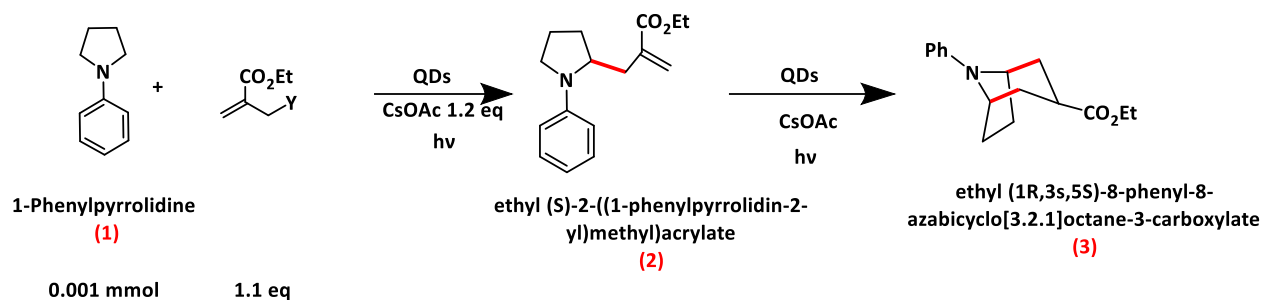
**Figure II-8: Typical reaction kinetics toward the formation of the final product or the selectivity to intermediate product.** A- Reaction kinetics using CdS QDs showing the complete oxidation of PhPy (black line), the formation of the mono-allylated intermediate product (red line), followed by the formation of the final bicyclic product (blue line). B- The reaction kinetics using InP-ZnS QDs showing the oxidation of the PhPyr (black line); the selective formation of the mono-allylated product (red line), without the formation of the final bicyclic product. The data plotted are collected from the integration of the UHPLC-MS peaks of the analyzed reaction aliquots after the comparison with the integrated peak of the standard sample of the products.

## II-5. Scope of radical traps.

The reaction optimization with QDs as photocatalyst was done using the ethyl 2-((phenylsulfonyl)methyl)acrylate as a sulfone-based allyl radical trap. However, using the Iridium catalyst the validity of the annulation process in the new reaction was proved by making 1-phenylpyrrolidine (1) react with a series of allyl radical traps bearing different leaving groups (Y), as was demonstrated in the published work with the colleagues from the university of Bern<sup>4</sup>. Therefore, we also tested the influence of other radical traps by selecting an acetate based radical tarp, namely ethyl 2-(acetoxymethyl)acrylate (Y = OAc) and a corresponding sulfide radical trap (Y = S-tert-dodecyl).

In the case of the Ir-catalyzed reactions<sup>4</sup>, the use of the acetate radical gave attractive results by affording a shorter reaction time. However, in the Quantum Dots case, the reaction is still requiring the 24 hours of irradiation to be completed. Entries 3 and 4 of Table II-9 show the results using CdS and CdSe QDs with the acetate radical trap. With the optimized reaction conditions and QDs' surface ligands, good yields were obtained with 72% and 70 % for CdS and CdSe QDs, respectively.

In the case of the sulfide radical trap (Y= St-Do), the desired cyclized product was also provided but with a lower reaction yield compared to the previous cases of the sulfone and acetate radical traps, where 55% and 50% yields were obtained using CdS and CdSe QDs (Entries 5 and 6), respectively. This is probably due to the release of thiols during the reaction due to the presence of the S-tert-docedyl part of this radical trap. It is well known that thiols are good ligands for QDs on the one side, and easy to be oxidized by the QDs on the other side<sup>39</sup>. Then, in this case, it is possible that surface layer of the QDs tends to change in the presence of the formed thiols, or that some of the photo-induced charges tend to interact with the thiols present during the reaction.



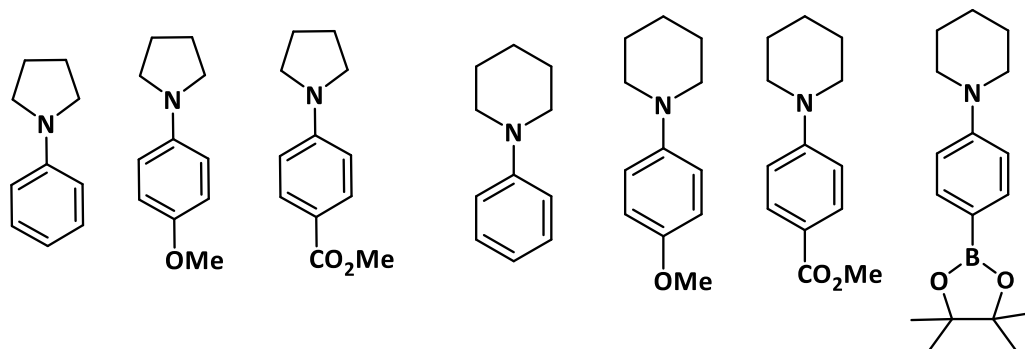
Entry	QDs	Surface Ligands	Solvent	Y (equiv)	cat.load % (Abs.)	Irradiation wavelength and Power	Irradiation Time for the max. Yield	Final bicyclic product (3) Yield %
1	CdS	OAc+ OPAc	TFT	SO <sub>2</sub> Ph (1.1)	0.1% (A=1.1)	455 nm 10 mW	24 hours	75%
2	CdSe	OAc+ OPAc	TFT	SO <sub>2</sub> Ph (1.1)	0.5% (A=0.9)	528 nm 50 mW	24 hours	73%
3	CdS	OAc+ OPAc	TFT	OAc (1.1)	0.1% (A=1.1)	455 nm 10 mW	24 hours	72%
4	CdSe	OAc+ OPAc	TFT	OAc (1.1)	0.5% (A=0.9)	528 nm 50 mW	24 hours	70%
5	CdS	OAc+ OPAc	TFT	St-Do (1.4)	0.1% (A=1.1)	455 nm 10 mW	24 hours	55%
6	CdSe	OAc+ OPAc	TFT	St-Do (1.4)	0.5% (A=0.9)	528 nm 50 mW	24 hours	50%

**Table II-9: Radical traps screening:** The photocatalytic results of QDs for the reaction of the synthesis of Tropane derivatives screening different radical traps. The formed C-C bonds are indicated in red. All the reactions run on the 0.001 mmol scale in trifluorotoluene. The reaction yield is determined by integrating the UHPLC-MS peaks compared to the peak of the corresponding standard of the reaction products.

## II-6. Reaction scope with different N- aryl amines.

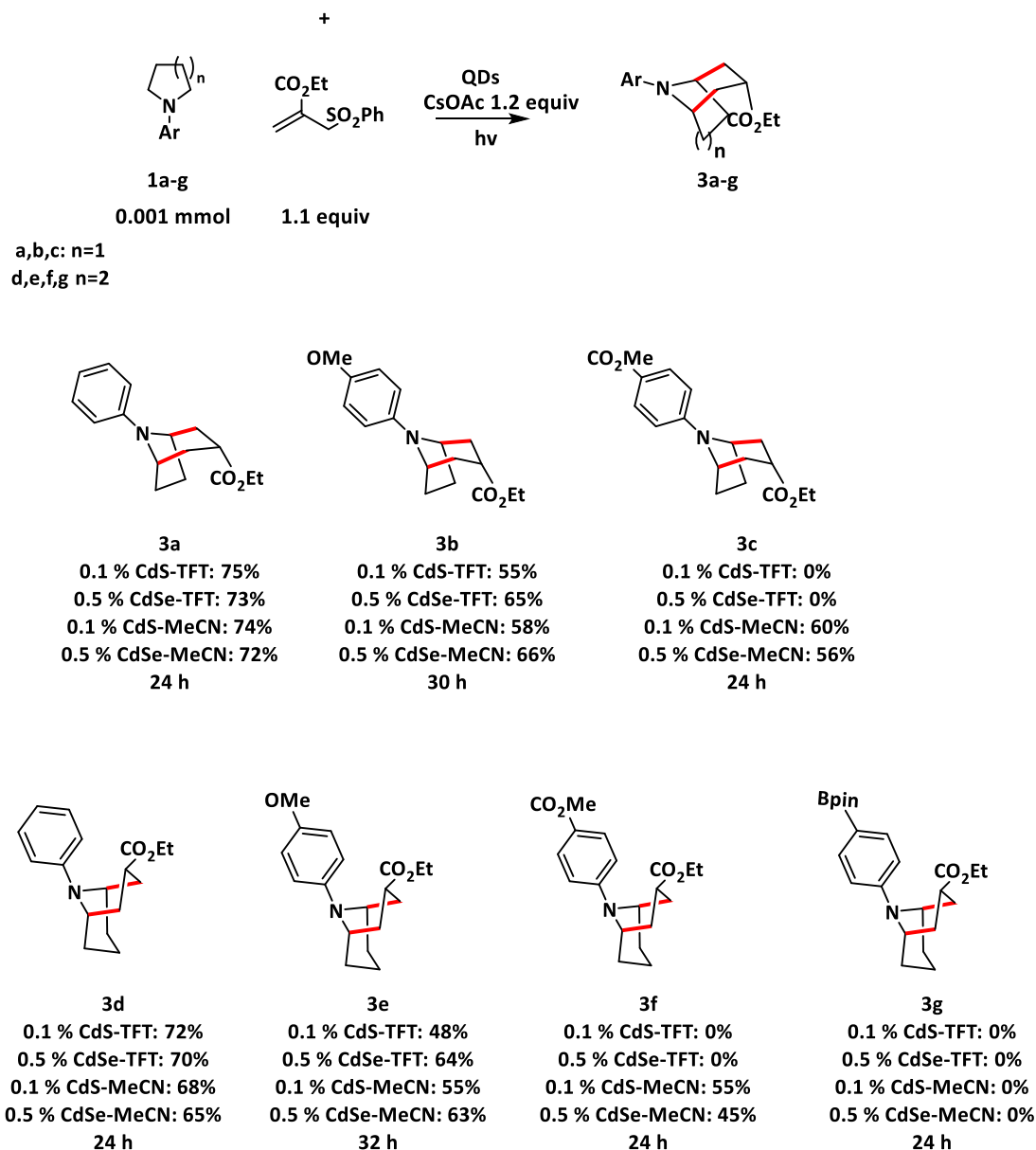
The possibility of expanding the scope of the reaction substrates is examined by selecting a few para-substituted N-arylpiperidines, in addition to some N-arylpiperidines (see Table II-10 for the N-aryl amine substrates), which were shown to be efficient for the preparation of homotropane 9-azabicyclo[3.3.1]nonane skeletons. Using the Ir(III) catalyst<sup>4</sup> specific para-substituents, for example methoxy or pinacolboronyl moieties, were proved to be successfully removed by deprotection methods to prepare the bicyclic alkaloid of the Tropane<sup>4</sup>. The results are collected in scheme II-3 after running the reactions in TFT or MeCN

with CdS or CdSe QDs using optimized reaction conditions and QDs with the partial ,ligand exchange in TFT and the complete ligand exchange in MeCN.



Redox Potential $E^\circ_{\text{V/SCE}}$	1a	1b	1c	1d	1e	1f	1g
	MeCN	+0.57	+0.19	+0.74	+0.51	+0.17	+0.75
TFT	+0.64	+0.29	+0.89	+0.66	+0.29	+1.00	+0.72

**Table II-10: Molecular structures and the redox potential of the N-Aryl amine substrates used for the reaction scope:** Top: scheme for 1a- Phenylpyrrolidine, 1b- p-methoxy-phenylpyrrolidine, 1c- p-ester-phenylpyrrolidine, 1d- PhenylPiperidine, 1e- p-methoxy- PhenylPiperidine, 1f- p-ester- PhenylPiperidine, and 1g Bpin- PhenylPiperidine. Bottom Table for the summarized redox potential for the one-electron oxidation of the reaction substrates calculated using DFT in TFT and MeCN.



**Scheme II-3: Reaction scope with the tested N-arylamines:** the results of the final product of the reactions tested with different substrates if N-aryl amines. . All the reactions run on the 0.001 mmol scale in trifluorotoluene or acetonitrile. The reaction yield is determined by integrating the UHPLC-MS peaks compared to the peak of the corresponding standard of the reaction products. (Representative chromatograms and MS spectra are SHOWN in the Appendix II in Figures A9 (page 165) to A18 (page 174))

The reaction worked well with the electron-rich p-methoxy-phenylpyrrolidine leading to product **3b**, which was obtained with a 55% yield using CdS QDs in TFT and 58% in MeCN. Using CdSe QDs the reaction worked slightly better, where 65% and 66% yields were obtained in TFT and MeCN, respectively. In this case, the presence of the methoxy substituent (electron-donating group) is expected to ensure a lower oxidation potential than the model N-Phenylpyrrolidines substrate. The results with the p-methoxy-phenylpyrrolidine using Ir(III)

catalyst gave results similar to ours with a 56% yield but always at higher reaction (0.2 mmol). Using DFT calculation, we calculate a redox potential of 0.19 V/SCE in MeCN and 0.29 V/SCE in TFT. Therefore, the oxidation of the starting amine is easily accessible using both CdS and CdSe QDs in TFT or MeCN, but a lower reaction yield was obtained compared with the case of the unsubstituted substrates **1a**, which could be related to the longer time needed or the completion of this reaction leading to less clean reaction medium. The estimated redox potentials of the amines are collected in Table II-10.

However, in the case of the electron-poor p-ester-phenylpyrrolidine where 42% yield was obtained using Ir(III)<sup>4</sup>, the results vary between the reactions performed in TFT and MeCN when using CdS or CdSe QDs. The reaction worked well when using CdS and CdSe QDs dispersed in MeCN by obtaining a yield of 60% and 56%, respectively, of the final product **3c**. On the other hand, running the reaction in TFT, the reaction did not work, and the p-ester-phenylpyrrolidine was not oxidized as it was recovered after the irradiation time. The DFT calculations for the oxidation potential of p-ester-phenylpyrrolidine in TFT and MeCN were also performed, showing that it is easier to oxidize **1c** in MeCN, as for this compound an oxidation potential of 0.74 V/SCE was calculated, compared to a higher oxidation potential of 0.89 V/SCE in TFT. Then, the difference in the reaction efficiency in the case of MeCN and TFT could be attributed to the difference in the oxidation potentials or to the better accessibility using the QDs in MeCN after the complete ligand exchange. The impact of the para-substituents (electron withdrawing or donating groups) on the redox potential was also investigated by electrochemical analysis using cyclic voltammetry (See section II-9).

Next, the N-arylpiperidines derivatives are also tested. The reaction worked in a similar way as in the case of N-arylpyrrolidines. The case of the unsubstituted phenylpiperidine worked well, and good reaction yields ranging between 65% and 72% of the final product **3d** are obtained using CdS and CdSe QDs in both used solvents (MeCN and TFT). Comparable yield is obtained in the case of Ir(III)<sup>4</sup> by reaching 67% at a scale of 3 mmol scale in this case. Then, with the electron-rich p-methoxy-phenylpiperidine, the reaction was efficient leading to the final product **3e** with 48-63% yield with both CdS and CdSe QDs in MeCN or TFT. Similar to the previous case, the electron-poor p-ester-phenylpiperidine was able to react only in MeCN and leading to the **3f** in 55% and 45% yield, using CdS and CdSe QDs respectively. Furthermore, another electron-poor substrate was examined by testing the

reaction with p-pinacolboron derivative of the arylpiperidines. Even though this substrate worked well in the case of Ir(III) catalyzed reaction (66% yield)<sup>4</sup>, in our case the reaction never worked with CdS or CdSe QDs and neither by changing the solvents between acetonitrile and trifluorotoluene, despite that the redox potential estimated by the DFT calculation (See Table II-10) seemed to be accessible for the oxidation using the QDs. The unsuccessful reaction in the case of the pinacolboron derivative could be attributed to the possible formation of homocouplings as this kind of reactivity was reported to be efficient using QDs<sup>40</sup> (See Chapter I section I-3.1.5, page 44).

The DFT calculation for the oxidation potentials is also performed for the N-aryl piperidines derivatives and showed clearly the effect of the p-substituents as well as the effect of the solvents. The redox potential for the one-electron oxidation of the un-substituted Phenylpiperidines leading to product **3d** is calculated to be 0.66 V/SCE in TFT and 0.51 in MeCN. The electron poor N-Phenylpiperidines are confirmed to be difficult to oxidize especially in TFT, where the redox potential of the p-ester-Phenylpiperidines is calculated to be equal to 0.75 V/SCE in MeCN and 1.00 V/SCE in TFT.

The photocatalytic results as well as the DFT calculations, show that it is difficult to photocatalyze the reaction in presence of N-arylated amines bearing an electron-poor moiety, which make the redox potential of the substrates to be relatively high compared with valence bands of the QDs. Moreover, the reactions could be more efficient in polar solvents (acetonitrile for instance) as the redox potentials for the substrates are lower by an average of 0.15 V/SCE than those in TFT as it is demonstrated by the DFT calculations. However, it is worth mentioning that in our case the results in acetonitrile for the electron poor substrates were not always reproducible. Not all the synthesized batches of QDs showed the same efficiency after their transfer to acetonitrile. We attributed it to either their poor colloidal stability, especially under long irradiation time (See section II-8 for the stability tests). The variation in the reproducibility of the QDs activity was reported in previous reports in the literature<sup>41</sup>. On the opposite, the reaction performed in TFT after the partial ligand exchange were always reproducible with the different batches of QDs.

## **II-7: Purification and re-use of the QDs after the reactions**

The separation of the reaction mixture from the catalyst used during the reaction is a crucial step to obtain a pure product at the end of the reaction, especially for the re-use of the catalyst. In the case of molecular catalysts, synthetic chemists need to apply some after-reaction workup to separate the catalyst from the reaction's products. Using molecular photocatalysts such as Iridium-based ones, the catalyst is lost during the purification steps. However, the simple purification during the QD-photocatalyzed reaction offers the possibility of collecting and reusing the QDs.

Interestingly, the use of Quantum Dots for photocatalytic reactions does not require a complicated workup to separate them from the reaction mixture at the end of the reaction. In this case, a simple centrifugation step for the reaction mixture can afford the precipitation of the Quantum Dots in the form of precipitate powders, and the reaction products will remain in the solution. After centrifugation, the solution of the reaction that will be free of Quantum Dots can then be cleanly analyzed.

## **II-8. Optimization of the ligand layer: Effect on the stability and the reusability of the QDs.**

As the photocatalytic results revealed, the surface ligand engineering is a crucial parameter for the photocatalytic efficiency of the QDs. We have investigated two different ligand exchange procedures using short-chain ligands. First, the use of C-8 octylphosphonic acid ligands (OPAc) allowed us to perform a partial ligand exchange by replacing a portion of the native oleate ligands. In this case, it is possible to maintain the polarity of the solvent without the need for a complete phase transfer to other solvents. This means that, when working in trifluorotoluene as a reaction solvent, it was possible to keep the same solvent after treating the QDs' surface with the OPAc ligands. Gratifyingly, the QDs were colloidally stable in this case and could retain their optical properties (the exciton peak) after treatment with the OPAc ligands and even after the 24 hours of irradiation during a first reaction round (See Figure II-9-A). The stability of the QDs in this case allowed us to re-use the QDs for several reactions (three times were checked) and the reaction yield after the re-use of the QDs did not drop drastically. After obtaining a 73% yield using CdS QDs in a first round, the yield was

almost the same (75%) in a second use of the QDs. The third round with the same QDs decreased the yield to 63% (See Figure II-9-B).

On the other hand, by using a short C-3 phosphonopropanoic acid ligand (PPAc) a total ligand exchange took place and a complete phase transfer occurred by transferring the QDs into polar solvents. The shorter chain of 3-carbon atoms in the case of the PPAc ligands compared to the 8-carbon atoms of the OPAC ligands and the 18-carbon atoms of the native oleic acid ligands, seems to induce a poor colloidal stability of the QDs and they tend to precipitate after a while and lose their colloidal stability. Moreover, upon irradiation (24 hours reaction,) the PPAc-coated QDs lost their optical properties by losing the peak of their exciton as shown in the UV-Vis spectra of Figure II-9-C. This low stability of the PPAc- QDs made them non reusable for further reactions, and consequently less attractive compared with the OPAC capped QDs.

Therefore, despite the enhancement in the photocatalytic activity of the QDs after the ligand exchange, the selection of the ligand is critical to maintain the stability and the properties of the QDs in order to be able to re-use them in further reaction runs.

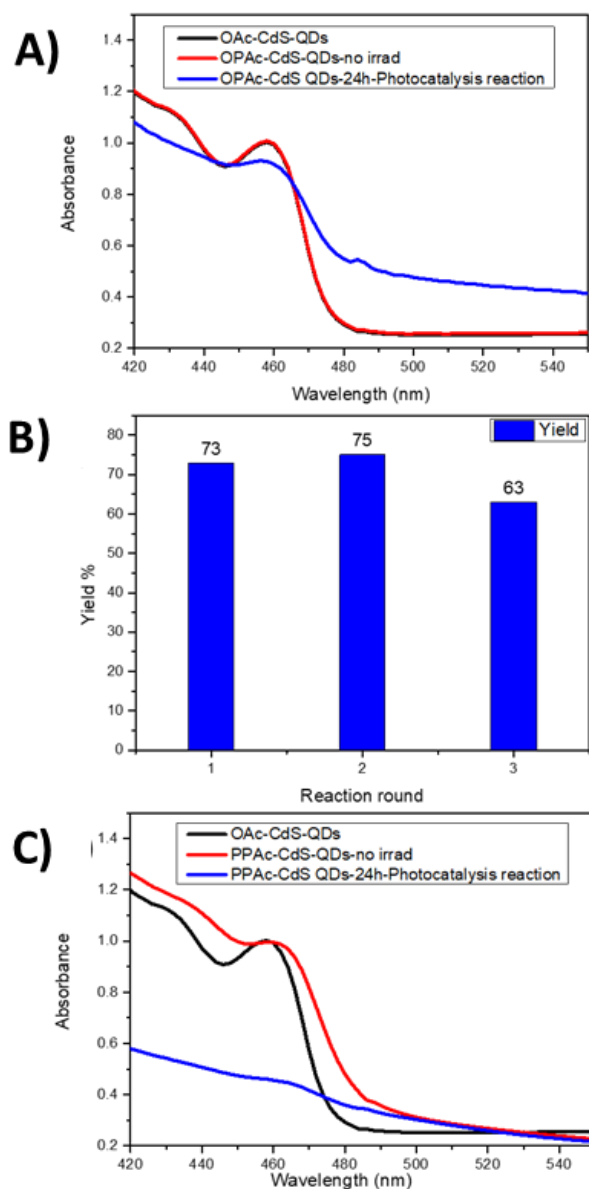
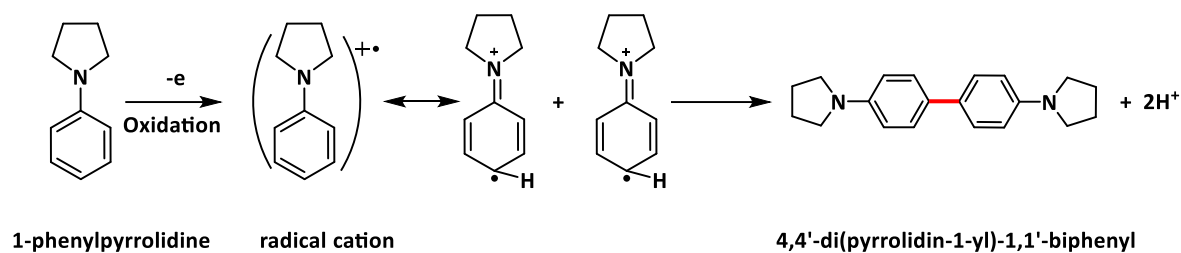


**Figure II-9: UV-Vis analysis of the QDs after ligand exchange and irradiation processes:** A)- UV-Vis spectrum of the as-synthesize CdS QDs capped with oleic acid ligand (black line), then after treating the QDs with OPAC ligands but before irradiation (red line) and after 24 hours of irradiation during a photocatalytic reaction (blue line). B)- histogram showing the re-cycling of the CdS QDs in TFT solvent and ligand exchanged with OPAC for the photocatalytic reaction after 3 reactions with the same QDs. C) UV-Vis spectrum of the as-synthesize CdS QDs capped with oleic acid ligand (black line), then after treating the QDs with PPAC ligands but before irradiation (red line) and after 24 hours of irradiation in a photocatalytic reaction (blue line).

## II-9: Electrochemical analysis: Investigations of the mechanistic steps (reaction's stopping step) and impact of the para-substituents of the N-Arylamines.

In order to investigate the effect of the para-substituents on the redox potential of the N-arylamines and to understand certain steps of the reaction's mechanism, electrochemical analysis were performed using a Cyclic Voltammetry setup connected to a three-electrode system. The three-electrodes system includes a glassy carbon disk ( $d=1\text{mm}$ ) as working electrode, a platinum wire as a counter electrode, and an Ag/AgCl reference electrode. The experiments were performed at room temperature in an argon-filled glovebox. Potential calibration was performed at the end of each data collection using the ferrocene/ferrocenium couple as an internal standard ( $E^\circ = 0.380\text{ V/SCE}$ ; see Appendix II Figure II-A2, page 157, for the Cyclic voltammogram of the ferrocene/ferrocenium couple).

Cyclic Voltammetry for 1mM of 1-phenylpyrrolidine (**1a**), p-methoxy-phenylpyrrolidine (**1b**), p-ester-phenylpyrrolidine (**1c**), and also for the final bicyclic product resulting from the p-methoxy- phenylpyrrolidine (**3b**) were recorded with 0.1M of  $[\text{Bu}_4\text{N}][\text{PF}_6]$  supporting electrolyte in acetonitrile solution. The recorded voltammograms show that **1a** possesses an irreversible electrochemical behavior with a main oxidation wave close to 0.62 V/SCE (Figure II-10-A). This anodic peak is attributed to the one-electron oxidation of **1a** into its radical cation. Electrochemical irreversibility of this process strongly indicates that the formed radical cations dimerize upon abstraction of two protons, yielding a benzidine-type product. Additionally, the voltammogram of **1a** exhibits two clear reduction peaks of significantly lower intensity at potentials close to 0.3 V and 0.5 V. They can be tentatively attributed to the oxidation of the benzidine-type dimerization product. Such dimerization is made possible by the lack of substituent in the 4- position of the aromatic ring for the tertiary amines. Upon the anodic oxidation of the 1-Phenylpyrrolidine an unstable cationic radical is formed, which would tend to dimerize to form benzidine-based compounds 4,4'-di(pyrrolidin-1-yl)-1,1'-biphenyl (See Scheme II-4).<sup>42,43</sup>



*Scheme II-4: Dimerization of cation radical generated from the oxidation of 1-phenylpyrrolidine to form benzidine compounds.*

The cyclic voltammogram of **1c** exhibits a quasi-reversible oxidation event at  $E_{1/2} = 0.91\text{V/SCE}$  (Figure II-10-C). Similarly, **1b** and its corresponding final bicyclic product **3b** exhibit quasi-reversible oxidation waves at  $E_{1/2} = 0.40$  and  $0.43\text{ V/SCE}$  respectively (Figure II-10-B & D). These results show clearly the effect of the para-substituent of the Aryl-amines on their oxidation potential. The presence of an electron-rich moiety has lowered the oxidation potential by  $0.21\text{ V}$  (by comparing **1a** with **1b**). On the other hand, the presence of an electron-poor moiety increased the oxidation potential by  $0.2\text{ V}$  which makes it more difficult to oxidize.

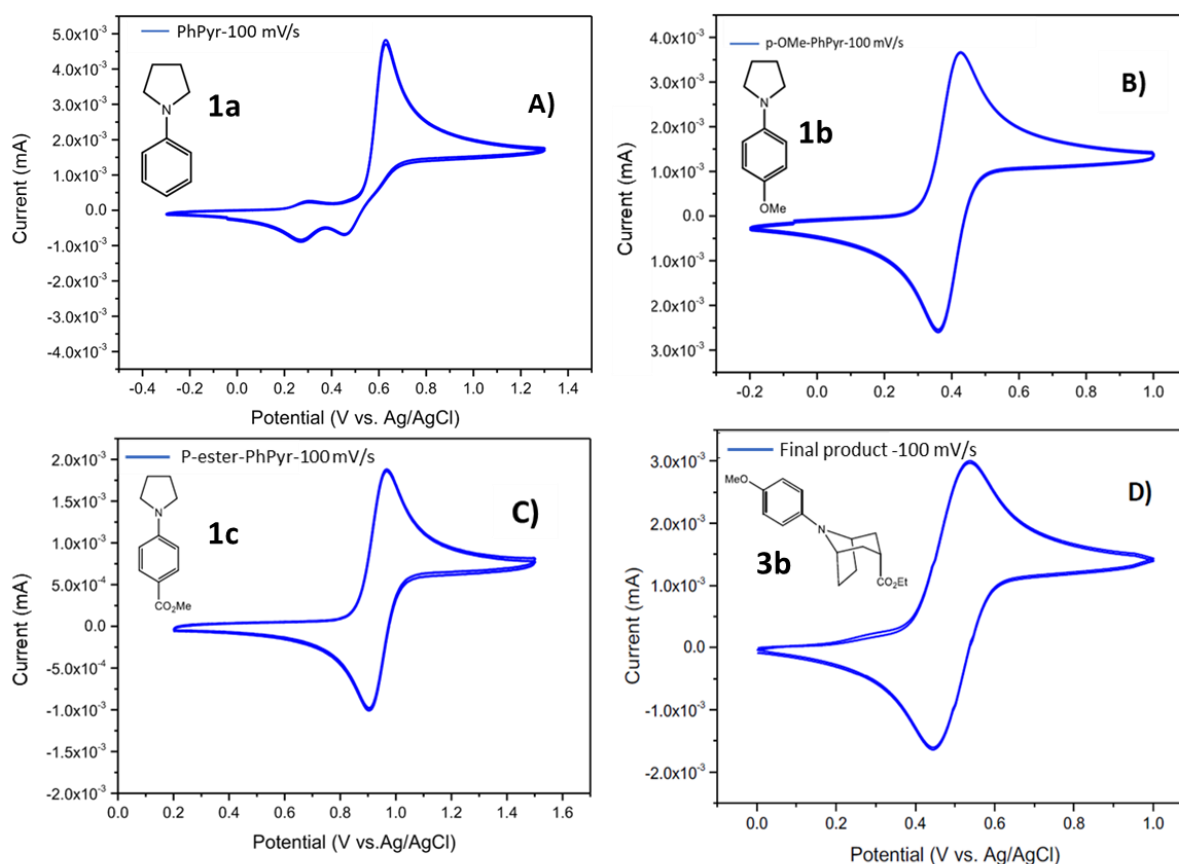


**Figure II-10: Electrochemical analysis:** Cyclic voltammograms of 1mM of A) 1-phenylpyrrolidine B) *p*-methoxy-phenylpyrrolidine, C) *p*-ester-phenylpyrrolidine and D) final bicyclic product of *p*-methoxy-phenylpyrrolidine. Voltammograms were recorded at 100 mV/s scan rate in acetonitrile containing  $[Bu_4N][PF_6]$  (0.1 M) as a supporting electrolyte. Potential calibration was performed ferrocene/ferrocenium couple as an internal standard ( $E^\circ = 0.380$  V/SCE).

The values of the oxidation potential estimated from the cyclic voltammetry analysis were compared to those calculated using DFT. Table II-11 summarizes the values of oxidation potential for substrates **1a**, **1b** and **1c**. The DFT-calculated oxidation potential of **1a** (0.57 V vs. SCE) was quite close to the experimental one deduced from electrochemistry (0.62 V vs SCE). However, the values of **1b** and **1c** vary by around 0.2 V between the two methods, knowing that DFT calculated values are relative values with an uncertainty of around  $\pm 0.1$  V.

N-aryl amine	Calculated $E_{ox}$ (DFT) V / SCE (MeCN)	Experimental $E_{ox}$ (electrochemistry) V / SCE (MeCN)
Phenylpyrrolidine ( <b>1a</b> )	0.57	0.62
<i>p</i> -methoxy- Phenylpyrrolidine ( <b>1b</b> )	0.19	0.4
<i>p</i> -ester- Phenylpyrrolidine ( <b>1c</b> )	0.74	0.91

**Table II-11: Impact of the Para-substituent on the redox potential of the arylamines.** Comparison of the oxidation potential of the *N*-arylamine between the DFT calculated values and the values estimated from the cyclic voltammetry

The voltammograms presented in figure II-10 show different electrochemical behavior in terms of the reversibility of the different compounds. The difference in the reversibility of the molecules could be related to their reactivity in the reaction. In our case, we optimized the reaction condition in the presence of a base that is supposed to deprotonate the formed radical cation and consequently make the corresponding radical more reactive and less electrochemically reversible. Therefore, the effect of the addition of a base is tested by recording the cyclic voltammograms of the studied compounds in the presence of 1.2 equivalent of a base, cesium pivalate in this case, which was selected as a more soluble alternative to cesium acetate.

The cyclic voltammogram of **1c** was very sensitive to the presence of the base. The addition of cesium pivalate leads to a new irreversible oxidation wave that appears at a slightly lower oxidation potential and with higher oxidation current than the oxidation event of the amine alone. This new wave is attributed to an oxidation event of the amine when it is in interaction with cesium pivalate, and to a possible proton-coupled electron transfer process<sup>44</sup>. Moreover, the reversibility of the oxidation event observed in the absence of base disappeared in the presence of cesium pivalate (Figure II-11-A1&2). The voltammograms of **1b** were also sensitive to the presence of the base, but less than in the case of **1c** as the newly formed event possesses a lower oxidative current than the initial event of **1b**, which still shows a small reduction event (Figure II-11-B1&2). This is in agreement with the fact that the photoredox reaction is slower in the case of **1b**. The observed effect of the base on the reversibility of the molecules shows clearly the deprotonation process that occurs during the reactions, and its importance for the reaction to proceed.

Interestingly, the voltammograms of the final product **3b** are almost not affected by the presence of the cesium pivalate base (Figure II-11-C1&2). This indicates that the cation radical of **3b** cannot be deprotonated by the base. This observation supports the fact the final bicyclic product is quite stable and is not further oxidized during the reaction.

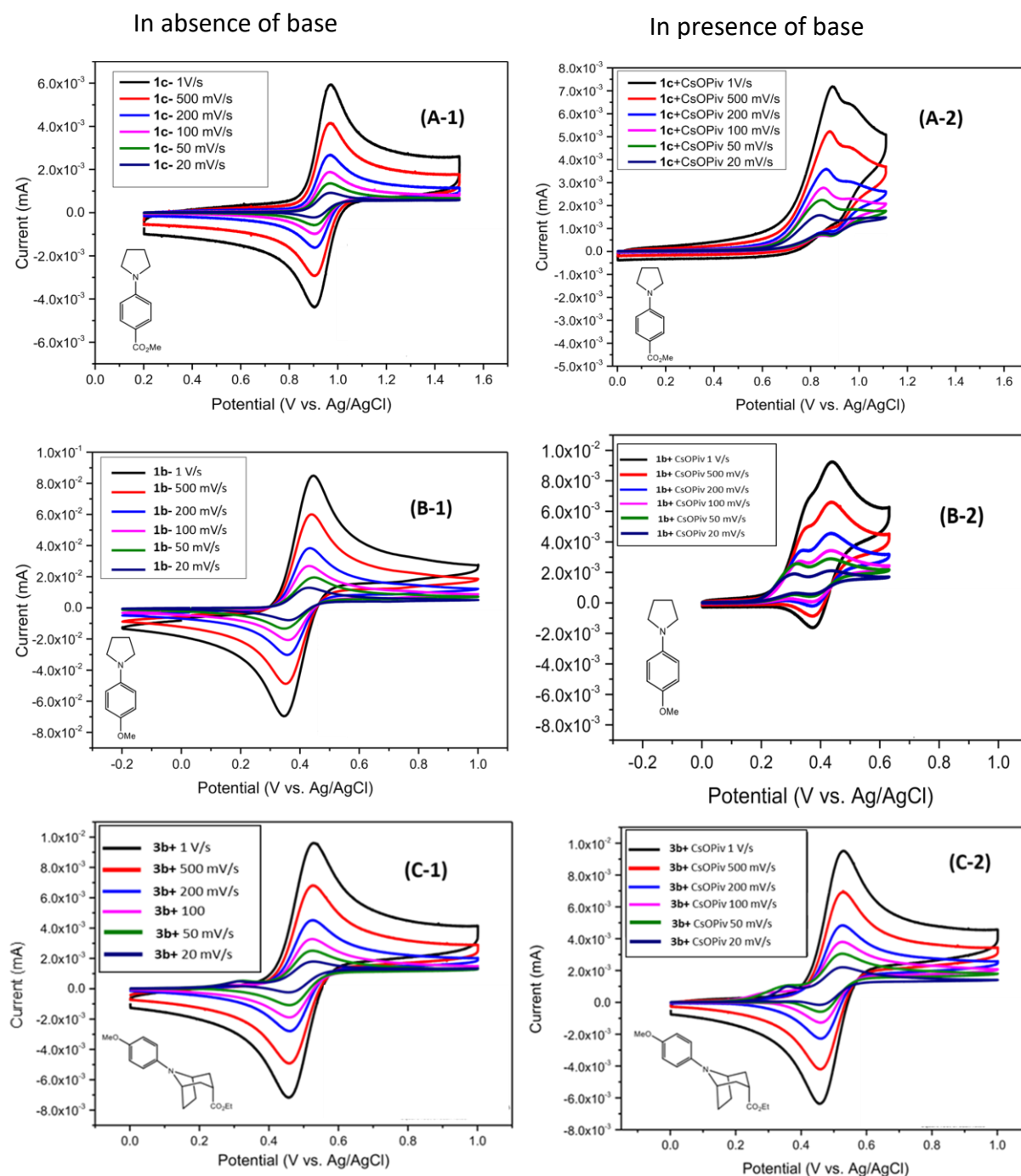


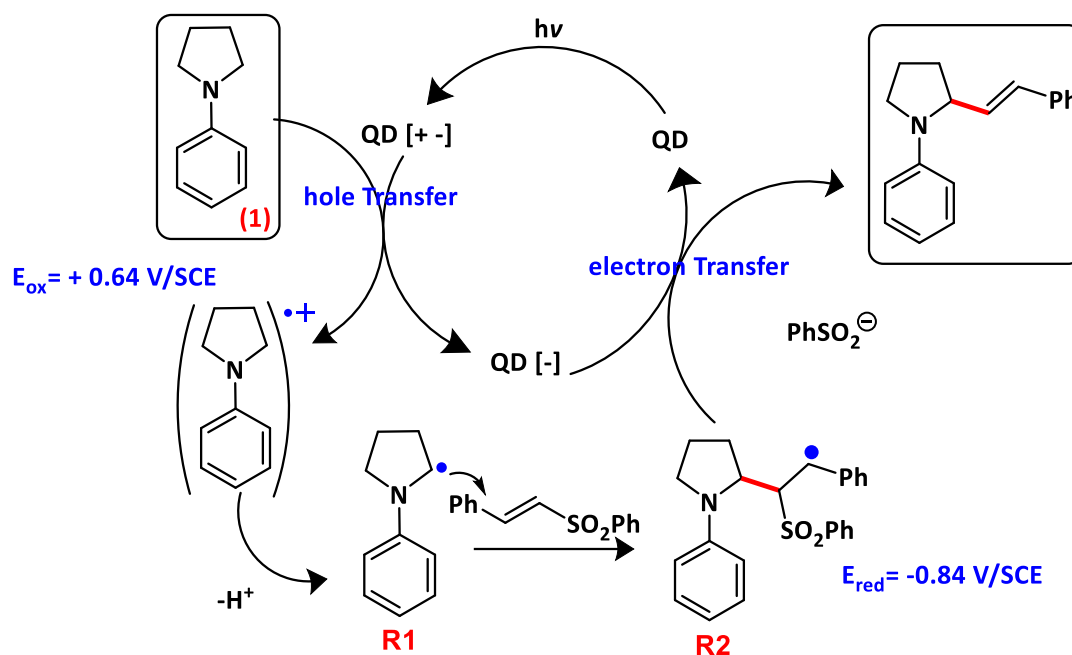
**Figure II-11: Electrochemical study of the effect of the base on the oxidation of the N-arylamines: A) Cyclic Voltammograms of 1mM of 1c, B) 1b, and C) 3b in presence or absence of 1.2mM of Cesium Pivalate base and recorded in 0.1 M  $[Bu_4N][PF_6]$  in acetonitrile at different scan rates.**

## II-10. Proposed catalytic mechanisms.

### II-10.1. Photocatalytic mechanism for the 1-step C-C vinylation coupling reaction.

The catalytic mechanism of the 1-step C-C vinylation coupling reaction was previously described by MacMillan<sup>9</sup> and Weiss<sup>10</sup>. Both MacMillan and Weiss proposed similar mechanistic steps, but the last reduction step to close the reaction cycle was proposed differently.

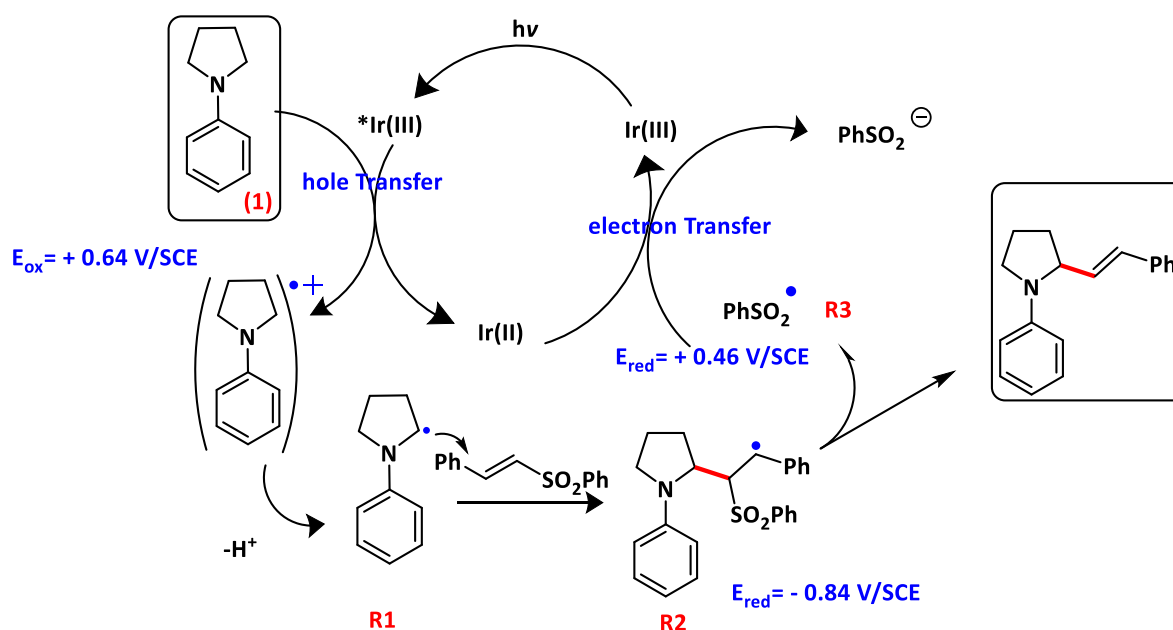
Scheme II-5 represents the catalytic mechanism as proposed by Weiss. The reaction is photocatalyzed using Quantum Dot (QD) that are excited by the convenient light source to create the exciton of electron-hole pair (QD [+·-], in the scheme). Then, an oxidation step for the phenylpyrrolidine ( $E_{\text{ox}} = 0.64 \text{ V/SCE}$ ) occurs to generate a cationic radical. The radical gets deprotonated to create the neutral  $\alpha$ -amino radical **R1**. The formed  $\alpha$ -amino radical attacks the carbon double bond of the phenyl trans-styryl sulfone, which acts as a radical trap to form the  $\beta$ -sulfonyl radical **R2**. Finally, a single electron transfer from the QD reduces **R2** ( $E_{\text{red}} = -0.84 \text{ V/SCE}$ ), eliminates a phenyl sulfonyl anion, and forms the C-C coupling product.



**Scheme II-5: Photocatalytic mechanism for the C-C vinylation coupling reaction as proposed by E.A Weiss; reaction between 1- phenylpyrrolidine (PhPyr), and phenyl trans-styryl sulfone using QDs. The redox potentials specified in the scheme are calculated by Dr. Jean Marie MOUESCA using DFT calculations.**

Scheme II-6 represents the catalytic mechanism as proposed by MacMillan. The reaction is photocatalyzed using  $\text{Ir}\{\text{dF}(\text{CF}_3)\text{ppy}\}_2(\text{dtbpy})\text{PF}_6 = \text{Ir}(\text{III})$  complex. Under visible light irradiation the  $\text{Ir}(\text{III})$  creates its excited-state  $\text{Ir}(\text{III})^*$ , which is a strong oxidant. Then, from the photoexcited complex a single-electron transfer occurs to oxidize the Phenyl pyrrolidine to generate the  $\alpha$ -amino radical **R1** after the deprotonation of the corresponding cation. **R1** reacts with the vinyl sulfone radical traps and generates the  $\beta$ -sulfonyl radical **R2**, which after elimination of a sulfinyl radical **R3** would provide the C-C vinylation product. The completion of the photocatalytic cycle in this case is proposed to be accomplished via reduction of the sulfinyl radical **R3** ( $E_{\text{red}} = +0.46\text{V}/\text{SCE}$ ) to give a sulfinate anion while regenerating the photocatalyst.

Comparing the reduction potential of **R2** and **R3**, it is clear that the reduction of **R3** ( $E_{\text{red}} = +0.46\text{V}/\text{SCE}$ ) is much easier than the reduction of **R2** ( $E_{\text{red}} = -0.84\text{V}/\text{SCE}$ ). Then, the mechanism proposed by MacMillan concerning the closure of the catalytic cycle seems more likely.

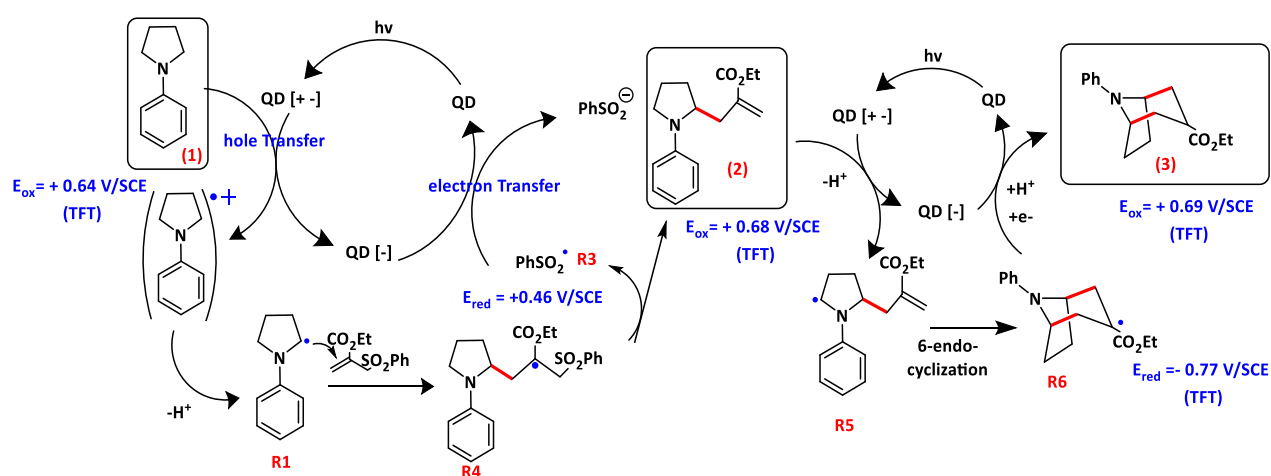


**Scheme II-6: Photocatalytic mechanism for the C-C vinylation coupling reaction as proposed by McMillan;** reaction between 1-phenylpyrrolidine (PhPyr), and phenyl trans-styryl sulfone using  $\text{Ir}\{\text{dF}(\text{CF}_3)\text{ppy}\}_2(\text{dtbpy})\text{PF}_6 = \text{Ir}(\text{III})$ . The redox potentials specified in the scheme are calculated by Dr. Jean Marie MOUESCA using DFT calculations.

## II-10.2. Photocatalytic mechanism for the 2-step Tropane derivatives synthesis reaction.

Scheme II-7 shows the reaction mechanism proposed for the 2 catalytic cycles of the reaction starting from 1-phenylpyrrolidine and ethyl 2-((phenylsulfonyl)methyl)acrylate (allyl sulfone trap) leading to the bicyclic skeleton of the tropane derivative using QDs. Under visible light irradiation, the QD create the electron-hole pair (exciton) and reach their excited state, with an electron in the conduction band and a hole in the valence band of the QD (QD [+], in the scheme). At this stage the hole in the valence band of the QD is able to oxidize 1-phenylpyrrolidine ( $E_{\text{ox}} = 0.64 \text{ V/SCE}$  in TFT) to its  $\alpha$ -amino radical cation, which create the  $\alpha$ -amino radical **R1** after deprotonation. Then, this radical adds to the double bond of the allyl sulfone radical trap, leading to an intermediate  $\alpha$ -ester radical **R4** which, after elimination of a sulfinyl radical **R3**, would provide the first C-C allylation intermediate product **2**. The completion of the first photocatalytic cycle is proposed to be accomplished via reduction of the sulfinyl radical **R3** ( $E_{\text{red}} = +0.46 \text{ V/SCE}$ ) to give a sulfinate anion, similar to what was proposed by MacMillan for the vinylation reaction.

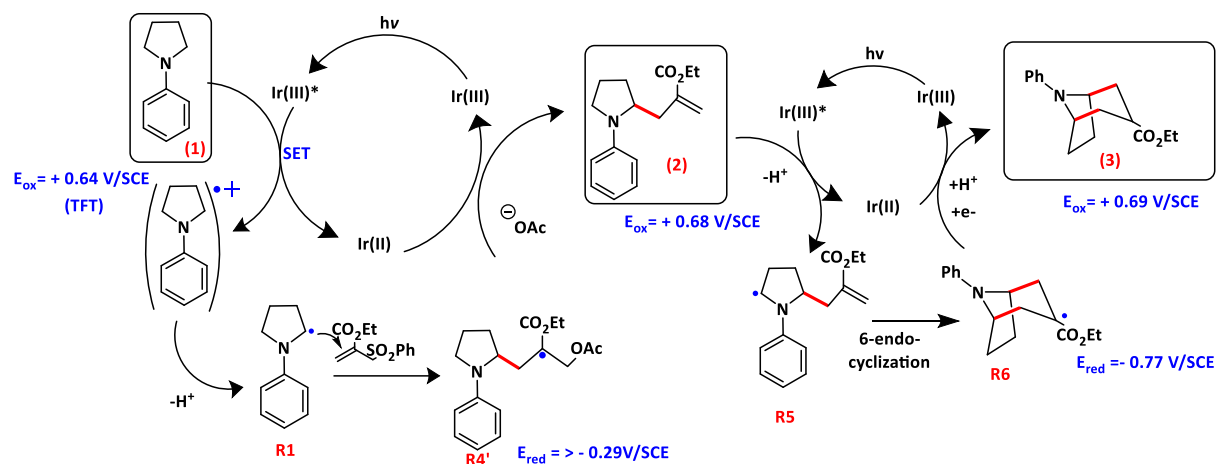
The second catalytic cycle starts after the formation of the intermediate product **2** which is ready to be oxidized by the QD. After oxidation of the intermediate product **2** by the excited QD, a subsequent deprotonation takes place and generates the  $\alpha$ -aminoalkyl radical **R5**. Then, **R5** undergoes a 6-endo-trig cyclization, leading to the bicyclic  $\alpha$ -ester radical **R6** (calculated reduction potential  $E_{\text{red}} = -0.77$  V/SCE). At this stage, if the excited QD is reducing enough, a reduction of the radical **R6** by a single electron transfer from the conduction band of the excited QDs takes place, thus closing the second catalytic cycle to finally produce the desired bicyclic product **3**, which was proved to be stable and not undergoing further oxidation (see the electrochemical analysis in section II-9).



**Scheme II-7: Photocatalytic mechanism of the 2-step Tropane derivatives reaction;** reaction between 1- phenylpyrrolidine (PhPyr), and ethyl 2-((phenylsulfonyl)methyl)acrylate. The oxidation potentials  $E_{\text{ox}}$  of PhPyr is  $+0.64$  V / SCE, the reduction potential of radical R3  $E_{\text{red}}$  is  $+0.46$  V /SCE, the oxidation of the intermediate product **2** is  $E_{\text{ox}} = + 0.68$  V /SCE and the reduction potential of the radical R6 is  $E_{\text{red}} = -0.77$  V /SCE. The redox potentials are calculated using DFT calculations by Dr. Jean-Marie MOUESCA.

In the work by our colleagues from the University of Bern, the reaction optimizations and investigations were done using ethyl 2-(acetoxymethyl)acrylate (acetate trap) as the radical trap. The use of the acetate trap is expected to induce a slight difference in the proposed catalytic mechanism, particularly in closing the first catalytic cycle. Scheme II-8 shows the catalytic mechanism in this case. The reaction starts by oxidizing the phenylpyrrolidine **1** to generate the radical **R1**. Then, **R1** reacts with the acetate trap **R4'** is estimated to be  $E_{\text{red}} > -0.29$  V/SCE. With this potential, such a radical is

expected to be easily reduced by the photocatalysts, which closes the first catalytic cycle by providing the mono-allylated pyrrolidine **2** after elimination of an acetate ion.

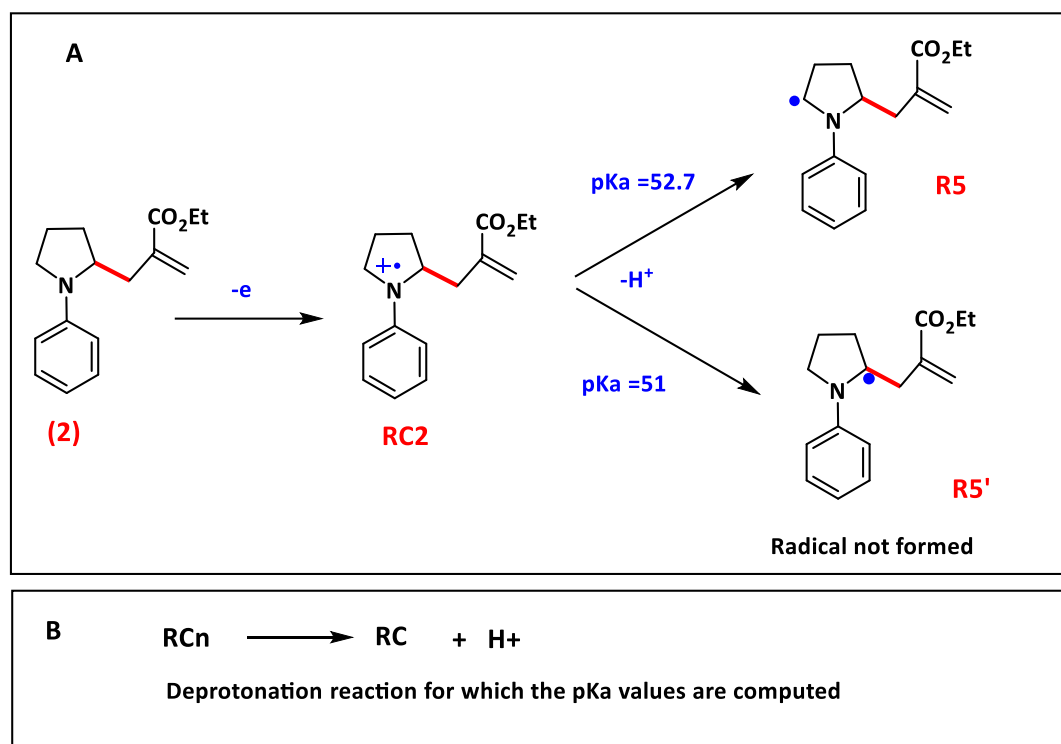


**Scheme II-8: Photocatalytic mechanism of the 2-step Tropane derivatives reaction proposed by the colleagues from the group of Renaud using  $\text{Ir}\{\text{dF}(\text{CF}_3)\text{ppy}\}_2\{\text{dtbpy}\}\text{PF}_6$  catalyst (Ir(III)); reaction between 1- phenylpyrrolidine (PhPyr), and ethyl 2-(acetoxymethyl)acrylate . The oxidation potentials  $E_{ox}$  of PhPyr is +0.64V / SCE, the reduction potential of radical R3  $E_{red}$  is +0.46 V /SCE, the oxidation of the intermediate product 2 is  $E_{ox} = +0.68 \text{ V / SCE}$  and the reduction potential of the radical R6 is  $E_{red} = -0.77 \text{ V / SCE}$ . The redox potentials are calculated using DFT calculations by Dr. Jean-Marie MOUESCA.**

### II-10.3. Selectivity of the radical formation and the stability of the final product: pKa calculations.

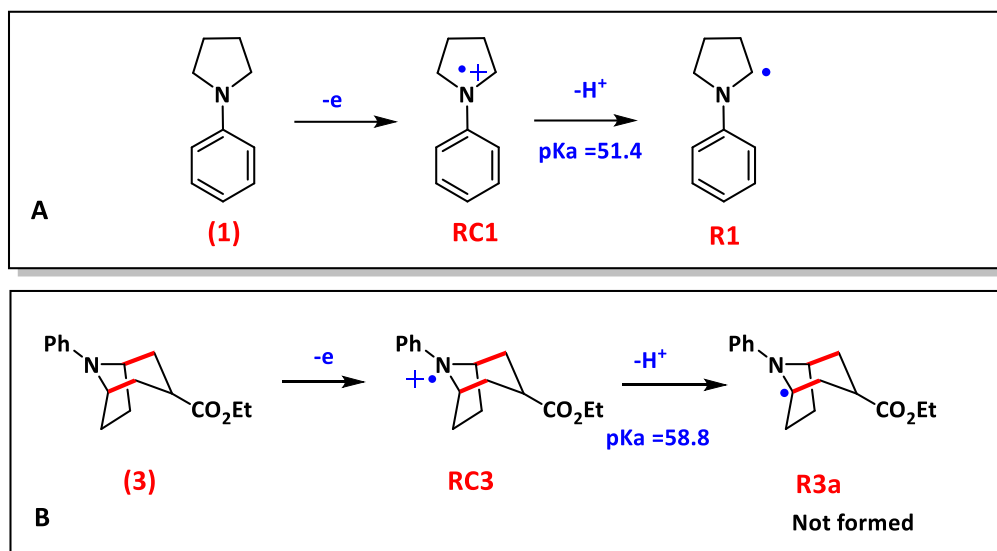
One of the main factors for the success of the Tropane derivatives reaction relies on the selectivity of the formed radicals. First, the oxidation of the mono-allylated intermediate (**2**) leads to the formation of the radical cation **RC2**. Then, after deprotonation of **RC2** it is possible to form two different radicals **R5** or **R5'** (see scheme II-9-A). The formation of **R5'** will make the cyclization step challenging and decrease the efficiency of the process to reach the targeted bicyclic product. However, when identifying the reaction products, no products were observed resulting from the radical **R5'**, even though it is not excluded that such products could be formed in small portions. This observation of the favorable formation of **R5** radical is referred to the regioselectively deprotonated **RC2** to form mainly the radical **R5**. To understand the selective formation of the radicals during the reaction mechanism, Dr. Jean-Marie MOUESCA calculated the pKa values for the deprotonation reaction of the radical cations (See Scheme II-9-B). The calculated pKa values for the radicals **R5** and **R5'** are very close 52.7 and 51 respectively (See Scheme II-9-A). However, we cannot use these values to

justify the selectivity of the formed radical. This type of selectivity for the less substituted position is well-reported and can be explained by both steric and stereoelectronic effects<sup>45,46</sup>.



**Scheme II-9: Selectivity of the radical formation.** A) The regioselectivity of radical formation after the deprotonation step, B) Equation of the reaction for which the pKa values are computed

Furthermore, the oxidation potential of the three amines **1** ( $E_{ox}=0.64$  V/SCE), **2** ( $E_{ox}=0.68$  V / SCE) and **3** ( $E_{ox}=0.69$  V/ SCE) present in the reaction solution are close to each other and can be easily oxidized by the QDs. However, only the radical cations **RC1** (calculated pKa = 51.4) and **RC2** (calculated pKa = 52.7) undergo an efficient deprotonation to generate the corresponding  $\alpha$ -amino radicals (See Scheme II-10-A). The deprotonation of the bicyclic radical **RC3** (pKa 58.4) is less favorable and, indeed, no product resulting from the bicyclic radical **R3a** has been observed (See Scheme II-10-B).



**Scheme II-10: pKa of the generated radicals.** A) oxidation of the starting material (1) and the pKa of the corresponding radical. B) the pKa of the radical possibly generated if the oxidation of the final product (3) occurred.

Our co-workers at the Renaud group, separately attempted to afford the allylation reaction of the pure bicyclic product **3** under standard reaction conditions. The reaction led only to partial consumptions of the starting material (**3**) without the formation of any new product.

The results of the pKa calculation with the electrochemical analysis presented in section II-9, indicate that the deprotonation of the radical generated by the oxidation final bicyclic product is not favorable. This observation is the key factor of the success of the process, as the final product of this reaction is quite stable and not transforming into other species.

#### II-10.4. Photocatalytic activity of the different types of QDs: Insights into the mechanistic redox steps

The photocatalytic results reported above show a clear variation in both the efficiency and the products' selectivity of the different types of QDs. In the case of the core CdS and CdSe and that of the inverted Type-I CdS-CdSe QDs, the best photocatalytic activity was obtained. We attribute that to the accessibility of the charge carriers (mainly holes in our reactions) is supposed to be the best among the QDs' structures we tested. In addition, the use of these types of QDs was helpful to expand their activity toward the 2-step tropane

derivatives reaction. They were able to accomplish the different redox processes at different stages of the catalytic mechanism due to their suitable oxidation and reduction capabilities.

The redox activity during the reaction starts with the first oxidation for the PhPyr ( $E_{\text{ox}} = 0.64 \text{ V / SCE}$ ). Then, the QDs could close the first cycle by reducing the sulfinyl radical **R3** ( $E_{\text{red}} = +0.46 \text{ V / SCE}$ ) which is expected to be easy to reduce. A second oxidation of the intermediate product (**2**) is also possible as the QDs are still able to enter a second cycle starting by a similar oxidation process ( $E_{\text{ox}} = 0.68 \text{ V / SCE}$ ), which is closed by the reduction of the bicyclic  $\alpha$ -ester radical **R6** having a reduction potential  $E_{\text{red}} = -0.77 \text{ V / SCE}$ . The reduction of the **R6**  $\alpha$ -ester radical needs a stronger reducing power by the QDs compared to that needed for the reduction of the **R3** radical. In this case, CdS, CdSe and core-shell CdS-CdSe QDs could ensure the reduction power to accomplish the closing of the second catalytic cycle. The position of the conduction band edge of CdS and CdSe QDs can be estimated to be close to  $E_{\text{C.B.}} = -1.4 \text{ V/SCE}$  for CdS, by taking into account a band gap of 2.6 eV for CdS QDs (460 nm) and a relative value of the valence band of 1.2 V/SCE. Similarly,  $E_{\text{C.B.}} = -1.2 \text{ V/SCE}$  was estimated for CdSe QDs having a band gap of 2.3 eV (540 nm) and a relative value of the valence band of 1.1 V/SCE (see Table II-1 section II-2).

On the other hand, using InP-ZnS QDs the reaction stopped after closing the first catalytic cycle without producing the final bicyclic product. In the case of this type of QDs, the conduction band of the InP-ZnS was previously estimated using electrochemical measurements,<sup>11,21</sup> and showed that the position of the conduction band is close to  $-0.9 \text{ V/SCE}$ . Then, taking into account the reported values of the conduction band of InP-ZnS, we can suppose that the reduction of the  $\alpha$ -ester radical **R6** ( $E_{\text{red}} = -0.77 \text{ V / SCE}$ ) is challenging in this case, which makes the InP-ZnS not able to close the second catalytic cycle and consequently be more selective to the first cycle and the formation of the intermediate mono-allylated product.

### Conclusion

In conclusion, we report the ability of semiconductor Quantum Dots (QDs) to photocatalyze a newly developed annulation strategy for synthesizing bicyclic alkaloid skeletons of Tropane derivatives. The reported reaction requires two successive charge transfer processes to perform two oxidation. We study different types and structures of Quantum Dots and show the effect of the QDs' structure efficiency on the charge transfer with the reaction substrate. We show that core structured CdS and CdSe QDs and inverted Type-I CdS-CdSe core-shell QDs are able to efficiently perform all the necessary redox steps to obtain the desired final product of the reaction with more than 70% yield. We also show that InP-ZnS QDs were selective towards only the first reaction step, which allows us to classify the tested Quantum Dots based on the desired photocatalytic process.

The optimization of the surface ligand layer of the Quantum Dots by mixing two ligands of different chain lengths is of significant impact on their photocatalytic activity and enhances their ability to produce the desired final product of the reaction. After optimizing the ligand layers, the best Quantum yield of 0.18% was obtained using CdS QDs for the one-step vinylation reaction. Furthermore, this partial ligand exchange retains the stability of the QDs and allows their re-use in more than one reaction round.

The findings described in Chapter II show that using the semiconductor QDs, it is possible to perform the desired two photoredox catalytic cycles in one reaction pot. The reactions are performed at a low reaction scale of 0.001 mmol, and relatively high yields are obtained. The upscaling of the reaction to reach the preparative organic chemistry scales is underway within the collaboration with the Renaud group at the University of Bern.

The highest Quantum Yield obtained is equal to 0.18%, which is typical for the QD-photocatalyzed reactions reported in the literature. Therefore, attempts to enhance the Quantum yield of the QD-photocatalyzed reactions will be explored in the next Chapter of this Thesis.

## References

- (1) Roush, W. R. Total Synthesis of Biologically Active Natural Products. *J. Am. Chem. Soc.* **2008**, *130* (21), 6654–6656. <https://doi.org/10.1021/ja8028813>.
- (2) Ravelli, D.; Protti, S.; Fagnoni, M. Carbon–Carbon Bond Forming Reactions via Photogenerated Intermediates. *Chem. Rev.* **2016**, *116* (17), 9850–9913. <https://doi.org/10.1021/acs.chemrev.5b00662>.
- (3) Kohnen-Johannsen, K. L.; Kayser, O. Tropane Alkaloids: Chemistry, Pharmacology, Biosynthesis and Production. *Molecules* **2019**, *24* (4), 796. <https://doi.org/10.3390/molecules24040796>.
- (4) Colson, E.; Andrez, J.; Dabbous, A.; Dénès, F.; Maurel, V.; Mouesca, J.-M.; Renaud, P. Tropane and Related Alkaloid Skeletons via a Radical [3+3]-Annulation Process. *Commun Chem* **2022**, *5* (1), 1–12. <https://doi.org/10.1038/s42004-022-00671-x>.
- (5) Xi, Z.-W.; Yang, L.; Wang, D.-Y.; Pu, C.-D.; Shen, Y.-M.; Wu, C.-D.; Peng, X.-G. Visible-Light Photocatalytic Synthesis of Amines from Imines via Transfer Hydrogenation Using Quantum Dots as Catalysts. *J. Org. Chem.* **2018**, *83* (19), 11886–11895. <https://doi.org/10.1021/acs.joc.8b01651>.
- (6) Xi, Z.-W.; Yang, L.; Wang, D.-Y.; Feng, C.-W.; Qin, Y.; Shen, Y.-M.; Pu, C.; Peng, X. Visible Light Induced Reduction and Pinacol Coupling of Aldehydes and Ketones Catalyzed by Core/Shell Quantum Dots. *J. Org. Chem.* **2021**, *86* (3), 2474–2488. <https://doi.org/10.1021/acs.joc.0c02627>.
- (7) Wang, P.; Zhang, J.; He, H.; Xu, X.; Jin, Y. Efficient Visible Light-Driven H<sub>2</sub> Production in Water by CdS/CdSe Core/Shell Nanocrystals and an Ordinary Nickel–Sulfur Complex. *Nanoscale* **2014**, *6* (22), 13470–13475. <https://doi.org/10.1039/C4NR04600E>.
- (8) Wang, P.; Wang, M.; Zhang, J.; Li, C.; Xu, X.; Jin, Y. Shell Thickness Engineering Significantly Boosts the Photocatalytic H<sub>2</sub> Evolution Efficiency of CdS/CdSe Core/Shell Quantum Dots. *ACS Appl. Mater. Interfaces* **2017**, *9* (41), 35712–35720. <https://doi.org/10.1021/acsami.7b07211>.
- (9) Noble, A.; MacMillan, D. W. C. Photoredox  $\alpha$ -Vinylolation of  $\alpha$ -Amino Acids and *N*-Aryl Amines. *J. Am. Chem. Soc.* **2014**, *136* (33), 11602–11605. <https://doi.org/10.1021/ja506094d>.
- (10) Zhang, Z.; Edme, K.; Lian, S.; Weiss, E. A. Enhancing the Rate of Quantum-Dot-Photocatalyzed Carbon–Carbon Coupling by Tuning the Composition of the Dot’s Ligand Shell. *J. Am. Chem. Soc.* **2017**, *139* (12), 4246–4249. <https://doi.org/10.1021/jacs.6b13220>.
- (11) Chakraborty, I. N.; Roy, S.; Devatha, G.; Rao, A.; Pillai, P. P. InP/ZnS Quantum Dots as Efficient Visible-Light Photocatalysts for Redox and Carbon–Carbon Coupling Reactions. *Chem. Mater.* **2019**, *31* (7), 2258–2262. <https://doi.org/10.1021/acs.chemmater.9b00086>.
- (12) te Velde, G.; Baerends, E. J. Numerical Integration for Polyatomic Systems. *Journal of Computational Physics* **1992**, *99* (1), 84–98. [https://doi.org/10.1016/0021-9991\(92\)90277-6](https://doi.org/10.1016/0021-9991(92)90277-6).
- (13) Nozik, A. J. Photoelectrochemistry: Applications to Solar Energy Conversion. *Annual Review of Physical Chemistry* **1978**, *29* (1), 189–222. <https://doi.org/10.1146/annurev.pc.29.100178.001201>.
- (14) *Physical and Chemical Applications of Dye-stuffs* | Prof. Dr. Fritz Peter Schäfer (auth.), F. P. Schäfer, H. Gerischer, F. Willig, H. Meier, H. Jahnke, M. Schönborn, G. Zimmermann (eds.) | download. <https://ka.fr1lib.org/book/5927909/d61a00> (accessed 2022-07-05).

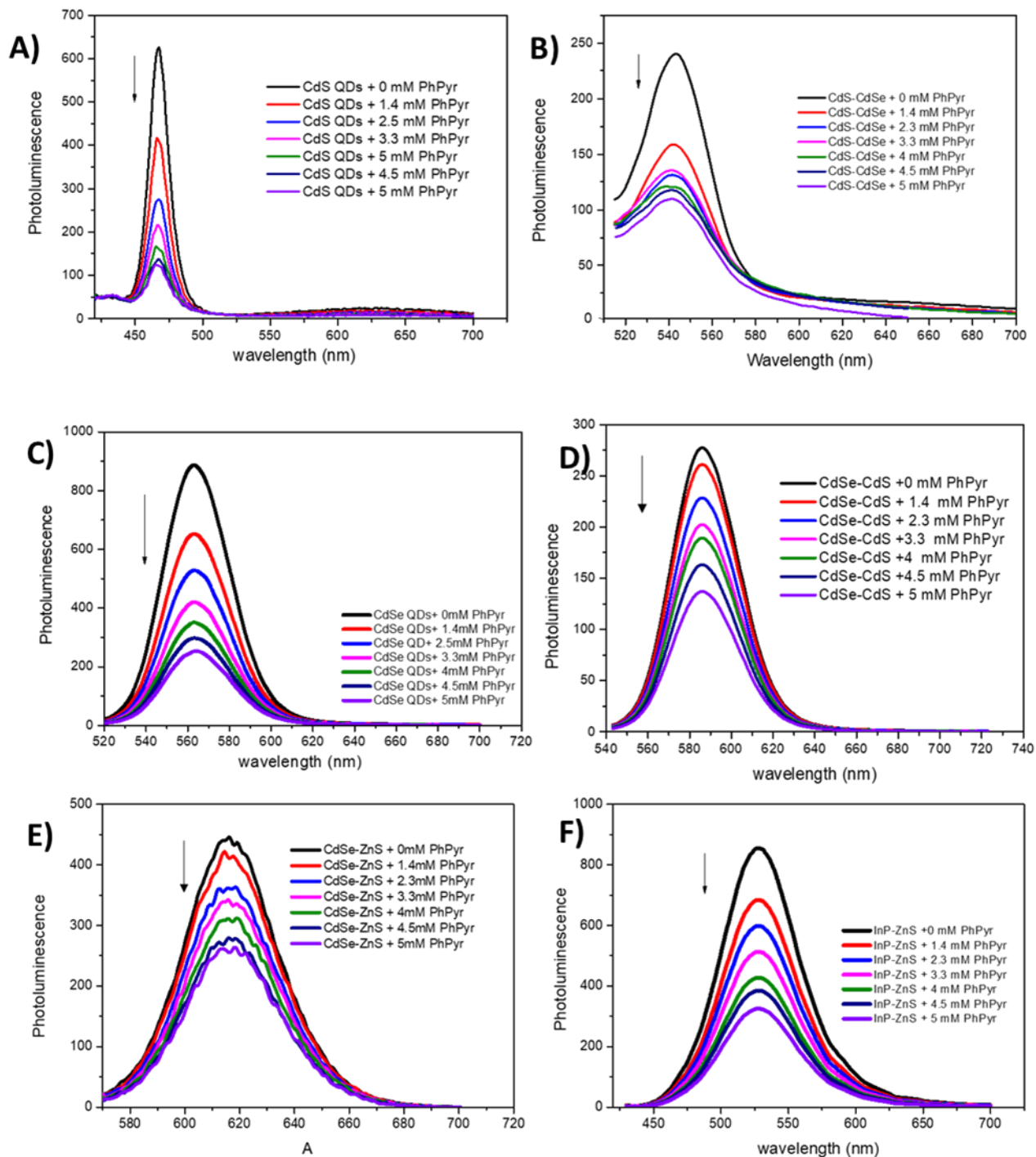
- (15) Nasir, J. A.; Rehman, Z. ur; Shah, S. N. A.; Khan, A.; Butler, I. S.; Catlow, C. R. A. Recent Developments and Perspectives in CdS-Based Photocatalysts for Water Splitting. *J. Mater. Chem. A* **2020**, *8* (40), 20752–20780. <https://doi.org/10.1039/D0TA05834C>.
- (16) Jasieniak, J.; Califano, M.; Watkins, S. E. Size-Dependent Valence and Conduction Band-Edge Energies of Semiconductor Nanocrystals. *ACS Nano* **2011**, *5* (7), 5888–5902. <https://doi.org/10.1021/nn201681s>.
- (17) Tamang, S.; Lincheneau, C.; Hermans, Y.; Jeong, S.; Reiss, P. Chemistry of InP Nanocrystal Syntheses. *Chem. Mater.* **2016**, *28* (8), 2491–2506. <https://doi.org/10.1021/acs.chemmater.5b05044>.
- (18) Wei, S.-H.; Zunger, A. Calculated Natural Band Offsets of All II–VI and III–V Semiconductors: Chemical Trends and the Role of Cation d Orbitals. *Appl. Phys. Lett.* **1998**, *72* (16), 2011–2013. <https://doi.org/10.1063/1.121249>.
- (19) Wang, J.; Xia, T.; Wang, L.; Zheng, X.; Qi, Z.; Gao, C.; Zhu, J.; Li, Z.; Xu, H.; Xiong, Y. Enabling Visible-Light-Driven Selective CO<sub>2</sub> Reduction by Doping Quantum Dots: Trapping Electrons and Suppressing H<sub>2</sub> Evolution. *Angewandte Chemie International Edition* **2018**, *57* (50), 16447–16451. <https://doi.org/10.1002/anie.201810550>.
- (20) Reiss, P.; Protière, M.; Li, L. Core/Shell Semiconductor Nanocrystals. *Small* **2009**, *5* (2), 154–168. <https://doi.org/10.1002/smll.200800841>.
- (21) Yu, S.; Fan, X.-B.; Wang, X.; Li, J.; Zhang, Q.; Xia, A.; Wei, S.; Wu, L.-Z.; Zhou, Y.; Patzke, G. R. Efficient Photocatalytic Hydrogen Evolution with Ligand Engineered All-Inorganic InP and InP/ZnS Colloidal Quantum Dots. *Nat Commun* **2018**, *9* (1), 4009. <https://doi.org/10.1038/s41467-018-06294-y>.
- (22) Zhao, J.; Wang, X.; Xu, Z.; C. Loo, J. S. Hybrid Catalysts for Photoelectrochemical Reduction of Carbon Dioxide: A Prospective Review on Semiconductor/Metal Complex Co-Catalyst Systems. *Journal of Materials Chemistry A* **2014**, *2* (37), 15228–15233. <https://doi.org/10.1039/C4TA02250E>.
- (23) Zhang, Z.; Rogers, C. R.; Weiss, E. A. Energy Transfer from CdS QDs to a Photogenerated Pd Complex Enhances the Rate and Selectivity of a Pd-Photocatalyzed Heck Reaction. *J. Am. Chem. Soc.* **2020**, *142* (1), 495–501. <https://doi.org/10.1021/jacs.9b11278>.
- (24) Yu, W. W.; Qu, L.; Guo, W.; Peng, X. Experimental Determination of the Extinction Coefficient of CdTe, CdSe, and CdS Nanocrystals. *Chem. Mater.* **2003**, *15* (14), 2854–2860. <https://doi.org/10.1021/cm034081k>.
- (25) Synthesis of Porphyrin–CdSe Quantum Dot Assemblies: Controlling Ligand Binding by Substituent Effects.
- (26) Jasieniak, J.; Smith, L.; van Embden, J.; Mulvaney, P.; Califano, M. Re-Examination of the Size-Dependent Absorption Properties of CdSe Quantum Dots. *J. Phys. Chem. C* **2009**, *113* (45), 19468–19474. <https://doi.org/10.1021/jp906827m>.
- (27) Niu, Y.; Pu, C.; Lai, R.; Meng, R.; Lin, W.; Qin, H.; Peng, X. One-Pot/Three-Step Synthesis of Zinc-Blende CdSe/CdS Core/Shell Nanocrystals with Thick Shells. *Nano Res.* **2017**, *10* (4), 1149–1162. <https://doi.org/10.1007/s12274-016-1287-3>.
- (28) Tessier, M. D.; Dupont, D.; De Nolf, K.; De Roo, J.; Hens, Z. Economic and Size-Tunable Synthesis of InP/ZnE (E = S, Se) Colloidal Quantum Dots. *Chem. Mater.* **2015**, *27* (13), 4893–4898. <https://doi.org/10.1021/acs.chemmater.5b02138>.
- (29) Impellizzeri, S.; Monaco, S.; Yildiz, I.; Amelia, M.; Credi, A.; Raymo, F. M. Structural Implications on the Electrochemical and Spectroscopic Signature of CdSe–ZnS Core–Shell Quantum Dots. *J. Phys. Chem. C* **2010**, *114* (15), 7007–7013. <https://doi.org/10.1021/jp1021032>.

- (30) Karan, S.; Majumder, M.; Mallik, B. Controlled Surface Trap State Photoluminescence from CdS QDs Impregnated in Poly(Methyl Methacrylate). *Photochem Photobiol Sci* **2012**, *11* (7), 1220–1232. <https://doi.org/10.1039/c2pp25023c>.
- (31) Purcell-Milton, F.; Visheratina, A. K.; Kuznetsova, V. A.; Ryan, A.; Orlova, A. O.; Gun'ko, Y. K. Impact of Shell Thickness on Photoluminescence and Optical Activity in Chiral CdSe/CdS Core/Shell Quantum Dots. *ACS Nano* **2017**, *11* (9), 9207–9214. <https://doi.org/10.1021/acsnano.7b04199>.
- (32) *Principles of Fluorescence Spectroscopy*.
- (33) AbouElhamd, A. R.; Al-Sallal, K. A.; Hassan, A. Review of Core/Shell Quantum Dots Technology Integrated into Building's Glazing. *Energies* **2019**, *12* (6), 1058. <https://doi.org/10.3390/en12061058>.
- (34) Vasudevan, D.; Gaddam, R. R.; Trinchì, A.; Cole, I. Core–Shell Quantum Dots: Properties and Applications. *Journal of Alloys and Compounds* **2015**, *636*, 395–404. <https://doi.org/10.1016/j.jallcom.2015.02.102>.
- (35) Maity, P.; Debnath, T.; Ghosh, H. N. Ultrafast Charge Carrier Delocalization in CdSe/CdS Quasi-Type II and CdS/CdSe Inverted Type I Core–Shell: A Structural Analysis through Carrier-Quenching Study. *J. Phys. Chem. C* **2015**, *119* (46), 26202–26211. <https://doi.org/10.1021/acs.jpcc.5b08913>.
- (36) Pan, Z.; Zhang, H.; Cheng, K.; Hou, Y.; Hua, J.; Zhong, X. Highly Efficient Inverted Type-I CdS/CdSe Core/Shell Structure QD-Sensitized Solar Cells. *ACS Nano* **2012**, *6* (5), 3982–3991. <https://doi.org/10.1021/nn300278z>.
- (37) Kodaimati, M. S.; McClelland, K. P.; He, C.; Lian, S.; Jiang, Y.; Zhang, Z.; Weiss, E. A. Viewpoint: Challenges in Colloidal Photocatalysis and Some Strategies for Addressing Them. *Inorg. Chem.* **2018**, *57* (7), 3659–3670. <https://doi.org/10.1021/acs.inorgchem.7b03182>.
- (38) Anderson, N. C.; Hendricks, M. P.; Choi, J. J.; Owen, J. S. Ligand Exchange and the Stoichiometry of Metal Chalcogenide Nanocrystals: Spectroscopic Observation of Facile Metal-Carboxylate Displacement and Binding. *J. Am. Chem. Soc.* **2013**, *135* (49), 18536–18548. <https://doi.org/10.1021/ja4086758>.
- (39) Calzada, R.; Thompson, C. M.; Westmoreland, D. E.; Edme, K.; Weiss, E. A. Organic-to-Aqueous Phase Transfer of Cadmium Chalcogenide Quantum Dots Using a Sulfur-Free Ligand for Enhanced Photoluminescence and Oxidative Stability. *Chem. Mater.* **2016**, *28* (18), 6716–6723. <https://doi.org/10.1021/acs.chemmater.6b03106>.
- (40) Chandrashekar, H. B.; Maji, A.; Halder, G.; Banerjee, S.; Bhattacharyya, S.; Maiti, D. Photocatalyzed Borylation Using Water-Soluble Quantum Dots. *Chem. Commun.* **2019**, *55* (44), 6201–6204. <https://doi.org/10.1039/C9CC01737B>.
- (41) Widness, J. K.; Enny, D. G.; McFarlane-Connelly, K. S.; Miedenbauer, M. T.; Krauss, T. D.; Weix, D. J. CdS Quantum Dots as Potent Photoreductants for Organic Chemistry Enabled by Auger Processes. *J. Am. Chem. Soc.* **2022**. <https://doi.org/10.1021/jacs.2c03235>.
- (42) Adams, R. N. Anodic Oxidation Pathways of Aromatic Hydrocarbons and Amines. *Acc. Chem. Res.* **1969**, *2* (6), 175–180. <https://doi.org/10.1021/ar50018a003>.
- (43) Seo, E. T.; Nelson, R. F.; Fritsch, J. M.; Marcoux, L. S.; Leedy, D. W.; Adams, R. N. Anodic Oxidation Pathways of Aromatic Amines. Electrochemical and Electron Paramagnetic Resonance Studies. *J. Am. Chem. Soc.* **1966**, *88* (15), 3498–3503. <https://doi.org/10.1021/ja00967a006>.

- (44) Costentin, C. Electrochemical Approach to the Mechanistic Study of Proton-Coupled Electron Transfer. *Chem. Rev.* **2008**, *108* (7), 2145–2179. <https://doi.org/10.1021/cr068065t>.
- (45) Lewis, F. D.; Ho, T.-I.; Simpson, J. T. Photochemical Addition of Tertiary Amines to Stilbene. Stereoelectronic Control of Tertiary Amine Oxidation. *J. Org. Chem.* **1981**, *46* (6), 1077–1082. <https://doi.org/10.1021/jo00319a007>.
- (46) Xie, J.; Rudolph, M.; Rominger, F.; Hashmi, A. S. K. Photoredox-Controlled Mono- and Di-Multifluoroarylation of C(Sp<sup>3</sup>)-H Bonds with Aryl Fluorides. *Angewandte Chemie International Edition* **2017**, *56* (25), 7266–7270. <https://doi.org/10.1002/anie.201700135>.

## Appendix Chapter II

Figure II-A1: Photoluminescence Quenching of the Quantum Dots by 1-phenylpyrrolidine.



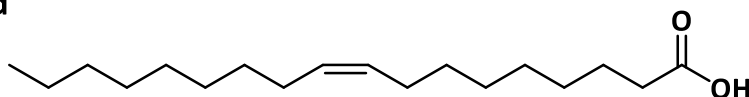
**Photoluminescence Quenching of the Quantum Dots by 1-phenylpyrrolidine.**

Photoluminescence spectra of the QDs recorded during the quenching experiments upon the successive addition of PhenylPyrrolidine (5mM in total) in trifluorotoluene, the spectra are shown as recorded during the experiment without the correction by the dilution factor.

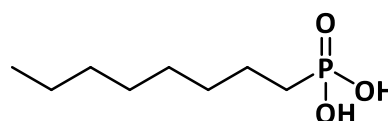
- A)** Photoluminescence quenching spectra of 0.5 $\mu$ M CdS QDs in TFT excited at 400 nm in the presence of successive addition of PhenylPyrrolidine. The evolution of the photoluminescence intensity showed a decrease of more than 70% of the initial intensity. The corresponding stern-volmer plot is represented in Figure II-4. Photoluminescence quenching spectra of 0.5 $\mu$ M CdS-CdSe QDs in TFT excited at 500nm in the presence of successive addition of PhenylPyrrolidine. The evolution of the photoluminescence intensity showed a decrease of more than 65% of the initial intensity. The corresponding stern-volmer plot is represented in Figure II-4.
- B)** Photoluminescence quenching spectra of 1 $\mu$ M CdSe QDs in TFT excited at 500 nm in the presence of successive addition of PhenylPyrrolidine. The evolution of the photoluminescence intensity showed a decrease of more than 65% of the initial intensity. The corresponding stern-volmer plot is represented in Figure II-4.
- C)** Photoluminescence quenching spectra of 0.5 $\mu$ M CdSe-CdS QDs in TFT excited at 500 nm in the presence of successive addition of PhenylPyrrolidine. The evolution of the photoluminescence intensity showed a decrease of more than 50% of the initial intensity. The corresponding stern-volmer plot is represented in Figure II-4.
- D)** Photoluminescence quenching spectra of 0.5 $\mu$ M CdSe-ZnS QDs in TFT excited at 550 nm in the presence of successive addition of PhenylPyrrolidine. The evolution of the photoluminescence intensity showed a decrease of almost 50% of the initial intensity. Which is at the limit of the real quenching behavior. The corresponding stern-volmer plot is represented in Figure II-4.
- E)** Photoluminescence quenching spectra of 0.1 $\mu$ M InP-ZnS QDs in TFT excited at 400 nm in the presence of successive addition of PhenylPyrrolidine. The evolution of the photoluminescence intensity showed a decrease of more than 60% of the initial intensity. The corresponding stern-volmer plot is represented in Figure II-4.

## Surface Ligands used for the optimization of the Quantum Dots.

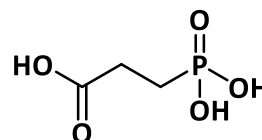
Oleic acid



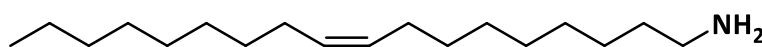
Octylphosphonic acid



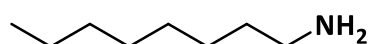
3-phosphonopropionic acid



Oleylamine

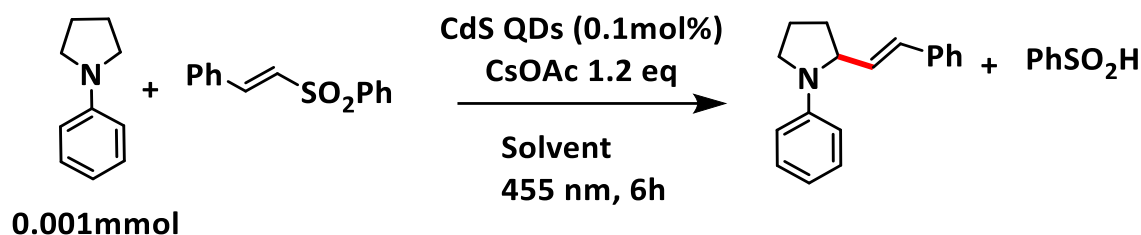


Octylamine



**Scheme II-A1:** Schematic representation of the molecular structure of the different ligands functionalizing the QDs' surface either during the synthesis (native ligands) or after ligand exchange.

**Table II-A1:** Solvent optimization using CdS QDs for the 1-Step Vinylation reaction



Entry	QDs' Surface Ligands	Solvent	Yield %
1	Oleic acid (native ligand)	Dichloromethane	52%
2	Oleic acid (native ligand)	Chloroform	0%
3	Oleic acid (native ligand)	Trifluorotoluene	49%
4	Phosphonopropionic acid (PPAc)	Water	8%
5	Phosphonopropionic acid (PPAc)	Ethanol	5%
6	Phosphonopropionic acid (PPAc)	Water: Ethanol (50:50)	7%
7	Phosphonopropionic acid (PPAc)	Water: Acetonitrile (50:50)	23%
8	Phosphonopropionic acid (PPAc)	Acetonitrile	67%

**Table II-A1: Optimization of the reaction's solvent investigated using CdS QDs and the C-C-vinylation reaction.** The reactions using oleic acid-capped QDs were tested without further optimization with other ligands. The use of dichloromethane was efficient, but the fact that this solvent is quite volatile makes the reaction's analysis not easy to handle. The reaction in chloroform was not successful. The use of Trifluorotoluene was efficient and easier to handle than dichloromethane.

The use of phosphonopropionic acid ligands was efficient to transfer the QDs to polar solvents. However, the reaction did not work well in pure water, ethanol, or in a mixture of both water and ethanol. The use of acetonitrile was the most efficient among the tested polar solvents.

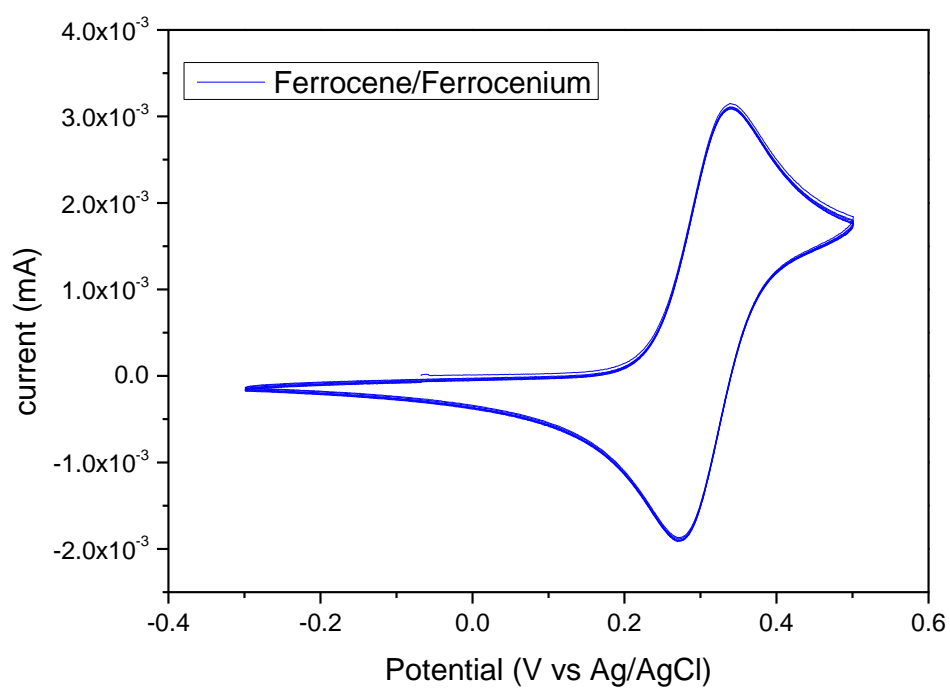


**Figure II-A2: Cyclic voltammograms of ferrocene/ferrocenium couple.** Recorded at 100 mV/s scan rate in acetonitrile containing  $[\text{Bu}_4\text{N}][\text{PF}_6]$  (0.1 M) as a supporting electrolyte. Used for the potential calibration as an internal standard.

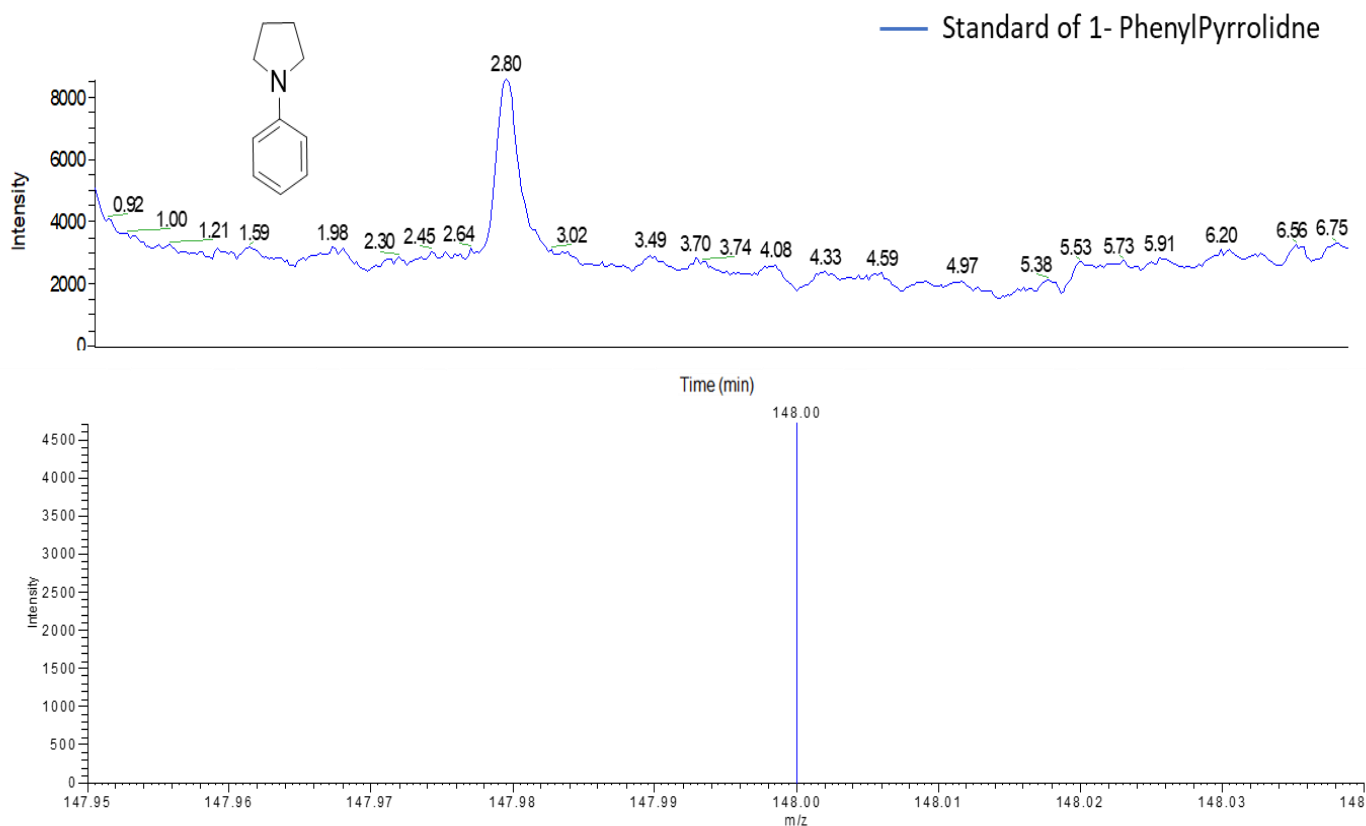


**Figure II-A3: UHPLC -MS analysis of the Phenylpyrrolidine.** Detection of corresponding UHPLC peak of the Phenylpyrrolidine by setting the MS detection transition at  $m/z = 148$  Da, which is the corresponding ionized form of the Phenylpyrrolidine in the positive mode. The MS detection was set using the SIM (single ion monitoring) scanning mode in which only the selected mass-to-charge ratio range was detected by the instrument, as opposed to the full spectrum range. The retention time of the detected peak is centered at 2.8 minutes.

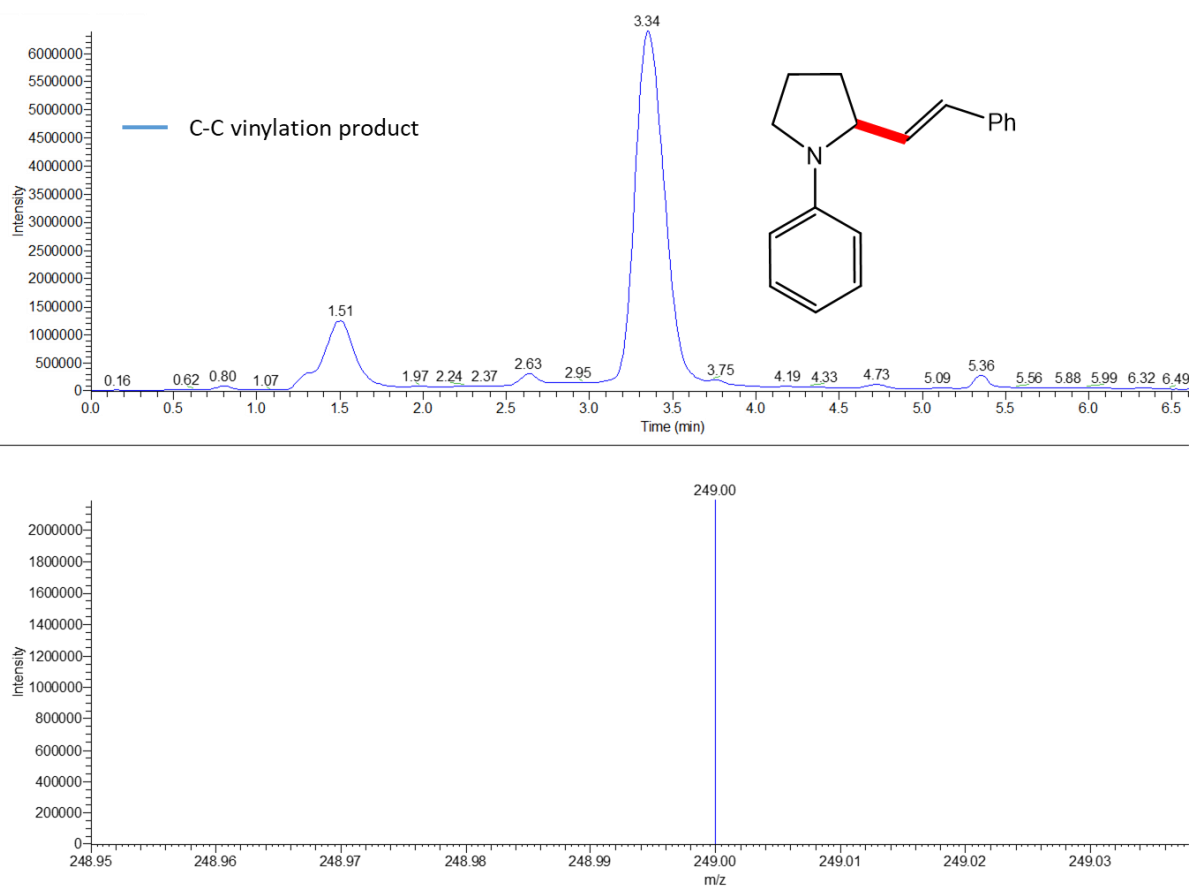


**Figure II-A4: UHPLC -MS analysis of (E)-(2-(2-phenylcyclopentyl)vinyl)benzene-the corresponding product of the vinylation reaction between 1-Phenylpyrrolidine and the phenyl trans-styryl sulfone .** Detection of corresponding UHPLC peak of the Phenylpyrrolidine by setting the MS detection transition at  $m/z = 249$  Da, the corresponding ionized form of the product in the positive mode. The MS detection was set using the SIM (single ion monitoring) scanning mode in which only the selected mass-to-charge ratio range was detected by the instrument, as opposed to the full spectrum range. The retention time of the detected peak is centered at 3.3 minutes.

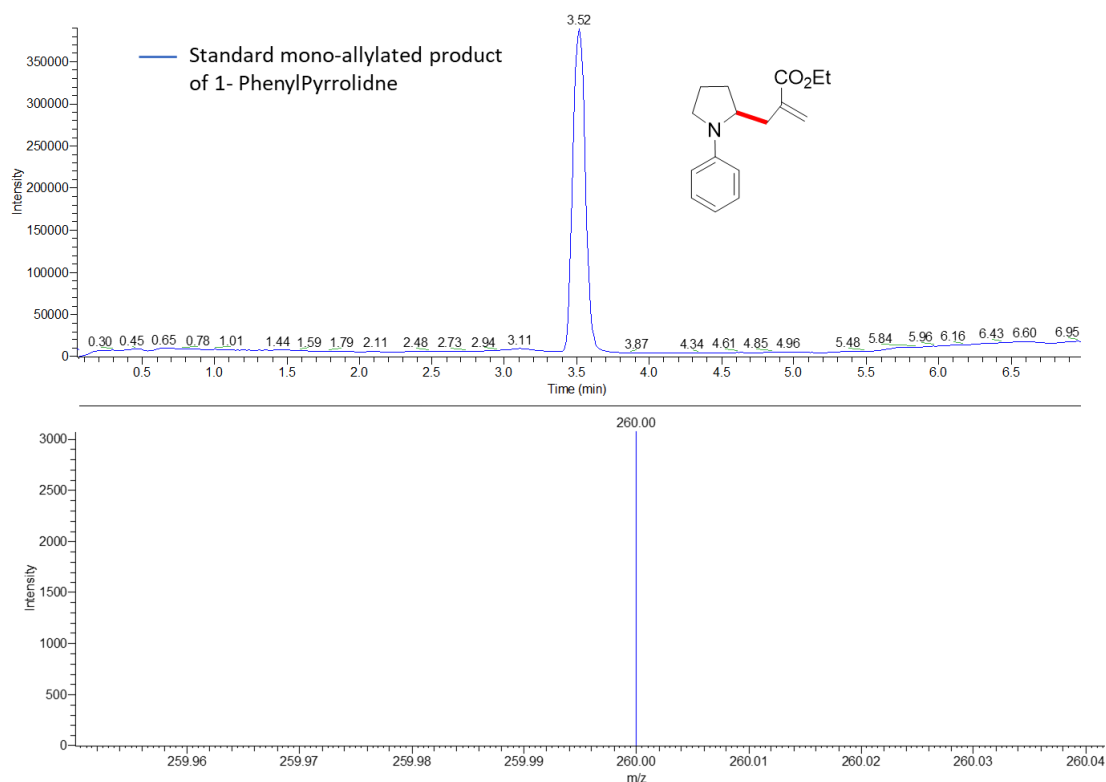


**Figure II-A5: UHPLC -MS analysis of a standard sample of the intermediate C-C mono-allylated product of the reaction between 1-Phenylpyrrolidine and the allylic traps.** Detection of corresponding UHPLC peak of the product by setting the MS detection transition at  $m/z = 260$  Da, the corresponding ionized form of the product in the positive mode. The MS detection was set using the SIM (single ion monitoring) scanning mode in which only the selected mass-to-charge ratio range was detected by the instrument, as opposed to the full spectrum range. The chromatogram shows one peak at a retention time of 3.5 minutes.

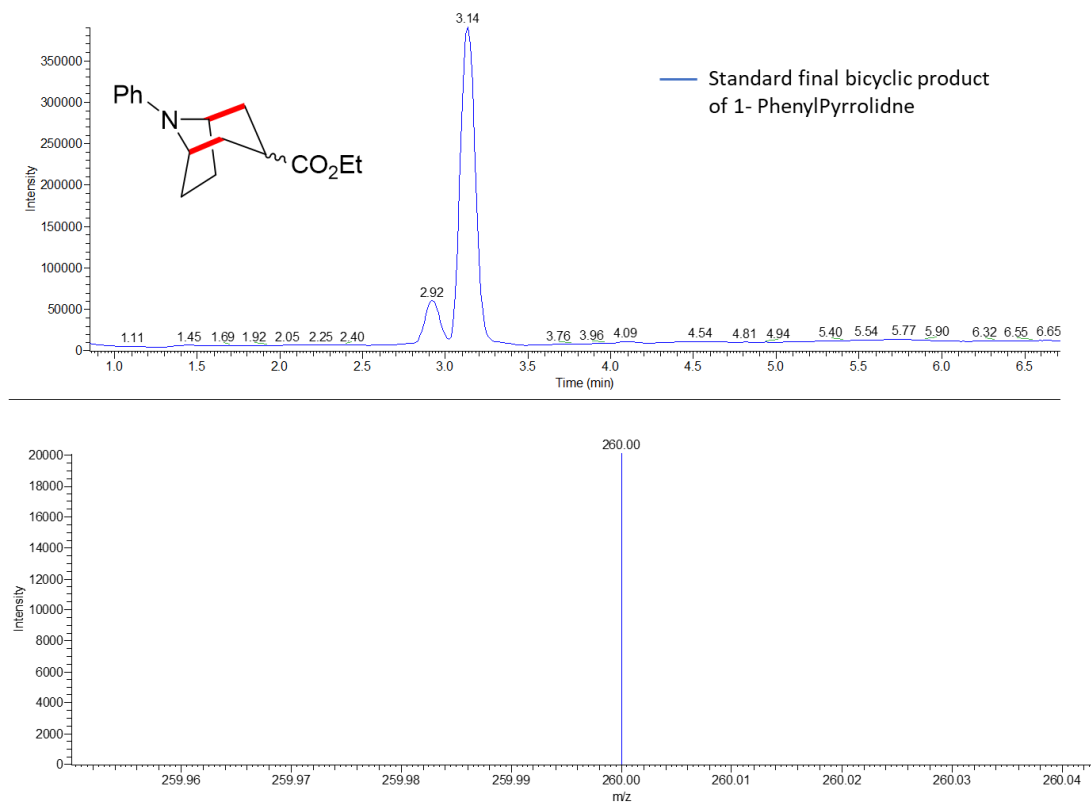


**Figure II-A6: UHPLC -MS analysis of a standard sample of the final bicyclic product of the reaction starting from 1-Phenylpyrrolidine in the presence of the allylic traps.** Detection of corresponding UHPLC peak of the product by setting the MS detection transition at  $m/z = 260$  Da, the corresponding ionized form of the product in the positive mode. The MS detection was set using the SIM (single ion monitoring) scanning mode in which only the selected mass-to-charge ratio range was detected by the instrument, as opposed to the full spectrum range. The chromatogram shows two peaks which correspond to the isomers of the product, one major peak at retention time of 3.1 minutes and the minor one at 2.9 minutes.

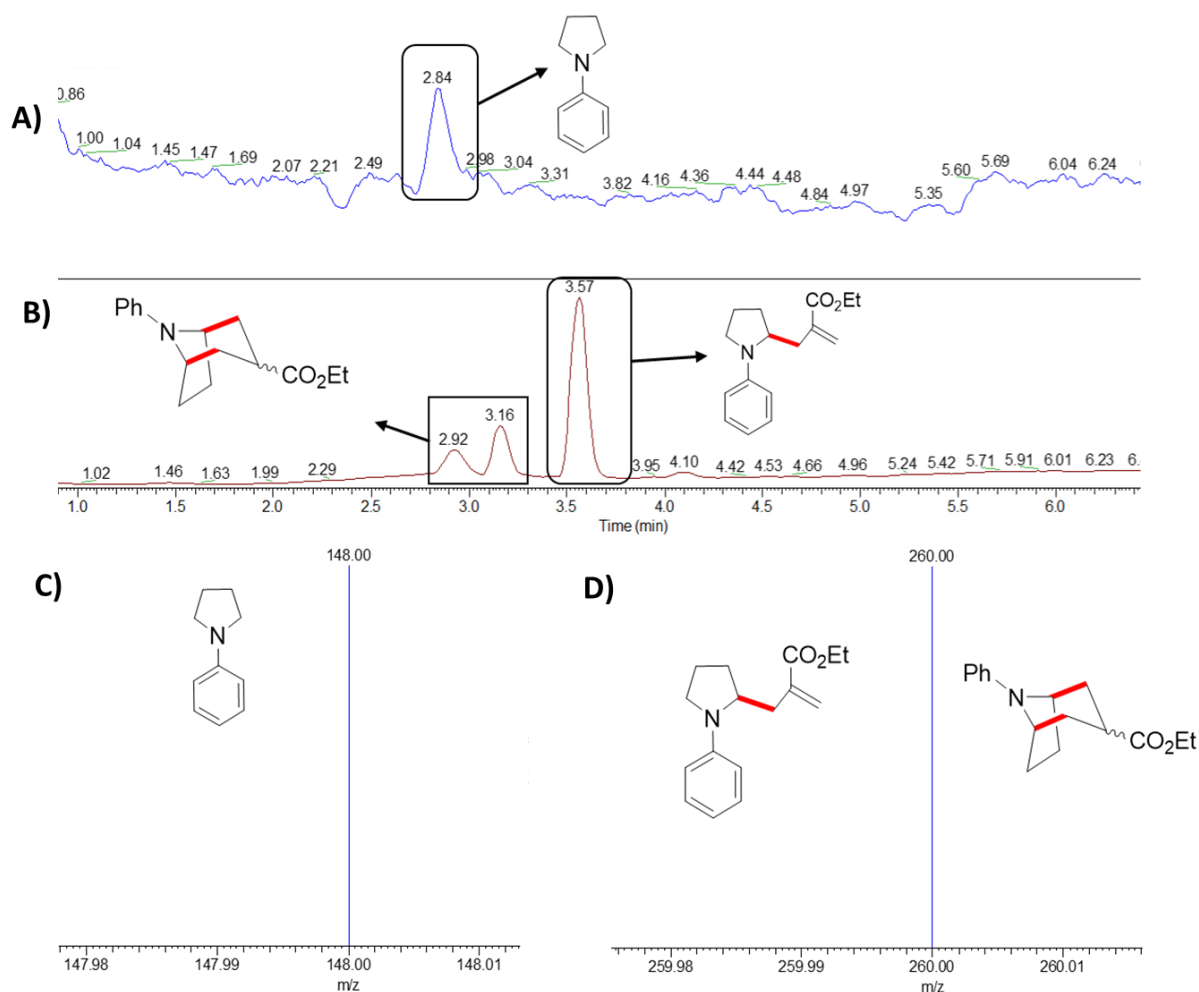


**Figure II-A7: Example of the UHPLC -MS analysis for an aliquot after 8 hours of irradiation:** A) the chromatogram corresponding the phenylpyrrolidine starting material which was detected based on the selected mass-to-charge ratio range  $m/z = 148$  Da as showed in (C).

B) The chromatogram corresponding to the mass of the corresponding  $m/z = 260$  Da (D) which correspond to the reaction products. Here a mix of the products is observed, the corresponding of the mono-allylated product at retention time of 3.5 minutes and the 2 peaks of the isomers of the final bicyclic product at retention time 2.9 and 3.1 minutes.

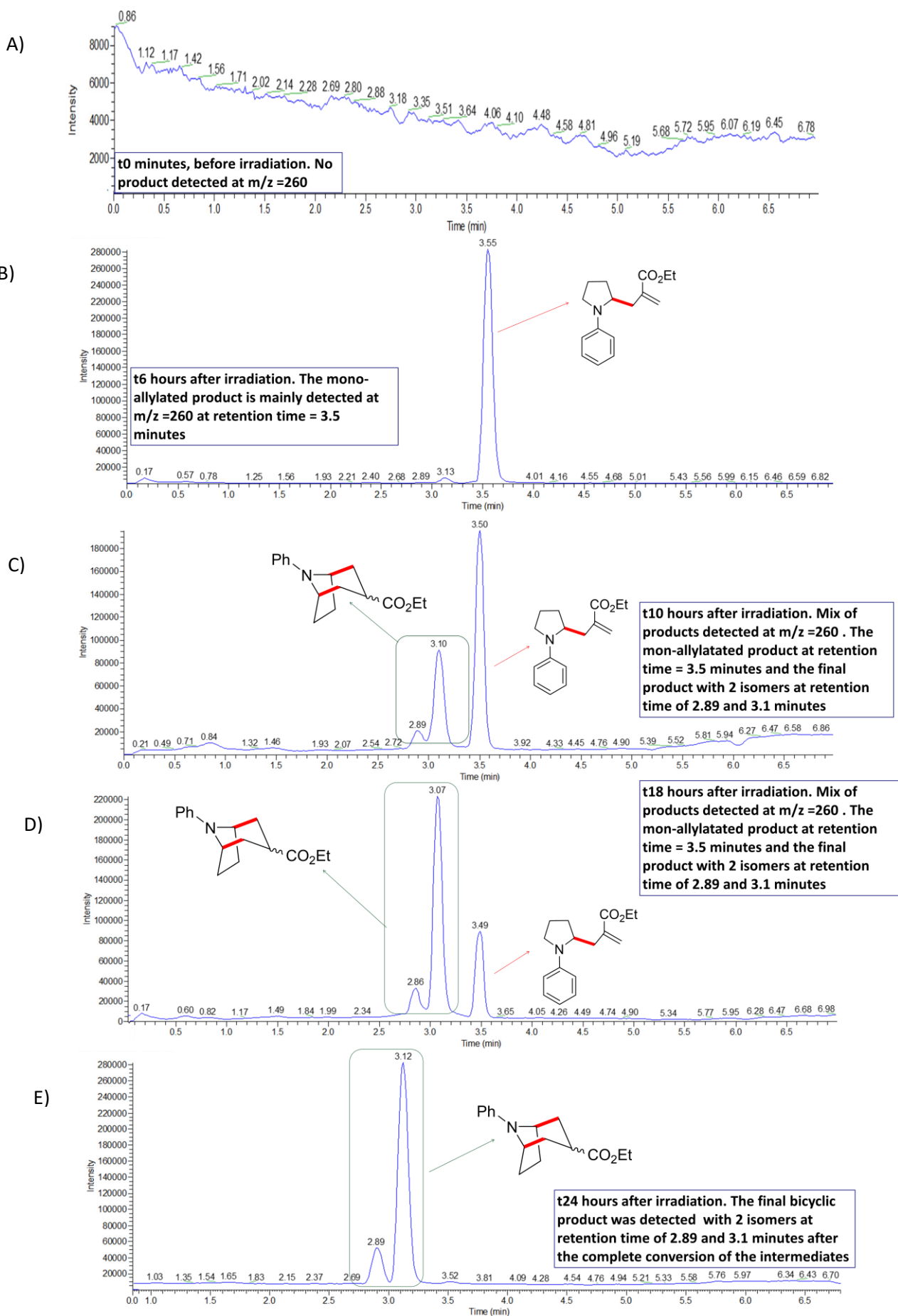


**Figure II-A8: The monitoring of the reaction's products evolution during the irradiation process.** The chromatograms are collected at the transitions corresponding the m/z ratio of 260 Da.

- A) Corresponds to an aliquot taken after mixing the reaction substrates in the presence of the QDs but before starting the irradiation ( $t_0$  minutes). In this case, no peak is observed with the corresponding products' mass.
- B) Corresponds to an aliquot taken after starting the irradiation and letting the reaction run for 6 hours. In this case, one peak is observed with the corresponding products' mass, but at the retention time of the intermediate mono-allylated product (3.5 minutes).
- C) Corresponds to an aliquot taken after starting the irradiation and letting the reaction run for 10 hours. In this case, 3 peaks are observed with the corresponding products' mass, one peak the retention time of the intermediate mono-allylated product (3.5 minutes), and the two others at the retention time correspond to isomers of the bicyclic product (2.9 and 3.5 minutes). The peak of the intermediate product is of higher area meaning that we have more mono-allylated product in this case.
- D) Corresponds to an aliquot taken after starting the irradiation and letting the reaction run for 18 hours. In this case, 3 peaks are observed with the corresponding products' mass, one peak the retention time of the intermediate mono-allylated product (3.5 minutes), and the two others at the retention time correspond to isomers of the bicyclic product (2.9 and 3.5 minutes). In this case, the peaks of the bicyclic product are of higher area (in total) than the intermediate products, but still indicating that the reaction is not completed.
- E) Corresponds to an aliquot taken after 24 hours of irradiation. In this case, 2 peaks are observed which correspond to the mass of the reaction product and with the retention time of the isomers of the final cyclic product. In this case, no peak of the intermediate product is observed, indicating that the reaction is completed.

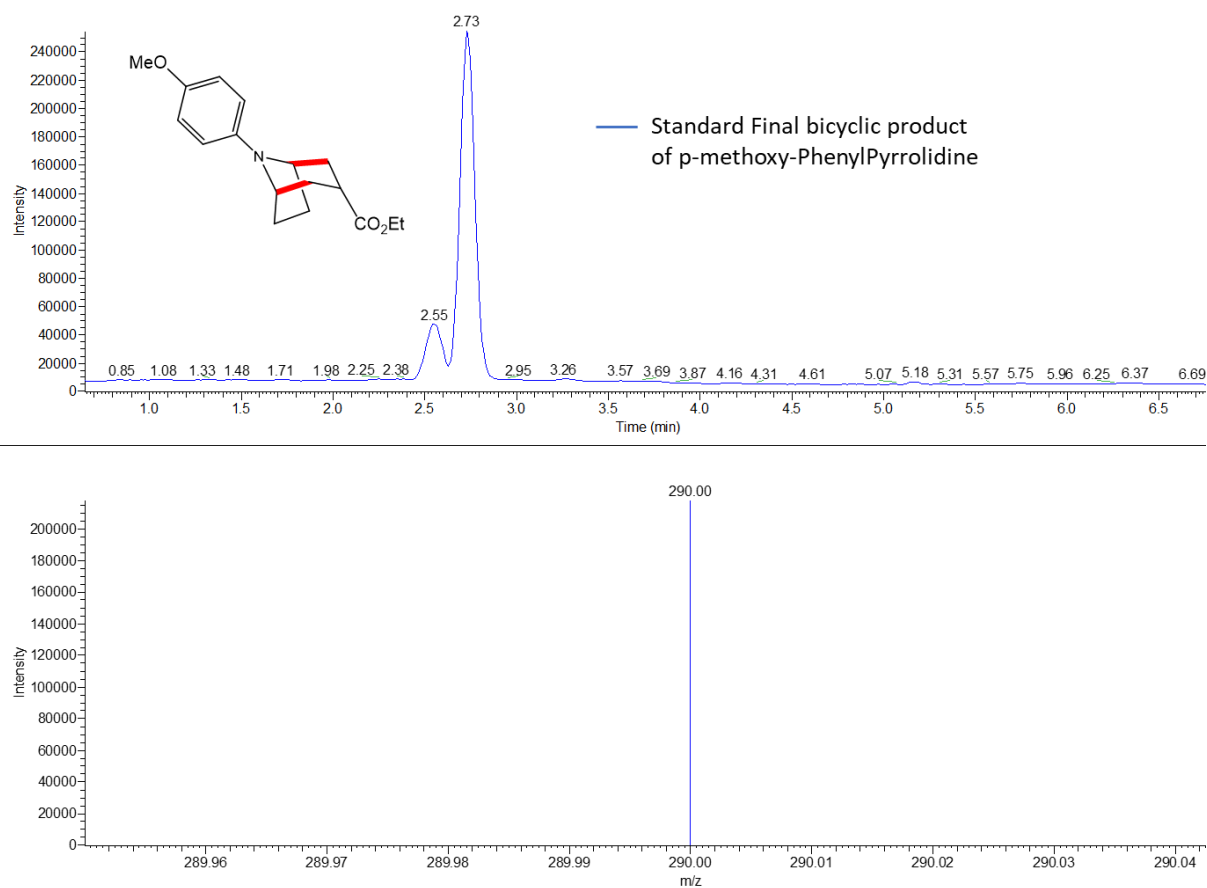


**Figure II-A9: UHPLC -MS analysis of a standard sample of the final bicyclic product of the reaction starting from p-methoxy-Phenylpyrrolidine in the presence of the allylic traps.** Detection of corresponding UHPLC peak of the product by setting the MS detection transition at  $m/z = 290$  Da, the corresponding ionized form of the product in the positive mode. The MS detection was set using the SIM (single ion monitoring) scanning mode in which only the selected mass-to-charge ratio range was detected by the instrument, as opposed to the full spectrum range. The chromatogram shows two peaks which correspond to the isomers of the product, one major peak at retention time of 2.7 minutes and the minor one at 2.5 minutes.

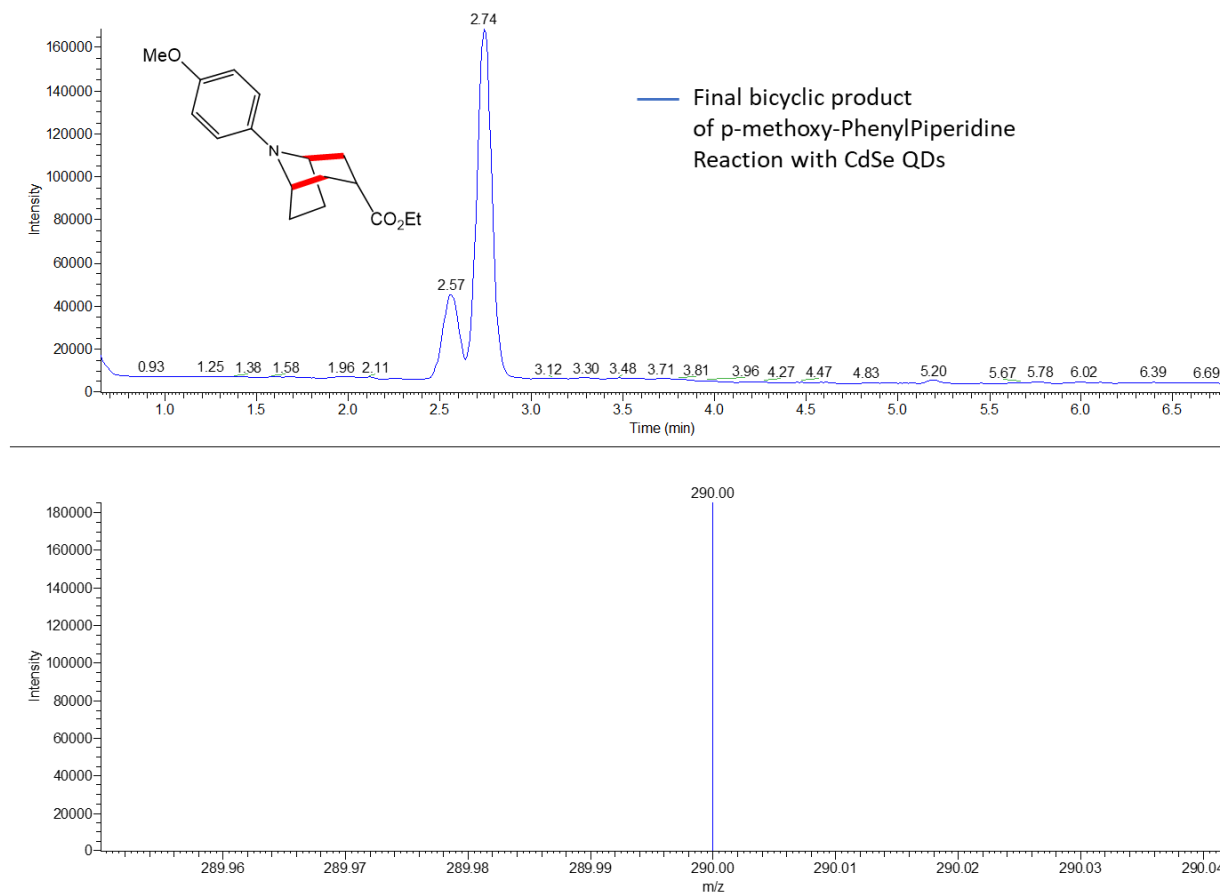


**Figure II-A10: UHPLC -MS analysis of an aliquot of the reaction with p-methoxy-phenylpyrrolidine after 30 hours of irradiation.** The chromatogram shows the peaks at identical times of the standard sample of the product and with the corresponding m/z selected by the mass spectrometer. The chromatogram indicates the completion of the reaction to final product.

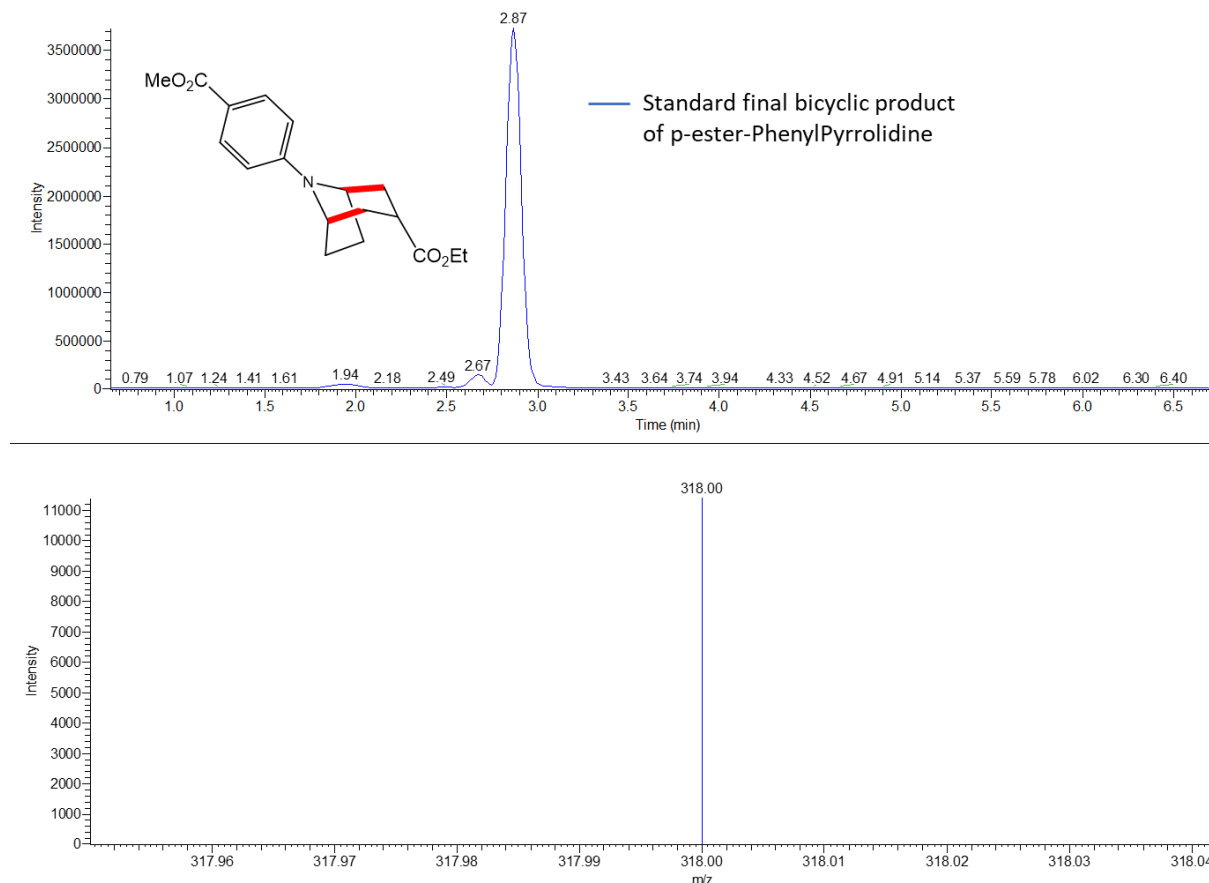


**Figure II-A11: UHPLC -MS analysis of a standard sample of the final bicyclic product of the reaction starting from p-ester-PhenylPyrrolidine in the presence of the allylic traps.** Detection of corresponding UHPLC peak of the product by setting the MS detection transition at  $m/z = 318$  Da, the corresponding ionized form of the product in the positive mode. The MS detection was set using the SIM (single ion monitoring) scanning mode in which only the selected mass-to-charge ratio range was detected by the instrument, as opposed to the full spectrum range. The chromatogram shows two peaks, one major peak at retention time of 2.8 minutes, and minor second peak at retention time of 2.6 minutes

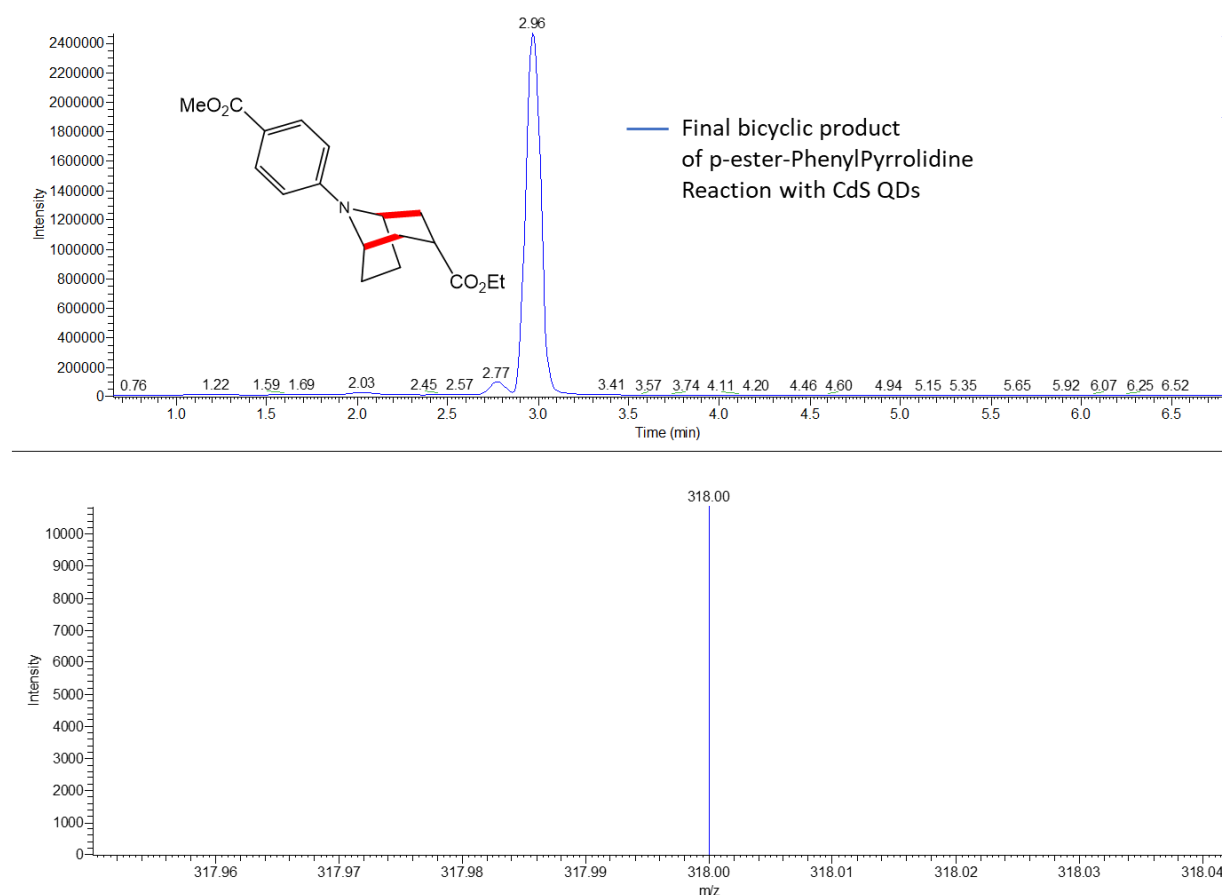


**Figure II-A12: UHPLC -MS analysis of an aliquot of the reaction with p-ester-phenylpyrrolidine after 24 hours of irradiation.** The chromatogram shows the peaks at identical times of the standard sample of the product and with the corresponding m/z selected by the mass spectrometer. The chromatogram indicates the completion of the reaction to final product.

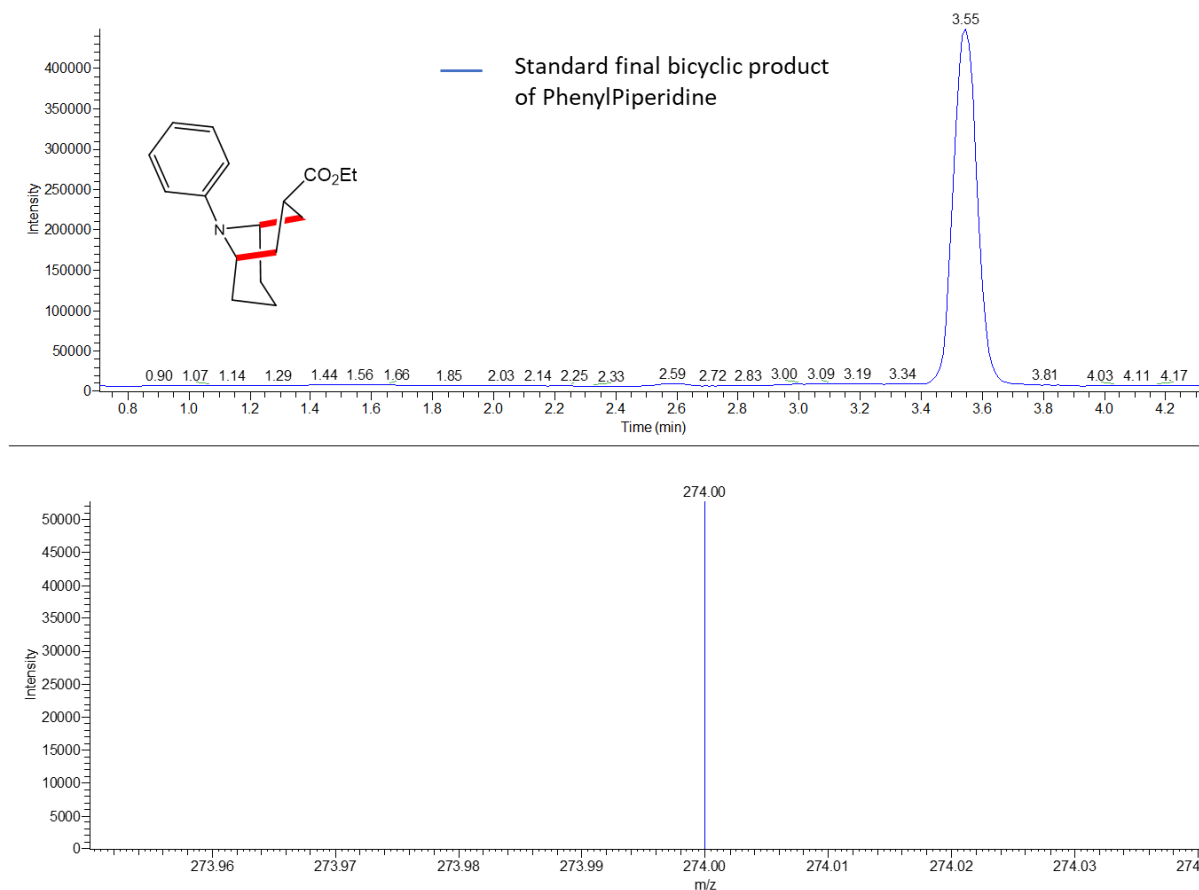


**Figure II-A13: UHPLC -MS analysis of a standard sample of the final bicyclic product of the reaction starting from PhenylPiperidine in the presence of the allylic traps.** Detection of corresponding UHPLC peak of the product by setting the MS detection transition at  $m/z = 274$  Da, the corresponding ionized form of the product in the positive mode. The MS detection was set using the SIM (single ion monitoring) scanning mode in which only the selected mass-to-charge ratio range was detected by the instrument, as opposed to the full spectrum range. The chromatogram shows one peak at retention time of 3.55 minutes.

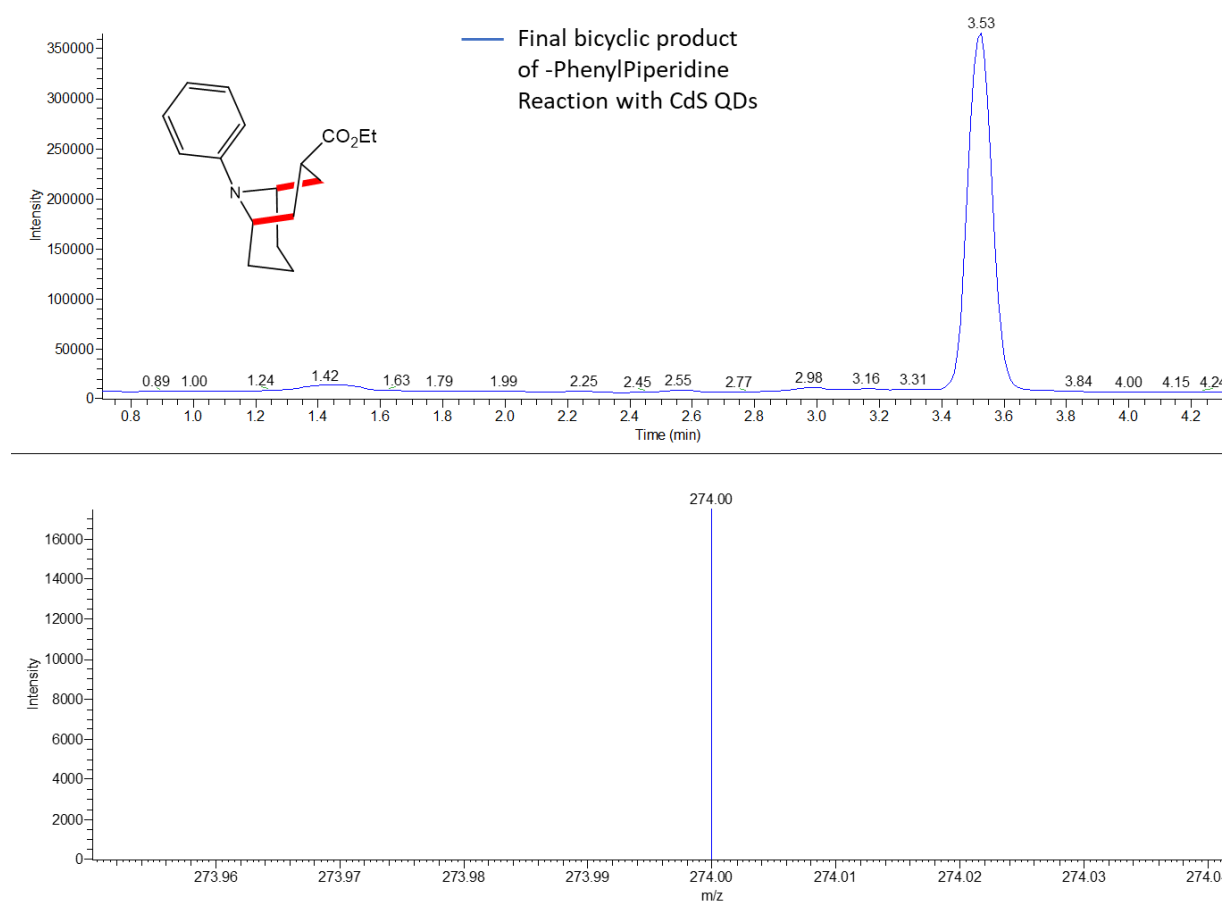


**Figure II-A14:** UHPLC -MS analysis of an aliquot of the reaction with 1-phenylPiperidine after 24 hours of irradiation. The chromatogram show the peaks at identical times of the standard sample of the product and with the corresponding m/z selected by the mass spectrometer. The chromatogram indicates the completion of the reaction to final product.

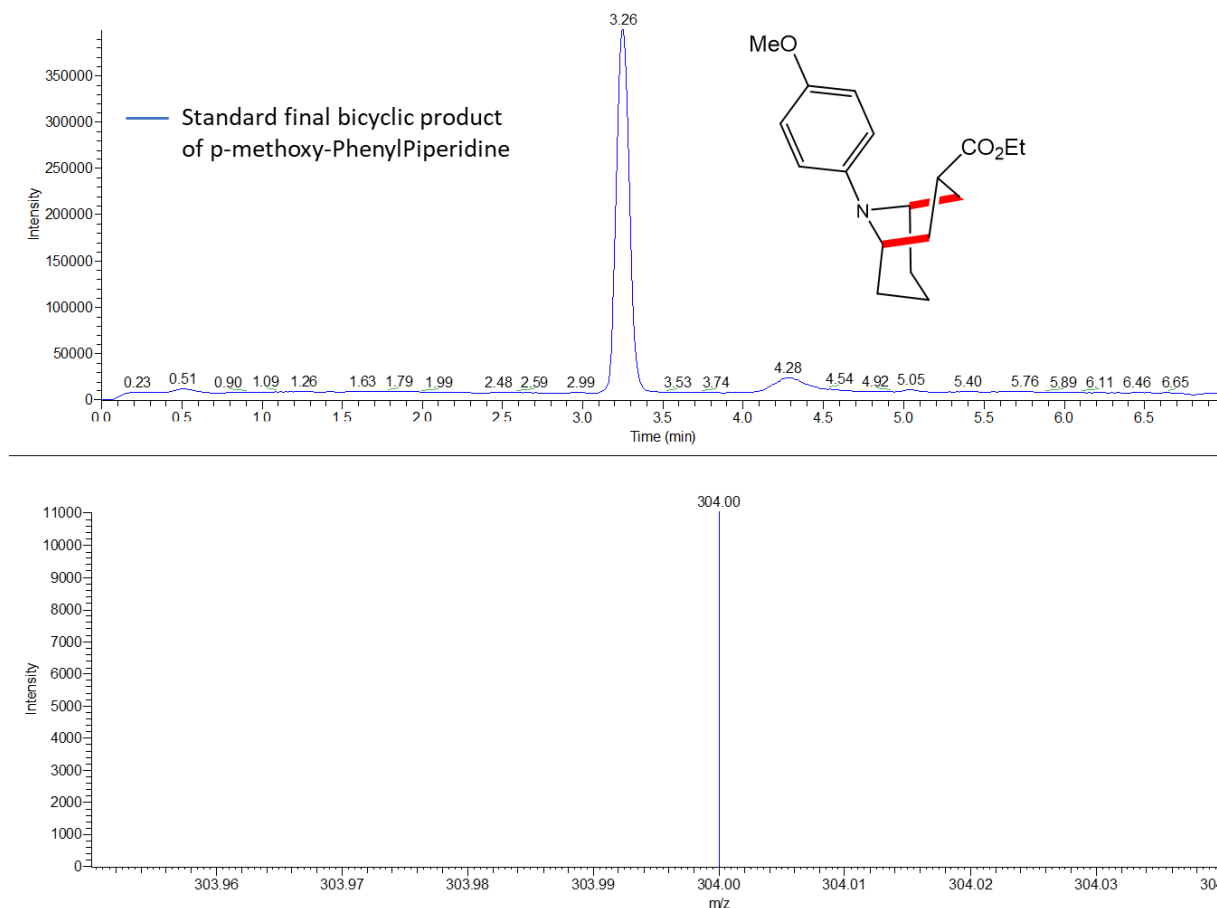


**Figure II-A15: UHPLC -MS analysis of a standard sample of the final bicyclic product of the reaction starting from p-methoxy-PhenylPiperidine in the presence of the allylic traps.** Detection of corresponding UHPLC peak of the product by setting the MS detection transition at  $m/z = 304$  Da, the corresponding ionized form of the product in the positive mode. The MS detection was set using the SIM (single ion monitoring) scanning mode in which only the selected mass-to-charge ratio range was detected by the instrument, as opposed to the full spectrum range. The chromatogram shows one peak at retention time of 3.2 minutes.

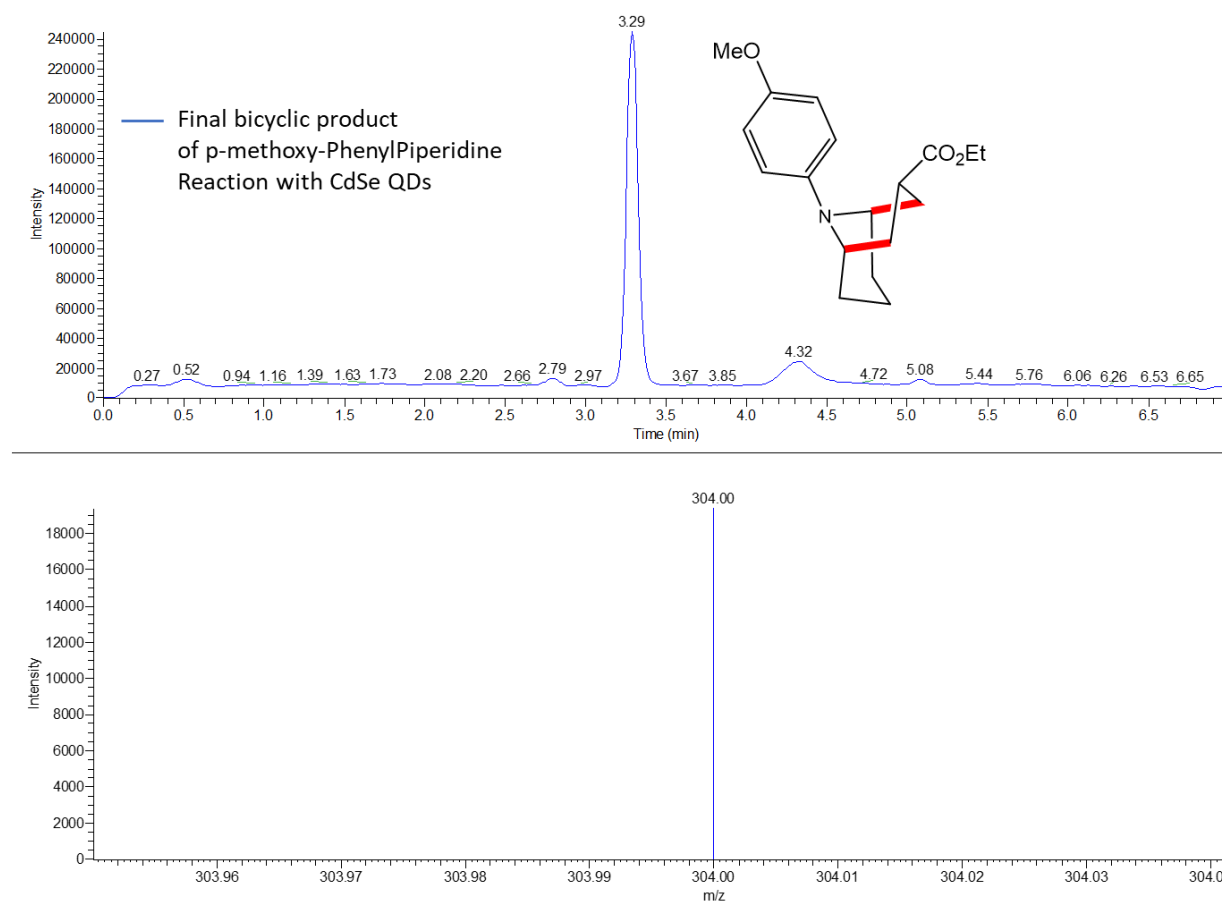


**Figure II-A16: UHPLC -MS analysis of an aliquot of the reaction with p-methoxy-phenylpiperidine after 32 hours of irradiation.** The chromatogram shows the peak at identical times of the standard sample of the product and with the corresponding m/z selected by the mass spectrometer. The chromatogram indicates the completion of the reaction to final product.

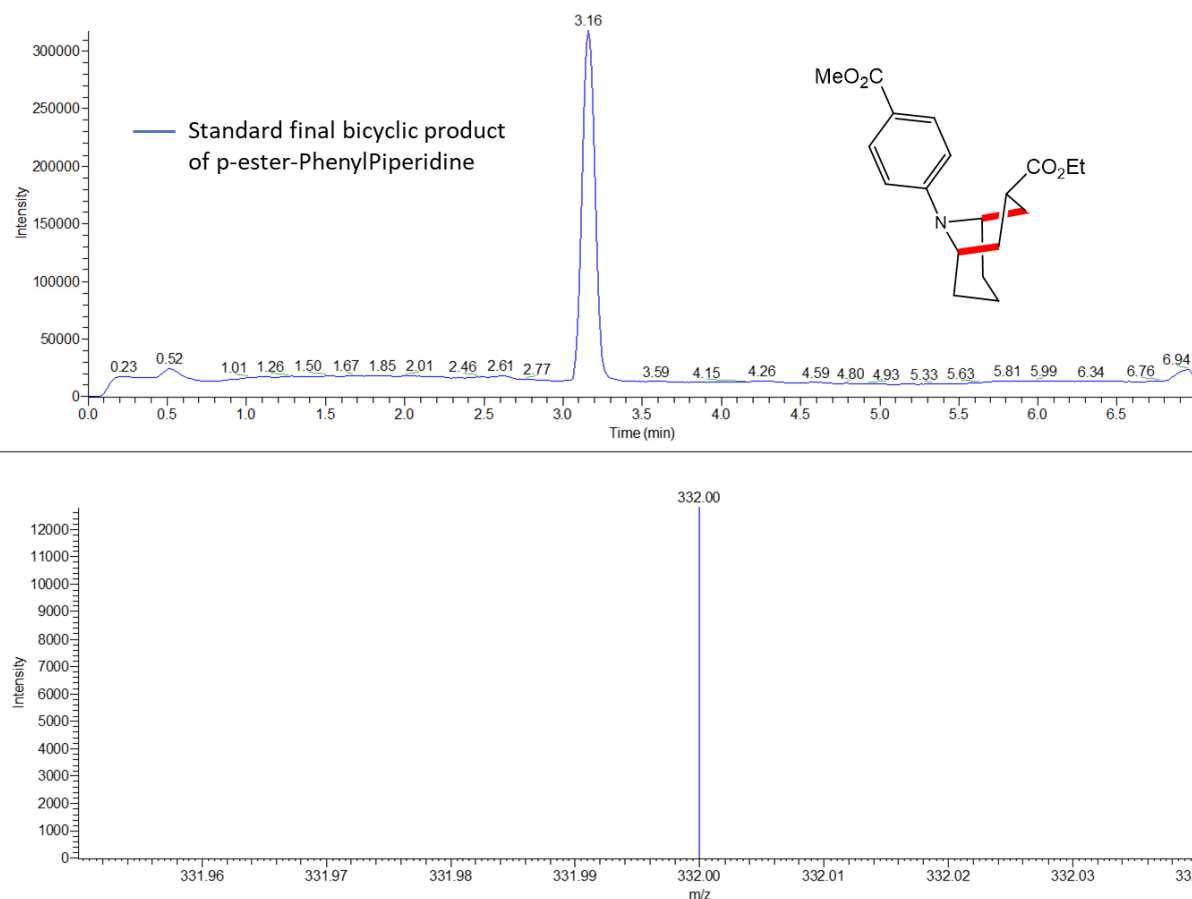


**Figure II-A17: UHPLC -MS analysis of a standard sample of the final bicyclic product of the reaction starting from p-ester-PhenylPiperidine in the presence of the allylic traps.** Detection of corresponding UHPLC peak of the product by setting the MS detection transition at  $m/z = 332$  Da, the corresponding ionized form of the product in the positive mode. The MS detection was set using the SIM (single ion monitoring) scanning mode in which only the selected mass-to-charge ratio range was detected by the instrument, as opposed to the full spectrum range. The chromatogram shows one peak at retention time of 3.1 minutes.

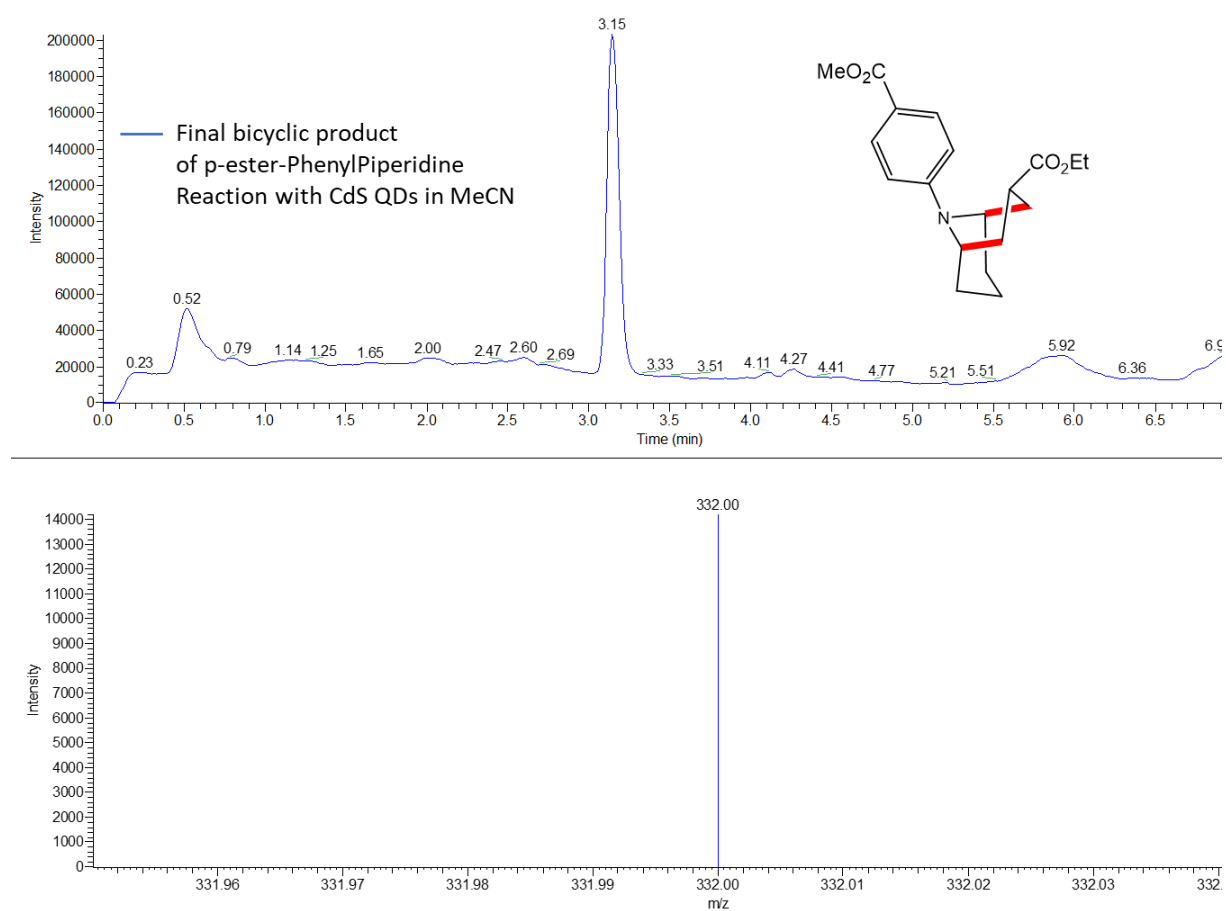


**Figure II-A18: UHPLC -MS analysis of an aliquot of the reaction with p-ester-phenylPiperidine after 24 hours of irradiation.** The chromatogram shows the peak at identical times of the standard sample of the product and with the corresponding m/z selected by the mass spectrometer. The chromatogram indicates the completion of the reaction to final product.





# CHAPTER III:

## Hybrid CdSe/ZnS Quantum Dots-Gold Nanoparticles Composites Assembled by Click Chemistry: Towards Affordable and Efficient Redox Photocatalysts Working with Visible Light

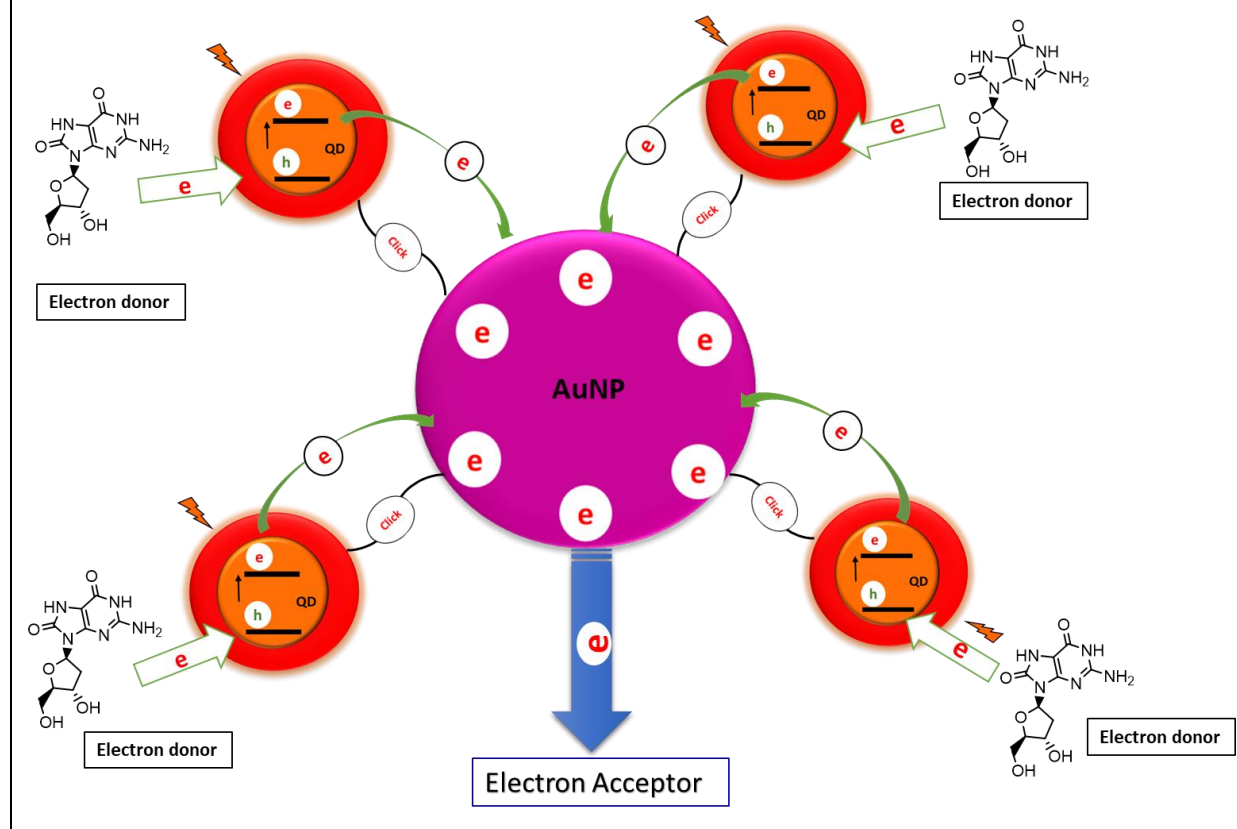


## Table of Content

CHAPTER III: .....	177
Hybrid CdSe/ZnS Quantum Dots-Gold Nanoparticles Composites Assembled by Click Chemistry: Towards Affordable and Efficient Redox Photocatalysts Working with Visible Light .....	177
Abstract .....	179
III- 1. Introduction.....	180
III-2. Synthesis and characterization of QD-AuNP composites.....	183
III-2.1 Synthesis and characterization of Gold nanoparticles (AuNP). .....	183
III-2.1 CdSe/ZnS core-shell Quantum Dots.....	187
III-2.3. Assembly of water-soluble CdSe/ZnS QD with AuNP by click reaction. ....	190
III-3. Probing the efficiency of QD-AuNP composites as photocatalysts.....	195
III-3.1. Effect of the QD concentration when using CdSe/ZnS QD alone as photocatalysts.....	195
III-3.2. Enhanced photocatalytic activity using QD-AuNP composites as photocatalysts.....	197
III-3.3. Quantitation of the photocatalytic activity improvement – Internal QY vs. QD absorbed photons. ....	202
III-3.3. Comparison of the photocatalytic activity of QD-AuNP by using irradiation in the QD exciton range (590nm) or in the AuNP plasmon resonance band range (528nm). ....	203
III-4 – Mechanistic Studies .....	206
III-4.1. Quenching of QD fluorescence in QD-AuNP composites.....	206
III-4.2-Blue shift of the plasmon band due to the accumulation of electrons when irradiating QD-AuNP composites in the presence of the electron donor. ....	207
III-4.3. Proposed mechanism for the charge separation within the QD-AuNP composite and for the charge transfers to the electron donor and acceptor during the different kinetic regimes. .....	211
III-4.4. Proposed mechanism for the absorption of light leading to photocatalysis with the QD- AuNP composites. ....	214
III-4.5 Possible enhancement of light absorption by QD in the QD-AuNP composites due to local electromagnetic field enhancement in the vicinity of AuNP.....	215
Conclusion.....	217
Appendix Chapter III: .....	218
References .....	232

## Abstract

This chapter presents the first draft of a publication that the writing of which is in progress. In the following, the introduction is re-written in order to better connect with the general introduction of this Thesis and with few adaptations in the main text.

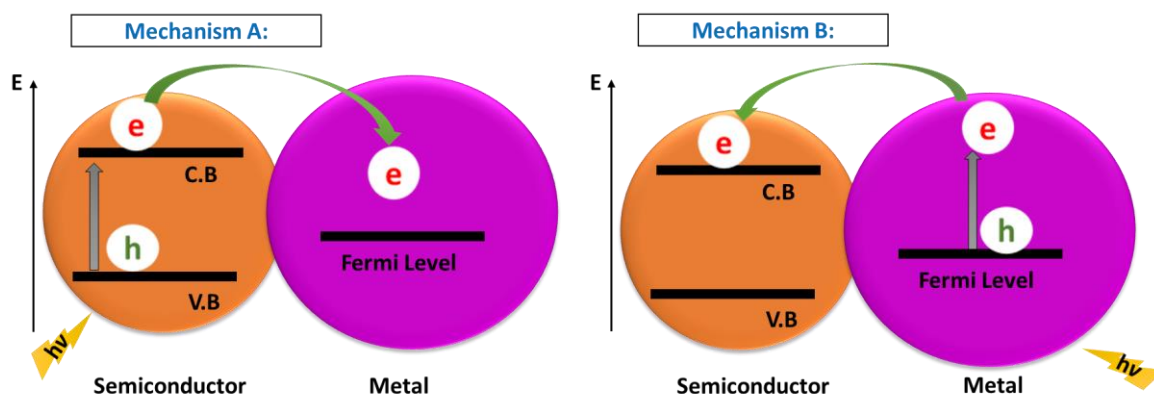
In this study, we designed a novel and modular semiconductor-metal hybrid nanostructure by assembling semiconductor Quantum Dots (QD) to Gold nanoparticles (AuNP). Here, we choose CdSe/ZnS QD and Gold nanoparticles to be chemically assembled by covalent bonds using a Copper-Catalyzed Azide-Alkyne Cycloaddition Click reaction. In order to afford the click reaction, we prepared water-soluble CdSe/ZnS QD and AuNP and then functionalized their surfaces with ligands bearing azide and alkyne functions, respectively. Preparing such a system aims primarily to improve the separation of the charges generated in the photoexcited QDs by favoring the electron transfer to the Gold Nanoparticles. The charge separation efficiency is proved by charging the Gold Nanoparticles with up to 7400 electrons/NP transferred from the QD upon their excitation. Moreover, the photocatalytic activity of the QD-AuNP hybrid nanostructure is compared to the activity of the bare QD and shows a significant enhancement in terms of speed and turnover number by achieving more than 1500 TON in 10 minutes compared to a maximum of 500 TON in 3 hours for the case of bare QD.

## III- 1. Introduction

As mentioned in Chapter I and from our investigations in Chapter II, the use of semiconductor Quantum Dots for photocatalytic organic reactions is an efficient candidate for visible light photocatalysis and affords good reaction yields. However, in most of the reported QD-photocatalyzed organic transformations and in our case for the reactions described in Chapter I, the Quantum Yield of the QD-catalyzed reactions is low, typically less than 1%. In addition, the QD-photocatalyzed reactions are usually slow, as most of the reported reactions require between 3 hours and up to 72 hours to complete the targeted reaction (See the literature survey in Chapter I, section I-3). This is primarily attributed to the charges recombination processes which limit the redox activity of the Quantum Dots<sup>1</sup>.

Therefore, to improve the efficiency of the QD-photocatalyzed reactions, it is crucial to suppress or limit the photo-induced charges recombination and to enhance their separation. One of the explored strategies to reach this objective is to design hybrid nanostructures of semiconductor-metal nanoparticles, such as semiconductor Quantum Dots and metal nanoparticles<sup>2-4</sup>. The preparation of semiconductor-metal hybrid structures significantly influences their optical properties<sup>5,6</sup> making them act as efficient photocatalysts<sup>4,7,8</sup> (See Chapter I, section I-4).

Semiconductor-metal hybrid nanostructures can induce an enhanced charge separation based on two different mechanisms depending on which part (the semiconductor or the metal) absorbs the light. If the semiconductor part absorbs the light, the photoexcited electron can be transferred to the metal part, while the holes remain in the semiconductor<sup>1,9,10</sup> (Scheme III-1 part A). However, if the light is absorbed by the metal part, photogenerated hot electrons are created and may be transferred to the conduction band of the semiconductor part, while holes remain in the metallic nanoparticle (Scheme III-1 part B)<sup>11-13</sup>. Both mechanisms promote the separation of photoexcited holes and electrons, but they induce flows of electrons in opposite directions, as mentioned above. Then, it is essential to select the most suited one for the targeted reaction.



**Scheme III-1: Schematic illustration of two possible mechanisms of charge carriers transfer in semiconductor-metal hybrid nanostructures** (recalled from Chapter I section I-4) : mechanism-A) Absorption of light by the semiconductor part and transfer of an electron from its conduction band to the metal part, mechanism -B) Absorption of light by the metal part in its plasmon band and transfer of an electron to the semiconductor.

Interestingly, recent reports have suggested new methodologies for preparing semiconductor Quantum Dots-metal nanoparticles hybrid nanostructures by assembling the particles through their surface ligands. For example, Fernandez et al.<sup>14</sup> designed hybrid nanostructures of CdSe/ZnS QDs and gold nanoparticles (AuNP) assembled through complementary artificial proteins functionalizing the surface of both the QD and the AuNP. Moreover, Sun et al.<sup>6</sup> prepared similar nanostructure of CdSe/ZnS QDs and AuNP, but connected using complementary DNA linkers. Furthermore, Strelow et al.<sup>15</sup> also prepared CdSe-based Quantum Dots assembled with AuNP but through chemical bonds. They encapsulated the QD with thiols-based PEG polymers and mixed them with citrate-capped AuNP. The QD linked to the AuNP thanks to the good affinity of thiols to the surface of the AuNP and formed quasi-covalent bonds. The three examples mentioned above of connected QD-metal nanostructures were well-characterized using various methods to prove the efficient connection between the particles and in some cases the influence on the optical properties photo-induced charge separation. However, they were not employed in photocatalytic applications.

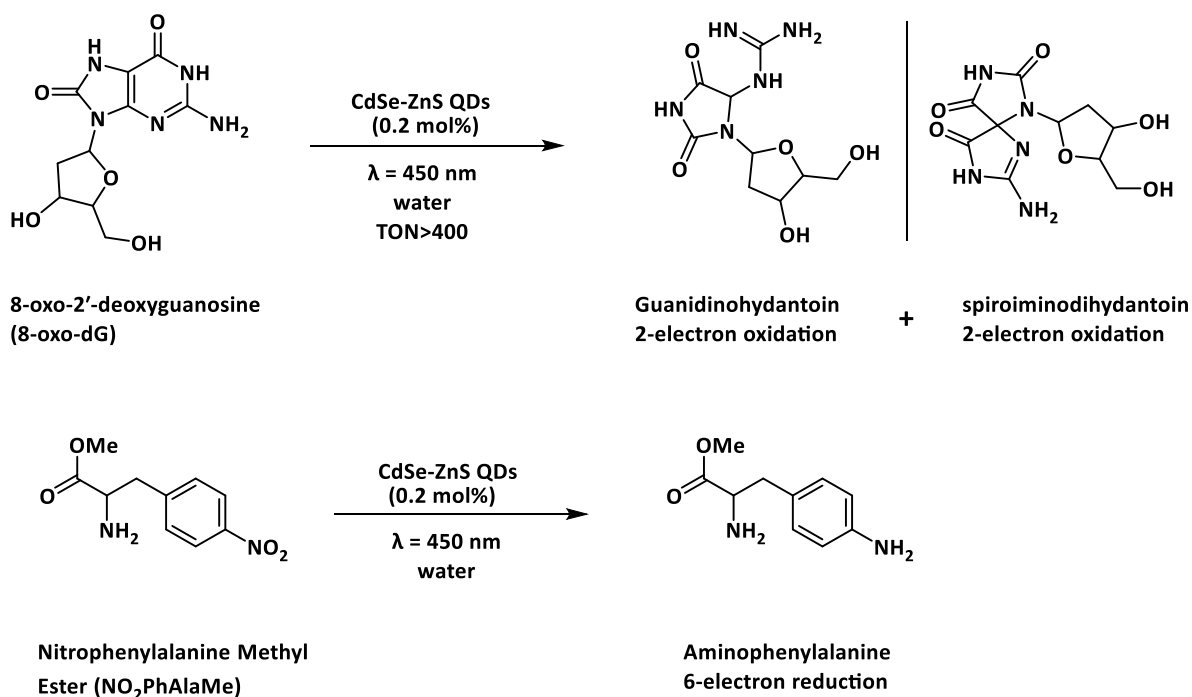
In this Chapter III, we report our attempts to design and study a novel semiconductor-metal hybrid nanocomposites prepared through covalent bonds using a click-chemistry reaction. Here, CdSe/ZnS core/shell Quantum Dots were chemically assembled with gold nanoparticles (AuNP) using a click-chemistry reaction. This project was initiated in collaboration between the CAMPE-CEA team (Dr. Vincent MAUREL) and the OPTIMA-CNRS

(Dr. Fabien DUBOIS) in order to prepare photocatalytically efficient hybrid nanocomposites. The idea of preparing such a nanocomposites is to enormously improve the charge separation of the electron-hole pairs formed in the photoexcited QD by favoring the transfer of the electrons to AuNP following mechanism (A) described in Scheme III-1. Then, to propose a simple method to synthesize hybrid nanocomposite that can significantly improve the photocatalytic properties of the QD-photocatalyzed reactions (faster reactions, high TON and improved Quantum Yield).

In this work, water-soluble CdSe/ZnS core-shell QD (average diameter ~10 nm) and AuNP (average diameter ~25 nm) are functionalized respectively by azide and alkyne clickable surface ligands. Then, they are assembled in an aqueous medium at room temperature using a CuAAC reaction (copper-catalyzed azide to alkyne cycloaddition)<sup>16</sup>. The click reaction enables the preparation of the desired nanocomposite suspension by the covalent connection of the QD to AuNP throughout their surface ligands.

In order to test the photocatalytic activity of the prepared QD-AuNP nanocomposite, we employ them in a complete photoredox system in the presence of 8-oxo-2'-deoxyguanosine (8-oxo-dG) as an electron donor and nitrophenylalanine derivatives as an electron acceptor (Scheme III-2). This photocatalytic system was previously published by our group (CAMPE-CEA), as a work within the Ph.D. Thesis of Timothée CHAUVIRÉ, using water-soluble CdSe/ZnS core-shell Quantum Dots<sup>17,18</sup>. Therefore, we compare the activity of the newly designed QD-AuNP nanocomposites with the counterpart's reference samples, i.e., bare QD, AuNP, and a mixture of non-connected QD and AuNP, as well as with the previously published results.

The reader is kindly invited to see the general introduction page 11 for the description of the share responsibilities between the collaborators of the following work.

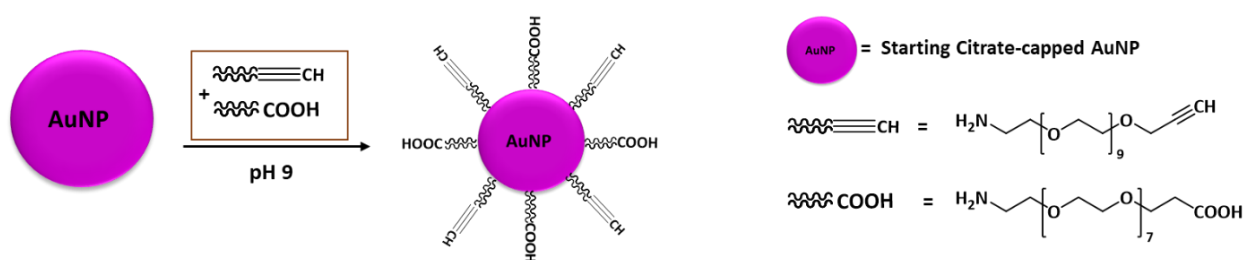


**Scheme III-2:** Previously reported<sup>17,18</sup> photocatalytic redox reaction using CdSe/ZnS QD for the simultaneous oxidation of 8-oxo-dG (electron donor) and the reduction of nitrophenylalanine derivatives (electron acceptor). Similar reduction and oxidation reactions are used in the present study as a model photoredox system to test QD-AuNP composites as photocatalysts.

## III-2. Synthesis and characterization of QD-AuNP composites.

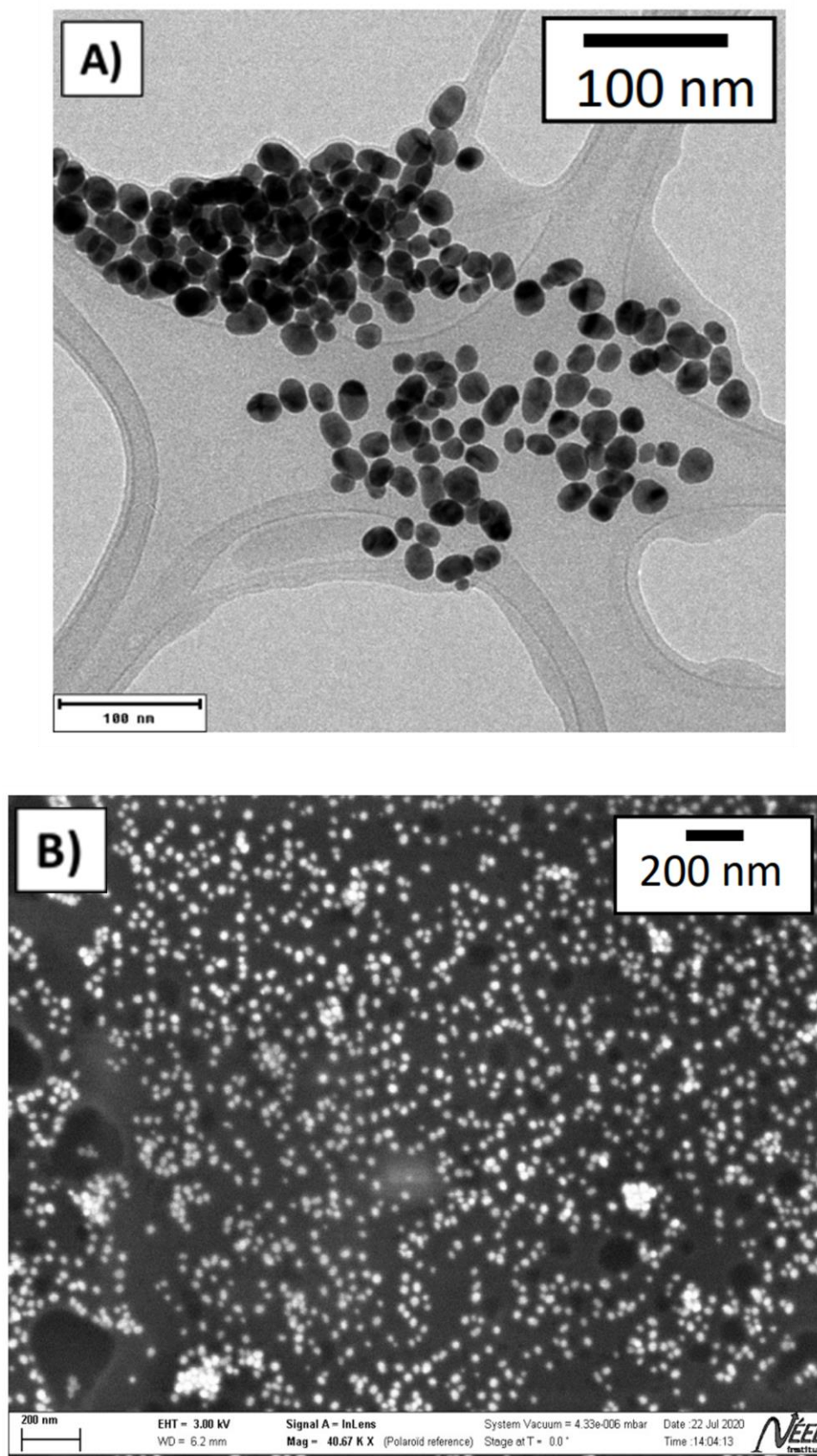
### III-2.1 Synthesis and characterization of Gold nanoparticles (AuNP).

Gold nanoparticles (AuNP) were prepared following the Turkevich-Frens classical method.<sup>19,20</sup> The detailed synthesis procedure is described in Chapter IV-3, page 251 (The preparation of the AuNP and their characterization were done in collaboration with Dr. Fabien DUBOIS from the OPTIMA-CNRS). This procedure is known to robustly lead to citrate-capped nanoparticles of spherical shape, fairly monodispersed in size. The as-synthesized AuNP were then functionalized by alkyne ligands following a typical ligand exchange process. In order to have a good coverage of the active chemical alkyne functions for the covalent click reaction while maintaining the colloidal stability of the suspension. A mixture of short-length chain of functional PEG composed of a 1:1 ratio of amino-PEG-alkyne and amino-PEG-COOH was used (Scheme III-3), the presence of terminal carboxylic acids ensured the stabilization of the surface charge density of the metallic nanoparticles.



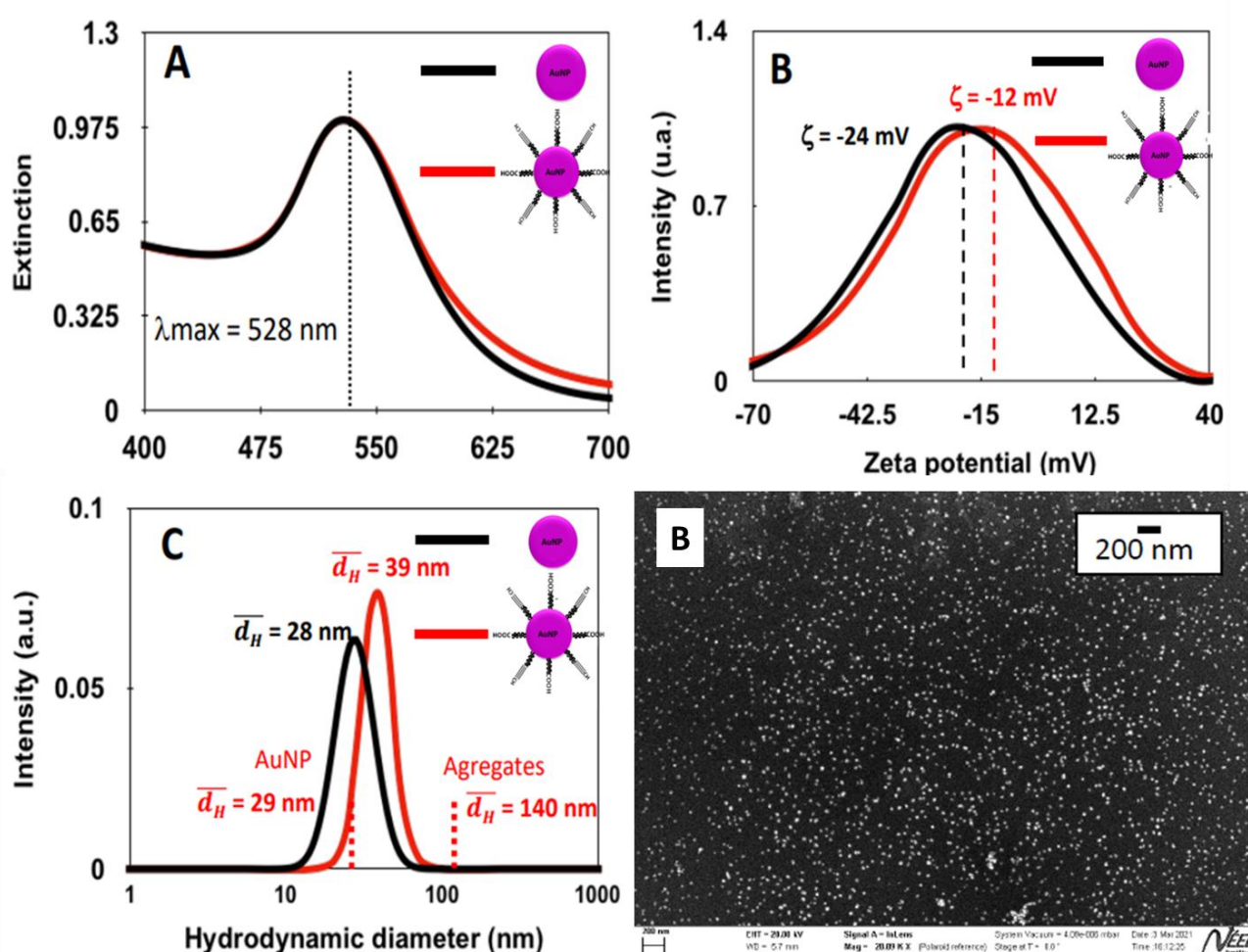
**Scheme III-3: Ligand exchange of the gold nanoparticles:** functionalization of the starting citrate-capped AuNP with mixture of alkyne ligands

The characterization of the AuNP was performed before and after functionalization using standard experimental means of UV-Visible optical spectroscopy, commercial Dynamic Light Scattering (DLS) and Transmission and Scanning Electron Microscopy (TEM and SEM). The TEM images of the initial AuNP (Figure III-1) confirm the formation of spherical particles with an averaged physical diameter of 25 nm. Their extinction spectrum (Figure III-2-A-black line) presents a band centered at 528 nm which is typical for the electrostatic plasmon resonance of individual AuNP of a few tens of nanometer in diameter<sup>21</sup>. Moreover, no additional resonance is observed at higher wavelengths, indicating a stable colloidal suspension of monodisperse AuNP.<sup>22</sup>



**Figure III-1: Microscopic characterization of the citrate-capped AuNP: A) TEM and B) SEM images of the as-synthesized citrate-capped AuNP before their surface functionalization.**

After the alkyne-ligands functionalization process, the extinction spectrum of the AuNP (Figure III-2-A, red line) does not change much except for the presence of a small signal around 650 nm, likely to be due to the partial neutralization-aggregation process leading to the formation of a few aggregates upon functionalization of the AuNP. In parallel, the zeta potential increases from -24 mV for the starting citrate-capped AuNP to -12 mV after the functionalization step (Figure III-2-B), thus confirming the modification of the surface chemistry due to the presence of the PEG ligands.



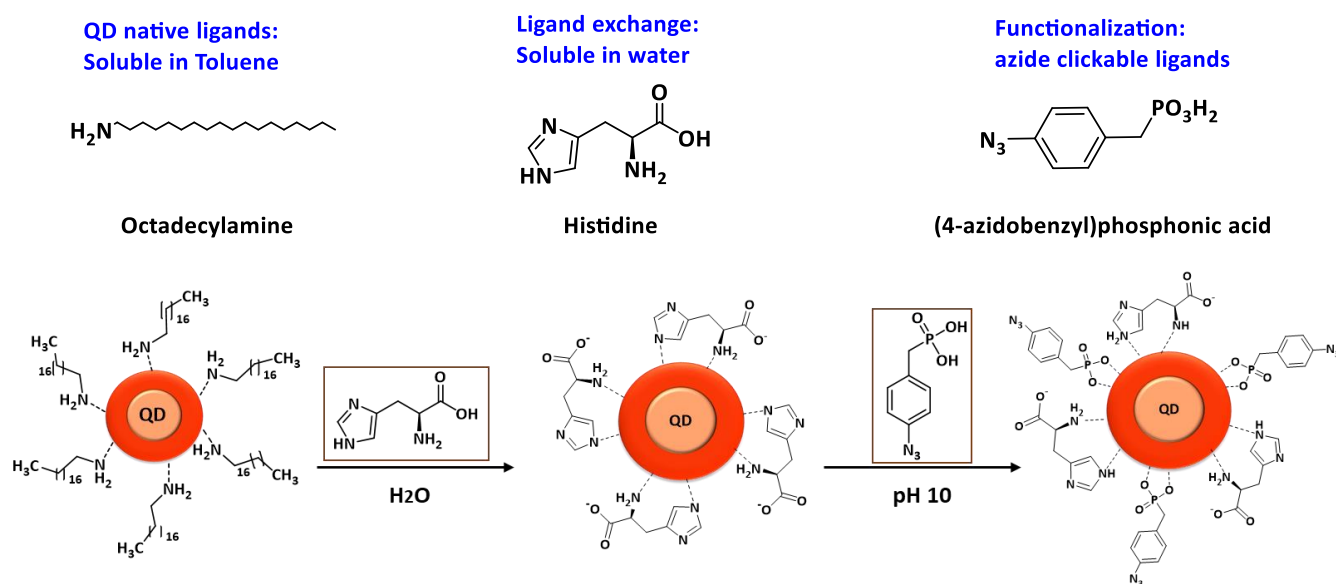
**Figure III-2: Characterization of the initial citrate-capped (black) and functionalized with alkyne clickable PEG ligands (red) AuNP: (A) Extinction spectra, (B) Zeta potential and (C) DLS-obtained size distribution. The modification of the mean diameter of the AuNP upon functionalization (solid line) is due to the formation of a few aggregates around 140 nm, that increases the value averaged over all the AuNP, while the majority of the AuNP remain isolated with an unchanged diameter (dashed line). This is visible on the SEM image of the functionalized AuNP (D).**

Figure III-2-C presents the size distribution of the hydrodynamic diameter of the AuNP obtained from the commercial DLS experiments, i.e. done in a large observation volume of a few  $\text{mm}^3$ . For the starting citrate-capped AuNP, the latter distribution is centered around 28 nm, which is in full agreement with the physical value obtained from the TEM images, the difference between the physical and hydrodynamic diameters is attributed to the charge layers surrounding the AuNP in suspension. After the functionalization of the AuNP, the size distribution shifts to higher values with an average diameter of 39 nm.

To further characterize the functionalized AuNP, DLS measurements under the confocal microscope, i.e. in a small observation volume of a few *fL* (*femtoliter*), were conducted using a home-made setup (in the Lab of Dr. Aude BARBARA). These analyses permitted to establish that the functionalization step induced the formation of a few large aggregates around 140 nm in averaged size while the majority of the AuNP stay isolated with a mean hydrodynamic diameter measured at 29 nm. These values are indicated by dashed lines in Figure III-2-C. The confocal DLS results are supported by the SEM image of the functionalized AuNP essentially presenting isolated nanoparticles of around 25 nm and very few aggregates (Figure III-2-D).

### III-2.1 CdSe/ZnS core-shell Quantum Dots.

Commercial octadecylamine capped CdSe/ZnS core/shell QD (purchased from NN-Labs) having their exciton position at 600 nm and initially dispersed in toluene were selected for the assembly with the AuNP in this study. The octadecylamine-capped CdSe/ZnS QD were transferred into water and then functionalized with azide clickable ligands in a two-step ligand exchange process (Scheme III-4). First, Histidine ligands were used to replace the native octadecylamine ligands and afford the phase transfer from toluene into aqueous medium<sup>23</sup>. Second, (4-azidobenzyl)phosphonic acid ligands, prepared in pH =10 controlled aqueous medium, were used to functionalize the water dispersed histidine-capped CdSe/ZnS QD (The detailed ligand exchange process is described in Chapter IV, section IV-2, page 249). The CdSe/ZnS QD were characterized by UV-Visible optical spectroscopy, steady state fluorescence, in addition to FCS measurements under a confocal microscope.



**Scheme III-4: Ligand exchange and surface functionalization of CdSe/ZnS core/shell QD:** Top: molecular structure of the ligands, bottom: ligand exchanges steps to replace the native octadecylamine with histidine followed by the functionalization using the azide ligand.

After functionalization, the QD appear to retain the position of their exciton at 600 nm as well as their good photoluminescence behaviour (Figure III-3). The confocal FCS measurement<sup>2</sup> showed that the colloidal stability of the QD was also maintained upon the functionalization process as a hydrodynamic diameter of  $d_H=12\pm 2$  nm was measured in the absence of the azide click ligands, while a slightly larger diameter of  $d_H=17.8 \pm 2$  nm was measured after the functionalization with the click ligands.

<sup>2</sup>The Detailed FCS analyses are not presented completely in this Thesis, but will be in the corresponding publication of this chapter

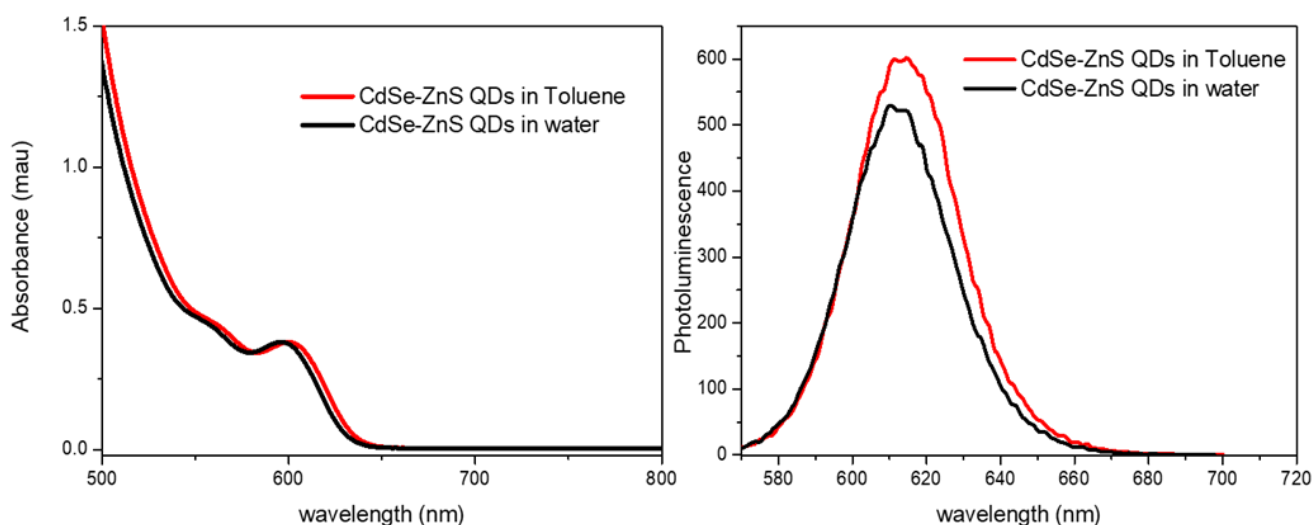


**Figure III-3: Optical characterization of the CdSe/ZnS QD before and after ligand exchange:** (Left) UV-Vis spectra of the CdSe/ZnS initially in Toluene before the ligand exchange (red) and after ligand exchange and phase transfer into water (black). (Right). Photoluminescence spectra of the CdSe/ZnS initially in Toluene before the ligand exchange (red) and after ligand exchange and phase transfer into water (black).

The purpose of the selection of CdSe/ZnS QD with an exciton position at 600 nm is to primarily target the excitation of the CdSe/ZnS QD by irradiating the assembled system (QD-AuNP) using a 590 nm wavelength light source, as the plasmon band of the AuNP is centered mainly at 528 nm. Then, connecting the QD (600 nm) and the AuNP (528 nm) and irradiating the system using a 590 nm wavelength light source should favor the light absorption by the QD more than the absorption by the AuNP. Therefore, our work relies on the hypothesis that the activity of the QD-AuNP composites is based on the charges mainly generated by the photo-excited QD following the mechanism A (Scheme III-1). Figure III-4 shows the extinction spectrum of the AuNP (black line) compared to the CdSe/ZnS QD with the exciton position at 600 nm (red line).

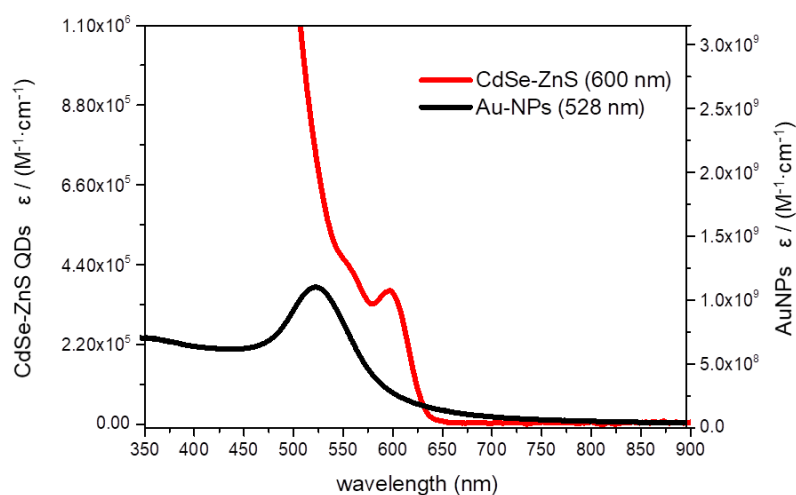
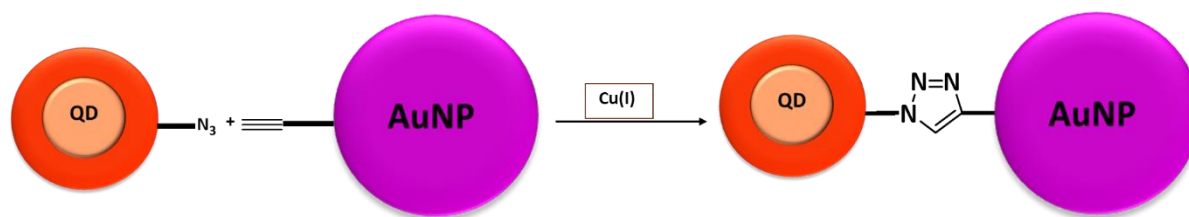


**Figure III-4:** Normalized UV-Vis absorbance spectra of CdSe/ZnS QDs and AuNP in water: AuNP-528nm (black line), CdSe-ZnS QD-600 nm (red line).

### III-2.3. Assembly of water-soluble CdSe/ZnS QD with AuNP by click reaction.

The QD-AuNP composites were prepared using CuAAC click reaction (Copper-Catalyzed Azide to Alkyne Cycloaddition)<sup>16</sup> to covalently connect the azide functionalized CdSe/ZnS QD to the alkyne functionalized AuNP (Scheme III-5). Starting with the AuNP of 25 nm in diameter, it is expected that a maximum of 30 CdSe/ZnS QD of 10 nm in diameter can cover the surface of the AuNP. To maximize the proportion of QD connected to the AuNP while restricting the proportion of free QD in solution after the reaction, we mixed 25 molar equivalents of QD in comparison to the concentration of AuNP. The click reaction was performed using CuSO<sub>4</sub>/Sodium ascorbate reagents in water with a pH=10, set by the use of a borax buffer. The in situ reduction of Cu (II) to Cu (I) produced the copper source which is needed to catalyze the click reaction. The reaction was performed under an inert atmosphere in order to avoid the presence of oxygen which can decrease the amount of Cu (I) by re-oxidizing it to Cu(II). Reference samples where no click is expected were also prepared in the same reaction conditions but without the presence of the azide ligands at the surface of the CdSe/ZnS QD.



**Scheme III-5: Assembly of QD and AuNP by click chemistry:** connection between azide-capped CdSe/ZnS QD and alkyne-capped AuNP to prepare a QD-AuNP composite by Cu(I) catalyzed click reaction

Field Emission Scanning Electron Microscopy (FESEM) images performed on the QD-AuNP composite system clearly indicate the successful connection of the QD to the AuNP (Figure III-5-A). The sample presents composites quite heterogeneous in shape and sizes with the presence of many small aggregates (<150 nm). As illustrated in Figure III-5-B, different types of morphologies were identified: large aggregates composed of gold nanoparticles connected to each other by QD indicating the success of the click chemistry reaction.

In addition, small aggregates such as dimers of AuNP connected by a unique QD, or composites formed by a single or a few QD connected to a single AuNP were also observed. On the opposite, the images obtained on the reference sample (Figure III-5-C) do not show these types of composites but only the presence of small aggregates of pure AuNP or pure QD.

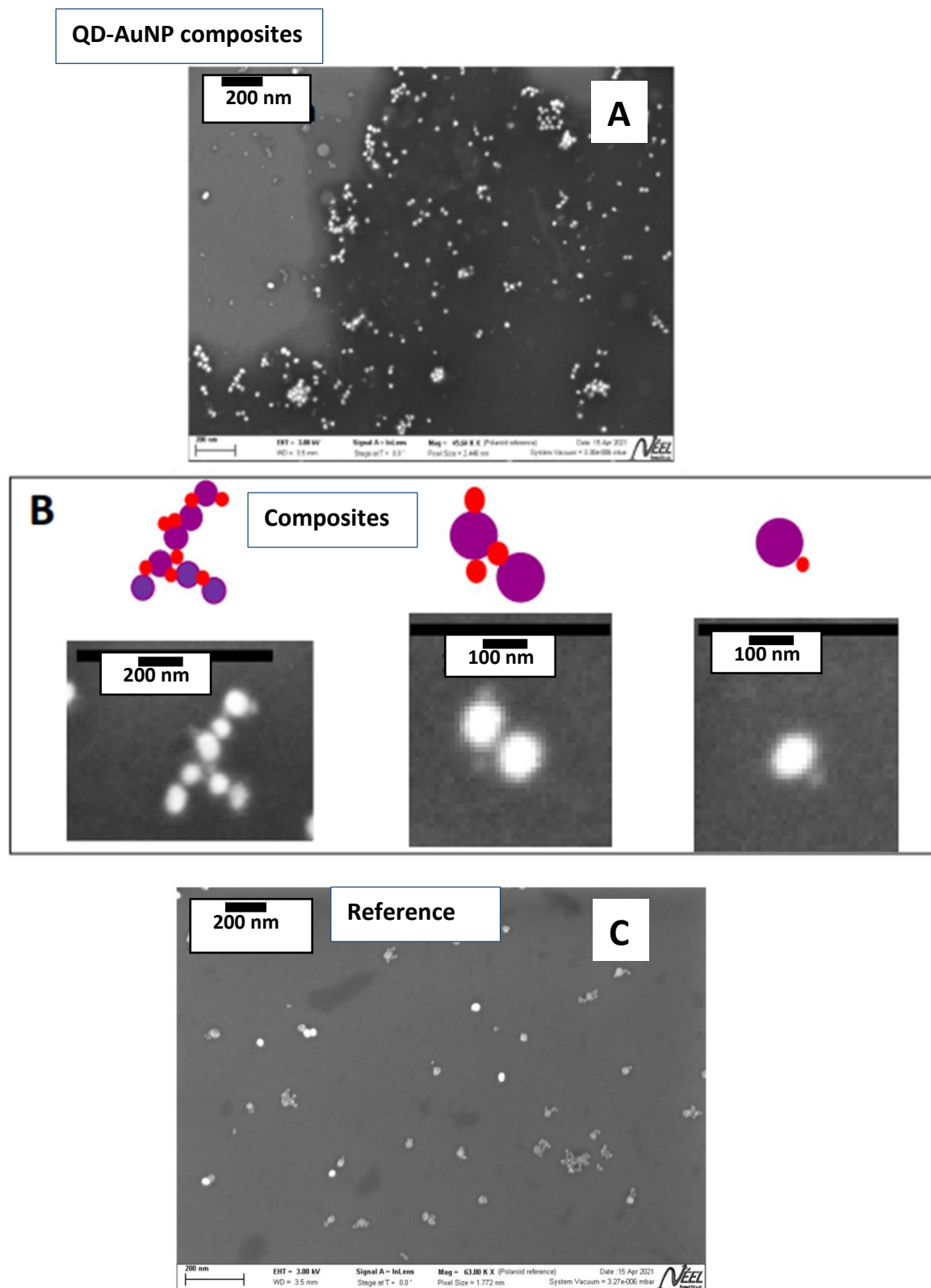


**Figure III-5: Field Emission Scanning Electron Microscopy images of the QD-AuNP composites and their corresponding reference samples: A) FESEM image of the QD-AuNP composites obtained by CuCAAC reaction. (B) FESEM image zooms and schemes of the different type of morphologies formed: multiple QD attached to multiple AuNP; dimer of AuNP sandwiching a QD and a single QD attached to a single AuNP. In the scheme, QD (resp. AuNP) are represented by red (resp. purple) spheres. C) Reference sample of non-connected QD and AuNP.**

Moreover, the standard DLS and the extinction measurements performed after 1 day of the samples preparation are shown in Figure III-6 A and B. Notably, an increase of the size distribution is observed on the composite sample and also, though to a lesser extent, on the reference sample, compared with the size distribution observed for pure AuNP samples. In both cases, this is a clear indication of the formation of aggregates containing more than one AuNP or QD and AuNP. Consistently, the extinction spectra (Figure III-6-B) still present the plasmon resonance of the individual AuNP as a main feature in addition to a slight broadening of the plasmon band, which is compatible with the presence of few and small aggregates.

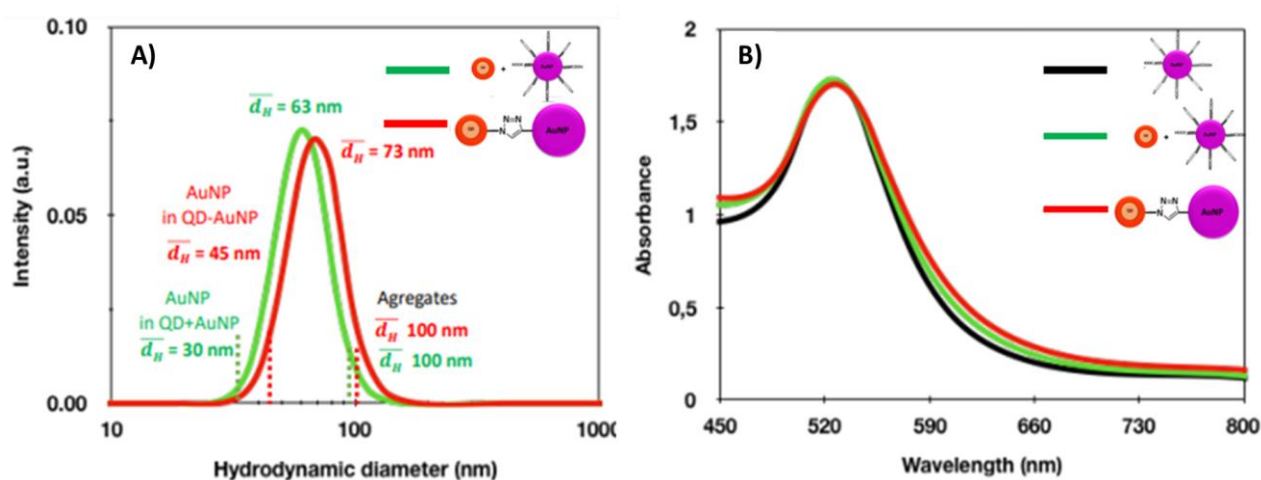


**Figure III-6: Optical characterization of the QD-AuNP composites and the corresponding reference samples.** A) DLS size distribution and (B) Extinction spectra of the functionalized AuNP (black), of the reference sample (green) and of the QD-AuNP composites (red) after one day of preparation. Dotted lines in (A) indicate the mean hydrodynamic diameters obtained from confocal DLS due to the presence of aggregates of a mean diameter of 100 nm in both samples (dashed lines) and non-aggregated AuNP in the reference sample at 30 nm (green dashed lines) and small aggregates of 45 nm in the composite sample (red dashed lines).

DLS and Fluorescence Correlation Spectroscopy (FCS) under a confocal microscope<sup>3</sup> have been performed to complement these results. These experiments are here of particular interest since they permit to selectively characterize the QD and AuNP within the same sample. Indeed, DLS measurements are mainly sensitive to the AuNP that scatter light much more than the QD while the FCS measurement, performed by measuring the fluorescence

<sup>3</sup> All FCS and DLS under a confocal microscope were performed and analyzed by Dr. Aude BARBARA from the OPTIMA-CNRS and the results, when presented, are used in this Thesis without detailed illustration of the data treatment methods.

signal of the QD, are only sensitive to the QD. The diffusion coefficient of the QD and that of the AuNP can thus be obtained independently and their comparison enables to check on the click reaction. Indeed, if the QD and the AuNP are connected they will have the same motion and thus the same diffusion coefficient. On the contrary, if the QD and the AuNP are not connected, they will evolve independently and therefore exhibit a different diffusion coefficient since they do not have the same size.

Confocal DLS measurements lead to a mean hydrodynamic diameter of  $d_H=73$  nm for the composite sample and  $d_H=63$  nm for the reference sample which are in full coherence with the size distributions obtained from standard DLS (See Figure III-6-A). However, and as for the functionalized-AuNP colloidal solutions, the data processing permits to establish that these mean diameters are the result of the combined scattering of a few large aggregates and primarily smaller AuNP or QD-AuNP composites. Interestingly, we observe that the larger aggregates are similar in the composite sample and in the reference sample, with a mean diameter around 100 nm. In the reference sample, the mean hydrodynamic diameter of the small objects is evaluated at  $d_H\sim 30$  nm, which corresponds to the size of isolated AuNP, whereas a larger mean diameter of  $d_H\sim 45$  nm is observed for the composite sample, which would correspond well to the size of QD-AuNP composites containing one AuNP surrounded with few QD. These values are also consistent with the FESEM observations i.e with the formation of many small aggregates composed of 2-4 initial AuNP upon the click reaction with the QD and to the absence of connection in the reference sample. It was established that a dimer of AuNP with an individual physical diameter of 25 nm could exhibit an apparent hydrodynamic diameter of 35 nm. Thus, for example a structure of 4 AuNP connected by 3 QD forming a chain could have an apparent hydrodynamic diameter of 50 nm<sup>24</sup>.

The DLS auto-correlation functions (ACF) corresponding to these results are presented in Figure III-7 together with FCS-ACF. For the reference sample (Figure III-7-A), one can see that the DLS and FCS ACF are indeed very different, which validates the absence of a combined motion of the AuNP and the QD. Moreover, the FCS analysis on the pure QD yields a mean hydrodynamic diameter of the QD of 10.45 nm corresponding to the value expected for non-aggregated QD. In contrast, the composite sample (figure III-7-B) present similar DLS and FCS ACFs indicating an identical motion of the QD and the AuNP.

These DLS and FCS results provide a robust indication of the successful click reaction in the composite sample leading to QD-AuNP composites with a mean hydrodynamic diameter of 45 nm and its non-occurrence in the reference sample i.e in the absence of the click ligands that mostly contain non-aggregated AuNP and QD.

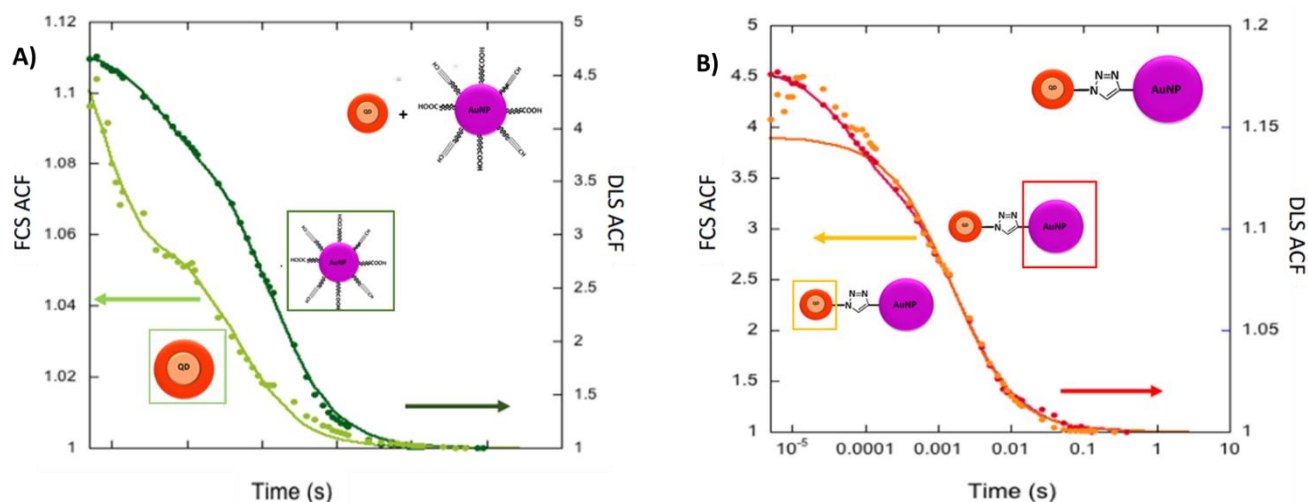


**Figure III-7: Comparison of the DLS (dark) and FCS (light) ACFs measured on the reference sample (green) and the composite sample (red).** In the reference sample where no click occurred, AuNP and QD present very different hydrodynamic behaviour due to their different diameters and their independent motion. In the composite sample, the AuNP and the QD present the same diffusion signing their joint motion and thus their QD-AuNP composite structure.

### III-3. Probing the efficiency of QD-AuNP composites as photocatalysts.

#### III-3.1. Effect of the QD concentration when using CdSe/ZnS QD alone as photocatalysts.

In a previous work<sup>18</sup>, our group (CAMPE-CEA) reported the ability of water-soluble CdSe/ZnS QD (with 1<sup>st</sup> exciton peak lying at  $\lambda=520\text{nm}$ ) to efficiently photocatalyze the oxidation of 8-oxo-dG and the reduction of NO<sub>2</sub>PhAla derivatives. In that previous study, the photoredox reaction was optimized for 2  $\mu\text{M}$  of CdSe/ZnS QD (520nm), 1mM of 8-oxo-dG (500 equiv. to the QD concentration), and 3mM of NO<sub>2</sub>PhAla derivatives as an electron acceptor (1500 equiv). The reaction proved to be efficient by accomplishing a turnover number (TON) of more than 400 in 3 hours of irradiation.

In the new approach described here, using QD-AuNP composites, we selected the CdSe/ZnS core-shell QD, which have their absorbance exciton peak at 600 nm in order to shift it from the peak of AuNP plasmon band (at 528 nm) and to favor the light absorption by the QD when irradiating the reaction mixture using a light source of wavelength of 590 nm. Moreover, before performing photocatalysis experiments, it was checked that both 8-oxo-dG and NO<sub>2</sub>PhAla efficiently quench the fluorescence of the selected CdSe/ZnS QD (600 nm) and kinetic quenching constants up to  $2.8 \times 10^{10} \text{ L}\cdot\text{mol}^{-1}\cdot\text{s}^{-1}$  and  $5.5 \times 10^9 \text{ L}\cdot\text{mol}^{-1}\cdot\text{s}^{-1}$ , respectively were obtained (the quenching experiments are described in the section A-3, page 220, of the appendix of this chapter).

The concentration of QD in the QD-AuNP samples reported here is typically optimized at 70nM in order to work with AuNP concentration (3nM) enabling a good colloidal stability and with 20-30 equivalents of QD relative to AuNP (as discussed in section III-2). Therefore, we investigated first the photocatalytic activity of QD alone at such low concentrations, from 400 nM to 70 nM, and setting the number of equivalents of the reaction substrate as 500 equiv. of 8-oxo-dG with respect to the concentration of the QD (Table III-1). While decreasing the concentration of the QD, the ability of the QD to catalyze the targeted reaction decreases progressively. A TON of 325 for the conversion of 8-oxo-dG was obtained for the 400 nM concentration of QD and dropped down to 85 TON for 70 nM concentrated QD. (The estimation of the reactions' substrates evolution are done based on HPLC analysis using standard commercial samples of each substrate).

Entry	[QD] (nM)	[8oxodG] ( $\mu\text{M}$ )	[NO <sub>2</sub> PhAla] ( $\mu\text{M}$ )	[8oxodG] conv. ( $\mu\text{M}$ ) in 10 min	[8oxodG] conv. ( $\mu\text{M}$ ) in 3h	[NO <sub>2</sub> PhAla] conv. ( $\mu\text{M}$ ) in 3h	TON in 3h
1	400	200	600	28 (14%)	130 (65%)	355 (59%)	325
2	200	100	300	10 (10%)	52 (52%)	150 (50%)	260
3	100	50	150	4 (8%)	12 (24%)	30 (20%)	120
4	70	35	105	~1 (2.8%)	6 (17%)	19 (18%)	85

**Table III-1: Impact of the reaction dilution on the photocatalytic activity of CdSe/ZnS QD on the conversion of 8-oxo-dG and NO<sub>2</sub>PhAla.** Data determined from the integration of the HPLC peaks of each of the 8-oxo-dG and NO<sub>2</sub>PhAla based on a commercial standard of each of the molecules. All the reaction are performed in aqueous medium under inert atmosphere and irradiated using  $\lambda=590 \text{ nm}$  LED. TON are computed for the conversion of 8-oxo-dG. HPLC chromatograms are collected in the appendix, Figure III-A4-1 page 221.

### III-3.2. Enhanced photocatalytic activity using QD-AuNP composites as photocatalysts.

The newly designed QD-AuNP (70nM CdSe/ZnS QD assembled with 3nM AuNP, irradiated using 590 nm LED), was tested for the same reaction and with the same conditions as in the bare QD case (Table III-1, entry 4). The results obtained showed much higher efficiency than bare QD. In the QD-AuNP composite case (**QD-Au** in Table III-2), 345 TON were achieved within the first 10 minutes and 385 TON totally in 3 hours (Table III-2 entry 1). In the following, unless stated otherwise, TON are computed vs. QD to enable comparison with bare QD case. This number is much higher than the one obtained after 3 hours (TON = 85) for the same concentration of QD without the AuNP and is comparable to the one obtained for a concentration of 400 nM of QD alone after three hours of irradiation. Therefore, the use of QD-AuNP composites increases both the speed and the efficiency of the reaction. A reference sample containing 70 nM QD and 3nM AuNP that were not assembled (**QD+Au** in Table III-2), was also tested. In this case, a TON of 100 for the conversion of the 8-oxo-dG was measured after three hours (Table III-2, entry 2). This modest improvement compared to the case of bare QD demonstrates that the connection of QD and AuNP is important for the better efficiency.

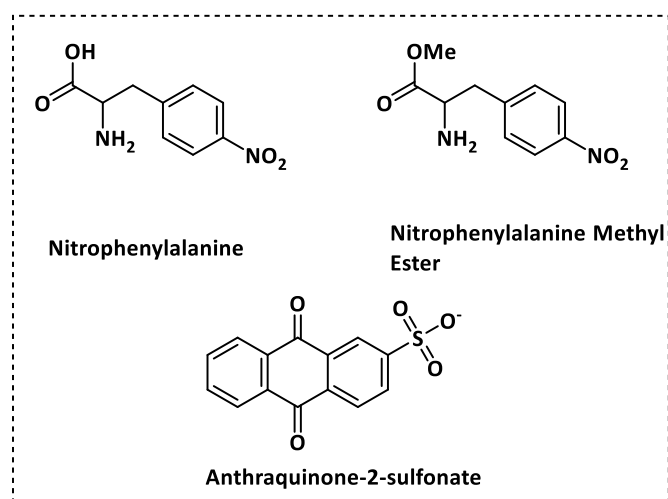
Then, more trials were performed for optimizing the performances and the activity of the QD-AuNP. First, the concentration of the reaction substrates (8-oxo-dG and NO<sub>2</sub>PhAla) was set fixed, but the concentration of the QD-AuNP composite was decreased (concentration of QD at 45nM, concentration of AuNP at 2 nM - Table III-2 entry 3). In this case, a higher TON (555) was achieved for the conversion of 8-oxo-dG. Then, a higher excess of the electron acceptor (NO<sub>2</sub>PhAla) was used in order to afford a better electron transfer from the QD and the AuNP (entry 5). This afforded a slightly higher TON (600). Finally, both a significant molar excess of 8-oxo-dG molecules (2600 equivalents as compared to the QD) and of NO<sub>2</sub>PhAla molecules (6 equivalents as compared to 8-oxo-dG) were added (entry 7). Under these conditions, a TON of 2311 was achieved for the conversion of the 8-oxo-dG molecules after 3 hours of irradiation, corresponding to a conversion rate of 86% of its initial concentration. For these three reaction conditions, reference experiments of non-connected QD and AuNP were tested (entries 4, 6 and 8). In each situation, the observed TON are systematically lower, by a factor of approximatively 5, than those observed using the QD-AuNP composites.

Entry	Cat.	[QD]/[Au] (nM)	[8oxodG] ( $\mu$ M)	acceptor (pH)	pH	[acceptor] ( $\mu$ M)	[8oxodG] conv. ( $\mu$ M) in 10 min	[8oxodG] conv. ( $\mu$ M) in 3h	[acceptor] conv. ( $\mu$ M) in 3h	TON in 3h
1	QD-Au	70/3	35	NO <sub>2</sub> PhAla	10	105	24 (68%)	27 (77%)	22 (20%)	385
2	QD+Au	70/3	35	NO <sub>2</sub> PhAla	10	105	~2 (5%)	7 (20%)	10 (9.5%)	100
3	QD-Au	45/2	35	NO <sub>2</sub> PhAla	10	105	20 (57%)	25 (71%)	21 (20%)	555
4	QD+Au	45/2	35	NO <sub>2</sub> PhAla	10	105	~1 (2%)	5 (14%)	15 (14%)	111
5	QD-Au	45/2	35	NO <sub>2</sub> PhAla	10	210	25 (71%)	27 (77%)	40 (19%)	600
6	QD+Au	45/2	35	NO <sub>2</sub> PhAla	10	210	~2 (5%)	6 (17%)	14 (6%)	130
7	QD-Au	45/2	120	NO <sub>2</sub> PhAla	10	720	77 (64%)	104 (86%)	250 (35%)	2311
8	QD+Au	45/2	120	NO <sub>2</sub> PhAla	10	720	5 (4%)	20 (16%)	50 (7%)	440
9	QD-Au	45/2	120	AQ-2S	10	720	52 (43%)	90 (75%)	-	2000
10	QD+Au	45/2	120	AQ-2S	10	720	3 (2%)	17 (14%)	-	370
11	QD-Au	45/2	120	NO <sub>2</sub> PhAlaMe	10	720	78 (65%)	108 (90%)	430 (60%)	2400
12	QD+Au	45/2	120	NO <sub>2</sub> PhAlaMe	10	720	5 (4%)	19 (16%)	86 (11%)	420
13	QD-Au	45/2	120	NO <sub>2</sub> PhAlaMe	7.4	720	82 (%)	118 (98%)	619 (85%)	2620
14	QD+Au	45/2	120	NO <sub>2</sub> PhAlaMe	7.4	720	6 (5%)	21 (17%)	120 (16%)	460
15	QD-Au	45/2	120	-	10	-	35 (29%)	42(35%)	-	930

**Table III-2: Optimization of the photoredox reaction's condition** to oxidize 8-oxo-dG and reduce NO<sub>2</sub>PhAla using the composites of CdSe-ZnS QDs and Au-NPs (QD-Au) the corresponding reference sample (QD+Au). All reactions are performed in aqueous solution under an inert atmosphere and irradiated using  $\lambda=590$  nm LED. HPLC chromatograms are collected in the appendix.

Regarding the kinetics of the photoredox reactions under the action of the QD-AuNP composites, the conversion of 8-oxo-dG exhibits two different regimes, a fast one during the first minutes of the reaction and a slower one after 20 minutes of irradiation (see Figure III-8-A). Interestingly, in the absence of molecular electron acceptor (Entry 15 and Figure III-8-A green plot), a fast conversion of 8-oxo-dG is also observed during the first minutes of the reaction, then the conversion reaches a plateau up to 3 hours of irradiation. These regimes will be discussed in section III-4.3, page 211.

Furthermore, since the AuNP used in the preparation of the QD-AuNP composites are functionalized with negatively charged PEG carboxylate ligands, the electrostatic interaction can play an important role for improving the transfer from AuNP to the electron acceptors<sup>25,26</sup>. To investigate this effect, three different acceptors with different expected electrostatic interactions were tested in the optimized reaction conditions (See scheme III-6). Beside Nitrophenylalanine (NO<sub>2</sub>PhAla), Anthraquinone-2-sulfonate (AQ-2S), and Nitrophenylalanine methyl ester (NO<sub>2</sub>PhAlaMe) at either pH=10 controlled medium or at pH=7.4 were tested. Figure III-8-A shows the reaction kinetics for the conversion of the 8-oxo-dG and the deduced TON (for the conversion of 8-oxo-dG), in each case. A similar behavior as that described for the reaction using NO<sub>2</sub>PhAla was observed: a fast conversion during the first minutes of the reaction followed by a progressive slow down starting after about 20 minutes and ending by a plateau after one hour and up to three hours of irradiation, whose height varies depending on the electron acceptor molecule.



**Scheme III-6: Chemical structures of the molecular electron acceptors: Nitrophenylalanine, nitrophenylalanine methyl ester, and anthraquinone-2-sulfonate.**

A less good conversion of 8-oxo-dG is observed in the presence of AQ-2S molecules (Table III-2 entry 9, Figure III-8-A, pink line) compared with NO<sub>2</sub>PhAla (Table III-2 entry 7, Figure III-8-A, black line). This is attributed to the purely repulsive electrostatic interaction between the negatively charged ligands AuNP and the negative charge of the sulfonate moiety of AQ-2S, while, at pH=10, a small fraction of NO<sub>2</sub>PhAla is in the zwitterionic neutral form (pK<sub>a</sub>=9.1 for the amino group of phenylalanine moieties). NO<sub>2</sub>PhAlaMe (Table III-2 entry 11 and Figure III-8-A, blue line) did not improve the photocatalytic activity at pH=10, compared with NO<sub>2</sub>PhAla, in spite of the introduction of a neutral ester moiety instead of the carboxylate moiety of NO<sub>2</sub>PhAla. This is attributed to the partial hydrolysis of this ester moiety as evidenced by HPLC analysis (See HPLC chromatograms in the section A-2, page 219, of the Appendix of this chapter). This hydrolysis was avoided by reducing the pH of the reaction medium to 7.4. At such pH, the use of the electron acceptor NO<sub>2</sub>PhAlaMe enabled a higher conversion of the 8-oxo-dG with a TON value of more than 2600 (Table III-2 entry 13 and Figure III-8-A, red line).

The influence of the electrostatic interaction between the electron acceptor and the AuNP and QD ligands was also clearly observed when monitoring the conversion of the NO<sub>2</sub>PhAla and NO<sub>2</sub>PhAlaMe. As it is showed in Figure III-8-B, the conversion of the NO<sub>2</sub>PhAlaMe at pH=7.4 medium (red curve) was almost 1.5 times better than at pH=10 (blue curve), which was itself twice higher than the conversion of the NO<sub>2</sub>PhAla (black curve).

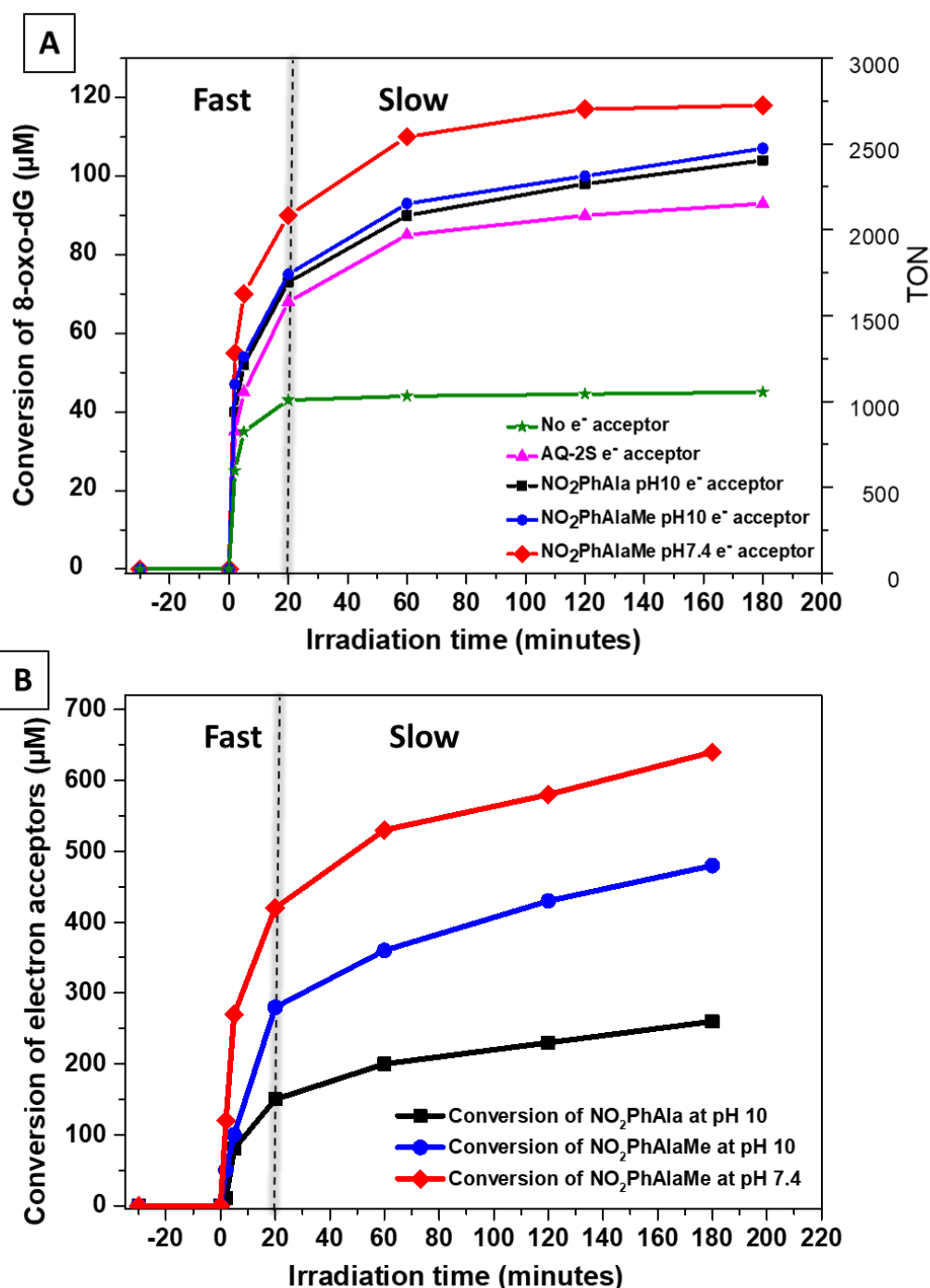


**Figure III-8 : Evolution of the Photocatalytic activity of the QDs-Au-NPs composite with different electron acceptor;** A) Conversion of 8-oxo-dG in the absence of any electron acceptor (green line), in the presence of AQ-2S as electron acceptor at pH 10 (pink line), in the presence of  $\text{NO}_2\text{PhAla}$  as electron acceptor at pH 10 (black line), in the presence of  $\text{NO}_2\text{PhAlaMe}$  as electron acceptor at pH=10 (blue line), and in the presence of  $\text{NO}_2\text{PhAlaMe}$  as electron acceptor at pH=7 (red line). B): conversion of electron acceptors; black line: conversion of  $\text{NO}_2\text{PhAla}$ , blue line: conversion of  $\text{NO}_2\text{PhAlaMe}$  at pH 10 (calculated based on the sum of the 2 HPLC peaks presents in the chromatograms), and red line: conversion of  $\text{NO}_2\text{PhAlaMe}$  at pH 7.4 .The concentration of the QDs was fixed at 45 nM of QDs assembled with 2 nM AuNP, the concentration of the electron donor 8-oxo-dG was set at  $120\mu\text{M}$  (~2600 Equiv) and a  $720\mu\text{M}$  concentrated electron acceptor (6 equiv compared with the 8-oxo-dG). The corresponding HPLC chromatograms are collected in the appendix of this Chapter Figures A4.2 to A4.4, pages 221 to 224.

### III-3.3. Quantitation of the photocatalytic activity improvement – Internal QY vs. QD absorbed photons.

In order to compare the photocatalytic performances of the bare QD or the QD-AuNP photocatalysts, first, we estimated the internal quantum yield (QY) using different concentrations of bare QD. Then we computed the “internal QY vs. QD absorbed photons”, which is obtained in the case of reactions photocatalyzed by QD-AuNP composites by considering only the photons that would be absorbed only by QD in the absence of AuNP (the corresponding absorbance is reported in the 4<sup>th</sup> column of Table III-3). The results of these computations of “internal QY vs. QD absorbed photons” (QY in the following) are summarized in Table III-3 (See Chapter IV, section IV-6, page 254, for the detailed calculation). The QY of the reaction performed using 400 nM QD was estimated to be 0.026% (Table III-3 entry 1), which is lower than the value (0.06%) our group reported previously<sup>18</sup> for a 2 $\mu$ M concentrated QD. The further decrease in the QD concentration to 70 nM induced a lower QY of 0.006% (Table III-3, entry 2). Interestingly, in the case of the 70 nM QD-AuNP composite, the obtained QY is 0.027% (Table III-3, entry 3), which is 4.5 times higher than in the case of 70 nM QD alone and very close to the case of 400 nM QD alone. This comparison shows that the connection of QD with AuNP, at constant QD concentration, is strongly beneficial to the photocatalytic activity. Moreover, in the case of optimized 45nM QD-AuNP composite, the QY was further improved up to 0.16% (Table III-3, entry 4), which outperforms the best results we previously reported with QD alone (0.06%) by a factor 2.7.

Entry	PhotoCat. [QD]	Table (entry)	Abs of QD	TON vs. QD (con of 8oxodG)	QY vs. QD
1	QD [400 nM]	1 (1)	0.140	325	0.026%
2	QD [70 nM]	1 (4)	0.025	85	0.006%
3	QD-AuNP [70 nM]	2 (1)	0.025	385	0.027%
4	QD-AuNP [45 nM]	2 (7)	0.016	2311	0.160%

**Table III-3: Estimated Quantum Yield (QY):** The estimated QY of the photoredox reaction using different concentrations of QD (alone or in composites) by considering the conversion of 8-oxo-dG after 3hours of irradiation

### III-3.3. Comparison of the photocatalytic activity of QD-AuNP by using irradiation in the QD exciton range (590nm) or in the AuNP plasmon resonance band range (528nm).

The influence of the excitation wavelength irradiation on the catalytic activities was studied by comparing experiments with irradiation at 590 nm (more favorable to QD excitation) and at 528 nm (more favorable to AuNP excitation). The results obtained for QD-AuNP composites (**QD-Au**) were compared with those obtained for some reference samples (QD + AuNP mixed but not connected (**QD+Au**), QD alone (**QD**) and AuNPs alone (**Au**)) and using NO<sub>2</sub>PhAlaMe electron acceptor at pH=7.4 (see Figure III-9).

Using the irradiation set-up at 590 nm, the higher performance of the QD-AuNP composite system for the conversion of 8-oxo-dG clearly appears, in particular with up to 2600 TON vs. QD (57200 TON vs AuNP) during the 3 hours of irradiation (Figure III-9-A red curve). Much lower values were achieved for the not connected QD and AuNP reference sample (TON=400 vs QD, TON=8800 vs AuNP blue curve), the QD alone sample (TON=500 vs QD, black curve), and the AuNP alone sample (TON=8200 vs AuNP, pink curve). The results of the conversion of NO<sub>2</sub>PhAlaMe (see Figure III-9-B) during the same reactions were also much better in the case of the composite QD-AuNP, by a factor of three as compared to the cases of the QD alone and that of the non-connected but mixed QD and AuNP and by a factor of six as compared to the case of AuNP alone.

The second set of experiments was performed with the same conditions but changing the irradiation set-up to a 528 nm Green LED. The red curve of Figure III-9-C shows the conversion of 8-oxo-dG by using the QD-AuNP composites as photocatalysts: up to 1200 TON were achieved. The QD alone case resulted in a low conversion of 8-oxo-dG with 260 TON, while the sample of the mixed QD and AuNP was relatively better than the QD alone by reaching a TON of 900 and pure AuNP showed a very similar photocatalytic activity. The conversion of the NO<sub>2</sub>PhAlaMe was also monitored in these experiments (Figure III-9-D), and the results showed very similar trends as for the conversion of 8-oxo-dG: QD-AuNP composites are slightly more efficient than AuNP alone, which exhibit very similar activity as the non-connected QD and AuNP nanoparticles, and at last QD alone exhibit much lower activity.

Noteworthy, it should be mentioned that, when irradiating at 528 nm the photocatalytic activity of the QD-AuNP composites is not negligible (around 50% of the activity obtained when irradiating at 590 nm) and that AuNP alone or not connected to QD also present a non-negligible activity when irradiating at this maximum plasmon resonance band wavelength (around 35% of the activity obtained with QD-AuNP composites when irradiating at 590 nm). Moreover, it is worth mentioning that the green LED ( $\lambda = 528$  nm) has a power of 2.5 times (50 mW) higher than that of the 590 nm yellow LED (20 mW) used in these experiments. Then, when normalized to the LEDs power, the photocatalytic activity of the QD-AuNP composites irradiated at 528 nm appears to be 20% of the activity when irradiated at 590 nm. And the photocatalytic activity of the bare AuNP at 528 nm is only 14% compared to QD-AuNP irradiated at 590 nm. The corresponding HPLC chromatograms of these experiments are collected in Figures III-A4.4 and III-A4.5 on pages 225 and 226.

All taken together, the results of the photocatalysis experiments reported in Figure III-9 show that the enhancement obtained when using the QD-AuNP composites as a redox photocatalyst is better when irradiating them at the wavelength of the QD exciton (590 nm). When working at this wavelength, the connection between QD and AuNP is crucial for the activity of the photocatalyst since non-connected particles exhibit much lower activities. Based on these features a possible mechanism for such QD-AuNP photocatalyst is proposed in the next section (III-4).

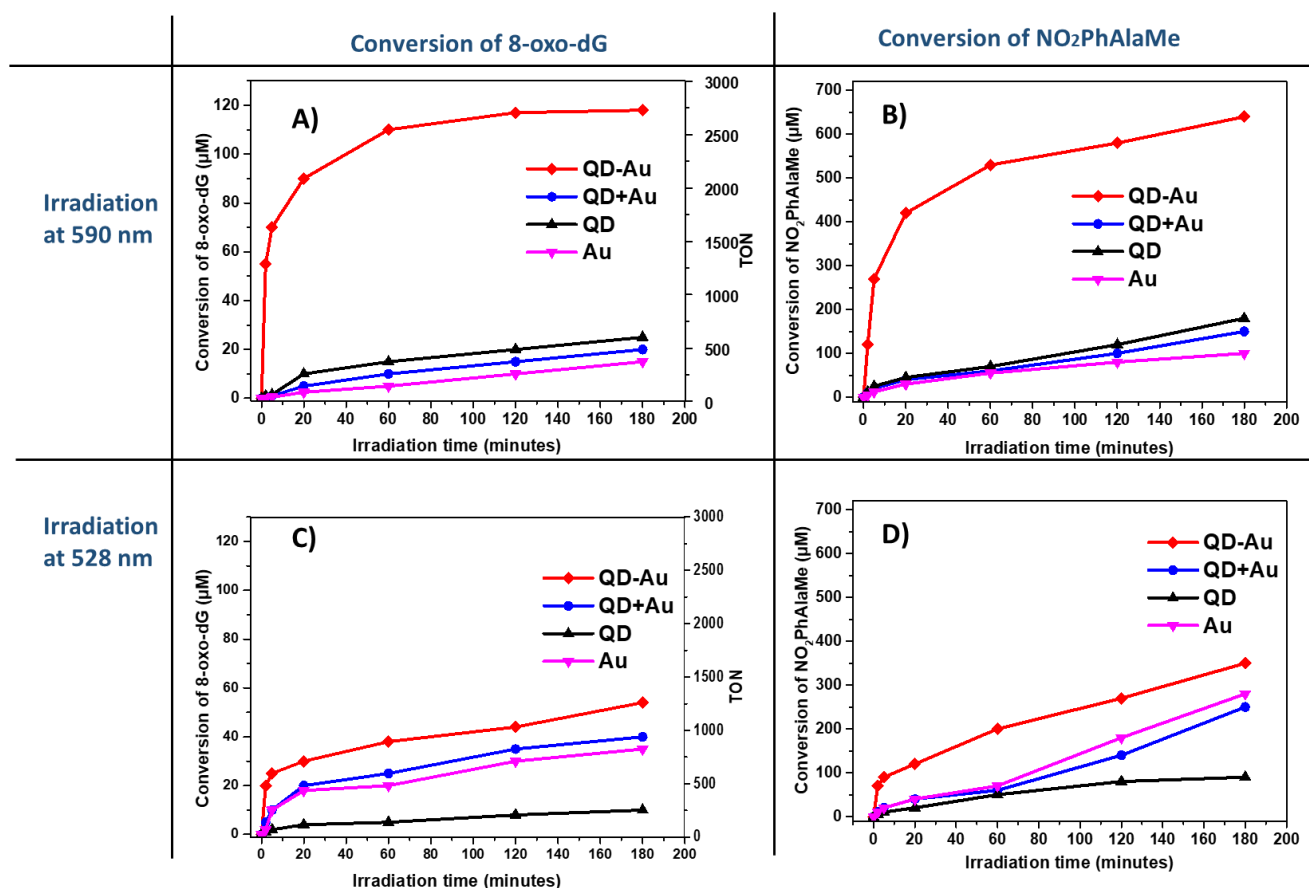


**Figure III-9: The HPLC monitored consumption of 8-oxo-dG and  $\text{NO}_2\text{PhAlaMe}$  with the different Photocatalysts;** A) Conversion of 8-oxo-dG by irradiating at  $\lambda = 590 \text{ nm}$ : Red curve using the QD-AuNP as photocatalyst, Blue curve using the ref of QD mixed with AuNP as photocatalyst, Black curve using the CdSe/ZnS QD alone as photocatalyst, Pink curve using the AuNP alone as photocatalyst. B) Conversion of  $\text{NO}_2\text{PhAlaMe}$  by irradiating at  $\lambda = 590 \text{ nm}$ : Red curve using the QD-AuNP as photocatalyst, Blue curve using the ref of QD mixed with AuNP as photocatalyst, Black curve using the CdSe/ZnS QD alone as photocatalyst, Pink curve using the AuNP alone as photocatalyst. C) Conversion of 8-oxo-dG by irradiating at  $\lambda = 528 \text{ nm}$ : Red curve using the QD-AuNP as photocatalyst, Blue curve using the ref of QD mixed with AuNP as photocatalyst, Black curve using the CdSe/ZnS QD alone as photocatalyst, Pink curve using the AuNP alone as photocatalyst. D) Conversion of  $\text{NO}_2\text{PhAlaMe}$  by irradiating at  $\lambda = 528 \text{ nm}$ : Red curve using the QD-AuNP as photocatalyst, Blue curve using the ref of QD mixed with AuNP as photocatalyst, Black curve using the CdSe/ZnS QD alone as photocatalyst, Pink curve using the AuNP alone as photocatalyst.

## III-4 – Mechanistic Studies

### III-4.1. Quenching of QD fluorescence in QD-AuNP composites.

The connection between the QD and the AuNP in the composites was intended to enhance the charges separation of the exciton after the photoexcitation of the QD by enabling an efficient electron transfer to the AuNP. In this hypothesis, the connection between QD and AuNP should induce a quenching of the radiative emission of the QD after the excitation. The fluorescence of the samples during the formation of the composites was monitored as a function of time in the presence of two different concentrations of CuSO<sub>4</sub>/sodium ascorbate (same concentration (1x) and two time more concentrated (2x) than the preparation of the composite - Figure III-10). To ensure that the quenching observed was not due to the presence of reagents (Cu cations, ascorbate, AuNP...), a reference experiment was performed in the same conditions of reagents but with histidine-only capped QD (without azide ligands – Figure III-10-A) or with amino-PEG-COOH-only capped AuNP (without alkyne ligands – Figure III-10-B).

In the absence of one of the clickable ligands at the surface of one of the two particles, the mixture of reagents induces a slight decrease in the fluorescence intensity as a function of time (less than 15 % decrease in the initial intensity after 60 minutes). However, in the actual conditions of CuAAC reaction, the quenching of the fluorescence is clearly observed with up to 50 % decrease of the initial fluorescence intensity after 60 minutes for the sample with the highest concentration in CuSO<sub>4</sub>/sodium ascorbate. Moreover, the kinetics of the observed fluorescence quenching depends on the concentration of the CuSO<sub>4</sub>/ascorbate reagent.

These results strongly support our conclusion that this quenching is due to the connection of QD at the surface of AuNP by the CuAAC reaction, which enables an efficient electron transfer from the excited QD to the AuNP.

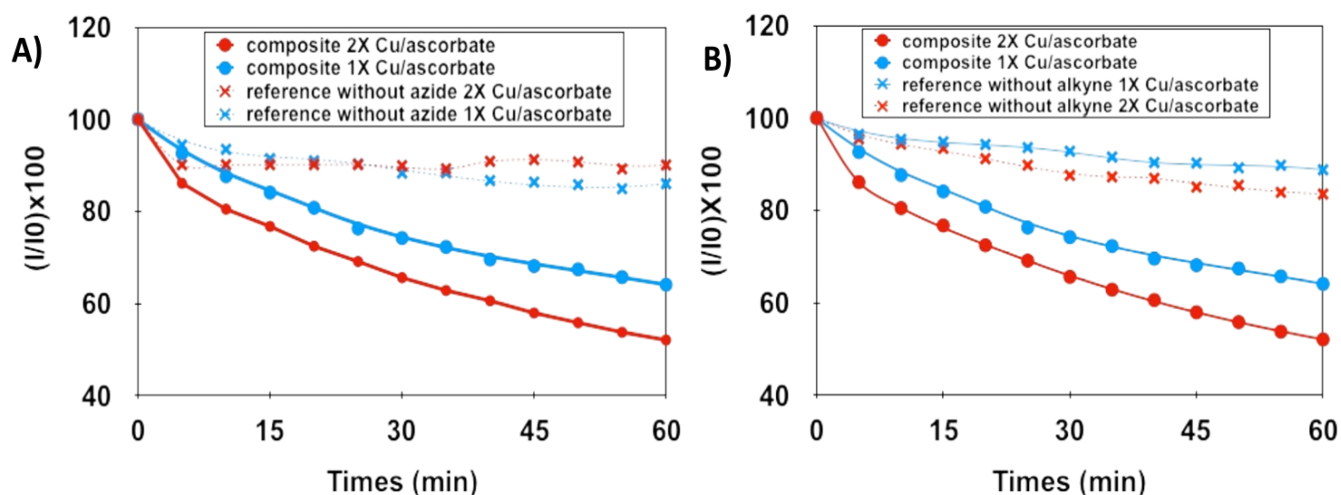


**Figure III-10: Monitoring of the fluorescence of CdSe/ZnS QD as a function of time during the formation of the composite in comparison with simple mixture of QD and AuNP (without click ligands).**  $\lambda_{exc} = 590 \text{ nm}$ ,  $\lambda_{em} = 620 \text{ nm}$ . A): Quenching of fluorescence during the click reaction in the same conditions than the formation of composites (1X Cu/ascorbate -  $[\text{CuSO}_4] = 0,67 \mu\text{M}$  and  $[\text{sodium ascorbate}] = 1,33 \mu\text{M}$  - blue line) or with twice more concentrated sulfate copper and sodium ascorbate (2X Cu/ascorbate -  $[\text{CuSO}_4] = 1,33 \mu\text{M}$  and  $[\text{sodium ascorbate}] = 2,66 \mu\text{M}$ ) (red line) in comparison with reference sample without azide ligands at the surface of QD: blue dots line = same conditions of the formation of the composite (1x Cu-ascorbate), red dots line = twice more concentrated sulfate copper and sodium ascorbate (2x Cu/ascorbate). B): same study but by comparison with in this case no alkyne ligands at the surface of AuNP using same conditions as the formation of composites (1x Cu/ascorbate - blue curve) or two more concentrated sulfate copper and sodium ascorbate (2x Cu/ascorbate-red curve).

### III-4.2-Blue shift of the plasmon band due to the accumulation of electrons when irradiating QD-AuNP composites in the presence of the electron donor.

A way to study the possible charge transfer mechanisms within the QD-AuNP composites is to monitor the plasmon extinction band of the AuNP connected to the QD while the latter are photoexcited in the presence of the electron donors, or electron acceptors. Indeed, if the redox reaction which takes place between the QD and the donor/acceptor molecules gives rise to an electron transfer between the QD and the AuNP, the plasmon extinction band will undergo a blue (or red) shift, resulting from the charging (or discharging) of the metal nanoparticles<sup>27-29</sup>.

In order to investigate this phenomenon, a colloidal solution of QD-AuNP composites was diluted to 20nM concentration in QD and irradiated using a 590 nm LED light source, in the presence of a high excess of 8-oxo-dG molecules acting as electron donors (2600 equiv. as

compared to the QDs concentration, i.e 52  $\mu$ M in concentration). The extinction spectra of the sample were recorded in situ in the irradiation setup and as a function of time. Figure III-7-A shows the latter spectra which are dominated by the plasmon extinction band of the AuNP around 529 nm. Upon excitation of the QD in presence of 8-oxo-dG, the plasmon extinction band undergoes a blue-shift that reaches a maximum of 4 nm after 50 minutes of irradiation (from  $\lambda=529$  nm to 525 nm, see Figure III-11-C). After that time, the extinction spectra of the sample did not evolve anymore and the irradiation was stopped.

Then, NO<sub>2</sub>PhAla was added as an electron acceptor to the sample to check on the possibility to extract the electrons stored at the AuNP surface and consequently discharge them. As Figure III-11-B and III-11-C show, as expected reverse behavior occurred: a red-shift was observed until the return of the plasmon extinction band to its original position (529nm). This observation indicates that the discharging process of the AuNP by the NO<sub>2</sub>PhAla electron acceptor is efficient.

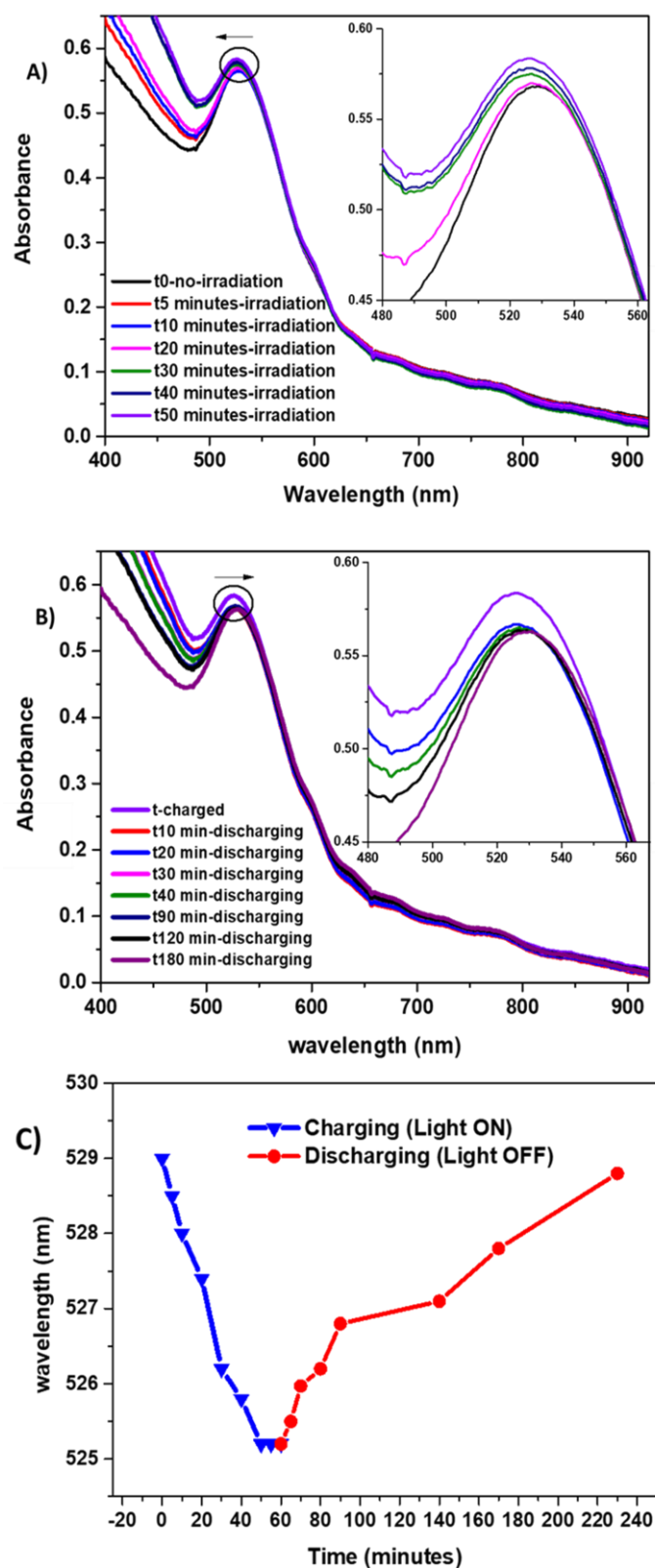


**Figure III-11:** The time evolution of the UV-Vis absorption spectra of Au-NPs during the photochemical charging and discharging process : (A) QD-AuNP composite sample of 20nM QDs' concentration in the presence of 52 $\mu$ M of 8-oxo-dG as electron donor and irradiated with 590 nm LED showing the charging of the AuNP; (B) After the addition of 312 $\mu$ M of NO<sub>2</sub>PhAla as electron acceptor and stopping the light irradiation which shows the discharging of the Au-NPs; (C) evolution of the wavelength of the absorption position of the AuNP during the charging/discharging process.

Furthermore, in order to make sure that the observed charge transfer occurs between the QD and the AuNP and via their connection, the same experiment was performed with two test samples, (i) a colloidal solution of non-connected QD and AuNP and (ii) a colloidal solution of AuNP. In both cases, the same concentration of 52  $\mu\text{M}$  of 8-oxo-dG molecules was added to the samples before irradiating them with a LED at 590 nm. Figure III-12 shows the time evolution of the extinction spectra for the two samples. Interestingly, no changes are observed as a function of time, which means that no electron injection at the surface of the AuNP took place.

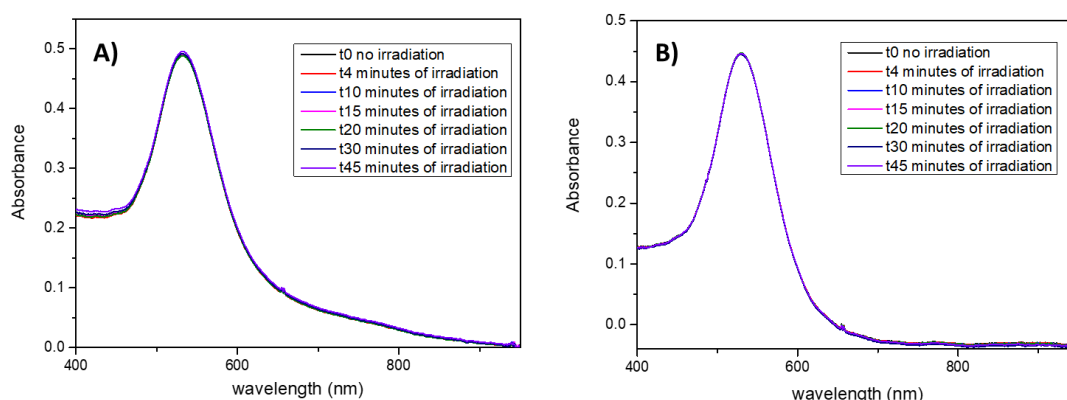


**Figure III-12:** The evolution of the extinction spectra of reference samples irradiated in the presence of the electron donor (A) non-connected QD and AuNP in the presence of 8-oxo-dG as electron donor and irradiated with 590 nm LED. (B) Sample of pure AuNP in the presence of 8-oxo-dG as electron donor and irradiated with 590 nm LED

The observed blue shift can be used to estimate the number of electrons accumulated in the AuNP during the charging process of QD-AuNP composites by using the relationship (1) existing between the position of the plasmon resonance extinction band and the conduction electrons density in metal NPs (See the section A-5, page 227, in the Appendix of this chapter for details):

$$\lambda_f \sim \lambda_i \left( 1 - \frac{\Delta N}{2N_i} \right) \quad (1)$$

where,  $\lambda_f$  is the maximum wavelength of the shifted plasmon extinction band after charging process,  $\lambda_i$  is initial maximum wavelength,  $N_i$  is the initial electron density of the AuNPs before the irradiation and  $N_f$  is the final electron density after the charging process and  $\Delta N = N_f - N_i$ .

According to equation (1), the observed blue-shift of 4 nm corresponds to a variation of 1.5% of the electron density. The bulk electron density of Au being worth  $6.10^{28} \text{ e}^-/\text{m}^3$ , this corresponds to a variation of  $9.10^{26} \text{ e}^-/\text{m}^3$  i.e 7400 electrons per AuNP of mean diameter  $d=25$  nm

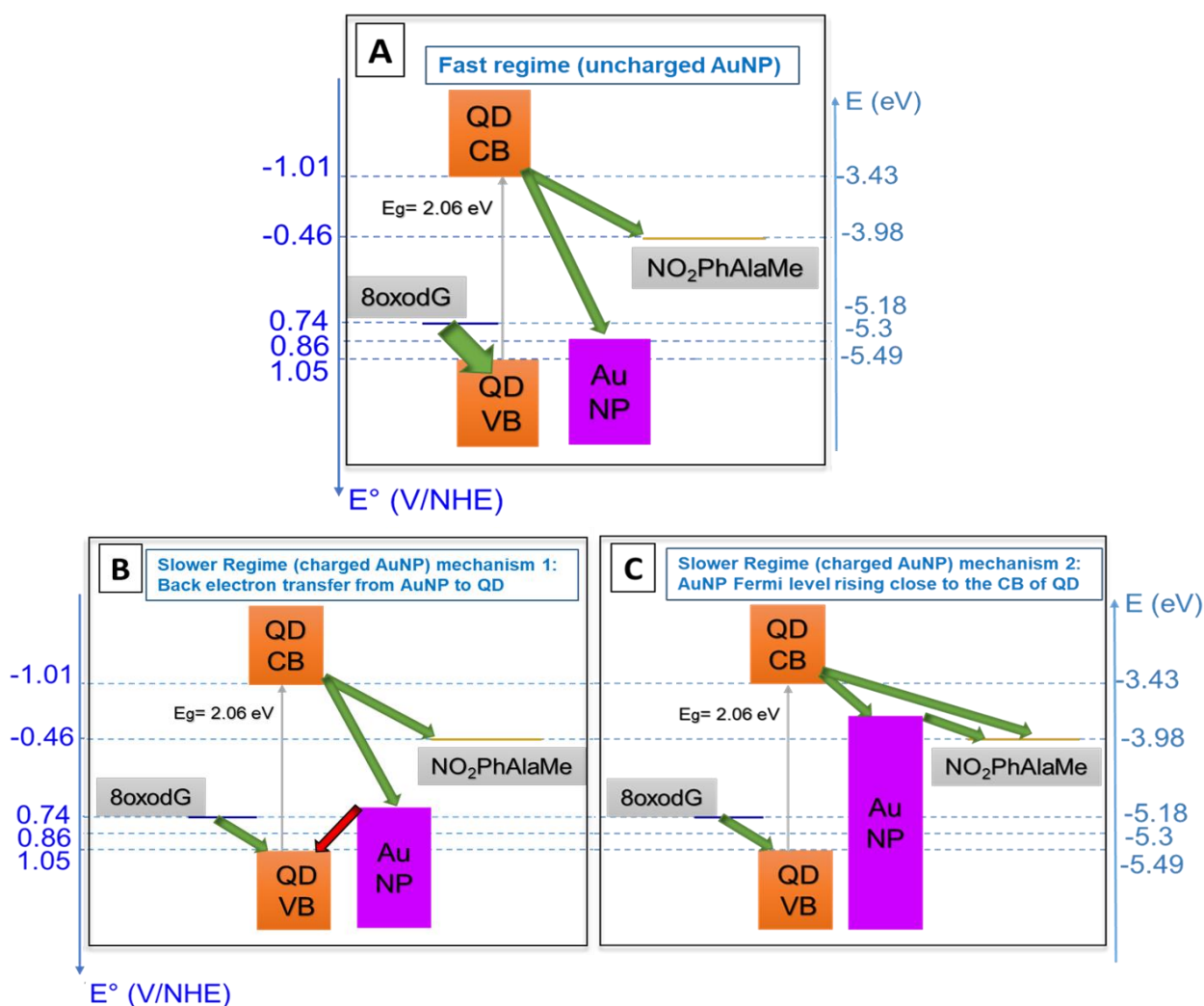
### **III-4.3. Proposed mechanism for the charge separation within the QD-AuNP composite and for the charge transfers to the electron donor and acceptor during the different kinetic regimes.**

In the photocatalysis experiments performed with QD-AuNP without adding any electron acceptor (See Figure III-8-A green curve), a significant conversion of 8-oxo-dG is observed and follows a fast kinetics during the first 20 minutes. However, our group reported previously that the CdSe/ZnS QD can not oxidize 8-oxo-dG in the absence of an appropriate electron acceptor<sup>17,18</sup>. These results, combined with the study of blue-shifted QD-AuNP absorption spectrum and the fluorescence quenching, strongly suggest a mechanism in which QD-AuNP composites photocatalyze the oxidation of 8-oxo-dG by using their AuNP components as (multi-)electron acceptors, which are able to accumulate thousands of electrons.

In the photocatalysis experiments performed with the complete photocatalytic system of QD-AuNP composites in the presence of both the electron donor and the acceptor (See Figure III-8), a fast regime is also observed in the first 20 minutes and a slower one in the next period of 3 hours. We propose here that the two successive kinetic regimes observed when using QD-AuNP composites as photocatalysts can be mainly explained by the change of charge states in their AuNP components and the corresponding rise of their Fermi level. Indeed, it was reported previously with Au-ZnO heterostructures<sup>30</sup> that the injection of the electrons can induce the rise of the AuNP Fermi level until it reaches an equilibration with the position of the conduction band of the ZnO semiconductor.

Scheme III-7-A represents the estimated energy levels for the nanoparticles under study prior any irradiation and the corresponding proposed mechanism for the fast regime. For CdSe/ZnS QD under study, our group (CAMPE-CEA) previously<sup>17</sup> estimated experimentally the redox potential of the valence band edge in the range (1.05 +/-0.1) V/NHE for slightly

smaller CdSe/ZnS QD (1<sup>st</sup> exciton at 520 nm instead of 600 nm). Since it is well-established that the valence band of such QD varies slightly with the size of the QD<sup>31</sup>, the valence band edge of the QD under study is considered to lie near the same value (1.05 +/- 0.1V/NHE). The energy level of the edge of the conduction band is then deduced to be in the range (-1.01 +/- 0.1) V/NHE by shifting from the energy corresponding to the 1<sup>st</sup> exciton absorption (600 nm corresponding to 2.06 eV). At last the Fermi level of AuNP before any irradiation is considered to be close to the energy level of bulk gold at (0.86 +/- 0.1)V/NHE.<sup>32,33</sup>



**Scheme III-7: Proposed mechanism and estimated Energy levels for QD, AuNP, electron donor and acceptor during the photocatalysis with QD-AuNP composites.** The energy levels considered for the QD and AuNP are those of separated nanoparticles measured by our group (see reference 17 for the values for QD) or from literature (for the values of the Fermi level of AuNP, see references 32 and 33). For the electron donor and acceptor, they are the experimental redox potentials either measured by our group (NO<sub>2</sub>PhAlaMe, reference 18) or from literature (8-oxo-dG<sup>34</sup> see reference 34).

Relying on these values and the experimental results, we propose the following mechanism for the fast regime (see Scheme III-7-A). When the QD-AuNP composite is irradiated at 590 nm an exciton is created in the QD part. Then, two electron transfer pathways from the CB of the QD are possible (thin green arrows in Scheme III-7-A): a first one to the Fermi level of the QD AuNP with a driving force close to 1.8 eV and a second one to the LUMO level of the NO<sub>2</sub>PhAla electron donor with a driving force of 0.55 eV. We propose that both pathways happen in the fast regime, but that the fast kinetics is mainly due to the electron transfer to AuNP attached to the QD, rather than to the electron acceptor lying in the surrounding solution. Moreover, as long as the AuNP component is not (or little) charged the driving force for the back electron transfer from AuNP Fermi Level to recombine with the hole at the valence band edge of the QD is quite small (0.2 eV). Therefore, the hole is maintained in the QD at the edge of valence band energy level. At this stage the hole probably has a much longer lifetime compared to a hole in an exciton for a bare QD. Then, the hole can oxidize the 8-oxo-dG electron donor with a good efficiency and the overall kinetics is fast (thick green arrows in Scheme III-7-A). During this fast regime, the electrons transferred from the QD conduction band to the AuNP can not be transferred further to the NO<sub>2</sub>PhAla electron acceptor, so they most probably accumulate at the surface of AuNP and raise their Fermi level. Then two hypotheses can be proposed that can explain the observed slower regime after 20 minutes of irradiation.

In the first hypothesis (see Scheme III-7-B mechanism 1), the charging of the AuNP component during the first 20 minutes has already induced a moderate (few 100 of meV) rise of the Fermi level. Then, the electrons following the pathway from the CB of QD to the Fermi level of AuNP (Red arrow in scheme III-7-B) have a sufficient driving force for back electron transfer to the VB of the QD and so can recombine with the corresponding holes. The slower observed kinetics would be then mainly due to the pathway in which electron are transferred from the CB of the QD component to the NO<sub>2</sub>PhAla electron donor in the surrounding solution.

In the second hypothesis (see Scheme III-7-C mechanism 2), the back electron transfer from the AuNP to the valence band of the QD is supposed to be not efficient, so that the charging of the AuNP component during the first 20 minutes results in an important rise of the Fermi level, which reaches a level close to that of the conduction band of the QD. Then, the AuNP components accept more electrons from the photoexcited QD components at a slower rate

compared with the fast regime, and they are able to transfer electron from their Fermi level to the NO<sub>2</sub>PhAla acceptor only at a moderate rate (thin green arrows in Scheme III-7-C). As in the previous hypothesis, the slow kinetics pathway due to the direct transfer from the CB of the QD component to the NO<sub>2</sub>PhAla electron donor would account for a part of the photocatalytic activity (thin green arrows in Scheme III-7-C).

The mechanism proposed here for the fast kinetic regime, relying on a fast electron transfer between the photoexcited QD and the AuNP in the composites followed by an accumulation of electrons in the AuNP component is supported by all our experimental results. However, it should be underlined that the two mechanistic hypotheses proposed for the slower regime can be criticized. For the first hypothesis, if the back electron transfer is so efficient that the Fermi level rises only by a few hundreds meV, staying well below the level the LUMO of the NO<sub>2</sub>PhAla electron acceptor, it is difficult to understand the results of the charging/discharging experiments, in which charged QD-AuNP composites are slowly, but efficiently discharged by this electron acceptor. For the second hypothesis the strong increase of the Fermi level (1.32 eV) necessary to make it lie above the LUMO of the NO<sub>2</sub>PhAla electron acceptor seems not compatible with the 4 nm blue shift observed in the charging/discharging experiments. Actually, Singh et al<sup>35</sup>, observed an increase of 96 meV of the energy of the Fermi level associated with a 2 nm blue shift of the plasmon band of citrate-capped AuNP (33 nm diameter). Further exploration of this slower regime in order to improve the electron transfer from AuNP to molecular electron acceptors is underway.

#### **III-4.4. Proposed mechanism for the absorption of light leading to photocatalysis with the QD-AuNP composites.**

The extinction coefficients of the nanoparticles used in this study at 590 nm wavelength are  $3.5 \cdot 10^5 \text{ M}^{-1} \cdot \text{cm}^{-1}$  for CdSe/ZnS QD and  $2.2 \times 10^8 \text{ M}^{-1} \cdot \text{cm}^{-1}$  for AuNP and the QD-AuNP composites are prepared with QD:AuNP ratio of typically 23:1. As a first approximation, if one considers that in QD-AuNP composites, QD and AuNP absorb light as if they were not interacting, 3.6 % of the incident light is absorbed by QD ( $A=0.016$ ) and 96.4 % by AuNP ( $A=0.44$ ) in photocatalysis experiments such as those reported in Figure III-9. This can favor the mechanism B starting with absorption of light by AuNP (see Scheme III-1), instead of the

mechanism A, starting with absorption of light by QD, which was intended when the QD-AuNP composites were designed.

However, three experimental evidences point towards the mechanism A as being the main pathway involved in the photocatalytic activity of QD-AuNP. First, the photocatalytic activity of QD-AuNP is much more efficient when irradiating them at 590 nm, than when irradiating at 528 nm (See Figure III-9), so a mechanism starting with the absorption of light by the QD, which have their first exciton maximum at 600 nm, is more likely. Second, the quenching of QD photoluminescence observed during the click chemistry reaction (see Figure III-10) selectively probes photoexcited QD and show that an important fraction of QD excitons are diverted from luminescence pathway to another one, most likely electron transfer to the connected AuNP. Third, the charging of AuNP when irradiated QD-AuNP composites by up to 7400 electrons per AuNP, which was characterized by the blue shift of the AuNP plasmon band (Figure III-11), demonstrates that electrons are efficiently transferred from photoexcited QD to AuNP in the QD-AuNP composites. All together, these three experiments show that the elementary steps constituting the Mechanism A are efficient when irradiating QD-AuNP composites at 590 nm.

#### **III-4.5 Possible enhancement of light absorption by QD in the QD-AuNP composites due to local electromagnetic field enhancement in the vicinity of AuNP.**

The photocatalytic activity for the conversion of 8-oxo-dG observed in the first minutes (Fast regime) for QD-AuNP composites irradiated at 590 nm is 24 times higher than for the bare QD irradiated in the same conditions (see Table III-1, entry 4 and Table III-2 entry 1). The near-field enhancement of the electromagnetic field in the vicinity of AuNP should contribute by improving the absorption of light by the QD in the composites. For evaluating this enhancement, a point-dipole approximated computation is proposed (see appendix section A-6). This point-dipole computation was benchmarked with computing the maximal enhancement factor obtained at a distance of 1nm for an isolated AuNP with 30nm radius in air  $EF_{\max} = 5.5$  ( $EF_{\max}$  being the enhancement of  $|E|^2$  at the most favorable orientation,  $|E|$  being the amplitude of the electric field of the incident light). This enhancement factor compares well with the experimental measurement of enhancement factors reported by Talley et al. for the same AuNP system ( $EF_{\max} = 7.3$ )<sup>36</sup>. For applying this point-dipole model to

the QD-AuNP reported here, the QD were considered to be at approximately 3 nm from the surface of AuNP with 12.5 nm ratio, in water medium. This leads to  $EF_{\max} = 4.1$  (at  $\lambda=590$  nm).

From this very approximate computation, it can be proposed that in the QD-AuNP composites, the proximity of AuNP enhances the light absorption by QD by a factor up to 4, consistent with the values reported by Coehn-Hoshen et al. for similar QD-AuNP systems<sup>37</sup>. Then, the further improvement of the photocatalytic activity (up to the experimental factor 24 mentioned above) can be attributed to the better charges separation due to the efficient electron transfer from QD to AuNP.

## Conclusion

We have developed a new methodology for preparing covalently linked semiconductor-metal nanocomposites based on a Click chemistry approach. Using Copper-Catalyzed Azide-Alkyne Cycloaddition reaction, we designed a modular hybrid CdSe/ZnS Quantum Dots (QD) and Gold nanoparticles (AuNP) nanocomposite. The obtained morphologies show the successful covalent assembly between the QD and the AuNP leading to the formation of heterogeneous structures of AuNP connected through single or several QD.

The photocatalytic activity of the novel nanocomposite shows improved efficiency and speed compared to the bare QD by achieving 5 times more turnover numbers in the complete reaction's time (3 hours), and the reaction could be 24 times faster in the first 10 minutes compared to the bare QD. The spectroscopic measurements on the photoexcited QD-AuNP nanocomposites suggest the accumulation of up to 7400 electrons per AuNP, which confirms the enhanced separation of the photo-induced charges generated on the excited QD, and supports our mechanistic propositions. Further investigation will be undertaken in our team to enhance the extraction of the electrons from the photocharged AuNP, and to employ the QD-AuNP composites in organic useful reactions.

## Appendix Chapter III:

## III-A1- UV-Vis spectra of the tested reactions' substrates

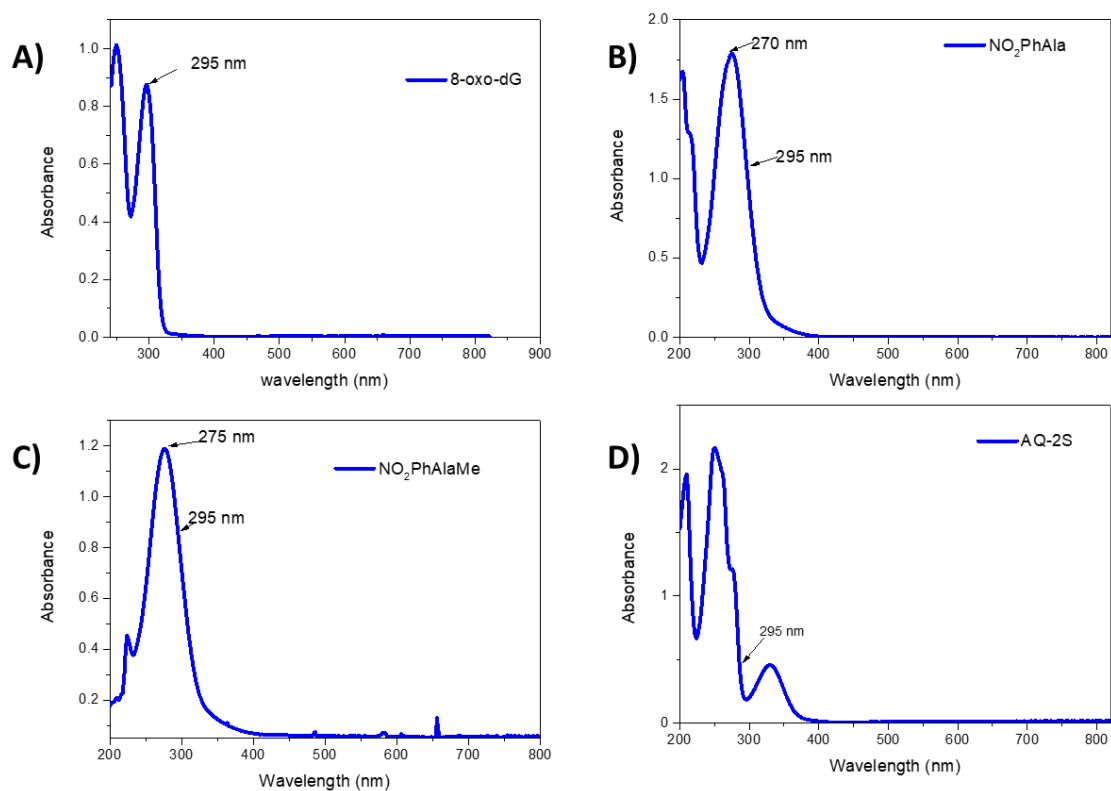


**Figure III-A1:** UV-Vis spectra of the reaction tested substrates: 100  $\mu$ M 8-oxo-dG (A), 70  $\mu$ M Nitrophenylalanine (B), 70  $\mu$ M Nitrophenylalanine-methylester (C), and 100 $\mu$ M Anthraquinone-2-sulfonate (D)

## III-A-2 HPLC chromatograms for reaction substrates

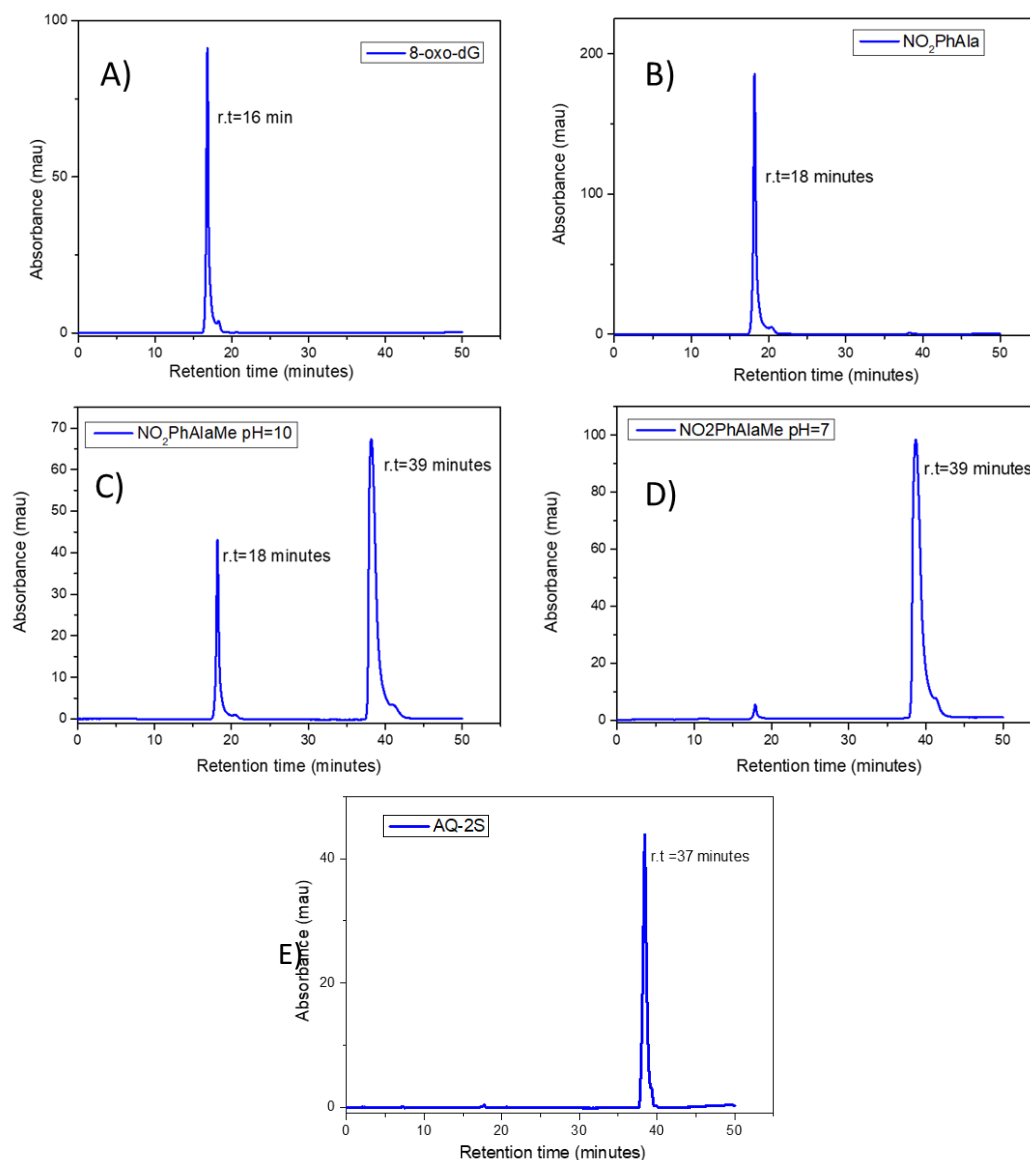


**Figure III-A2:** HPLC chromatograms for reaction substrates using HPLC detection method with wavelength detection at 295 nm: A) Chromatogram of 120 $\mu$ M 8-oxo-dG in pH =10 aqueous medium showing HPLC peak with retention time at 16 minutes, B) Chromatogram of 720 $\mu$ M NO<sub>2</sub>PhAla in pH 10 aqueous medium showing HPLC peak with retention time at 18 minutes, C) Chromatogram of 720 $\mu$ M NO<sub>2</sub>PhAlaMe in pH 10 aqueous medium showing 2 HPLC peak with retention time at 18 and 39 minutes and D) Chromatogram of 720 $\mu$ M NO<sub>2</sub>PhAla in pH 7 aqueous medium showing HPLC peak with retention time at 39 minutes. E) Chromatogram of 720 $\mu$ M Anthraquinone-2-sulfonate in aqueous medium showing HPLC peak with retention time at 37 minutes.

### III-A-3 Photoluminescence Quenching of the CdSe/ZnS QD in the presence of either 8-oxo-dG or NO<sub>2</sub>PhAla

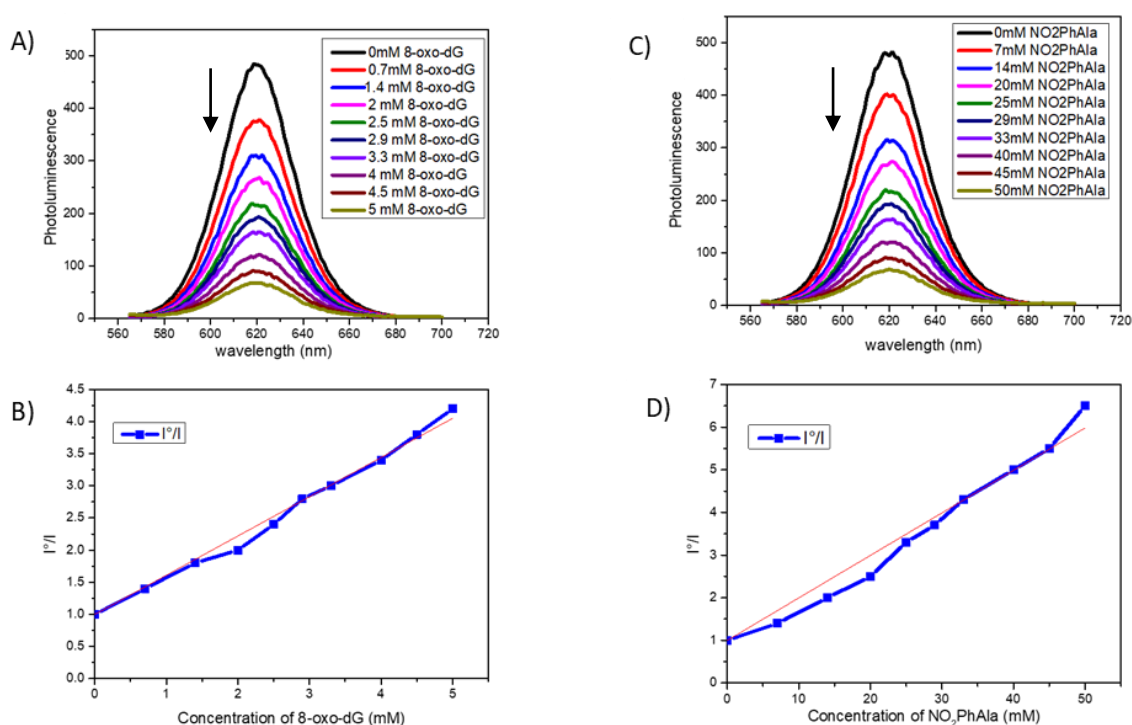


**Figure III-A3:** Quenching of the CdSe/ZnS (600nm) QD photoluminescence by the electron donor (8-oxo-dG) and the electron acceptor (NO<sub>2</sub>PhAla). The fluorescence experiments were carried for 1 $\mu$ M of CdSe/ZnS QD in the presence of 8-oxo-dG reaching 5mM (A) and reaching 50mM of NO<sub>2</sub>PhAla (C). Stern–Volmer plots  $I^0/I = f([\text{quencher}])$  are plotted for the quenching with 8-oxo-dG (B) and NO<sub>2</sub>PhAla (D).

The fluorescence quenching of water soluble CdSe/ZnS core-shell QD was observed by adding 5mM of 8-oxo-dG to check the possible hole transfer from the QD to the electron donor 8-oxo-dG (frame-A). The plotted Stern-Volmer plot (frame B) is linear and its slope  $K_{S.V.} = 575 \text{ L}\cdot\text{mol}^{-1}$  and the bimolecular quenching constant can be estimated to be  $k_q = 2.8 \times 10^{10} \text{ L}\cdot\text{mol}^{-1}\cdot\text{s}^{-1}$  by considering a fluorescence lifetime of 20 ns<sup>38</sup> for CdSe/ZnS QD. The linear shape of the Stern–Volmer plot and as the  $k_q$  is close  $10^{10} \text{ L}\cdot\text{mol}^{-1}\cdot\text{s}^{-1}$  indicates that the fluorescence quenching of the CdSe/ZnS QD due the presence of 8-oxo-dG is a dynamic quenching behavior.

In addition, a quenching of the QD photoluminescence was observed by adding 50mM of NO<sub>2</sub>PhAla to check the possible electron transfer from the QDs to the electron acceptor (Frame C). The plotted Stern-Volmer plot (frame D) is linear and its slope  $K_{S.V.} = 109 \text{ L}\cdot\text{mol}^{-1}$

and the bimolecular quenching constant can be estimated to be  $k_q = 5.5 \times 10^9 \text{ L}\cdot\text{mol}^{-1}\cdot\text{s}^{-1}$  by considering a fluorescence lifetime of 20 ns for CdSe/ZnS QD. The linear shape of the Stern–Volmer plot and the  $k_q$  is lower than  $10^{10} \text{ L}\cdot\text{mol}^{-1}\cdot\text{s}^{-1}$  indicates that the fluorescence quenching of the CdSe/ZnS QDs due the presence of NO<sub>2</sub>PhAla is a dynamic quenching behavior.

#### III-A-4 Monitoring the decay of the reactions' substrate during the photocatalysis experiments

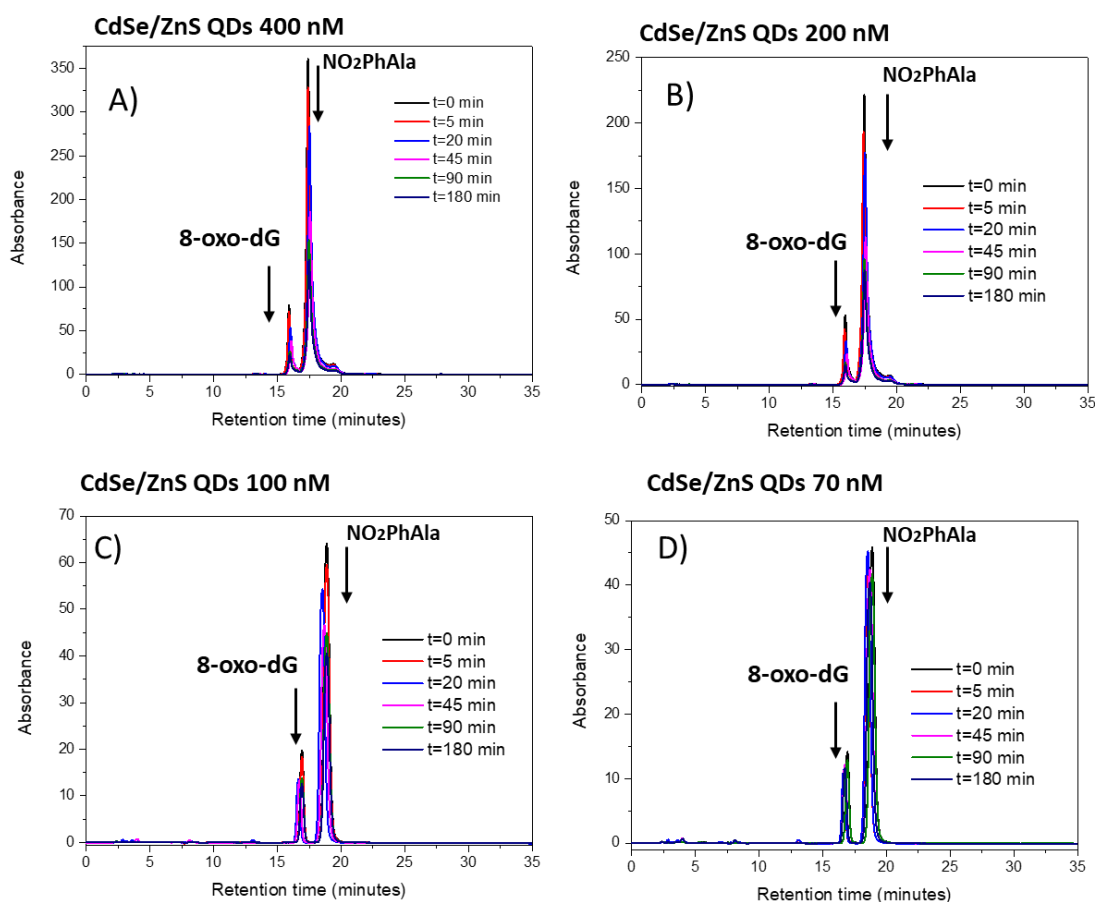


**Figure III-A-4.1:** Monitoring the decay of the reactions' substrate of 8-oxo-dG and NO<sub>2</sub>PhAla under the action of CdSe/ZnS QD irradiated by 590 nm LED light source using HPLC detection with fixed wavelength at 295 nm: A) The decay of the 8-oxo-dG and NO<sub>2</sub>PhAla during the reaction with 400 nM CdSe/ZnS QDs in the presence of 500 equiv of 8-oxo-dG and 1500 equiv of NO<sub>2</sub>PhAla. B) The decay of the 8-oxo-dG and NO<sub>2</sub>PhAla during the reaction with 200 nM CdSe/ZnS QD in the presence of 500 equiv of 8-oxo-dG and 1500 equiv of NO<sub>2</sub>PhAla. C) The

decay of the 8-oxo-dG and NO<sub>2</sub>PhAla during the reaction with 100 nM CdSe/ZnS QDs in the presence of 500 equiv of 8-oxo-dG and 1500 equiv of NO<sub>2</sub>PhAla. D) The decay of the 8-oxo-dG and NO<sub>2</sub>PhAla during the reaction with 70 nM CdSe/ZnS QD in the presence of 500 equiv of 8-oxo-dG and 1500 equiv of NO<sub>2</sub>PhAla.

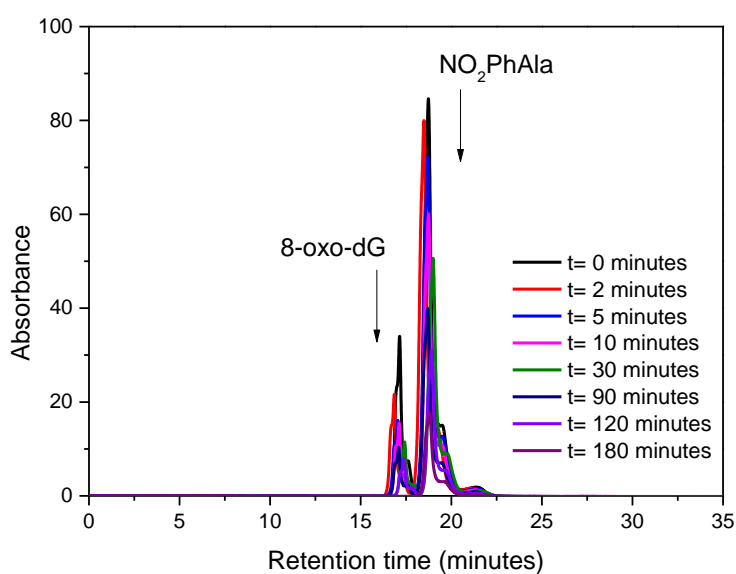


**Figure III-A-4.2:** Monitoring the decay of the reactions' substrate of 8-oxo-dG and NO<sub>2</sub>PhAla in pH=10 medium irradiated using 590 nm LED light source using HPLC detection with fixed wavelength at 295 nm: The decay of the 8-oxo-dG and NO<sub>2</sub>PhAla in the photoredox reaction mediated by the **QD-AuNP composite** as photocatalyst.

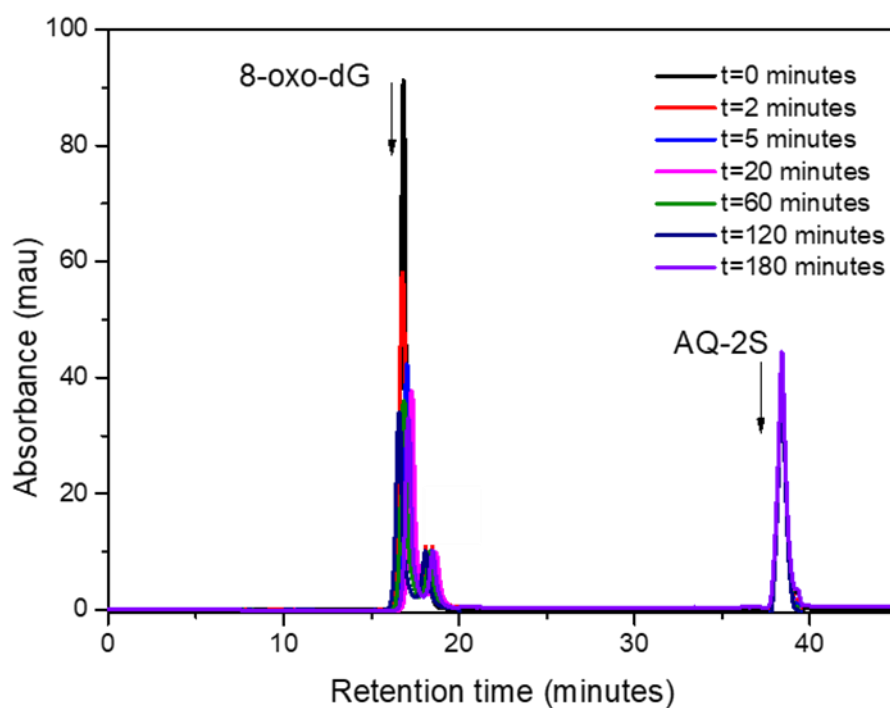


**Figure III-A-4.3:** Monitoring the decay of the reactions' substrate of 8-oxo-dG and Anthraquinone-2-sulfonate irradiated using 590 nm LED light source using HPLC detection with fixed wavelength at 295 nm: The decay of the 8-oxo-dG in the reaction photocatalyzed with **QD-AuNP composite**, and in presence of Anthraquinone-2-sulfonate as electron acceptor which appears it corresponding HPLC peak observed to be not decreasing during the reaction.

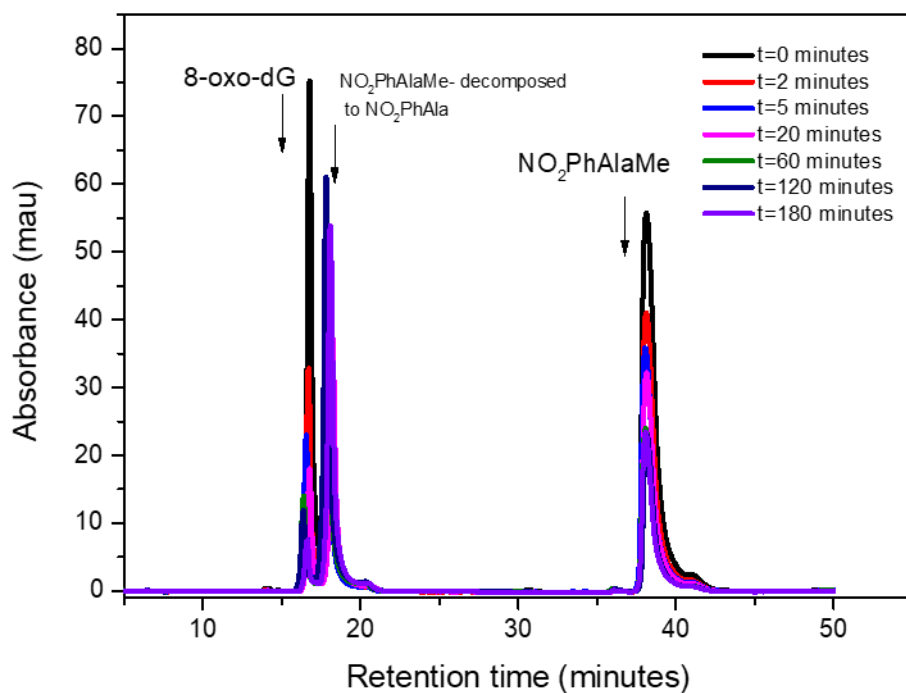


**Figure III-A-4.3:** Monitoring the decay of the reactions' substrate of 8-oxo-dG and NO<sub>2</sub>PhAlaMe in pH 10 medium irradiated using 590 nm LED light source using HPLC detection with fixed wavelength at 295 nm: The decay of the 8-oxo-dG in the reaction photocatalyzed with **QD-AuNP composite**, and NO<sub>2</sub>PhAlaMe as electron acceptor which tends to hydrolyze at pH=10 and forms a new HPLC peak at the retention time of NO<sub>2</sub>PhAla.

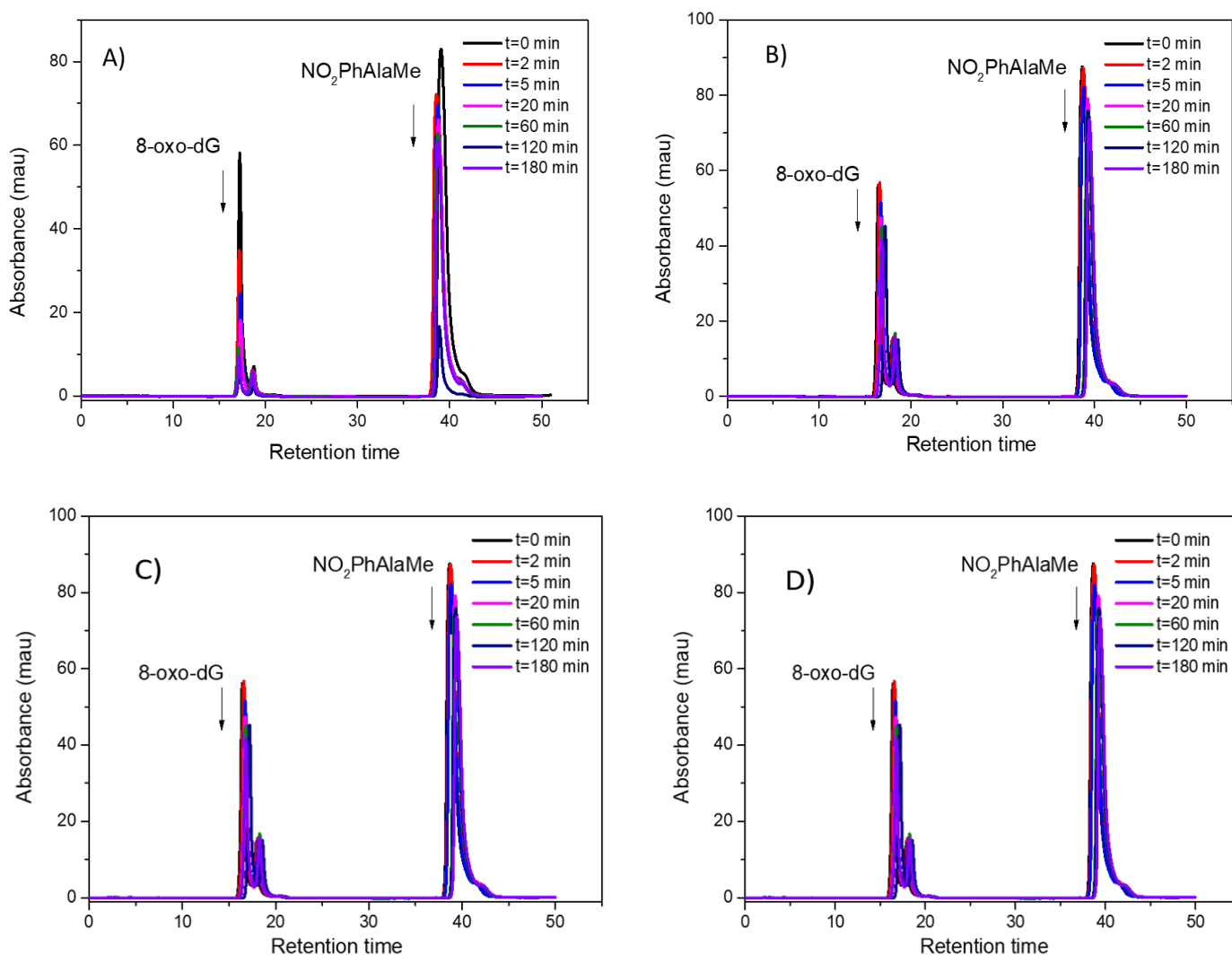


**Figure III-A-4.4:** Monitoring the decay of the reactions' substrate of 8-oxo-dG and NO<sub>2</sub>PhAlaMe in pH 7.4 controlled medium irradiated using 590 nm LED light source using HPLC detection with fixed wavelength at 295 nm: A) the decay of the 8-oxo-dG and NO<sub>2</sub>PhAlaMe in the photoredox reaction mediated by the **QD-AuNP composite** as photocatalyst, B) the decay of the 8-oxo-dG and NO<sub>2</sub>PhAlaMe in the under the action of the **reference** sample of non-connected QD and AuNP, C) the decay of the 8-oxo-dG and NO<sub>2</sub>PhAlaMe in the reaction using **CdSe/ZnS QD alone** as photocatalyst, and D) the decay of the 8-oxo-dG and NO<sub>2</sub>PhAlaMe in the reaction of the **AuNP alone** as photocatalyst.

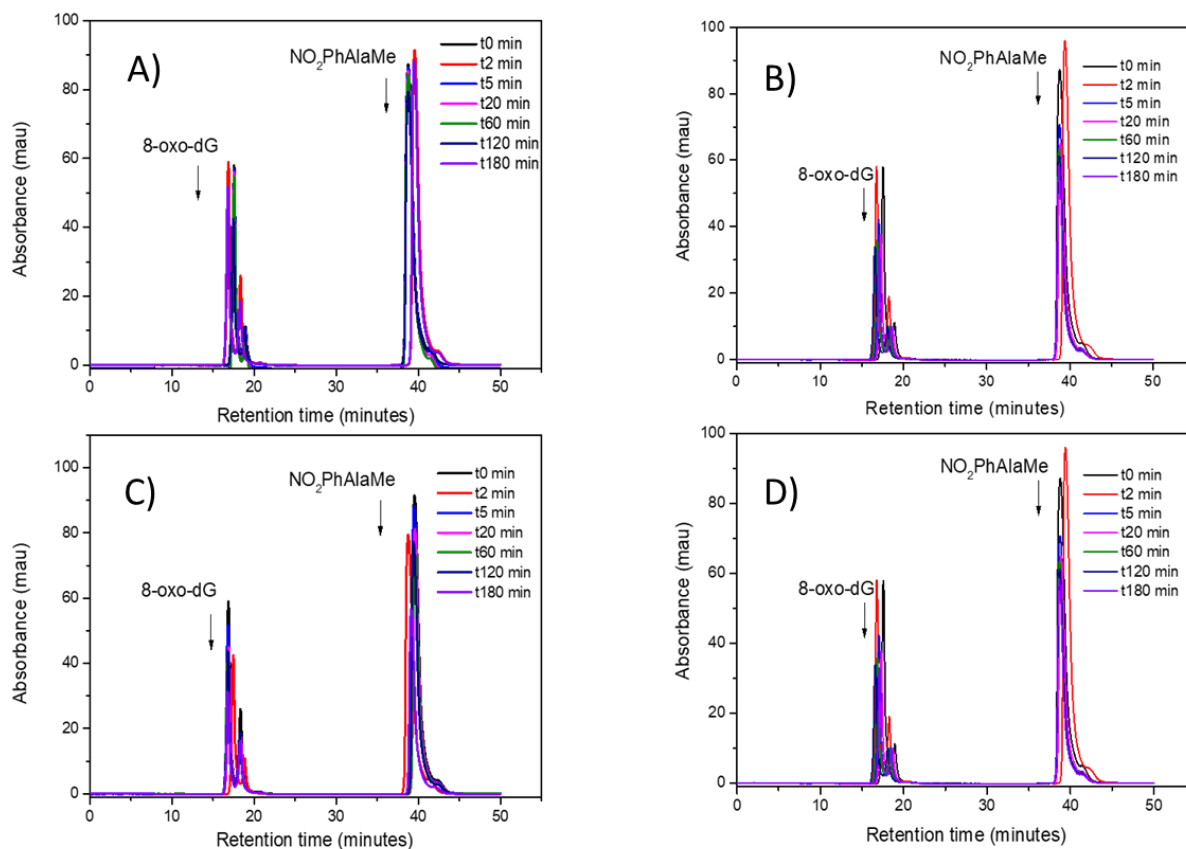


**Figure III-A-4.5:** Monitoring the decay photo-redox reaction substrate in pH 7.4 controlled medium irradiated using 528 nm LED light source using HPLC detection with fixed wavelength at 295 nm: A) the decay of the 8-oxo-dG and NO<sub>2</sub>PhAlaMe in the photoredox reaction mediated by the **QD-AuNP composite** as photocatalyst, B) the decay of the 8-oxo-dG and NO<sub>2</sub>PhAlaMe in the photoredox reaction mediated by the **reference** of non-connected QDs and Au NPs as photocatalyst, C) the decay of the 8-oxo-dG and NO<sub>2</sub>PhAlaMe in the photoredox reaction mediated by the CdSe/ZnS **QD alone** as photocatalyst, and D) the decay of the 8-oxo-dG and NO<sub>2</sub>PhAlaMe in the photoredox reaction mediated by the **AuNP alone** as photocatalyst.

### III-A-5: Estimation of the surface charge of the AuNP obtained from their plasmon band shift.

The shift of the AuNP plasmon band upon the charging/discharging of the particles takes its origin in the fact that the resonance frequency of the plasmon depends on the volume density of the electrons at the Fermi level. As it was stated in section III-4.2 of chapter III, the plasmon band of the AuNP was measured by UV-Vis optical spectrometry which gives access to the extinction coefficient  $\varepsilon$  of the particles in solution. This coefficient results from the scattering and absorption properties of the particles and is fully described by the Mie theory for spherical NP<sup>39</sup>. When the NP are much smaller in diameter than the optical wavelength, the electrostatic approximation can be applied to the Mie theory and the extinction factor of a unique NP takes a simple and analytical expression<sup>21</sup> given by:

$$\varepsilon = \frac{24\pi^2 r^3 \varepsilon_m^{3/2}}{\lambda} \frac{\varepsilon''(\omega)}{(\varepsilon'(\omega) + 2\varepsilon_m)^2 + \varepsilon''^2(\omega)}$$

where  $\varepsilon_m$  and  $\varepsilon(\omega) = \varepsilon'(\omega) + i\varepsilon''(\omega)$  are the dielectric constant of the solvent and of the Au-NPs respectively, with  $\omega = \frac{2\pi c}{\lambda}$  the angular frequency,  $c$  the speed of light in vacuum,  $\lambda$  the optical wavelength and  $r$  is the radius of the NPs.

In the visible range, the dielectric constant of the AuNP is well described by the Drude model<sup>40</sup> and expresses as:  $\varepsilon(\omega) = \varepsilon_\infty - \frac{\omega_p^2}{\omega^2 - i\omega\gamma}$  where  $\varepsilon_\infty$  is the high frequency dielectric constant,  $\gamma$  is a damping factor and  $\omega_p = \sqrt{\frac{Ne^2}{m\varepsilon_0}}$  is the bulk plasma frequency, with  $N$  the volume density of the conduction electrons,  $m$  the mass of the electrons, and  $\varepsilon_0$  the vacuum permittivity.

The extinction coefficient is maximum at the resonance condition  $\varepsilon'(\omega_{res}) = -2\varepsilon_m$  which corresponds to the plasmon resonance of the spherical AuNP. Considering that the damping is small compared to  $\omega$ , this resonance condition writes as  $\varepsilon_\infty - \frac{\omega_p^2}{\omega_{res}^2} = -2\varepsilon_m$  and, after simple calculations, one can obtain the resonance wavelength dependency on the conduction electron density:

$$\lambda_{res} = \frac{2\pi c}{\omega_{res}} = 2\pi c \sqrt{\frac{m\varepsilon_0(\varepsilon_\infty + 2\varepsilon_m)}{Ne^2}} \quad \text{Eq.1}$$

As observed in the extinction spectra, this formula shows that as the AuNP are charged/discharged,  $N$  increases/decreases and the resonance wavelength decreases/increases.

If we note  $\Delta N$  the variation of the conduction electron density upon a charging or a discharging process, and  $N_i$  the initial electron density, we obtain from Eq. 1 that

$$\lambda_{res} \sim \lambda_i \left( 1 - \frac{\Delta N}{2N_i} \right)$$

Where,  $\lambda_i$  is the initial resonance wavelength when the AuNP are not charged ( $\Delta N=0$ ).

#### III-A-6: Near-field enhancement of the electromagnetic field based on the point-dipole approximation

When a metal nanoparticle (NP) is irradiated with an electromagnetic (EM) wave of a wavelength ( $\lambda$ ), the spatial variation of the electromagnetic field at the scale of the nanoparticle is very small and we can consider that the nanoparticle is subjected to a uniform field. Thus, all the electrons generated in the nanoparticle will have the same behavior. Then, the nanoparticle will polarize under the action of the electric field and will behave like a dipole oscillating in time with dipole moment:

$$\vec{p} = \alpha \epsilon_0 \epsilon_m \vec{E}_0$$

where  $\alpha$  is the polarizability of the nanoparticle,  $\epsilon_0$  is the permittivity,  $\epsilon_m$  is the dielectric constant of the medium surrounding the nanoparticle, and  $\vec{E}_0$  the incident field.

The electromagnetic field created by an oscillating dipole could be described as in Figure III-A-6

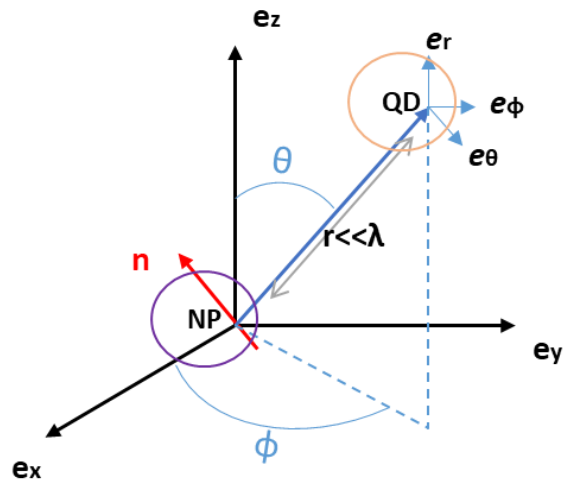


Figure III-A-6: Nanoparticle as an oscillating dipole

In the optical near field approximation conditions the distance between the two nanoparticles ( $r$ ) is considered much smaller than the wavelength ( $\lambda$ ),  $r \ll \lambda$ , and the amplitude of the electric field associated with the oscillating dipole is dominated by the term in  $1/r^3$ , hence we can write:

$$\vec{E}_{NF} \sim \frac{e^{i(\vec{k}\vec{r}-\omega t)}}{4\pi\epsilon_0\epsilon_m} (3\vec{e}_r(\vec{n}\cdot\vec{e}_r) - \vec{n}) \frac{P}{r^3} = \frac{e^{i(\vec{k}\vec{r}-\omega t)}}{4\pi\epsilon_0\epsilon_m} (2n_r\vec{e}_r - n_\theta\vec{e}_\theta - n_\phi\vec{e}_\phi) \frac{P}{r^3}$$

and

$$|\vec{E}_{NF}|^2 \sim \frac{1}{(4\pi\epsilon_0\epsilon_m)^2} (4n_r^2 + n_\theta^2 + n_\phi^2) \left| \frac{P}{r^3} \right|^2$$

Then in the case of a nanoparticle the dipole moment is  $\vec{p} = \alpha \epsilon_0 \epsilon_m \vec{E}_0$ , then the electric near field is considered as:

$$|\vec{E}_{NF}|^2 \sim \left| \frac{\alpha}{4\pi r^3} \right|^2 (4n_r^2 + n_\theta^2 + n_\phi^2) |\vec{E}_0|^2$$

And the amplification of the electric near field is then:

$$EF = \frac{|\vec{E}_{NF}|^2}{|\vec{E}_0|^2} = \left| \frac{\alpha}{4\pi r^3} \right|^2 (4n_r^2 + n_\theta^2 + n_\phi^2)$$

Moreover, from Mie theory the polarizability of a nanoparticle having a dielectric constant  $\epsilon(\omega)$  is given as:

$$\alpha = 4\pi a^3 \frac{\epsilon(\omega) - \epsilon_m}{\epsilon(\omega) + 2\epsilon_m}$$

Where  $a$  is the radius of the nanoparticle, then we can obtain that:

$$EF = \frac{a^6}{r^6} \left| \frac{\epsilon(\omega) - \epsilon_m}{\epsilon(\omega) + 2\epsilon_m} \right|^2 (4n_r^2 + n_\theta^2 + n_\phi^2)$$

Considering that:

$$\vec{n} = \cos\theta \vec{e}_r - \sin\theta \vec{e}_\theta$$

We can obtain finally:

$$EF = \frac{a^6}{r^6} \left| \frac{\epsilon(\omega) - \epsilon_m}{\epsilon(\omega) + 2\epsilon_m} \right|^2 (3\cos\theta + 1)$$

Knowing that, the amplification of the field is maximal at the extremities of the dipole ( $\theta=0$ ) and minimal at  $90^\circ$ .

Interestingly, Talley et al.<sup>36</sup> experimentally measured the near field enhancement of 60 nm AuNP irradiated at  $\lambda = 633$  nm and obtained  $\sqrt{EFmax}=2.7$  as the electric field at 1 nm from the AuNP surface. Therefore in order to confirm the validity of the equation proposed above we used the data from the report of Talley et al. and we calculated  $\sqrt{EFmax} = 2.35$  using the proposed equation which compares well with the experimental value reported.<sup>36</sup>

Then, we applied this equation on the case of our QD-AuNP. In our case, the size of the AuNP are of 25 nm in diameter ( $a = 12.5$  nm), the  $\epsilon_m$  of water is 1.77 and we propose that the QD and the AuNP are separated by 3 nm (then  $r=3$ ), and at the excitation wavelength of  $\lambda=590$  nm the permittivity<sup>41</sup>  $\epsilon = -8.77 + i1.576$ .

Using the point dipole approximation proposed by the dipole oscillation formula:

$$EFmax = 4 \left( \frac{12.5^6}{15.5^6} \right) \left( \frac{(-8.77 - 1.77)^2 + 1.576^2}{(-8.77 + 2 \cdot 1.77)^2 + 1.576^2} \right) = 4.1$$

Then from the above calculation, we obtained a maximal enhancement factor of 4.1 for the light intensity at the QDs position due to the presence of AuNP connected to them.

## References

- (1) Dana, J.; Debnath, T.; Maity, P.; Ghosh, H. N. Enhanced Charge Separation in an Epitaxial Metal–Semiconductor Nanohybrid Material Anchored with an Organic Molecule. *J. Phys. Chem. C* **2015**, *119* (38), 22181–22189. <https://doi.org/10.1021/acs.jpcc.5b06055>.
- (2) Maity, P.; N. Ghosh, H. Strategies for Extending Charge Separation in Colloidal Nanostructured Quantum Dot Materials. *Physical Chemistry Chemical Physics* **2019**, *21* (42), 23283–23300. <https://doi.org/10.1039/C9CP03551F>.
- (3) Mondal, N.; Samanta, A. Ultrafast Charge Transfer and Trapping Dynamics in a Colloidal Mixture of Similarly Charged CdTe Quantum Dots and Silver Nanoparticles. *J. Phys. Chem. C* **2016**, *120* (1), 650–658. <https://doi.org/10.1021/acs.jpcc.5b08630>.
- (4) Yuan, L.; Geng, Z.; Xu, J.; Guo, F.; Han, C. Metal-Semiconductor Heterostructures for Photoredox Catalysis: Where Are We Now and Where Do We Go? *Advanced Functional Materials* **2021**, *31* (27), 2101103. <https://doi.org/10.1002/adfm.202101103>.
- (5) Cai, C.-J.; Wang, Y.-T.; Ni, C.-C.; Wu, R.-N.; Chen, C.-Y.; Kiang, Y.-W.; Yang, C. C. Emission Behaviors of Colloidal Quantum Dots Linked onto Synthesized Metal Nanoparticles. *Nanotechnology* **2019**, *31* (9), 095201. <https://doi.org/10.1088/1361-6528/ab5826>.
- (6) Sun, D.; Tian, Y.; Zhang, Y.; Xu, Z.; Sfeir, M. Y.; Cotlet, M.; Gang, O. Light-Harvesting Nanoparticle Core–Shell Clusters with Controllable Optical Output. *ACS Nano* **2015**, *9* (6), 5657–5665. <https://doi.org/10.1021/nn507331z>.
- (7) Achermann, M. Exciton–Plasmon Interactions in Metal–Semiconductor Nanostructures. *J. Phys. Chem. Lett.* **2010**, *1* (19), 2837–2843. <https://doi.org/10.1021/jz101102e>.
- (8) Soni, U.; Tripathy, P.; Sapra, S. Photocatalysis from Fluorescence-Quenched CdSe/Au Nanoheterostructures: A Size-Dependent Study. *J. Phys. Chem. Lett.* **2014**, *5* (11), 1909–1916. <https://doi.org/10.1021/jz5006863>.
- (9) Chauhan, H.; Kumar, Y.; Dana, J.; Satpati, B.; Ghosh, H. N.; Deka, S. Photoinduced Ultrafast Charge Separation in Colloidal 2-Dimensional CdSe/CdS–Au Hybrid Nanoplatelets and Corresponding Application in Photocatalysis. *Nanoscale* **2016**, *8* (34), 15802–15812. <https://doi.org/10.1039/C6NR03610D>.
- (10) Camargo, F. V. A.; Ben-Shahar, Y.; Nagahara, T.; Panfil, Y. E.; Russo, M.; Banin, U.; Cerullo, G. Visualizing Ultrafast Electron Transfer Processes in Semiconductor–Metal Hybrid Nanoparticles: Toward Excitonic–Plasmonic Light Harvesting. *Nano Lett.* **2021**, *21* (3), 1461–1468. <https://doi.org/10.1021/acs.nanolett.0c04614>.
- (11) Wu, K.; Rodríguez-Córdoba, W. E.; Yang, Y.; Lian, T. Plasmon-Induced Hot Electron Transfer from the Au Tip to CdS Rod in CdS–Au Nanoheterostructures. *Nano Lett.* **2013**, *13* (11), 5255–5263. <https://doi.org/10.1021/nl402730m>.
- (12) Dong, H.; Feng, J.; Liu, J.; Wan, X.; Zhang, J.; Wang, Z.; Chen, H.; Weng, Y.-X. Shell Thickness Dependence of the Plasmon-Induced Hot-Electron Injection Process in Au@CdS Core–Shell Nanocrystals. *J. Phys. Chem. C* **2021**, *125* (36), 19906–19913. <https://doi.org/10.1021/acs.jpcc.1c05900>.
- (13) Chiu, Y.-H.; Chang, K.-D.; Hsu, Y.-J. Plasmon-Mediated Charge Dynamics and Photoactivity Enhancement for Au-Decorated ZnO Nanocrystals. *J. Mater. Chem. A* **2018**, *6* (10), 4286–4296. <https://doi.org/10.1039/C7TA08543E>.
- (14) Fernandez, M.; Urvoas, A.; Even-Hernandez, P.; Burel, A.; Mériadec, C.; Artzner, F.; Bouceba, T.; Minard, P.; Dujardin, E.; Marchi, V. Hybrid Gold Nanoparticle–Quantum Dot

- Self-Assembled Nanostructures Driven by Complementary Artificial Proteins. *Nanoscale* **2020**, *12* (7), 4612–4621. <https://doi.org/10.1039/C9NR09987E>.
- (15) Strelow, C.; Theuerholz, T. S.; Schmidtke, C.; Richter, M.; Merkl, J.-P.; Kloust, H.; Ye, Z.; Weller, H.; Heinz, T. F.; Knorr, A.; Lange, H. Metal–Semiconductor Nanoparticle Hybrids Formed by Self-Organization: A Platform to Address Exciton–Plasmon Coupling. *Nano Lett.* **2016**, *16* (8), 4811–4818. <https://doi.org/10.1021/acs.nanolett.6b00982>.
- (16) Kolb, H. C.; Finn, M. G.; Sharpless, K. B. Click Chemistry: Diverse Chemical Function from a Few Good Reactions. *Angewandte Chemie International Edition* **2001**, *40* (11), 2004–2021. [https://doi.org/10.1002/1521-3773\(20010601\)40:11<2004::AID-ANIE2004>3.0.CO;2-5](https://doi.org/10.1002/1521-3773(20010601)40:11<2004::AID-ANIE2004>3.0.CO;2-5).
- (17) Chauvire, T. Développement de systèmes photochimiques à base de Quantum Dots hydrosolubles de type coeur CdSe et coeur-coquille CdSe/ZnS. 261.
- (18) Chauviré, T.; Mouesca, J.-M.; Gasparutto, D.; Ravanat, J.-L.; Lebrun, C.; Gromova, M.; Jouneau, P.-H.; Chauvin, J.; Gambarelli, S.; Maurel, V. Redox Photocatalysis with Water-Soluble Core–Shell CdSe–ZnS Quantum Dots. *J. Phys. Chem. C* **2015**, *119* (31), 17857–17866. <https://doi.org/10.1021/acs.jpcc.5b04396>.
- (19) Turkevich, J.; Stevenson, P. C.; Hillier, J. A Study of the Nucleation and Growth Processes in the Synthesis of Colloidal Gold. *Discuss. Faraday Soc.* **1951**, *11* (0), 55–75. <https://doi.org/10.1039/DF9511100055>.
- (20) Frens, G. Controlled Nucleation for the Regulation of the Particle Size in Monodisperse Gold Suspensions. *Nature Physical Science* **1973**, *241* (105), 20–22. <https://doi.org/10.1038/physci241020a0>.
- (21) *Absorption and Scattering of Light by Small Particles | Wiley Online Books*. <https://onlinelibrary.wiley.com/doi/book/10.1002/9783527618156> (accessed 2022-06-28).
- (22) Blatchford, C. G.; Campbell, J. R.; Creighton, J. A. Plasma Resonance — Enhanced Raman Scattering by Absorbates on Gold Colloids: The Effects of Aggregation. *Surface Science* **1982**, *120* (2), 435–455. [https://doi.org/10.1016/0039-6028\(82\)90161-3](https://doi.org/10.1016/0039-6028(82)90161-3).
- (23) Zylstra, J.; Amey, J.; Miska, N. J.; Pang, L.; Hine, C. R.; Langer, J.; Doyle, R. P.; Maye, M. M. A Modular Phase Transfer and Ligand Exchange Protocol for Quantum Dots. *Langmuir* **2011**, *27* (8), 4371–4379. <https://doi.org/10.1021/la104542n>.
- (24) Adamczyk, Z.; Sadlej, K.; Wajnryb, E.; Ekiel-Jeżewska, M. L.; Warszyński, P. Hydrodynamic Radii and Diffusion Coefficients of Particle Aggregates Derived from the Bead Model. *Journal of Colloid and Interface Science* **2010**, *347* (2), 192–201. <https://doi.org/10.1016/j.jcis.2010.03.066>.
- (25) Roy, S.; Roy, S.; Rao, A.; Devatha, G.; Pillai, P. P. Precise Nanoparticle–Reactant Interaction Outplays Ligand Poisoning in Visible-Light Photocatalysis. *Chem. Mater.* **2018**, *30* (23), 8415–8419. <https://doi.org/10.1021/acs.chemmater.8b03108>.
- (26) Roy, S.; Jain, V.; Kashyap, R. K.; Rao, A.; Pillai, P. P. Electrostatically Driven Multielectron Transfer for the Photocatalytic Regeneration of Nicotinamide Cofactor. *ACS Catal.* **2020**, *10* (10), 5522–5528. <https://doi.org/10.1021/acscatal.0c01478>.
- (27) Rostalski, J.; Quinten, M. Effect of a Surface Charge on the Halfwidth and Peak Position of Cluster Plasmons in Colloidal Metal Particles. *Colloid Polym Sci* **1996**, *274* (7), 648–653. <https://doi.org/10.1007/BF00653063>.
- (28) Henglein, A.; Mulvaney, P.; Linnert, T. Chemistry of Agn Aggregates in Aqueous Solution: Non-Metallic Oligomeric Clusters and Metallic Particles. *Faraday Discuss.* **1991**, *92* (0), 31–44. <https://doi.org/10.1039/FD9919200031>.

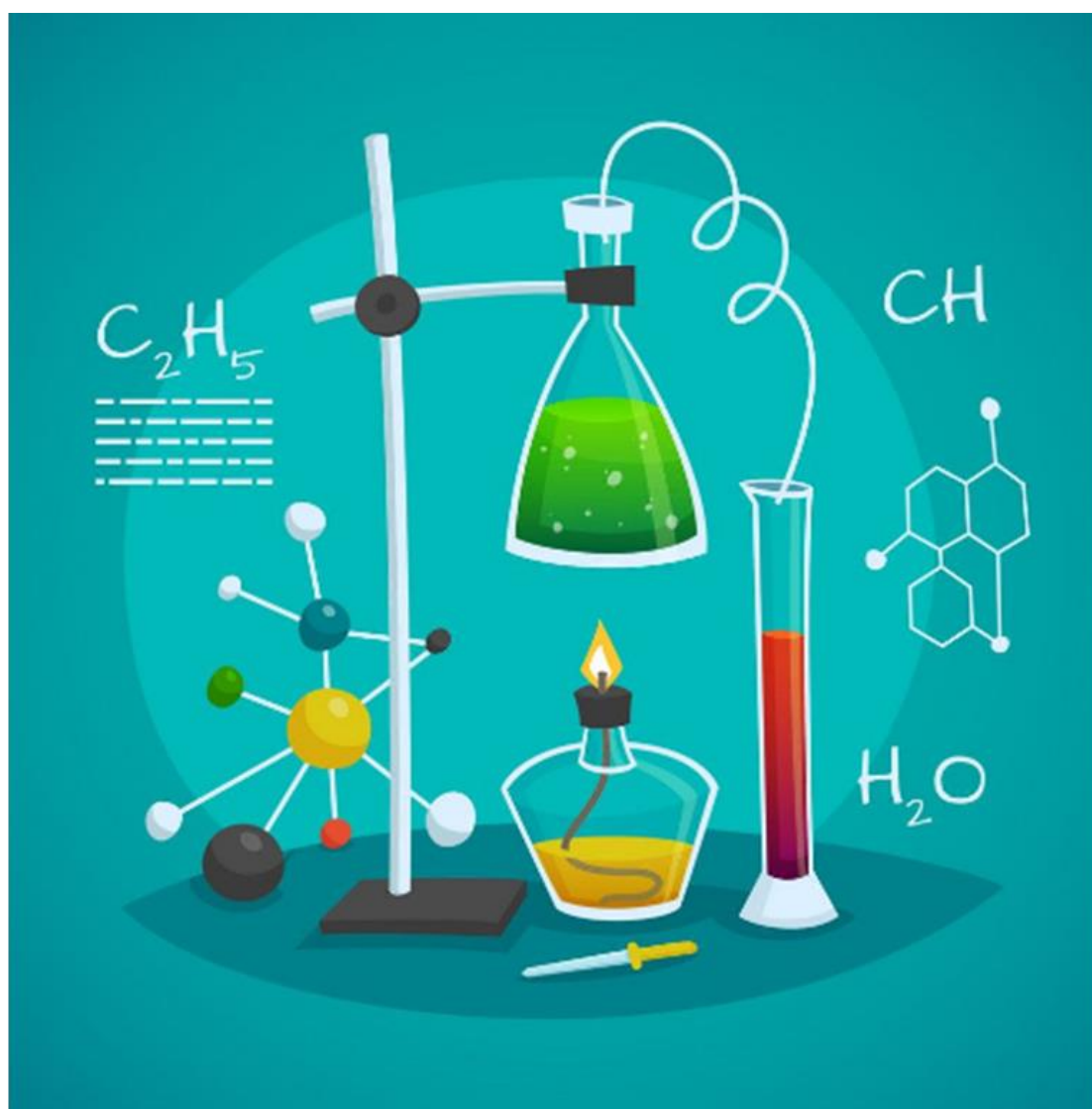
- (29) Ung, T.; Giersig, M.; Dunstan, D.; Mulvaney, P. Spectroelectrochemistry of Colloidal Silver. *Langmuir* **1997**, *13* (6), 1773–1782. <https://doi.org/10.1021/la960863z>.
- (30) Wood, A.; Giersig, M.; Mulvaney, P. Fermi Level Equilibration in Quantum Dot–Metal Nanojunctions. *J. Phys. Chem. B* **2001**, *105* (37), 8810–8815. <https://doi.org/10.1021/jp011576t>.
- (31) Jasieniak, J.; Califano, M.; Watkins, S. E. Size-Dependent Valence and Conduction Band-Edge Energies of Semiconductor Nanocrystals. *ACS Nano* **2011**, *5* (7), 5888–5902. <https://doi.org/10.1021/nn201681s>.
- (32) Scanlon, M. D.; Peljo, P.; Méndez, M. A.; Smirnov, E.; Girault, H. H. Charging and Discharging at the Nanoscale: Fermi Level Equilibration of Metallic Nanoparticles. *Chem. Sci.* **2015**, *6* (5), 2705–2720. <https://doi.org/10.1039/C5SC00461F>.
- (33) Kim, Y.; Smith, J. G.; Jain, P. K. Harvesting Multiple Electron–Hole Pairs Generated through Plasmonic Excitation of Au Nanoparticles. *Nature Chem* **2018**, *10* (7), 763–769. <https://doi.org/10.1038/s41557-018-0054-3>.
- (34) Steenken, S.; Jovanovic, S. V.; Bietti, M.; Bernhard, K. The Trap Depth (in DNA) of 8-Oxo-7,8-Dihydro-2′-deoxyguanosine as Derived from Electron-Transfer Equilibria in Aqueous Solution. *J. Am. Chem. Soc.* **2000**, *122* (10), 2373–2374. <https://doi.org/10.1021/ja993508e>.
- (35) Singh, A. N.; Devnani, H.; Jha, S.; Ingole, P. P. Fermi Level Equilibration of Ag and Au Plasmonic Metal Nanoparticles Supported on Graphene Oxide. *Phys. Chem. Chem. Phys.* **2018**, *20* (41), 26719–26733. <https://doi.org/10.1039/C8CP05170D>.
- (36) Talley, C. E.; Jackson, J. B.; Oubre, C.; Grady, N. K.; Hollars, C. W.; Lane, S. M.; Huser, T. R.; Nordlander, P.; Halas, N. J. Surface-Enhanced Raman Scattering from Individual Au Nanoparticles and Nanoparticle Dimer Substrates. *Nano Lett.* **2005**, *5* (8), 1569–1574. <https://doi.org/10.1021/nl050928v>.
- (37) Cohen-Hoshen, E.; Bryant, G. W.; Pinkas, I.; Sperling, J.; Bar-Joseph, I. Exciton–Plasmon Interactions in Quantum Dot–Gold Nanoparticle Structures. *Nano Lett.* **2012**, *12* (8), 4260–4264. <https://doi.org/10.1021/nl301917d>.
- (38) Impellizzeri, S.; Monaco, S.; Yildiz, I.; Amelia, M.; Credi, A.; Raymo, F. M. Structural Implications on the Electrochemical and Spectroscopic Signature of CdSe–ZnS Core–Shell Quantum Dots. *J. Phys. Chem. C* **2010**, *114* (15), 7007–7013. <https://doi.org/10.1021/jp1021032>.
- (39) Mie, G. Beiträge Zur Optik Trüber Medien, Speziell Kolloidaler Metallösungen. *Annalen der Physik* **1908**, *330* (3), 377–445. <https://doi.org/10.1002/andp.19083300302>.
- (40) Ashcroft\_Mermin.Pdf.
- (41) Johnson, P. B.; Christy, R. W. Optical Constants of the Noble Metals. *Phys. Rev. B* **1972**, *6* (12), 4370–4379. <https://doi.org/10.1103/PhysRevB.6.4370>.





# CHAPTER IV:

## Materials and Methods



*Life is an experiment, so test your hypotheses*

**Table of content**

CHAPTER IV:.....	237
Materials and Methods .....	237
Abstract .....	239
Solvents and chemicals .....	239
IV-1. Quantum Dots' Synthesis.....	240
IV-1.1. Synthesis and purification of CdS Quantum Dots.....	241
IV-1.2. Purification of the synthesized CdS QDs. ....	242
IV-1.3. Synthesis of CdSe Quantum Dots. ....	243
IV-1.4. Synthesis of Inverted type-I CdS-CdSe Quantum Dots.....	244
IV-1.5. Synthesis of Quasi Type-II CdSe-CdS Quantum Dots.....	246
IV-1.6. Synthesis of InP and InP-ZnS Quantum Dots.....	248
IV-2. Ligand exchange procedures. ....	249
IV-2.1. Ligand exchange using Histidine and (4-azidobenzyl)phosphonic acid. ....	249
IV-2.2. Ligand exchange using 3-phosphonoproponic (PPAc). ....	250
IV-2.3. Partial ligand exchange using octylphosphonic acid (OPAc). ....	251
IV-3. Synthesis and Functionalization of Gold Nanoparticles (AuNP).....	251
IV-3.1 Synthesis of Gold Nanoparticles .....	251
IV-3.1 Functionalization of Gold Nanoparticles.....	252
IV-4. Synthesis of CdSe/ZnS-AuNP Nanocomposites (QD-AuNP) .....	252
IV-5. Estimation of the Quantum Dots characteristics: QDs' diameter, extinction coefficient, and concentration.....	253
IV-6. Irradiation Setups: Light power and Quantum Yield.....	254
IV-6.1. Visible light irradiation setups. ....	254
IV-6.2. Measurement of the light power of the irradiation setups.....	255
IV-6.3. Calculation of the reactions' Quantum Yield. ....	256
IV-7. Experimental protocols.....	264
IV-7.1 Photocatalysis Experiments.....	264
IV-7.2- Photoluminescence quenching.....	265
IV-7.3- Photochemical charging/discharging experiments in the case of QD-AuNP nanocomposites.....	265
IV-7.4- Cyclic voltammetry.....	266
IV-8 –Detection of reactions' products using UV-HPLC or UHPLC-MS. ....	267
IV-9. Analyses and characterization techniques. ....	268
References .....	269

## Abstract

In this chapter IV, we present all the experimental protocols, the instrumentation for the experiments, and their analysis. We describe in detail the procedures used for synthesizing the different Quantum Dots. We also show the methods followed for the ligands exchange and the optimization of the surface ligands layer. In addition to the synthesis and functionalization of the Gold nanoparticles, and the preparation of the nanocomposites of Quantum Dots and gold nanoparticles. Moreover, we describe the methods used to calculate the Quantum Dots' properties, such as their diameter, extinction coefficient, and the reactions' Quantum Yields. Furthermore, we describe the experimental protocols for the photocatalysis experiments and the analysis of the reactions' outcomes. Finally, we present all the instrumental techniques used for the characterizations and the analyses of the different experiments performed during this Thesis.

## Solvents and chemicals

All solvents and chemical reagents were purchased from commercial suppliers such as Sigma Aldrich or Alfa Aesar and used as received without further purification. Some commercial Quantum Dots (CdSe-ZnS and oleate-capped InP-ZnS core-shell QDs) were purchased from the NN-Laboratories (Fayetteville, AR, USA).

In the project of the Quantum Dots-photocatalyzed Tropane derivatives synthesis presented in Chapter II, the substrates of the reaction, such as the N-Aryl amines, the radical traps, and the corresponding reactions' standard products used were synthesized and characterized by our colleagues from the Renaud group at the University of Bern. The complete information concerning the synthesis and the characterization data of the reactions' standards can be found in the reference 1 (Colson et al.<sup>1</sup>)

In the project of the hybrid Quantum Dots connected to Gold nanoparticles presented in Chapter III. The synthesis of the Gold nanoparticles and their characterization were performed by the OPTIMA group at the CNRS of Grenoble (See sections IV-3 and 4). The azide click ligands used for the QD functionalization were synthesized, following the procedure described by Schönweiz et al.<sup>2</sup>, by Maureen FUMAT, a L3 trainee student, whom I co-supervised with Dr. Vincent MAUREL.

## IV-1. Quantum Dots' Synthesis

The semiconductor Quantum Dots were synthesized using hot injection methods (Figure IV-1) following literature procedures with certain modifications for each type of Quantum Dots (QDs). During the synthesis the UV-Vis absorbance spectra were recorded in order to stop the growth at the targeted QDs' size (the spectra of the all the QDs are presented in chapter II, section II-3, page 102)

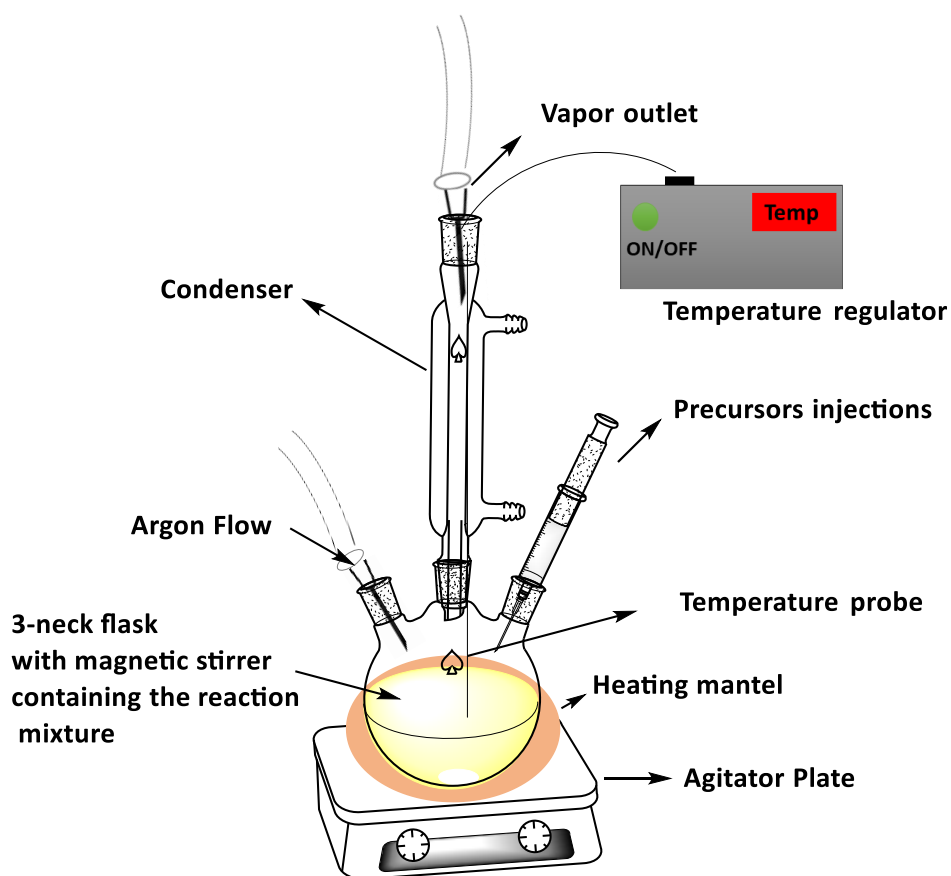


**Figure IV-1: : Quantum Dots synthesis setup.** A three-necked flask in a heating mantel, with an agitator plate, a condenser and a temperature regulator.

### IV-1.1. Synthesis and purification of CdS Quantum Dots.

CdS core Quantum Dots were synthesized by preparing a cadmium precursor of cadmium Oleate and a sulfur precursor of elemental sulfur (S) in octadecene as a non-coordinating solvent<sup>3,4</sup>. The growth of the CdS QDs was monitored based on their optical properties using UV-Vis spectroscopy, and then stopped after reaching the targeted exciton position.

**Preparation of the Cadmium-precursor:** In a 100 ml 2-neck round bottom flask, we prepared a mixture of 255 mg of cadmium oxide (CdO, Aldrich >99.99%), 6.3 mL of oleic acid (technical grade 90%), and 13.7 mL of octadecene (ODE, technical grade 90%). First, the mixture was degassed using Argon bubbling for 30 minutes while maintaining a vigorous stirring. Then, the mixture was heated under Argon flow at 250 °C until the mixture became completely clear (after almost 20 minutes), indicating the formation of Cadmium Oleate (Cd(oleate)<sub>2</sub>). The temperature was fixed at 220°C to maintain the solubility of the Cd-precursor.

**Preparation of the Sulfur-precursor:** In a 50 ml 2 neck-round bottom flask, we prepared a mixture of 64 mg of elemental sulfur (99.98%) in 20 mL of octadecene and degassed the mixture for 30 minutes using Argon bubbling. The mixture was heated at 180 °C until the mixture became of clear yellow color (it required 25 minutes).

**Quantum Dots synthesis:** In a 100 ml 3-neck round bottom flask connected to a condenser, 6 mL of octadecene were degassed for 30 minutes using Argon bubbling and then heated under Argon flow until the temperature reached 220 °C. Next, we injected 4ml of Cd-precursor and 2 mL of S-precursor, increased the temperature to 260 °C, and held this temperature for 2 minutes. Then, we lowered the temperature to 220°C, added 1 mL of S-precursor and 1 mL of Cd-precursor, and let the mixture set at 220 °C for 1 min. The injection of cadmium and sulfur precursors induced a shift in the wavelength position of the QDs' exciton, which indicates the successful growth of the QDs. (See figure IV-2-A). We repeated the consecutive addition of 1ml of each precursor (Cadmium and sulfur) until the QDs reached the desired size (5 repetitions for CdS QDs of D=5.7 nm with an exciton absorption peak at  $\lambda=460$  nm). Finally, the reaction was stopped by cooling the mixture to room temperature and adding 20 ml of pure toluene.

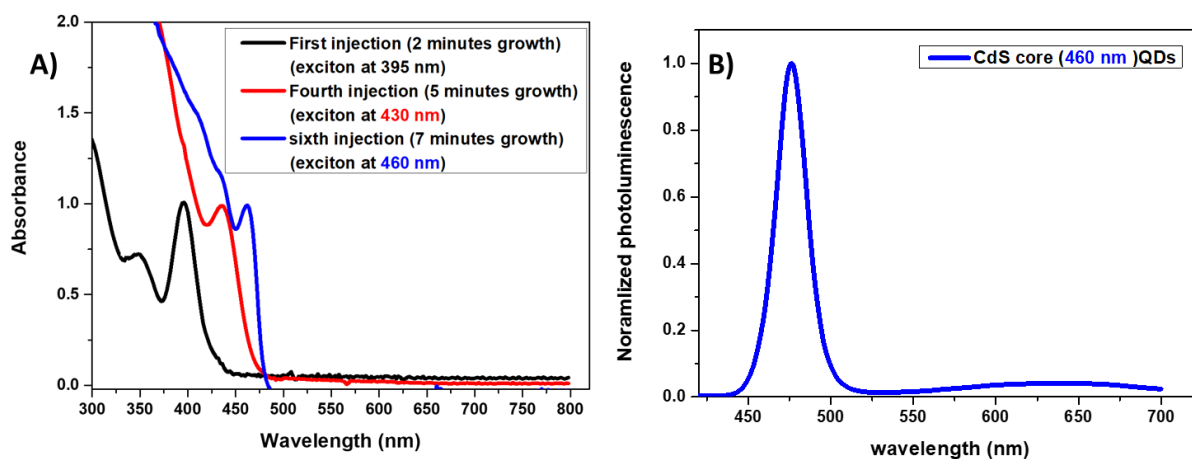


**Figure IV-2: Optical characterization of the CdS QDs.** A) UV-Vis absorbance spectra of the CdS QDs after different precursors injections during the synthesis. B) Photoluminescence spectra of the CdS QDs.

### IV-1.2. Purification of the synthesized CdS QDs.

The QDs' solution was separated into several centrifuge tubes, and to each tube, 5 ml of acetone was added to every 7.5 ml of the reactions' solution. The tubes were centrifuged for 12 minutes at a speed of 1500 rpm. The centrifugation produced a white pellet refers to the un-reacted  $\text{Cd(oleate)}_2$  and a yellow-colored supernatant with QDs. The yellow supernatant was decanted from the white  $\text{Cd(oleate)}_2$  solid<sup>4</sup>.

Then, the supernatant was distributed among new centrifuge tubes, and methanol was added to achieve a 3:1 ratio of methanol: QDs supernatant (in our case, 3ml of QDs and 9 ml MeOH). We shook the mixture and centrifuged it at 3900 rpm for 10 min. The QDs precipitated, forming a powder pellet of QDs and a clear supernatant. We discarded the supernatant and dissolved the pellet in toluene. Next, we re-precipitated the QDs with a three times excess of methanol (3:1 MeOH:toluene), shook the mixture, and centrifuged at 3900 rpm for 10 min. We discarded the supernatant and dissolved the pellet with toluene. Then, a 3:1 ratio of acetone was added to the QDs in toluene, we shook the mixture, and centrifuged at 3900 rpm for 10 min. We discarded the supernatant and dissolved the QDs pellet with toluene. The acetone and methanol washings were repeated five times each, and a yellow pellet was formed after each centrifugation. Then, for the last purification step, 5 ml of

<sup>4</sup>In some cases, the centrifugation step produced a yellow pellet. This pellet was re-dispersed in 2ml toluene and mixed with 1ml of acetone. Then, the tubes were shaken, and new centrifugation was done to obtain a white pellet of  $\text{Cd(Oleate)}_2$  and yellow supernatant with QDs.

acetone was added to the QDs pellet, and the tubes were sonicated for 1 minute to re-disperse the QDs. The solution was centrifuged for 15 minutes at 3900 rpm and the acetone supernatant was discarded. This washing with acetone was repeated five times in order to get rid of any excess reagent (Octadecene, in particular) from the synthesis. Finally, the QDs were stored in toluene.

### IV-1.3. Synthesis of CdSe Quantum Dots.

CdSe core QDs were synthesized by preparing a cadmium precursor of cadmium oleate and mixed with a selenium suspension prepared in octadecene<sup>5</sup>. The growth of the CdSe QDs was monitored until reaching an exciton position at wavelength  $\lambda = 540$  nm.

In a 3-neck round-bottom flask, 300mg of cadmium oxide (Aldrich, >99.99%) were added to 20 ml of octadecene (technical grade 90%) and 2 ml of oleic acid (technical grade 90%). The mixture was degassed for 30 minutes using Argon bubbling while maintaining a vigorous stirring for the whole synthesis procedure. After degassing, the reaction flask was kept under argon flow and then heated to 260°C. Heating was maintained until the solution became clear, indicating the in situ formation of Cd(oleate)<sub>2</sub>. The mixture was then cooled to 120°C, and Selenium (Se 100 mesh, 99.99%) suspension in octadecene was injected while maintaining the argon flow and the stirring. The selenium precursor was prepared by dispersing selenium powder (100 mg) in 2ml octadecene at room temperature; the solution was sonicated for 2 minutes then degassed for 30 minutes and sonicated for 2 more minutes before the injection.

Then for the growth of the QDs, the temperature was raised to 250°C. The mixture's color changed from black just after the addition of the Se powder to yellow and then to dark orange, indicating the production and growth of the QDs. The solution temperature was maintained at the 250-260°C range for 5 minutes to obtain QDs of the desired size (3 nm at  $\lambda = 540$  nm). Finally, the reaction was stopped by cooling the mixture to room temperature and adding 20 ml of pure toluene. The synthesized CdSe QDs were purified using the same procedure as for the CdS QDs mentioned above.

### IV-1.4. Synthesis of Inverted type-I CdS-CdSe Quantum Dots.

CdS-CdSe core-shell QDs were synthesized starting from a previously purified sample of core CdS QDs (core diameter = 5.7 nm) and then cadmium and selenium precursors were injected for the CdSe shell<sup>6,7</sup>. The growth of the CdSe shell was targeted for two monolayers. As a result, after the shell growth, the exciton position is red-shifted to wavelength position  $\lambda=530$ .

The purified CdS core QDs (10 $\mu$ M) were loaded into a three-neck flask containing 16.6 mL of octadecene (ODE) and 0.9ml of (0.3M) Oleylamine (technical grade 90%). The solution was degassed for 30 minutes using argon bubbling. Then, the mixture was maintained under argon flow and heated to 230 °C for the shell growth. Precise amounts of cadmium and selenium precursors in ODE solutions corresponding to one monolayer of CdSe were alternatively injected into the solution with an equimolar ratio. The growth of each CdSe monolayer was completed at 260 °C for 20 minutes. The CdSe shell thickness was controlled by the amount of the precursor injected (See the calculation below).

**Precursor's preparation:** 0.2 M cadmium precursor was prepared by dissolving 248 mg of cadmium oxide in 5.6 mL of Oleic acid and 4.4 mL of ODE at 230 °C. The Se precursor (0.2M) solution was prepared by dispersing 78 mg of selenium powder in 5ml ODE at room temperature and degassed for 30 minutes, before the injection, the solution was sonicated for 2 minutes.

**Shell growth:** When the solution of CdS core was heated to 230°C the growth of the CdSe shell was started by adding 1:1 Cd:Se solutions. For the first monolayer, 642  $\mu$ l of 0.2M of cadmium and 642  $\mu$ l of 0.2M of selenium were added at T =230°C and then the temperature was raised to 260 °C and held for 20 minutes. Then, the second monolayer was similarly grown by injecting 802  $\mu$ l of 0.2M of cadmium and 802  $\mu$ l of 0.2M of selenium and the temperature was held at 260°C for 20 minutes.

Finally, the reaction was stopped by cooling the mixture to room temperature and adding 20 ml of pure toluene. The synthesized CdS-CdSe core-shell QDs were purified using the same procedure as for the CdS QDs mentioned above.

Calculations of the volumes needed for the shell growth were performed based on the method used by Chen et al.<sup>8</sup>:

CdS core Diameter = 5.7 nm, then the radius of the CdS core = 2.85 nm

Lattice Constant (for zinc blende) = 0.608 nm

Thickness of each monolayer (t):  $t = \sqrt{3}/3 \times a = 0.35$  nm

Molecular Weight of CdSe (M) = 191.3 g/mol

Density of CdSe (D) = 5.82 g/cm<sup>3</sup>

Moles of CdS core QDs used in this volume of stock ( $n_1$ ) =  $1.75 \times 10^{-7}$  mole

- Volume needed for the first CdSe monolayer:

Radius of core + 1 monolayer ( $r_1$ ):  $r_1 = r_0 + t = 2.85 + 0.35 = 3.2$  nm

Where  $r_0$  is the radius of the CdS core,  $r_1$  is the radius of the core plus 1<sup>st</sup> monolayer and  $t$  is the thickness of one monolayer

Then, the volume for the first layer ( $V_1$ ) equals  $V_1 = 4/3 \times \pi (r_1^3 - r_0^3) = 4.027 \times 10^{-20}$  cm<sup>3</sup>

The mass of CdSe needed for the first monolayer is  $V_1 \times D = 2.34 \times 10^{-19}$  g.

The number of moles of CdSe to be added per particle of CdS is  $1.22 \times 10^{-21}$  mole/particle.

Then, the number of moles of CdSe to be added to the CdS stock is  $1.28 \times 10^{-4}$  mol.

Finally, the volume needed for the first monolayer of CdSe is equal to 642  $\mu$ l of 0.2M ( $1.28 \times 10^{-4}$  mol) of cadmium precursor and 642  $\mu$ l of 0.2M of selenium precursor.

- Volume needed for the Second CdSe monolayer:

Following exactly the same calculations mentioned above but taking into account the radius of the CdS core and the first monolayer of CdSe, the volume needed for the growth of the second monolayer of the CdSe shell is 802  $\mu$ L of 0.2M cadmium precursor and 802  $\mu$ l of 0.2M of selenium precursor.

### IV-1.5. Synthesis of Quasi Type-II CdSe-CdS Quantum Dots.

CdSe-CdS core-shell QDs were synthesized following a one-pot method described in literature by Peng and co-workers<sup>9</sup>. The growth of the three monolayers for the CdS resulted in an exciton position at wavelength  $\lambda=573$  nm.

In order to follow the one-pot synthesis of CdSe-CdS core shell QDs, a different way was used for the CdSe core than the one mentioned above (Section IV-1.3). In this case, core CdSe were synthesized starting from cadmium stearate ( $\text{CdSt}_2$ ) instead of cadmium oleate. The CdSe core were prepared as follow, in a three necked flask, 132 mg of commercial cadmium stearate (MP biomedical, Strasbourg, France) was solubilized in 3.5 mL ODE. The solution was degassed by Argon bubbling for 30 minutes with continuous stirring. Then, the temperature of the mixture was increased to 250°C, until the solubility of  $\text{CdSt}_2$  in ODE was accomplished after the formation of clear solution. Selenium suspension was prepared by dissolving 21.7 mg in 2.5 mL ODE and degassed for 30 minutes. This suspension was sonicated for 2 minutes before the injection. The growth of the CdSe core was allowed for 8 minutes and at 250°C.

Then for the growth of the CdS shell, in a 3-neck round bottom flask, 17.1 mL dodecane (Aldrich  $\geq 99\%$ ), 4.725 mL oleylamine, and 4.5 mL core CdSe were mixed. This mixture was degassed using argon for 1 hour. The temperature was then progressively raised to 80°C. For the growth of the CdS Shell, cadmium diethyldithiocarbamate ( $\text{Cd}(\text{DDTC})_2$ ) was used as a source for the formation of the CdS shell.  $\text{Cd}(\text{DDTC})_2$  was synthesized starting from sodium diethyldithiocarbamate and cadmium acetate dehydrate (See below). The volumes needed for the growth of each CdS monolayer were calculated following a similar method to the one used for the synthesis of the inverted type I CdS-CdSe core-shell QDs (Detailed calculation is described below).

222  $\mu\text{L}$  of 0.1 M  $\text{Cd}(\text{DDTC})_2$  (prepared in a mix of 1.125 mL dodecane and 0.375 mL oleylamine) as the CdS shell precursor was quickly injected into the above mentioned mixture containing CdSe core under Argon flow. The temperature was then increased to 160°C, while the stirring was continued, and maintained constant at 160°C for 20 minutes for the growth of the first monolayer of the CdS shell. Next, a second injection of 326  $\mu\text{L}$  of 0.1 M  $\text{Cd}(\text{DDTC})_2$  was made while maintaining the temperature at 160°C. The temperature was held constant

for 20 minutes for the growth of the second monolayer of CdS shell. Then a third injection was done by injection 451  $\mu\text{L}$  of 0.1M Cd(DDTC)<sub>2</sub> for the growth of the third CdS monolayer. Finally, the reaction mixture was cooled down and 20 ml of toluene was added to stop the reaction. The synthesized QDs were purified and stored in Toluene.

**Synthesis of cadmium diethyldithiocarbamate (Cd(DDTC)<sub>2</sub>):** The synthesis procedure used adapted from a literature method<sup>9</sup>, where 2.69 g of cadmium acetate dihydrate (CdAc<sub>2</sub>·2H<sub>2</sub>O) was dissolved in 10 mL of distilled water in a first flask. Next, 3.42 g of sodium diethyldithiocarbamate (NaDDTC) was dissolved in 60 mL distilled water in a second flask. The NaDDTC solution was mixed with the cadmium acetate solution in a dropwise manner using Pasteur Pipettes while the latter was continuously stirred. Then, formation of the white precipitate of Cd(DDTC)<sub>2</sub> was observed. The stirring was continued for 1 hour even after the addition of NaDDTC was complete. The thick white precipitate was collected in several 50 mL Falcon tubes, washed with distilled water and centrifuged at 3900 rpm for 10 minutes. The clear water phase was discarded, and the process was repeated 3 times. Finally, the white precipitate of Cd(DDTC)<sub>2</sub> was collected and dried for further use.

Calculations of the volumes needed for the shell growth were performed based on the method used by Chen et al.<sup>8</sup> similar to the calculation described for the inverted type-I CdS-CdSe QDs in section IV-1.4:

CdSe core Diameter = 2.87 nm, then the radius of the CdS core = 1.43 nm

Lattice Constant (for Wurtzite) = 0.6843 nm

Thickness of each monolayer (t): t= 0.34 nm

Molecular Weight of CdS (M) = 144.63 g/mol

Density of CdS (D) = 4.58 g/cm<sup>3</sup>

Moles of CdSe core QDs used in this volume of stock ( $n_1$ ) =  $1.04 \times 10^{-7}$  mole

- Volume needed for the first CdSe monolayer:

Radius of core + 1 monolayer ( $r_1$ ):  $r_1 = r_0 + t = 1.77$  nm

Where  $r_0$  is the radius of the CdSe core,  $r_1$  is the radius of the core plus 1<sup>st</sup> monolayer and  $t$  is the thickness of one monolayer.

Then, the volume for the first layer ( $V_1$ ) equals  $V_1 = \frac{4}{3} \times \pi (r_1^3 - r_0^3) = 1.112 \times 10^{-20}$  cm<sup>3</sup>

The mass of CdS needed for the first monolayer is  $V_1 \times D = 5.09 \times 10^{-20}$  g.

The number of moles of CdS to be added per particle of CdSe is  $3.52 \times 10^{-22}$  mole/particle.

Then, the number of moles of CdS to be added to the CdSe stock is  $2.2 \times 10^{-5}$  mol.

Finally, the volume needed for the first monolayer of CdS is equal to 222  $\mu$ l starting from 0.1M ( $2.2 \times 10^{-5}$  mol) Cd(DDTC)<sub>2</sub>. It was considered that the moles of CdS is equivalent to the moles of Cd(DDTC)<sub>2</sub> since both the compounds have equal number of cadmium atoms.

- Volume needed for the Second and third CdS monolayer:

Following exactly the same calculations mentioned above but taking into account the radius of the CdSe core in addition to the first and second monolayer of CdS respectively, the volume needed for the growth of the second monolayer of the CdS shell is 326 $\mu$ L of 0.1 M Cd(DDTC)<sub>2</sub>, and 451 $\mu$ L for the third monolayer.

### IV-1.6. Synthesis of InP and InP-ZnS Quantum Dots.

InP core QDs and InP-ZnS core-shell QDs were prepared starting from indium bromide as an indium precursor and aminophosphine as phosphorus precursor as described by Tessier et al.<sup>10</sup>.

For the synthesis of the InP core QDs, 160 mg of indium bromide (Aldrich, 99.99%), as indium precursor, and 560 mg of zinc bromide (Aldrich, 99.99%) were mixed in 5ml of oleylamine, which is used as a coordinating solvent during this synthesis. The addition of zinc halides in the described procedure of InP QDs was shown to assist in controlling the growth of the QDs size. The reaction mixture is stirred and degassed for 60 minutes using Argon bubbling. Then, the mixture was heated to 180 °C under Argon flow. Upon reaching 180 °C, 0.45 mL of tris(diethylamino)-phosphine (Aldrich 97%) as phosphorus precursor was injected into the reaction mixture. After the injection, the temperature was maintained at 180°C for 30 minutes for the InP core QDs synthesis to proceed. At the end of the reaction, the temperature was cooled down, and 20ml of toluene was added to stop the reaction.

Furthermore, the synthesized InP core QDs were purified as follows: the reaction mixture was separated into different centrifuge tubes, and a ratio of 1:1 ethanol: QDs solution was shaken and centrifuged at 3900 rpm for 10 minutes. Then, the QDs precipitate as powder

pellet and the clear supernatant was decanted. This washing process using ethanol was repeated three times, and finally, the QDs were stored in toluene.

**Synthesis of InP-ZnS QDs:** The InP-ZnS core-shell QDs were synthesized in a one-pot process. An InP QDs synthesis was performed exactly the same as mentioned above. Then, instead of cooling down the temperature after the 30 minutes of the core synthesis, slow injection of 1 mL of saturated TOP-S was performed. TOP-S solution was prepared by mixing 28.8 mg of elemental sulfur in 4 mL of trioctylphosphine (TOP, technical grade 90%) under an inert atmosphere. Then, after 60 minutes of the reaction time, the temperature was increased from 180 to 200 °C. At 120 minutes, 1 g of Zinc stearate ( $\text{Zn}(\text{stearate})_2$ , 10-12% Zn basis) dissolved in 4 mL of octadecene (ODE) was slowly injected. The temperature was raised from 200 to 220 °C. Then after 150 minutes, an injection of 0.7 mL of TOP-S was done, and the temperature was increased from 220 to 240 °C. At 180 minutes, a slow injection of 0.5 g of  $\text{Zn}(\text{stearate})_2$  in 2 mL of ODE was performed, and the temperature was increased to 260 °C. Finally, after 210 minutes of the whole synthesis time, the reaction was stopped, and the temperature was cooled down and followed by the addition of 20 ml of toluene. InP/ZnS nanocrystals are then purified using ethanol precipitation as mentioned for the InP core and then stored in toluene.

## IV-2. Ligand exchange procedures.

### IV-2.1. Ligand exchange using Histidine and (4-azidobenzyl)phosphonic acid.

The ligand exchange using Histidine ligands was applied particularly for CdSe-ZnS Core-Shell QDs to transfer them into water. The commercially purchased CdSe-ZnS core-shell QDs are initially coated with octadecylamine ligands, making them soluble in toluene and other non-polar organic solvents. In this case, the ligand exchange using Histidine ligands was performed following a procedure reported by zylstra et al.<sup>11</sup> with slight modification. First, 500  $\mu\text{L}$  of core-shell CdSe-ZnS QDs in toluene were dried using a vacuum pump and dispersed in chloroform ( $\text{CHCl}_3$ ) as an intermediate solvent. Next, 500  $\mu\text{L}$  of a solution with 0.1 M histidine and 0.25 M NaOH in 3:1 methanol:  $\text{H}_2\text{O}$  is added to the QDs coated with octadecylamine ligands in  $\text{CHCl}_3$ . After mixing and being shaken for 1 minute, immediate phase separation of QDs from the organic phase to the aqueous phase was observed forming a clear phase and colored one. Then decantation of the clear phase with no QD was done, and 300 $\mu\text{L}$  of a 1mM

histidine and 2.5 mM NaOH solution in Milli-Q water was added to the aqueous phase containing the QDs. This aqueous solution was washed 4 times with  $\text{CHCl}_3$ . The QDs were cleaned of excess histidine through filtration with a 30 kDa centrifugal filter. Finally, the QDs were suspended in distilled water. The absorbance spectra of the QDs before and after the ligand exchange are presented in Chapter III, section III-2.

Then in order to afford the connection of the CdSe/ZnS QDs with the gold nanoparticles using click reaction, the CdSe/ZnS QDs were functionalized with (4-azidobenzyl)phosphonic acid ligands in second step. The obtained water-soluble core/shell CdSe/ZnS QD were dispersed in a pH=10 borax buffered solution. Then, 500  $\mu\text{M}$  of 4-Azido-benzyl-phosphoric acid (azido click ligand) prepared in borax buffer (pH=10 ) were added in a second partial ligand exchange step to have CdSe/ZnS QD coated with a mix of histidine and 4-Azido-benzyl-phosphoric acid ligands in borax buffered solution ready for the click reaction with the AuNPs.

### **IV-2.2. Ligand exchange using 3-phosphonopropionic (PPAc).**

In order to transfer oleate-capped QDs (CdS or CdSe) from toluene into polar solvents (such as acetonitrile), we adapted a procedure described by Calzada et al.<sup>12</sup> First, a stock of 0.1M phosphonopropionic acid ligands was prepared in a solution of isopropanol, then 500 equivalents of PPAc were added to the QDs in toluene. A few seconds later, the QDs started to flocculate due to the replacement of oleate ligands from the surface of the QDs by the PPAc ligands. Then, centrifugation for the solution was done at 3900 rpm for 5 minutes, which resulted in a clear supernatant and a precipitated QDs powder pellet. Next, we discarded the clear supernatant and suspended the QDs in Dimethylformamide (DMF). DMF was used as an intermediate polar solvent to re-solubilize the QDs. Then, to transfer the QDs from DMF, we diluted the PPA-capped QDs in DMF with 10 mM KOH in water (a molar ratio KOH: PPAc of 5:1). This KOH solution was degassed using Argon bubbling for 1 hour. Finally, we removed the DMF from the water/DMF mixture by washing the solution 3 times with chloroform. The washing resulted in a slightly cloudy solution; then, it was degassed using Argon bubbling for 40 minutes to clarify the solution of QDs by evaporating the excess of chloroform. The QDs were concentrated and cleaned of excess ligands via two successive filtrations with a 30 kDa centrifugal filter and re-suspended in the polar solvent needed for the reaction, such as acetonitrile. The absorbance spectra of the QDs before and after the ligand exchange are presented in Chapter II, section II-8.

### IV-2.3. Partial ligand exchange using octylphosphonic acid (OPAc).

The partial exchange of the native ligands of the QDs with octylphosphonic acid was done in order to enhance the permeability of the reaction substrates to the QDs' surface. This ligand exchange is intended to afford a partial replacement of the native ligands on the QDs' surface. The addition of OPAc was done as follows: First, a stock of concentrated solution of OPAc (10mM typically) ligand was prepared under an inert atmosphere and in the same solvent used for the photocatalytic reaction with the QDs. Then, a solution of known concentration of QDs (e.g. 1 $\mu$ M of CdS QDs) was prepared in the same solvent. The number of equivalents of OPAc was calculated and added to the QDs, taking into account the dilution factor. The mixture was stirred in the dark under an inert atmosphere for 1 hour before starting the photochemical reaction. The absorbance spectra of the QDs before and after the partial ligand exchange are presented in Chapter II, section II-8.

## IV-3. Synthesis and Functionalization of Gold Nanoparticles (AuNP)

### IV-3.1 Synthesis of Gold Nanoparticles

The synthesis of the Gold nanoparticles protocols are optimized and performed by Dr. Fabien DUBOIS and Dr. Pierre BAUER from the OPTIMA team, and are reproduced here for the better understanding of Chapter III.

The Gold nanoparticles (AuNP) are synthesized using the Turkevich-Frens classical method<sup>13,14</sup>. In detail, using the reduction of chloroauric acid aqueous solution in the presence of sodium citrate, spherical citrate-capped nanoparticles are expected to grow with an optimized relative large size. AuNP were prepared by the reduction of Tetrachloroauric acid (HAuCl<sub>4</sub>) with Trisodium citrate at 100° C. Therefore, 100 mL of a 1.6 mM HAuCl<sub>4</sub> aqueous solution was boiled in a two-necked round flask while stirring vigorously. Then, 10 mL of a 38.8 mM trisodium citrate aqueous solution was rapidly added to the boiling mixture, resulting in a color change from light yellow to deep red. After boiling for 10 min, the AuNP colloids were cooled to room temperature and filtered through a 0.45  $\mu$ m filter before use. The concentration of the AuNPs obtained was roughly estimated by calculating the ratio of the total mass of gold to the mass of a 25 nm physical diameter gold sphere (Determined by the

microscopic imaging as shown in Chapter III) thus by neglecting the removed hypothetical aggregates. This yields an upper-bound estimate of  $\sim 3$  nM of NPs.

### IV-3.1 Functionalization of Gold Nanoparticles

The prepared citrate-capped AuNP are functionalized with aqueous Alkyne ligands by a typical exchange ligand process. In the presence of a mixture of short length chain functional PEGs composed of an equimolar ratio of amino-PEG-alkyne and amino-PEG-COOH the AuNP are functionalized in order to afford their connection with the CdSe-ZnS QDs. This composition mixture presented a good coverage of the active chemical alkyne functions for the covalent click reaction mixed with the presence of terminal carboxylic acids for stabilizing the charges surface densities of the metallic nanoparticles.

The functionalized-AuNP were prepared one day before the CdSe-ZnS QD-AuNP composites synthesis. The ligand functionalization started by injecting a 15/15 ( $\mu\text{L}$ ) volumic ratio of 0.125 mM Propargyl-PEG<sub>9</sub>-amine/ Amino-PEG<sub>8</sub>-acid aqueous solutions and 10  $\mu\text{L}$  of a NaOH aqueous solution (10 mM) into 5 mL of citrate-capped AuNP. The mixture was then stirred overnight and filtered through a 0.45  $\mu\text{m}$  filter before their use.

### IV-4. Synthesis of CdSe/ZnS-AuNP Nanocomposites (QD-AuNP)

The CdSe/ZnS QD-AuNP composites were prepared using CuAAC click reaction (copper catalyzed azide to alkyne cycloaddition) using the previously prepared azide functionalized CdSe/ZnS QD and alkyne functionalized AuNP. The reaction was performed using CuSO<sub>4</sub>/Sodium ascorbate reagents in water, under an inert atmosphere in order to avoid the presence of oxygen which can decrease the amount of Cu(I) source by oxidizing it to Cu(II). Reference samples were prepared in the same conditions of reaction but without the presence of azide ligands at the surface of the QDs (Water-soluble QDs functionalized only histidine ligands).

#### Composites synthesis protocol

Typically, 500  $\mu\text{L}$  of Milli-Q water, 1 mL of 3 nM functionalized amino-PEG AuNPs and 1.35 mL of a 12.5 mM borax buffer (pH =10) were mixed. Then, 400  $\mu\text{L}$  of 200 nM of CdSe/ZnS QDs coated with histidine and 4-(Azido-benzyl)-phosphoric acid ligands in borax buffered solution was added under agitation. The colloidal suspension was degassed using Argon bubbling for a

few minutes to remove any traces of oxygen before the addition of 40  $\mu\text{L}$  of a 0.1 mM sodium ascorbate solution and 40  $\mu\text{L}$  of a 0.05 mM copper sulfate solution, then the reaction was kept for more than 24 hours to let the click reaction proceed. The suspensions were concentrated and purified using Vivaspin 2 (2 mL) concentrators. Successive centrifugations (3x) were performed at 3000 rpm for 3 min to increase the concentration of particles in suspension.

Reference samples were prepared in the same conditions than for the preparation of the composites (same concentration of QD and AuNP, same buffer pH condition, same concentrations of Copper sulfate and sodium sulfate reagents) but using histidine capped QDs (without azide ligands) or using amino-PEG-COOH capped Au-NPs (without alkyne ligands).

#### IV-5. Estimation of the Quantum Dots characteristics: QDs' diameter, extinction coefficient, and concentration.

As described in Chapter I (section I-2) of this Thesis, the properties of the Quantum Dots could be determined using the equations reported in the literature depending on the absorption position of the QDs' exciton. For example, considering CdS QDs, Yu et al.<sup>15</sup> reported the equations useful for the estimation of the CdS diameter and their extinction coefficient depending on the exciton position (Eq.1 and Eq.1'). Therefore, using equation Eq.1 for CdS QDs having an exciton position at  $\lambda=460$  nm we calculated their diameter to be 5.7 nm, and using Eq.1' the extinction coefficient was calculated to be  $\epsilon= 1.18 \times 10^6 \text{ L.mol}^{-1}.\text{cm}^{-1}$  (Table IV-1).

$$D_{\text{CdS}} = (-6.6521 \times 10^{-8})\lambda^3 + (1.9557 \times 10^{-4})\lambda^2 - (9.2352 \times 10^{-2})\lambda + (13.29) \quad \text{Eq.1}$$

$$\epsilon = 21536 (D)^{2.3} \quad \text{Eq.1'}$$

Moreover, Jasieniak et al.<sup>16</sup> reported the equations used for the estimation of the CdSe QDs' diameter the corresponding extinction coefficient based on the exciton position (Eq.2 and Eq.2'). Here, for CdSe QDs having an exciton position at  $\lambda=540$  nm we calculated their diameter to be 3 nm and the extinction coefficient  $\epsilon= 1.78 \times 10^5 \text{ L.mol}^{-1}.\text{cm}^{-1}$  (Table IV-1).

$$D_{\text{CdSe}} = (1.62974 \times 10^{-9})\lambda^4 - (2.85743 \times 10^{-6})\lambda^3 + (1.8873 \times 10^{-3})\lambda^2 - (0.54736)\lambda + 59.60816 \quad \text{Eq.2}$$

$$\epsilon = 155\,507 + 6.6705 \times 10^{13} \exp\left(\frac{-E(\text{eV})}{0.10551}\right) \quad \text{Eq.2'}$$

Similarly, Reiss and co-workers developed an equation for the estimation of the diameter of InP based QDs in addition to an equation relating the diameter with their extinction coefficient<sup>17</sup> (Eq.3 and Eq.3'). Then, for InP QDs having an exciton position at  $\lambda=450$

nm we calculated their diameter to be 2.8 nm and the corresponding extinction coefficient  $\epsilon = 1.2 \times 10^5 \text{ L.mol}^{-1}.\text{cm}^{-1}$  (Table IV-1).

$$D_{\text{InP}} = (-3.7707 \times 10^{-12})\lambda^5 + (1.0262 \times 10^{-8})\lambda^4 - (1.0781 \times 10^{-5})\lambda^3 + (5.4550 \times 10^{-3})\lambda^2 - (1.3122)\lambda + 119.9 \quad \text{Eq.3}$$

$$\epsilon = (3046.1) (D)^3 - (76532) (D)^2 + (5.5137 \times 10^5) (D) - (8.9839 \times 10^5) \quad \text{Eq.3'}$$

The same equation were used for the core-shell structured QDs in order to estimate their diameter and the corresponding extinction coefficient. All the values were reported in Chapter-II, section II-3 of this Thesis. Then, after estimating the corresponding extinction coefficient of each type of QDs, the actual concentration of each sample of QDs was calculated following the Beer-Lambert law

Type of QDs	Exciton position ( $\lambda$ nm)	Diameter (nm)	$\epsilon(\text{L.mol}^{-1}.\text{cm}^{-1})$	Band gap $E_g$ (eV)
CdS core	460 nm	5.7 nm	$1.2 \times 10^6$	2.69 eV
CdSe core	540 nm	3.0 nm	$1.8 \times 10^5$	2.29 eV
InP core	450 nm	2.8 nm	$1.2 \times 10^5$	2.75 eV

*Table IV-1: Summary of the properties of Quantum Dots. The obtained excition postion of the CdS, CdSe and InP Core-QDs, thoir calculated diameter and extinction position.*

## IV-6. Irradiation Setups: Light power and Quantum Yield.

### IV-6.1. Visible light irradiation setups.

The used irradiation setups are based on LED sources. The LED system is of Oslon4 power star type, purchased from Osram Opto-Semiconductors. The complete setup is home-made prepared with the help of Christian LOMBARD (Engineer in the CAMPE team). The setup consists of a LED system, a 3D-printed sample holder fitted for the reaction vial, and a metallic heat sink (Figure IV-3). Three different setups were designed with different LED wavelengths to be suitable for the irradiation wavelength needed for the reaction. A LED system with a dominant emission wavelength of 455 nm was designed for the Blue light irradiation, a LED system with a dominant emission wavelength of 528 nm for the Green light irradiation, and a third LED system with a dominant emission wavelength of 590 nm for the Yellow light irradiation (See Table IV-2).

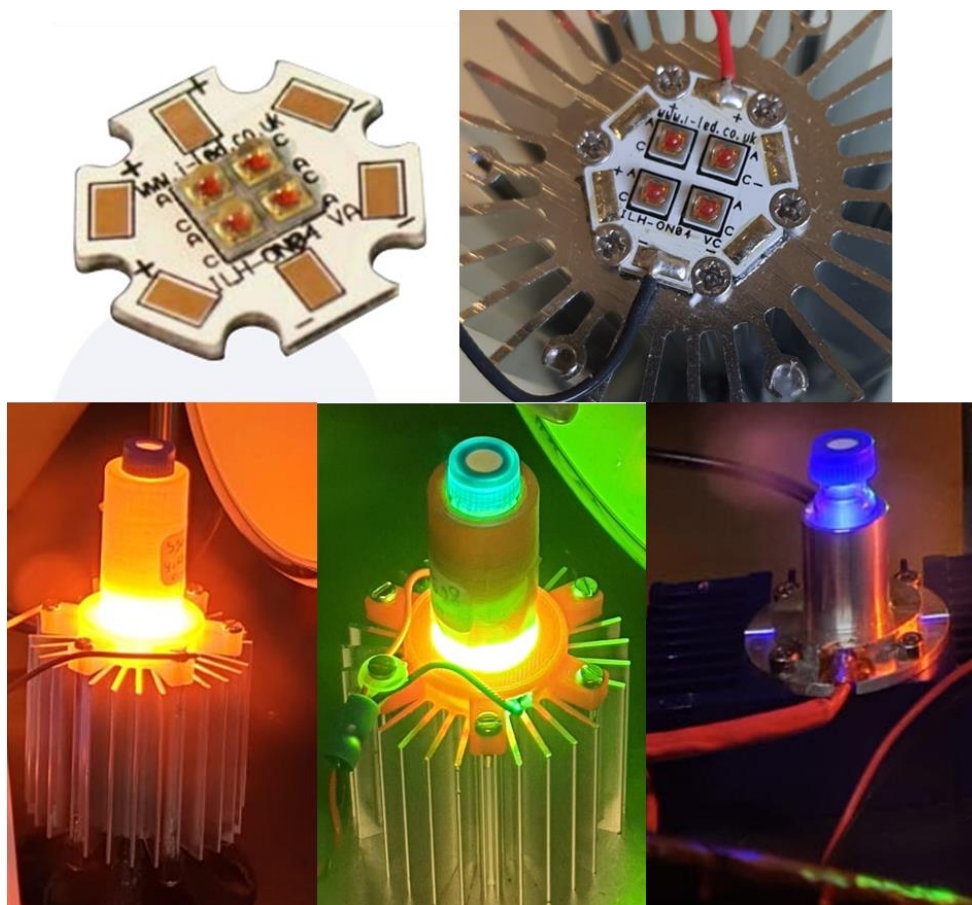


*Figure IV-3: Irradiation setups. Home-made setups consist of LED systems of different wavelength.*

#### **IV-6.2. Measurement of the light power of the irradiation setups.**

The power of the light sent by the irradiation setups was measured using a Thorlabs-PM100D power meter connected to a Thorlabs-S310C power sensor head, designed for power measurements up to 15W (Figure IV-4). The head sensor has a built-in thermistor to control the overheating of the sensor. The Light power measured for the different LED irradiation setups used in our photocatalytic experiments is collected in Table IV-2.

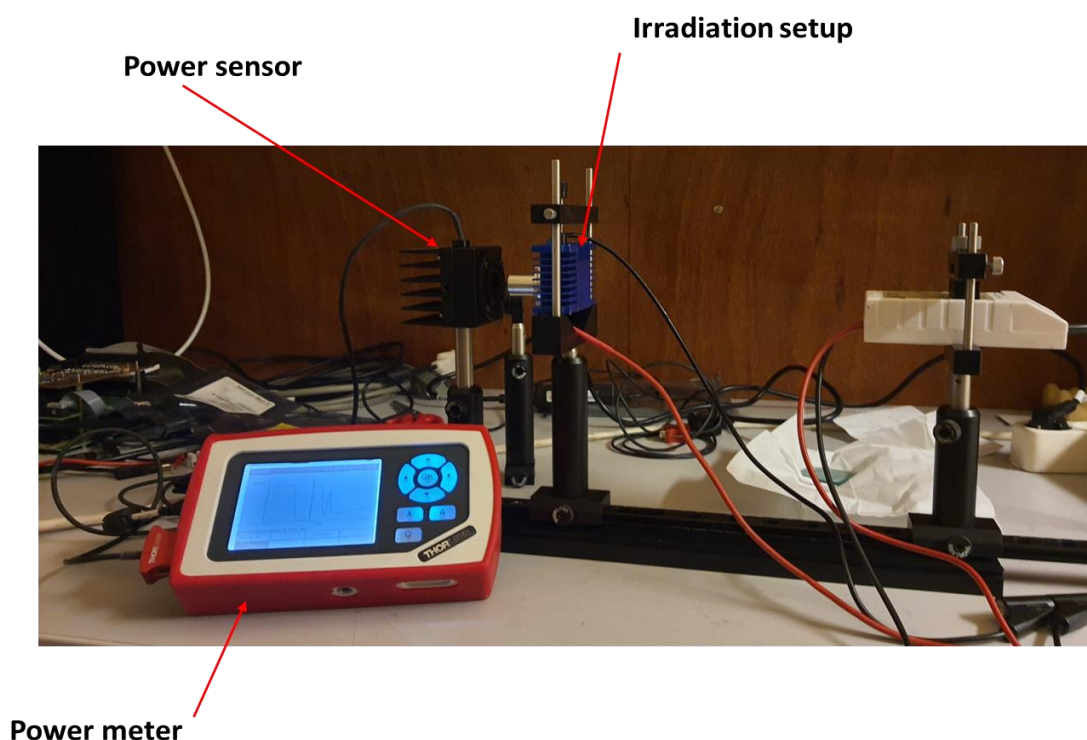


**Figure IV-4:** System used for the measurement of the light power sent by the irradiation setup. System consist of a power sensor connected to a power meter to read the measure power.

Irradiation Setup	Wavelength (nm)	Light Power (mW)
Blue Light ILH-ON04-DEBL-SC201	455 nm	10 mW
Green Light ILH-ON04-TRGR-SC201	528 nm	50 mW
Yellow Light ILH-ON04-YELL-SC201	590 nm	20 mW

**Table IV-2:** The light power measured for the different irradiation setups with their corresponding wavelength. The measured power is of  $\pm 1$  uncertainty.

### IV-6.3. Calculation of the reactions' Quantum Yield.

The Quantum Yield (QY) can be determined by the ratio of the number of moles of product formed per second ( $n_{\text{product}}$ ) to the number of moles of photons absorbed per second ( $n_{\text{photon}}$ ) by the photocatalyst **Eq.4**, Quantum Dots in our case. The number of photons absorbed can be estimated using chemical actinometry or by measuring the power of light sent by the used irradiation setup.

$$QY = \frac{\text{moles of product per second (n}_{\text{product}})}{\text{moles of photons absorbed per second (n}_{\text{photon}})} \quad \text{Eq.4}$$

#### IV-6.3.1 Ferrioxalate Actinometry

The number of photons absorbed during a photocatalytic reaction can be estimated using chemical actinometry methods. A chemical actinometer constitutes a chemical system that undergoes a light-induced reaction when irradiated at a specific wavelength and at which the quantum yield of this reaction is known. Then, the chemical actinometry allows to determine the intensity of the light received by a reaction medium. In our case, and for the reactions' mixtures irradiated using blue light ( $\lambda=455$  nm), we selected Ferrioxalate Actinometry to determine the number of photons absorbed and, consequently, the Quantum yield for the blue light QD-photocatalyzed reactions. Ferrioxalate Actinometry<sup>18,19</sup> is an easy to handle actinometry system and the corresponding reaction (Scheme IV-1) can be activated by blue light irradiation. The evolution of the reaction could be followed using UV-Vis absorbance measurements.

##### Ferrioxalate conversion mechanism

In order to determine the amount of Ferrioxalate converted during the irradiation, a Ferrioxalate solution (see the synthesis below) is prepared in the same reaction vial as the one used for the photocatalysis experiments; then, several aliquots are collected at different irradiation times. Next, the collected aliquots are mixed with phenanthroline, which creates a  $[\text{Fe}^{\text{II}}(\text{Phen})_3]^{2+}$  complex (Scheme IV-1) from the  $[\text{Fe}^{\text{II}}(\text{C}_2\text{O}_4)_2]_3^{2-}$  complex generated during the irradiation of the Ferrioxalate solution. The  $[\text{Fe}^{\text{II}}(\text{Phen})_3]^{2+}$  complex exhibits an absorbance peak at a wavelength close to 510 nm. Then the evolution of the absorbance peak at 510 nm is used for the determination of the conversion of the Ferrioxalate (See Figure IV-5).



*Scheme IV-1: Ferrioxalate actinometry mechanism. The reaction corresponding to the conversion of the ferrioxalate during its irradiation and the complexation with Phenanthroline.*

The conversion of the ferrioxalate and the formation of the  $[\text{Fe}^{\text{II}}(\text{Phen})_3]^{2+}$  complexes proceed as described in Scheme IV-1. Upon irradiation, a photon reacts with the ferrioxalate complex  $[\text{Fe}^{\text{III}}]$  (reaction (1)). The ferrioxalate complex is then transformed into the  $[\text{Fe}^{\text{II}}]$  complex and generates a radical derived from the oxalate. This radical allows the reduction of a second ferrioxalate complex  $[\text{Fe}^{\text{III}}]$  into  $[\text{Fe}^{\text{II}}]$  (reaction (2)). Then after the addition of phenanthroline,  $[\text{Fe}^{\text{II}}(\text{Phen})_3]^{2+}$  complex is formed (reaction (3)). The Quantum Yield of the Ferrioxalate reaction is described in equation Eq.5. It is known from literature that, at  $\lambda = 455$  nm the Quantum Yield of the Ferrioxalate is to 1.12<sup>18</sup>.

$$\text{QY}_{\text{Ferrioxalate}} = \frac{\text{moles of Ferrioxalate consumed}}{\text{moles of photons Absorbed } (n_{\text{photon/ferrioxalate}})} \quad \text{Eq.5}$$

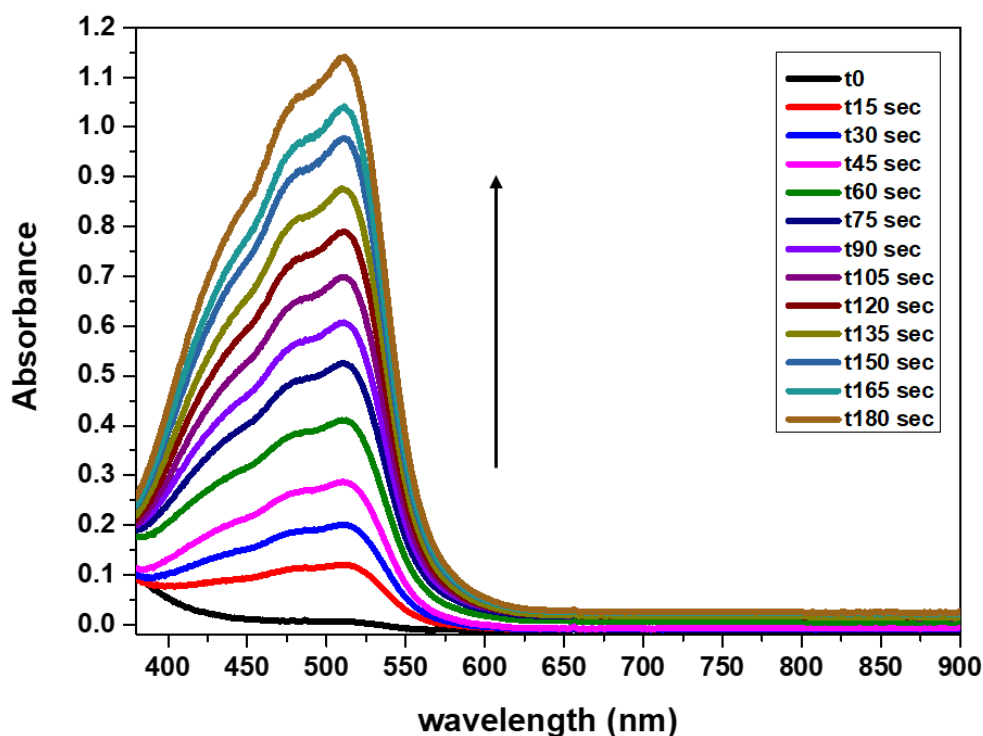


*Figure IV-5: The evolution of the UV-Vis of the  $[Fe^{II}(Phen)_3]^{2+}$  complex during the Ferrioxalate Actinometry. The spectra recorded after the mixing the aliquots collected during the irradiation of Ferrioxalate solution (aliquots during 180 sec of irradiation) and mixed with phenanthroline.*

### Synthesis of Ferrioxalate complex

Ferrioxalate complex is synthesized by reaction of iron(III) chloride ( $FeCl_3$ ) with potassium oxalate  $K_2C_2O_4$ . The synthesis was performed in a total volume of 25mL by mixing 6.25mL of 1M  $FeCl_3$  (1 volume) with 18.75mL of 1.5M  $K_2C_2O_4$  (3 volumes). The mixture is heated to 45°C and stirred for 6h in the dark (the flask being covered by aluminum foil to avoid the entrance of light). The reaction resulted in green crystals of Ferrioxalate. The Ferrioxalate crystals are then purified by performing 3 successive recrystallizations in warm water (60°C) under red light to avoid the photodegradation of the Ferrioxalate. The synthesis took place in a specific room equipped with red-light similar to a photography laboratory.

### Titration protocol: Ferrioxalate irradiation and addition of Phenanthroline to form the $[\text{Fe}^{\text{II}}(\text{Phen})_3]^{2+}$ complex

The experiment was done in a nitrogen filled glove-box under red light to avoid the undesired photodegradation of the Ferrioxalate. In a 2 ml HPLC vial, a solution of 0.02M Ferrioxalate is prepared in 1 ml of 0.1M sulfuric acid ( $\text{H}_2\text{SO}_4$ ) and irradiated using the blue LED irradiation setup (455 nm, see section IV-6.1). The concentration of Ferrioxalate was checked using the Beer-Lambert law ( $\lambda=390\text{nm}$ ,  $\epsilon_{390}=312 \pm 2 \text{ L}\cdot\text{mol}^{-1}\cdot\text{cm}^{-1}$ ).

At each irradiation time, a volume of  $24\mu\text{L}$  of the Ferrioxalate solution is collected and mixed with  $96\mu\text{L}$  of 0.025 M Phenanthroline prepared in distilled water, and  $12\mu\text{L}$  of sodium acetate buffer (NaOAc) prepared in 0.15 M  $\text{H}_2\text{SO}_4$ . The total volume of each aliquot was complete to  $240\mu\text{L}$  using distilled water.

The prepared aliquots were kept in the dark for 1 hour to ensure the complexation process between the Phenanthroline. After 1 hour, the collected samples were characterized using the UV-Vis spectrometer, and the corresponding spectra are plotted in Figure IV-3.

#### IV-6.3.2 Calculation of the Quantum Yield using the Ferrioxalate actinometry.

The absorbance peak at  $\lambda=510 \text{ nm}$ , which evolves due to the formation of the  $[\text{Fe}^{\text{II}}(\text{Phen})_3]^{2+}$  complex indicates the amount of Ferrioxalate  $[\text{Fe}^{\text{III}}]$  complex consumed. Knowing that the molar extinction coefficient of the complex  $[\text{Fe}^{\text{II}}(\text{Phen})_3]^{2+}$  complex is  $\epsilon_{510}=11100 \text{ L}\cdot\text{mol}^{-1}\cdot\text{cm}^{-1}$ . Then, the amount of Ferrioxalate consumed can be estimated according to the equation **Eq.6**

$$n_{\text{Ferrioxalate consumed}} = \frac{A_{510} \cdot V}{\epsilon_{510} \cdot l} \quad \text{Eq.6}$$

Where  $A_{510}$  is the absorbance  $[\text{Fe}^{\text{II}}(\text{Phen})_3]^{2+}$  complex at  $\lambda=510 \text{ nm}$  collected from the data represented in Figure IV-5,  $V$  is the total volume of the Ferrioxalate irradiated solution in the reaction vial at the time of each collected aliquot and  $l$  is the light path Then, the calculated amount of converted Ferrioxalate at each irradiation time is plotted in Figure IV-6-A. The maximum conversion of Ferrioxalate during the 180 seconds of irradiation is  $7.12 \times 10^{-6} \text{ mol}$ .

After subtracting the consumed amount of Ferrioxalate from the initial amount used at the beginning of the irradiation (See the protocol below), we could plot the amount of consumed or decomposed Ferrioxalate (Figure IV-6-B).

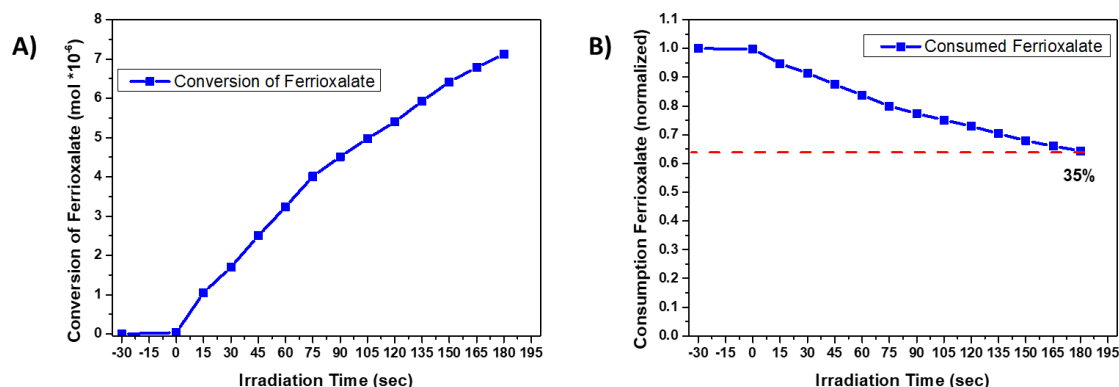


**Figure IV-6: Evolution of the Ferrioxalate complex during the irradiation.** A) Conversion of the Ferrioxalate and B) the amount of consumed Ferrioxalate. The data are determined based on the equation mentioned in the Text.

Then, taking equations Eq.5 and Eq.6 together we can determine the number of moles of photon absorbed after the maximum conversion of the Ferrioxalate according to equation Eq.7

$$\text{moles of photons Absorbed } (n_{\text{photon/ferrioxalate}}) = \frac{\text{moles of Ferrioxalate consumed}}{QY_{\text{Ferrioxalate}}} \quad \text{Eq.7}$$

Then, in order to calculate the Quantum Yield of the QD-photocatalyzed reaction, we should determine the number of moles of photons absorbed by the QDs ( $n_{\text{photon/QDs}}$ ) during the time of the photocatalytic reaction based on the number of moles of photons calculated using the Ferrioxalate actinometry. Therefore, the number of moles of photons absorbed by the QDs is calculated using equation Eq.8

$$(n_{\text{photon/QDs}}) = n_{\text{photon/ferrioxalate}} \cdot \frac{1 - 10^{-A_{455}(\text{QDs})}}{1 - 10^{-A_{455}(\text{ferrioxalate})}} \quad \text{Eq.8}$$

Where  $n_{\text{photon/ferrioxalate}}$  is the number of moles of photon absorbed by the Ferrioxalate calculated using Eq.7,  $A_{455}(\text{QDs})$  is the absorbance of the QDs during the photocatalytic reaction at  $\lambda = 455$  nm and  $A_{\text{ferrioxalate}}$  is the absorbance of the Ferrioxalate solution at  $\lambda = 455$  nm during the actinometry experiment.

Finally, after calculating the number of moles of the photon absorbed by the QDs during the photocatalytic reaction, we could estimate the Quantum yield of the reaction using the equation Eq.9

$$(QY_{QDs}) = \frac{t(\text{ferrioxalate})}{t(QDs)} \cdot \frac{n_{\text{product by QDs}}}{n_{\text{Ferrioxalate consumed}}} \cdot \frac{1-10^{-A_{455}(\text{ferrioxalate})}}{1-10^{-A_{455}(QDs)}} \cdot QY_{\text{ferrioxalate}} \quad \text{Eq.9}$$

**Sample calculation of the Quantum Yield:** Case of CdS QD-photocatalyzed C-C coupling reaction described in Chapter II (section II-4.4). The reaction yield obtained is 68% on a reaction scale of 0.001 mmol (680 TON) in 3 hours. Using equation Eq.8 we could calculate the number of moles of photon absorbed by the CdS QDs during the 3 hours irradiation to be  $3.465 \times 10^{-8}$  mol.

$\lambda_{\text{irrad}} = 455\text{nm}$ ,  $A_{QDs} = 1.1$  (for CdS QDs),  $A_{\text{ferrioxalate}} = 1.3$  (at  $\lambda=455\text{nm}$ ),  $l=1$  cm (light path in the reaction vial)

$t = 3 \text{ h} = 10800 \text{ s}$       Moles produced =  $6.8 \times 10^{-7}$  mol

Ferrioxalate reaction: 180 s, Quantum Yield at 455 nm = 1.12, amount of Ferrioxalate converted is  $7.12 \times 10^{-6}$  mol (From Figure IV-6-A).

Then using equation Eq.9 we calculated a Quantum Yield of **0.18%**.

#### IV-6.3.3 Measurement of the 455 nm LED setup power using the Ferrioxalate actinometry.

In order to confirm the power of light measured by the power sensor (section IV-6.2), we could calculate the power using the moles of photon absorbed during the Ferrioxalate actinometry. The number of moles of photons per second ( $n_{\text{photon}}$ ) could be calculated after measuring the power of light send by the irradiation setup by the following equation (Eq.10), where  $P_{\text{abs}}$  (J/s) being the power of light absorbed by the sample,  $\lambda$  is the wavelength of the LED source in meters, Planck's constant ( $h$ ),  $c$  is the speed of light and  $N_A$  being the Avogadro's number

$$n_{\text{photon}} = \frac{P_{\text{abs}} \times \lambda}{hc \times N_A} \quad \text{Eq.10}$$

Then, the Power of light absorbed by the sample could be represented as in equation Eq.11, where  $P_i$  is the initial incident light sent by the LED setup and  $A$  is the absorbance at the corresponding wavelength of the LED setup.

$$P_{\text{abs}} = P_i \cdot (1-10^{-A}) \quad \text{Eq.11}$$

Therefore, by substituting Eq.11 in Eq.10 we can calculate the initial power using eq.12

$$P_i = \frac{P_{\text{abs}}}{1-10^{-A}} = \frac{n_{\text{photon}} hc \cdot N_A}{\lambda \cdot 1-10^{-A}} \quad \text{Eq.12}$$

From the Ferrioxalate actinometry the  $n_{\text{photon/ferrioxalate}} = 3.5317 \times 10^{-8}$  mol calculated using Eq.7. And the absorbance of the ferrioxalate sample at 455 nm is 1.3.

Then  $P_i = 9.8 \text{ mW}$ , which is in good accordance with the power measured using the power meter setup (10 mW) in section IV-6.2. Thus, the actinometry measurement validates the value for the setup power measured using the power meter. Therefore for the further calculations of the Quantum yield for reactions under the irradiation of the green and the yellow LEDs we rely on the power measured as mentioned in section IV-6.2.

#### IV-6.3.4 Calculation of the Quantum Yield using the measured power

In order to calculate the QY of a QD-photocatalyzed reaction, we can use equation Eq.11 to alternatively calculate the power absorbed by the QDs during the photochemical reaction irradiated with the different LEDs, with  $A$  (in Eq.11) being the absorbance of the QDs at the corresponding irradiation wavelength.

For example, in the case of CdS QDs with absorbance equals 1.1 at  $\lambda = 455 \text{ nm}$  we calculated the absorbed power to be  $P_{\text{abs(QD)}} = 9.2 \times 10^{-3} \text{ W}$ .

Then, using equation Eq.10 and the calculated  $P_{\text{abs(QD)}}$ , we could calculate the moles of photons absorbed by the QDs during the photochemical reaction of the same case of CdS QDs (at  $\lambda = 455 \text{ nm}$ ) to be  $n_{\text{photon(QD)}} = 3.496 \times 10^{-8} \text{ mol}$ .

Taking the case of CdS QD-photocatalyzed C-C coupling reaction described in Chapter II (section II-4.4). The reaction yield obtained is 68% on a reaction scale of 0.001 mmol (680 TON) in 3 hours, then the number of moles produced =  $6.29 \times 10^{-11} \text{ mol/s}$ .

Using Eq.4 the QY is calculated to be **0.18%**.

Same way of computation was used for all the calculated Quantum Yields for the QD-photocatalyzed reactions by taking into account the power of light measured for the green and yellow LED setups as described in section IV-6.2.

### IV-7. Experimental protocols.

#### IV-7.1 Photocatalysis Experiments.

All photocatalytic reactions were carried out in a 2ml clear glass screw cap HPLC vial (See Figure IV-7-A) under an inert atmosphere in a nitrogen-filled glovebox. All the stock solutions of the reactions' reagents and the Quantum Dots were dissolved in degassed solvents placed in the glovebox. The total volume and the concentrations of the reactions' reagent were adapted to the reaction's scale, and the reaction medium was maintained under continuous stirring using a magnetic stirring bar over the complete irradiation time. The reaction mixtures were set for irradiation using the home-made irradiation setup connected to Osolon4 power Star LED source of suitable wavelength (See section IV-6). During the irradiation, small volume aliquots ( $\sim 30\mu\text{l}$ ) were taken for the analyses at specific intervals of time during the reaction (Figure IV-7-B). All the aliquots were taken inside the glovebox, and the reaction vial was opened only in the glovebox. Then, samples of the collected aliquots were injected in UV-HPLC or UHPLC-MS systems for the analyses.

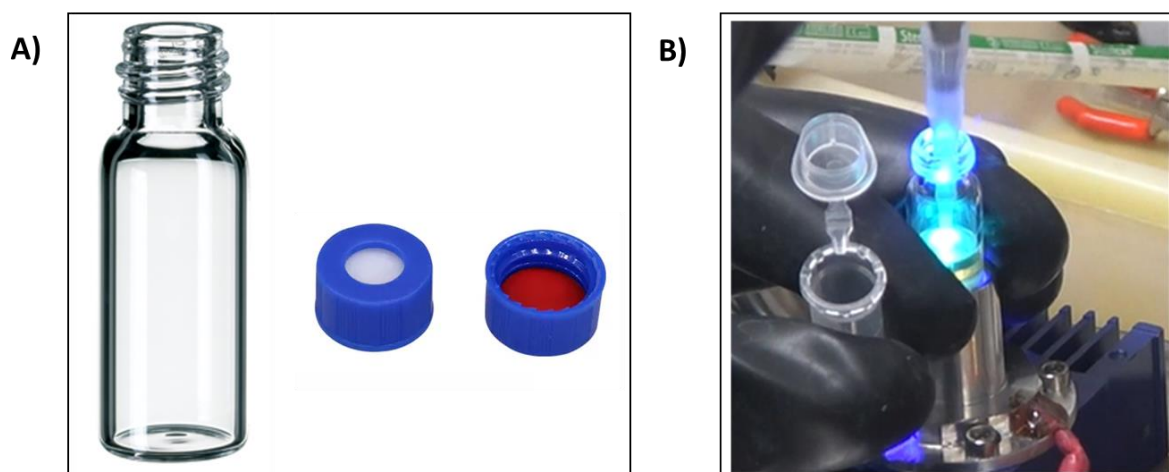


**Figure IV-7: Reaction vessels used for the photocatalysis experiments.** A) 2ml clear glass screw cap HPLC vial with a septum bonded cap. B) Aliquots collection for the analysis.

### IV-7.2- Photoluminescence quenching.

The photoluminescence quenching experiments were carried out in a Quartz Fluorescence micro-cuvette (Figure IV-8). To start the quenching experiments, 120 $\mu$ L of the QDs solution of known concentration and corresponding absorbance close to 0.5 at the excitation wavelength were filled in the cuvette. Using PerkinElmer LS 55 spectrometer, the initial photoluminescence spectrum of the QDs was recorded before the addition of the quencher. Then, specific volumes from the stock solution of the quencher were added consecutively to the cuvette containing the QDs solution. The photoluminescence was recorded after each addition of the quencher. The addition of the quencher stopped after adding up to 120 $\mu$ L of the quencher and taking into account the targeted concentration of the added quencher.



*Figure IV-8: 200  $\mu$ L Quartz Fluorescence cuvette. The cuvette used for the quenching experiments.*

### IV-7.3- Photochemical charging/discharging experiments in the case of QD-AuNP nanocomposites.

The photochemical charging measurements of the AuNP (Described in Chapter III, section III-4) were performed using a UV-Vis absorbance spectrometer connected through fibers optics connection to a sample holder placed in a Nitrogen-filled glovebox to monitor the evolution of the absorbance band position of the nanoparticles. The solutions were prepared in QS 10.00mm Hellma Quartz cuvette and irradiated with the convenient irradiation setup of 590 nm yellow LED. In this particular experiment, a home-made setup was designed to connect the sample holder (for the cuvette) to the absorbance spectrometer. For the irradiation during the experiments, the Light was guided from the irradiation setup to the

cuvette placed in the sample holder using a Quartz rod to ensure an efficient irradiation (see Figure IV-9). The experimental conditions were set for a composite sample of 20nM QDs concentrated samples for the charging of the composite experiment. Moreover, a reference sample of non-connected QDs with no click ligands and mixed with AuNP, and pure AuNP, but with the same experimental conditions as in the case of the QD-AuNP nanocomposites case were also tested. The light source was stopped for the discharging process, and 310 $\mu$ M of NO<sub>2</sub>PhAla as electron acceptor was added. The UV-Vis absorbance was measured using the same cuvette when placed and maintained at a fixed geometry in the spectrometer sample holder.

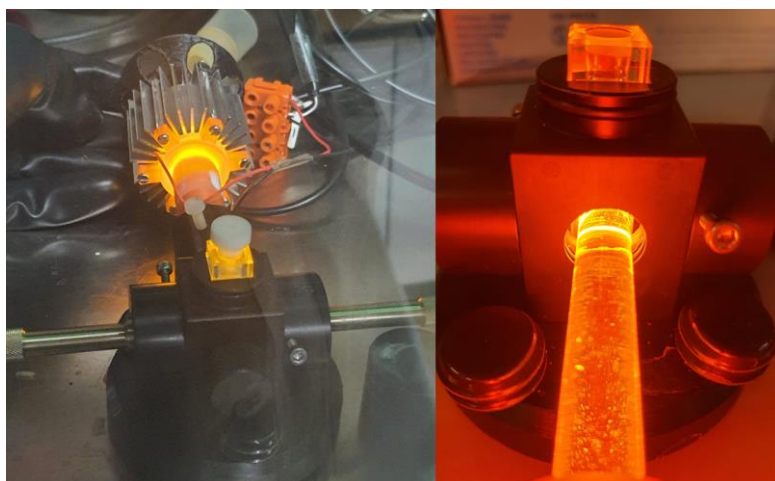


**Figure IV-9:** Setup used during the photochemical charging/discharging experiments. The Light from the irradiation setup was guided to the cuvette using Quartz rod.

### IV-7.4- Cyclic voltammetry.

The cyclic voltammetry experiment were done with the supervision of Dr. Julie ANDREZ (Researcher in the CAMPE team). Cyclic voltammetry experiments were carried out for 1mM of the tested compounds prepared in the presence of 0.1M of [Bu<sub>4</sub>N][PF<sub>6</sub>] supporting electrolyte in acetonitrile solution. All the experiments were done at room temperature in an argon-filled glovebox. Data were collected using a BioLogic SP-300 potentiostat connected to a three-electrodes system, including a glassy carbon disk (d=1mm) working electrode, a platinum wire counter electrode, and an Ag/AgCl reference electrode. The voltammograms of each compound were recorded at different scan rates (from 20 mV/s to 20 V/s). Potential calibration was performed at the end of each data collection cycle using the ferrocene/ferrocenium couple as an internal standard ( $E^\circ = 0.630$  V/NHE).

## IV-8 –Detection of reactions' products using UV-HPLC or UHPLC-MS.

The monitoring of the reaction's evolution and determining the corresponding reactions' yield were performed using UV-HPLC or UHPLC-MS analysis. For the analyses, several aliquots were collected during the reaction using a micropipette, as shown in Figure IV-7-B. Before the injections in the HPLC systems, the aliquots were centrifuged in order to precipitate the QDs. After centrifugation, the samples of the reactions' aliquots were collected and diluted in solvents compatible with the HPLC columns such as water or acetonitrile. The dilution was done to reach a range of 10-100 nM concentration to avoid the contamination of the HPLC columns and for optimal detection by the MS spectrometer. The dilution in acetonitrile was essential in the case of the reaction performed in TFT. The samples were prepared for the HPLC injections in HPLC vial equipped with the corresponding inserts. The optimization of the HPLC and the MS detection methods were done with help and the supervision of Dr. Jean Luc RAVANAT (Researcher at the SYMMES unit, CIBEST team). The injections of the samples and the instrumental usage of the HPLC systems were done with the help of Dr. Jean Luc RAVANAT and M. Sylvain CAILLAT (Technician at the SYMMES unit, CIBEST team).

**UV-HPLC.** UV-HPLC analyses were performed using an Agilent Technologies 1200 series apparatus equipped with XTerra C18 RP18, 3.5  $\mu\text{m}$ , 4.6x250 mm column filled with silica beads and coupled with a photodiode array absorbance detector. In addition, the wavelength of the absorbance detection was set to be suitable for each reaction substrate or product. For the monitoring of the decay of 8-oxo-dG and nitrophenylalanine derivatives (described in Chapter III), the elution gradients were set for acetonitrile in ammonium formate (5mM) as HPLC buffer. The elution gradients were set for acetonitrile from 0% to 15% in ammonium formate (5mM) as HPLC buffer for the first 25 minutes and then from 15% to 80% in 15 min. Substrates decay was monitored by absorbance detection (DAD) at wavelength  $\lambda = 295 \text{ nm}$  and wavelength  $\lambda = 230$  for possible product formation.

**UHPLC-MS.** The UHPLC-MS analyses were performed with a triple quadrupole mass spectrometer TSQ Quantum Ultra from Thermo Scientific connected to a Thermo Accela pump, an Accela autosampler, an Accela photodiode array detector, and equipped with HALO 90 Å Phenyl-Hexyl, 2.7 $\mu\text{m}$ , 2.1 x 100 mm UHPLC column filled with silica beads. The elution gradients were set for 12 minutes of total elution time (short time needed using the UHPLC

column), starting with acetonitrile from 0% to 50% in ammonium formate (2mM) buffer for the first 20 minutes and then reaching 80% of acetonitrile for the last 2 minutes. The mass spectrometry detections were performed using Selected Ion Monitoring (SIM) mode, which allows the mass spectrometer to detect specific compounds with very high sensitivity. In SIM mode, the instrument collects the data at the masses of interest instead of stepping the mass filter over a wide range of masses. This mode of operation typically results in significantly increased sensitivity.

### IV-9. Analyses and characterization techniques.

**UV-Visible Absorbance spectroscopy.** The UV-Vis absorbance spectroscopic characterizations of the Quantum Dots and other chemicals were performed using Hewlett Packard (hp) HP 8H52 diode array spectrophotometer. The measurements were done using quartz cuvettes and recorded over a wavelength range of 190 nm to 820 nm with a 2 nm step. The UV-Vis absorbance measurements during the photochemical charging/discharging experiments in the case of the QD-AuNP composites were performed using a TIDAS® S 500 MCS UV/VIS 1961 diode array spectrometer connected through fibers optics connection to a cuvette sample holder placed in a Nitrogen-filled glovebox to monitor the evolution of the absorbance behavior of the AuNPs.

**Photoluminescence spectroscopy.** The photoluminescence spectra were recorded using a PerkinElmer LS 55 spectrometer having a wavelength range between 200 to 800 nm and a power of 120 V, 1.25 A, 50/60 Hz. The excitation wavelength, the range and the width of the slits were adapted for each sample.

**Electronic microscope imaging:** Transmission electron microscopy (TEM) was performed on a Philips CM300 microscope operating at 300 kv. The TEM grid was prepared by depositing and drying a dilute 10 mL drop of colloidal suspension on a carbon-coated copper grid. Images were collected on a TemCam F416 TVIPS. The samples were prepared in the CAMPE team but the imaging were done in the OPTIMA team by Dr. Fabien DUBOIS. The data treatment were done using ImageJ software.

## References

- (1) Colson, E.; Andrez, J.; Dabbous, A.; Dénès, F.; Maurel, V.; Mouesca, J.-M.; Renaud, P. Tropene and Related Alkaloid Skeletons via a Radical [3+3]-Annulation Process. **2021**. <https://doi.org/10.26434/chemrxiv-2021-gq1jb-v2>.
- (2) Schönweiz, S.; Knoll, S.; Anjass, M.; Braumüller, M.; Rau, S.; Streb, C. "CLICKable" Azide-Functionalized Phosphonates for the Surface-Modification of Molecular and Solid-State Metal Oxides. *Dalton Trans.* **2016**, 45 (41), 16121–16124. <https://doi.org/10.1039/C6DT03370A>.
- (3) Yu, W. W.; Peng, X. Formation of High-Quality CdS and Other II–VI Semiconductor Nanocrystals in Noncoordinating Solvents: Tunable Reactivity of Monomers. *Angewandte Chemie International Edition* **2002**, 41 (13), 2368–2371. [https://doi.org/10.1002/1521-3773\(20020703\)41:13<2368::AID-ANIE2368>3.0.CO;2-G](https://doi.org/10.1002/1521-3773(20020703)41:13<2368::AID-ANIE2368>3.0.CO;2-G).
- (4) Zhang, Z.; Rogers, C. R.; Weiss, E. A. Energy Transfer from CdS QDs to a Photogenerated Pd Complex Enhances the Rate and Selectivity of a Pd-Photocatalyzed Heck Reaction. *J. Am. Chem. Soc.* **2020**, 142 (1), 495–501. <https://doi.org/10.1021/jacs.9b11278>.
- (5) Chambrier, I.; Banerjee, C.; Remiro-Buenamañana, S.; Chao, Y.; Cammidge, A. N.; Bochmann, M. Synthesis of Porphyrin–CdSe Quantum Dot Assemblies: Controlling Ligand Binding by Substituent Effects. *Inorg. Chem.* **2015**, 54 (15), 7368–7380. <https://doi.org/10.1021/acs.inorgchem.5b00892>.
- (6) Wang, P.; Wang, M.; Zhang, J.; Li, C.; Xu, X.; Jin, Y. Shell Thickness Engineering Significantly Boosts the Photocatalytic H<sub>2</sub> Evolution Efficiency of CdS/CdSe Core/Shell Quantum Dots. *ACS Appl. Mater. Interfaces* **2017**, 9 (41), 35712–35720. <https://doi.org/10.1021/acsami.7b07211>.
- (7) Pan, Z.; Zhang, H.; Cheng, K.; Hou, Y.; Hua, J.; Zhong, X. Highly Efficient Inverted Type-I CdS/CdSe Core/Shell Structure QD-Sensitized Solar Cells. *ACS Nano* **2012**, 6 (5), 3982–3991. <https://doi.org/10.1021/nn300278z>.
- (8) Chen, D.; Zhao, F.; Qi, H.; Rutherford, M.; Peng, X. Bright and Stable Purple/Blue Emitting CdS/ZnS Core/Shell Nanocrystals Grown by Thermal Cycling Using a Single-Source Precursor. *Chem. Mater.* **2010**, 22 (4), 1437–1444. <https://doi.org/10.1021/cm902516f>.
- (9) Niu, Y.; Pu, C.; Lai, R.; Meng, R.; Lin, W.; Qin, H.; Peng, X. One-Pot/Three-Step Synthesis of Zinc-Blende CdSe/CdS Core/Shell Nanocrystals with Thick Shells. *Nano Res.* **2017**, 10 (4), 1149–1162. <https://doi.org/10.1007/s12274-016-1287-3>.
- (10) Tessier, M. D.; Dupont, D.; De Nolf, K.; De Roo, J.; Hens, Z. Economic and Size-Tunable Synthesis of InP/ZnE (E = S, Se) Colloidal Quantum Dots. *Chem. Mater.* **2015**, 27 (13), 4893–4898. <https://doi.org/10.1021/acs.chemmater.5b02138>.
- (11) Zylstra, J.; Amey, J.; Miska, N. J.; Pang, L.; Hine, C. R.; Langer, J.; Doyle, R. P.; Maye, M. M. A Modular Phase Transfer and Ligand Exchange Protocol for Quantum Dots. *Langmuir* **2011**, 27 (8), 4371–4379. <https://doi.org/10.1021/la104542n>.
- (12) Calzada, R.; Thompson, C. M.; Westmoreland, D. E.; Edme, K.; Weiss, E. A. Organic-to-Aqueous Phase Transfer of Cadmium Chalcogenide Quantum Dots Using a Sulfur-Free Ligand for Enhanced Photoluminescence and Oxidative Stability. *Chem. Mater.* **2016**, 28 (18), 6716–6723. <https://doi.org/10.1021/acs.chemmater.6b03106>.
- (13) Turkevich, J.; Stevenson, P. C.; Hillier, J. A Study of the Nucleation and Growth Processes in the Synthesis of Colloidal Gold. *Discuss. Faraday Soc.* **1951**, 11 (0), 55–75. <https://doi.org/10.1039/DF9511100055>.

- (14) Frens, G. Controlled Nucleation for the Regulation of the Particle Size in Monodisperse Gold Suspensions. *Nature Physical Science* **1973**, *241* (105), 20–22. <https://doi.org/10.1038/physci241020a0>.
- (15) Yu, W. W.; Qu, L.; Guo, W.; Peng, X. Experimental Determination of the Extinction Coefficient of CdTe, CdSe, and CdS Nanocrystals. *Chem. Mater.* **2003**, *15* (14), 2854–2860. <https://doi.org/10.1021/cm034081k>.
- (16) Jasieniak, J.; Smith, L.; van Embden, J.; Mulvaney, P.; Califano, M. Re-Examination of the Size-Dependent Absorption Properties of CdSe Quantum Dots. *J. Phys. Chem. C* **2009**, *113* (45), 19468–19474. <https://doi.org/10.1021/jp906827m>.
- (17) Reiss, P.; Protière, M.; Li, L. Core/Shell Semiconductor Nanocrystals. *Small* **2009**, *5* (2), 154–168. <https://doi.org/10.1002/sml.200800841>.
- (18) Kuhn, H. J.; Braslavsky, S. E.; Schmidt, R. Chemical actinometry (IUPAC Technical Report). *Pure and Applied Chemistry* **2004**, *76* (12), 2105–2146. <https://doi.org/10.1351/pac200476122105>.
- (19) Vandekerckhove, B.; Piens, N.; Metten, B.; Stevens, C. V.; Heugebaert, T. S. A. Practical Ferrioxalate Actinometry for the Determination of Photon Fluxes in Production-Oriented Photoflow Reactors. *Org. Process Res. Dev.* **2022**, *26* (8), 2392–2402. <https://doi.org/10.1021/acs.oprd.2c00079>.





## General Conclusion and Perspectives

This thesis explores the use of different kinds of semiconductor Quantum Dots (QDs) as photocatalysts for organic reactions. In the first part, we show the ability of QDs to photocatalyze a newly developed organic reaction targeting the synthesis of natural products of Tropane derivatives. The success of this reaction requires two successive charge transfer processes from the photoexcited QDs. Therefore, we study and compare the activity of different types and structures of Quantum Dots to perform the desired reaction's steps. We show that core structured CdS and CdSe QDs are able to perform all the required redox steps to obtain the desired final product of the reaction.

The activity of the core-shell structured QDs varies according to the delocalization and the accessibility of the charge carriers. For example, the activity of the inverted type-I QDs, which have the electron and the hole delocalized in the outer shell of the QDs, was efficient and comparable to the activity of the core CdSe QDs. However, type-I and quasi type-II QDs show low activity for our reaction as the holes in these structures of QDs are localized in the core of the QDs. Moreover, we show that InP-ZnS QDs were selective towards only the first reaction step, probably due to their low reducing conduction band edge position.

The surface functionalization of the QDs by mixing two ligands of different chain lengths (short and long) significantly influences their photocatalytic activity. This ligand layer optimization ensures a better permeability for the reaction substrates to reach the QDs' surface and perform the desired redox processes. In addition, this ligand layer optimization retains the stability of the QDs and makes them reusable for more than one reaction round. In this context, the best Quantum yield of the photocatalytic reaction is measured to be 0.18% using CdS QDs for the one-step reaction.

As a perspective for this part, the upscaling of the QD-photocatalyzed Tropane synthesis reaction is underway. This is taking place within the collaboration with our colleagues for the Renaud group in Switzerland in order to run the QD-photocatalyzed reactions on preparative chemistry scales.

Furthermore, the investigation of the use of QDs to photocatalyze new carbon-carbon coupling reactions starting by oxidative radical generation from sulfone or sulfinate-based compounds is also underway in close collaboration with the Renaud group.

Quantum Dots photocatalyzed organic reactions exhibit low quantum yields, and the reactions require a long irradiation time to be completed. This is referred to the fast charge recombination. Therefore, improving the charge separation in the photoexcited QDs is essential for enhancing their photocatalytic activity. In this context, we have designed a hybrid CdSe/ZnS Quantum Dots (QD) and Gold nanoparticles (AuNP) nanocomposite intended to enhance the separation of the charges generated by the QDs. The QD-AuNP nanocomposites are prepared by a new methodology based on forming covalent bonds linking the semiconductor QDs to AuNP using a Click chemistry approach.

The photocatalytic activity of the newly designed QD-AuNP nanocomposite is tested on a complete redox system consisting of 8-oxo-dG molecules as electron donors and nitrophenylalanine derivatives as electron acceptors. The QD-AuNP composites exhibit higher efficiency and speed than the bare QD by achieving 5 times more turnover numbers in the complete reaction's time, and the reaction is 24 times faster in the first minutes of the irradiation time. Furthermore, the mechanistic studies on the photoexcited QD-AuNP nanocomposites indicate the transfer of up to 7400 electrons per AuNP from the photoexcited QDs.

The prepared QD-AuNP composites are stabilized in an aqueous medium, so the transfer and the preparation of such QD-AuNP composites in organic solvents is considered the next step for this project. Moreover, the use of the QD-AuNP composites for organic bond formation reactions, such as the reactions described in Chapter II, is also one of the main future perspectives of this Thesis.



## Abstract

During the last decade, the development of visible-light photocatalysts has revolutionized the synthetic organic chemistry field. Colloidal semiconductor nanocrystals, commonly known as Quantum Dots (QDs), have shown great promise as photocatalysts for various organic transformations, including oxidations, reductions, and, most recently, bond-forming reactions. QDs possess several encouraging properties for photocatalysis, including their size-tunable oxidation and reduction potentials and their high extinction coefficient values in the visible domain. In addition, due to their optical and size properties, QDs can interact with several substrates at once using very low catalytic loadings. In this Thesis, we have prepared different types and structures of QDs such as CdS, CdSe, and InP core-type QDs and different types of core-shell QDs such as CdSe-CdS, CdS-CdSe, CdSe-ZnS, and InP-ZnS. We also optimized the surface ligands layer to ensure better interaction between the QDs' and the reaction substrates. After testing the photophysical properties and the possible charge transfer between the QDs and the desired reaction's substrates, we used the prepared QDs as photocatalysts for newly developed reactions aiming to prepare value-added natural products (such as Tropane derivatives). Furthermore, we designed a new kind of semiconductor-metallic hybrid nanostructure by assembling CdSe-ZnS QDs with Gold nanoparticles (AuNP). The QD-AuNP nanostructures were chemically assembled using a click chemistry approach benefiting from the surface ligands functionalizing the QDs and the AuNP. The prepared hybrid structure enhanced the photocatalytic catalytic activity compared to the bare QDs-photocatalyzed reaction. The enhanced activity referred to the better charge separation and the new optical properties in the QD-AuNP hybrid nanostructure.

## Résumé

Au cours de la dernière décennie, le développement des photocatalyseurs à lumière visible a révolutionné le domaine de la chimie organique synthétique. Les nanocristaux semi-conductrices colloïdales, communément appelés Quantum Dots (QDs), se sont révélés très prometteurs en tant que photocatalyseurs pour diverses transformations organiques, notamment les oxydations, les réductions et plus récemment, les réactions de formation de liaisons. Les QDs possèdent plusieurs propriétés encourageantes pour la photocatalyse, notamment leurs potentiels oxydation et réduction ajustables en fonction de leurs tailles et leurs valeurs élevées de coefficient d'extinction dans le domaine visible. De plus, grâce à leurs propriétés optiques et leurs tailles, les QDs peuvent interagir avec plusieurs substrats à la fois en utilisant de très faibles charges catalytiques. Dans cette thèse, nous avons préparé différents types et structures de QDs tels que des QDs de type cœur CdS, CdSe et InP et différents types de QDs cœur-coquille tels que CdSe-CdS, CdS-CdSe, CdSe-ZnS et InP-ZnS. Nous avons également optimisé la couche de ligands de surface pour assurer une meilleure interaction entre les QDs et les substrats de réaction. Après avoir testé les propriétés photophysiques et le transfert de charge possible entre les QDs et les substrats de la réaction souhaitée, nous avons utilisé les QDs préparés comme photocatalyseurs pour des réactions nouvellement développées visant à préparer des produits naturels à haute valeur ajoutée (tels que des dérivés de Tropane). De plus, nous avons conçu un nouveau type de nanostructure hybride semi-conducteur-métallique en assemblant des QDs CdSe-ZnS avec des nanoparticules d'or (AuNP). Les nanostructures QD-AuNP ont été assemblées chimiquement à l'aide d'une approche de chimie click profitant des ligands de surface fonctionnalisant les QDs et les AuNP. La structure hybride préparée a amélioré l'activité photocatalytique par rapport à la réaction photocatalysée par les QDs nus. L'amélioration de l'activité est due à une meilleure séparation des charges et aux nouvelles propriétés optiques de la nanostructure hybride QD-AuNP.